DOE/ER-0045/7

Alloy Development for Irradiation Performance

Semiannual Progress Report
For Period Ending September 30, **1981**

U.S. Department of Energy
Office of Fusion Energy

Printed in the United States of America. Available from
National Technical Information Service
U.S. Department of Commerce
5285 Port Royal Road, Springfield. Virginia 22161
NTIS price codes—Printed Copy: A16 Microfiche A01

DOE/ER-0045/7
Distribution
Category
UC-20, 20c

ALLOY DEVELOPMENT FOR IRRADIATION PERFORMANCE SEMIANNUAL PROGRESS REPORT FOR PERIOD ENDING SEPTEMBER 30, 1981

ARGONNE NATIONAL LABORATORY

GENERAL ATOMIC COMPANY

HANFORD ENGINEERING DEVELOPMENT LABORATORY

McDONNELL DOUGLAS ASTRONAUTICS COMPANY

MASSACHUSETTS INSTITUTE OF TECHNOLOGY

NAVAL RESEARCH LABORATORY

OAK RIDGE NATIONAL LABORATORY

SANDIA NATIONAL LABORATORIES

WESTINGHOUSE FUSION POWER SYSTEMS

Date Published: March 1982

Prepared by
OAK RIDGE NATIONAL LABORATORY
Oak Ridge, Tennessee 37830
operated **by**
UNION CARBIDE CORPORATION
for the
DEPARTMENT OF ENERGY
Under Contract No. W-7405-eng-26

Reports previously issued in this series are as follows:

DOE/ET-0058/1	Period Ending March 31, 1978
DOE/ET-0058/2	Period Ending June 30, 1978
DOE/ET-0058/3	Period Ending September 30, 1978
DOE/ET-0058/4	Period Ending December 31, 1978
DOE/ET-0058/5	Period Ending March 31, 1979
DOE/ET-0058/6	Period Ending June 30, 1979
DOE/ET-0058/7	Period Ending September 30, 1979
DOE/ER-0045/1	Period Ending December 31, 1979
DOE/ER-0045/2	Period Ending March 31, 1980
DOE/ER-0045/3	Period Ending June 30, 1980
DOE/ER-0045/4	Period Ending September 30, 1980
DOE/ER-0045/5	Period Ending December 31, 1980
DOE/ER-0045/6	Period Ending March 31, 1981

FOREWORD

This report is the fourteenth in a series of Technical Progress Reports on *"Alloy Development for Irradiation Performance"* (ADIP), which is one element of the Fusion Reactor Materials Program, conducted in support of the Magnetic Fusion Energy Program of the U.S. Department of Energy. Other elements of the Materials Program are

- *Damage Analysis and Fundamental Studies (DAFS)*
- *Plasma-Materials Interaction (PMI)*
- *Special-Purpose Materials (SPM)*

The first seven reports in this series are numbered DOE/ET-0058/1 through 7. This report is the seventh in a new numbering sequence that begins with DOE/ER-0045/1.

The ADIP program element is a national effort composed of contributions from a number of National Laboratories and other government laboratories, universities, and industrial laboratories. It was organized by the Materials and Radiation Effects Branch, Office of Fusion Energy, DOE, and a Task Group on *Alloy Development* for *Irradiation Performance,* which operates under the auspices of that Branch. The purpose of this series of reports is to provide a working technical record of that effort for the use of the program participants, for the fusion energy program in general, and for the Department of Energy.

This report is organized along topical lines in parallel to a Program Plan of the same title *so* that activities and accomplishments may be followed readily relative to that Program Plan. Thus, the work of a given laboratory may appear throughout the report. Chapters 1, 2, 8, and 9 review activities on analysis and evaluation, test methods development, status of irradiation experiments, and corrosion testing and hydrogen permeation studies, respectively. These activities relate to each of the alloy development paths. Chapters 3, 4, 5, 6, and 7 present the ongoing work on each alloy development path. The Table of Contents is annotated for the convenience of the reader.

This report has been compiled and edited under the guidance of the Chairman of the Task Group on *Alloy Development for Irradiation Performance.* E. E. Bloom, Oak Ridge National Laboratory, and his efforts and those of the supporting staff of ORNL and the many persons who made technical contributions are gratefully acknowledged. T. C. Reuther, Materials and Radiation Effects Branch, is the Department of Energy Counterpart to the Task Group Chairman and has responsibility for the ADIP Program within DOE.

D. L. Vieth, Chief
Materials and Radiation Effects Branch
Office of Fusion Energy

CONTENTS

The compatibility of solid Li_2O, $LiAlO_2$, and Li_2SiO_3 breeding materials with several commercial alloys has been investigated at 873 and 973 K. The results show that Li_2O is the most reactive and $LiAlO_2$ is the least reactive of the three breeding materials. The reaction scales on alloys exposed with Li_2O ceramic contain Li_5FeO_4 and $LiCrO_2$ compounds. The formation of those compounds may explain the greater interaction between the alloys and Li_2O material. Compatibility tests at 773 K are in progress. A compatibility-test facility is being constructed to study the alloy/ceramic interactions in a flowing helium environment containing known amounts of moisture.

1. ANALYSIS AND EVALUATION STUDIES

1.1 FUNCTIONAL REQUIREMENTS FOR FUSION REACTOR FIRST WALLS — A. O. Adegbulugbe and J. E. Meyer (Massachusetts Institute of Technology)

To be reported in the next semiannual report.

1.2 MATERIALS HANDBOOK FOR FUSION ENERGY SYSTEMS - J. W. Davis (McDonnell Douglas Astronautics Company - St. Louis) and T. K. Bierlein (Hanford Engineering Development Laboratory)

1.2.1 ADIP Task

Task Number **1.A.1** - Define material property requirements and make structural life predictions.

1.2.2 Objective

To provide a consistent and authoritative source of material property data for **use** by the fusion community in concept evaluation, design, safety analysis, and performance/verification studies of various fusion energy systems. A secondary objective is the early identification of areas in the materials data base where insufficient information or voids exist.

1.2.3 Summary

The second publication package of data sheets for the MHFES has been released and the third publication package should be released by the time this report is printed. The second publication package contains revisions of the handbook introductory pages along with data sheets on the elevated temperature fatigue crack growth of 20% cold worked type 316 stainless steel. The third publication package, which is currently in printing, contains information on a glass epoxy laminate called G-10CR which is used in superconducting magnets. Data sheets on the electrical resistivity, tritium permeability, and irradiation induced swelling of 20% cold work stainless steel have been received and currently under review prior to publication.

1.2.4 Progress and Status

During the first six months of this year, the primary thrust of the materials handbook was directed towards establishing a format, page classification, a method for preparing pages, and a process for reviewing the data pages prior to publication. Very little effort was devoted to actual data sheet preparation. As a consequence the handbook contained

only a limited amount of information which related to the unirradiated properties of 316 stainless steel. It was not until May that actual engineering information started to find its way into the handbook. This was the effect of irradiation on the elevated temperature fatigue strength of 20% cold worked stainless steel which was prepared by M. L. Grossbeck of ORNL. To rectify this situation a substantial effort was launched to try to get information into the handbook. This effort is starting to bear fruit in that a number of data pages are either in preparation, review, or have been published. The first of these covers the elevated temperature fatigue crack growth of 20% cold worked 316 stainless steel which was prepared by A. M. Ermi of HEDL. These data pages differ from similar data pages found in other material data books in that they contain extrapolations into the near-threshold regions of crack growth. This information was needed because a number of structural analysts in trying to assess the life of a first wall were making their own extrapolations of the data and ending up with a wide range of conclusions regarding component lifetimes depending on how the extrapolations were made. In an effort to get consistency in this analysis it was decided by the Analysis and Evaluation task group that a goal for the handbook would be to get the material scientists who are familiar with crack growth data to make these extrapolations which would be based on their "best guess" of what the material response should be. These data pages formed the basis for the second publication package which was released in June. Also during this time frame data sheets relating to the electrical resistivity and tritium permeability of 20% cold worked 316 stainless steel were being prepared by R. F. Mattas of ANL. These data sheets have been reviewed by the Analysis and Evaluation task group and returned to Dr. Mattas for revision. The revised data sheets were subsequently returned to the handbook and are now in the process of being reviewed by the Analysis and Evaluation task group prior to their release for publication. Publication of these data pages is anticipated for early next year. In addition to receiving data pages on physical and mechanical properties, predictive equations have also been submitted. The handbook received two separate equations describing irradiation induced stress free swelling, one submitted by P. J. Maziasz of ORNL and the other by

F. A. Garner of HEDL. Since each of these equations predicts a different swelling rate, work is in progress to try to resolve the differences prior to their release. Publication of a final swelling equation is not anticipated before the middle of next year. All of the data sheets previously described focused on the properties of 316 stainless steel for use in the first wall structure of the Fusion Engineering Device (FED). However in the design of a fusion reactor, properties will be needed on a variety of materials in addition to those planned for use in the first wall. One area in which material property information is needed now is in the design of superconducting magnets. Superconducting magnets are currently planned for use on near term machines such as EBT-P and MFTF-B and longer term devices such as FED and DEMO along with the commercial designs. In order to support the near term design projects and the longer range conceptual designs, requests were made to various organizations active in the field of superconducting magnets to provide data sheets. In response to this request data sheets were provided by G. P. Lang of MDAC for the G-10CR (glass epoxy laminate) which is used as an insulator in superconducting magnets. These data sheets cover a wide range of properties including both physical and mechanical and were prepared in support of the EBT-P project. All of these data sheets have been reviewed and approved by the Analysis and Evaluation task group and are planned for release in the 3rd publication package which should be available in early December.

1.2.5 Future Work

The effort for the handbook over the next 6 months will continue to be directed towards the preparation of data sheets for a wide range of materials. Currently planned data sheets will cover ferritic steels, magnet case steel, solid lithium compounds, and armor or tile materials.

2. TEST MATRICES AND METHODS DEVELOPMENT

2.1 Neutron Source Characterization for Materials Experiments – L. R. Greenwood (Argonne National Laboratory)

2.1.1 ADIP/DAFS Tasks

ADIP Task I.A.2 – Define Test Matrices and Procedures

DAFS Task II.A.l – Fission Reactor Dosimetry

2.1.2 Objective

To characterize neutron environments in terms of neutron flux and spectra as well as fundamental damage parameters @PA, PKA, transmutation) and to measure these exposure parameters during materials irradiations.

2.1.3 Summary

Dosimetry results are presented for the MFE2 and MFE4A irradiations in ORR. The status of all the experiments is summarized in Table 2.1.1.

2.1.4 Progress and Status

2.1.4.1 Dosimetry Results for the ORR-MFE2 Experiment

Dosimeters have been counted from the ORR-MFE2 experiment which was irradiated from September 1, 1978 to March 24, 1980 in position E7 of the Oak Ridge Research Reactor. The sample was out of the reactor for 154 days; hence, the total time in core was 416 days. The average power level was 19.24 MW (26.4 MW in core) and the accumulated exposure was 10,972 MWD. Sixteen small dosimetry capsules (Co-Al, Fe, Ni, and Ti wires) were included with the experimental assemblies, one in each assembly on level 1-4, labeled E-V. Two 30-cm long dosimetry

TABLE 2.1.1

STATUS OF REACTOR EXPERIMENTS

Facility/Experiment	Status and Comments
ORR - MFEl	Completed 12/79
- MFE2	Completed 6/81
- MFE4A	Completed 8/81
- MFE4B,C	Irradiation in Progress
- TBC07	Completed 7/80
- TRIO	Planning in Progress
HFIR - CTR 32	Samples Received 5/81
- CTR 30,31	Irradiation in Progress
- CTR 34,35	Samples Provided 9/81
- T1,T2	Irradiation in Progress
- T3	Samples Provided 9/81
- RB1,2,3	Samples Provided 9/81
Omega West - Spectral Analysis	Completed 10/80
- HEDL1	Completed 5/81
EBR II - X287	Completed 9/81

tubes were welded to the outside of the assembly on the east side. One tube contained the above mentioned wires. The other contained helium accumulation monitors and radiometric wires. All radiometric samples have been gamma counted as well as selected helium samples. The latter have been sent to Rockwell International (D. Kneff and H. Farrar IV) for helium analysis.

Six reactions were analyzed from the dosimetry wires, namely, $^{59}Co(n,\gamma)$, $^{58}Fe(n,\gamma)$, $^{54}Fe(n,p)$, $^{46}Ti(n,p)$, $^{58}Ni(n,p)$, and $^{60}Ni(n,p)$. However, as was found with MFE1, the two nickel reactions have very large burnup corrections since ^{58}Co is converted to ^{60}Co in the high thermal flux. Hence, the nickel reactions are considered highly unreliable and have not been used. Additional measurements were obtained from the helium samples, namely, $^{63}Cu(n,\alpha)$ and $^{93}Nb(n,\gamma)$ at selected locations.

Table 2.1.2 lists the mean measured reaction rates for each level. Horizontal gradients on each level appear to be less than 10% in all cases and are usually less than the ±2% statistical variations in the data.

Fluence values can be derived from the reaction rates assuming that the spectrum is known. The spectrum was measured previously in position E7 at low power during January 1979.[1] A comparison of the present reaction rates with those measured previously should roughly scale with the difference in reactor power (19.24 MW/0.965 MW = 19.94). The measured ratio is 17.3 at the peak flux position (level 4), and vertical

TABLE 2.1.2

MEAN REACTION RATES FOR ORR-MFE2

Position E7; average power = 19.24 MW (26.4 MW Live).

Values are mean of four samples on each level; accuracy ±5%.

		$\sigma\phi^b$ (atom/atom-s)				
Level	Height, cm[a]	$^{59}Co(n,\gamma)$ (x 10^{-9})	$^{59}Fe(n,\gamma)$ (x 10^{-11})	$^{54}Fe(n,p)$ (x 10^{-12})	$^{46}Ti(n,p)$ (x 10^{-13})	$^{63}Cu(n,\alpha)^c$ (x 10^{-14})
1	11.4	2.63	7.00	5.00	6.46	3.17
2	5.0	3.13	8.67	5.59	7.53	3.64
3	2.4	3.31	9.31	5.93	8.00	3.83
4	−9.1	3.82	10.89	6.38	8.80	4.06

[a] Height above vertical midplane. Capsules were located at the bottom of levels 1, 2, and 4 and at the top of level 3.

[b] Burnup corrections included; self-shielding negligible.

[c] Data extrapolated from helium tube position; accuracy ±7%.

gradients appear to be quite close to those measured previously. This difference is probably due to differences in fuel loading.

The five reaction rates at each level in Table 2.1.2 were thus used with the STAYSL computer code to adjust the spectrum measured at low power with 28 reactions, cadmium covers, and fission foils. The spectral analysis showed no evidence for any spectral shift between high power (30 MW) and low power (1MW). In fact, all flux groups and reaction rates were adjusted by less than 10%.

Complete fluence and DPA gradients have been measured, as shown in Figure 2.1.1. It is important to note that the gradient measurements were made with long wires located on the east side of the experimental assembly. The fast flux was about 8% higher at this position than at the sample locations; although, the thermal flux was the same at both locations. Horizontal gradients within the samples were less than 2% and have thus been neglected. The gradients were averaged over each of the four levels and recommended average fluence values are given in Table 2.1.3.

Damage parameters were then computed and also averaged over the four levels. Recommended DPA and helium production values are also listed in Table 2.1.3. The damage calculations were performed using our recently revised damage cross sections based on ENDFIB-V. The (n,γ) reaction is also included; however, the contribution to the total damage is generally less than 2%, the exceptions being Co(13%) and Mn(5%). Caution should be used in these two cases since neutron self-shielding and burnup effects would drastically alter the results.

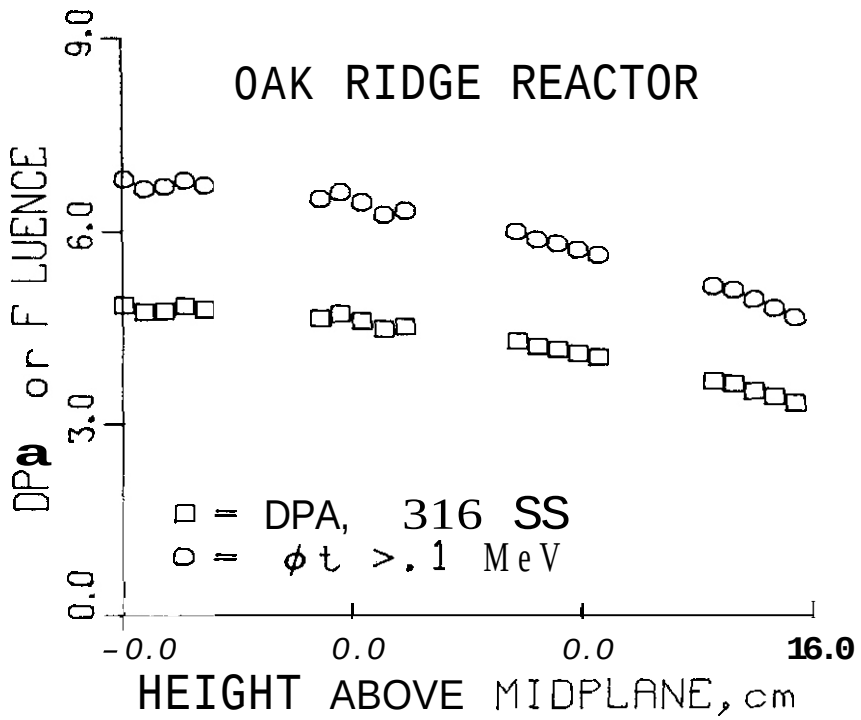

Figure 2.1.1. DPA in 316 stainless steel and neutron fluence >0.1 MeV (x 10^{22} n/cm^2-s) gradients are shown for the MFE2 experiment in ORR.

TABLE 2.1.3

AVERAGE FLUENCES AND DAMAGE PARAMETERS
FOR VARIOUS LEVELS FOR ORR-MFE2

Gradients averaged at each level; cross sections from ENDF/B-V, (n,γ) included: helium in appm (±15%); DPA (±10%).

	LEVEL							
	1		2		3		4	
Height, cm:	11.4, 16.2		4.8, 9.5		-1.9, 2.8		-3.8, -9.5	
Fluence ($x10^{21}$ n/cm^2):								
Total:	12.04		14.40		15.97		16.93	
Thermal:	3.14		3.87		4.44		4.74	
>0.11 MeV:	4.89		5.78		6.41		6.78	
>1.0 MeV:	2.33		2.71		3.01		3.17	
Element:	DPA	He	DPA	He	DPA	He	DPA	He
Al	6.17	2.06	7.28	2.46	8.04	2.69	8.50	2.77
Ti	3.60	1.83	4.32	2.14	4.77	2.35	5.04	2.47
V	4.16	0.08	4.91	0.09	5.41	0.09	5.72	0.10
Cr	3.74	0.55	4.40	0.65	4.86	0.72	5.13	0.75
Mn	3.96	0.41	4.68	0.49	5.17	0.53	5.48	0.55
Fe	3.32	0.88	3.90	1.04	4.30	1.14	4.55	1.18
co	3.76	0.43	4.47	0.52	4.93	0.57	5.25	0.58
Ni[a]	3.53	153.	4.17	248.	4.58	325.	4.86	386.
cu	3.21	0.75	3.80	0.90	4.19	0.98	4.42	1.02
Zr	3.55	0.09	4.19	0.10	4.63	0.11	4.89	0.11
Nb	3.25	0.18	3.85	0.21	4.24	0.23	4.48	0.24
Mo	2.37	-	2.82	-	3.09	-	3.28	-
Ta	0.91	-	1.07	-	1.19	-	1.25	-
316 SS[b]	3.40	16.0	4.00	25.6	4.41	33.4	4.67	39.6

[a] Thermal helium production included.

[b] Composition assumed as: Cr(16), Mn(2), Fe(70), Ni(10), Mo(2).

Helium cross sections were also taken from ENDFIB-V. The thermal process for nickel was computed using the equations in ORNL/TM-6361 (1979) with the total thermal flux below 0.5 eV. This procedure was found to agree with measured helium rates for the OFF-MFE1 experiment. Of course, H. Farrar IV and D. Kneff (Rockwell International) will report precise helium measurements for a variety of materials.

All of the fluence and damage parameter gradients can be well-described by a simple quadratic formula:

$$f(x) = N(1 + bx + cx^2)$$

where x is the height above midplane (cm), and the other variables are given in the following table.

Quantity	b	c	n
Fluence	-0.01101	-0.0004690	6.45×10^{21} n/cm^2
DPA (316 SS)	-0.01101	-0.0004690	4.47 DPA
He(Ni)	-0.03010	-0.0006364	330.1 appm

Additional DPA, FKA, and helium values are available (37 isotopes) on request.

2.1.4.2 Analysis of the ORR-MFE4A Experiment

Dosimetry samples have been analyzed from the MFE4A irradiation in ORR. The experiment started on June 12, 1980 and ended on January 20, 1981 with a total exposure of 5471 MWD. Fe, Ni, Ti, and Co-V wires measuring about 6" in length were irradiated near the center of the assembly. Six reactions were measured at five different locations along the length of the wire. The (n,p) reactions were gamma-counted from ^{54}Fe, ^{46}Ti, ^{58}Ni, and ^{60}Ni; however, the two nickel reactions cannot be used

since about half of the ^{58}Co is converted to ^{60}Co in the high thermal flux. The thermal flux was determined by counting the (n,γ) reaction products from ^{58}Fe and ^{59}Co.

Fast gradients were found to vary by less than 5% along the length of the wires (6"). However, the thermal gradients were larger and showed a 10% change. The measured reaction rates near the center of the wire (about maximum flux) are listed in Table 2.1.4 and compared to those measured previously during the ORR-MFE2 experiment. As can be seen, the $^{59}Co(n,\gamma)$ reaction is about 15% higher than the $^{58}Fe(n,\gamma)$ results, when compared to previous measurements. In fact, both thermal reactions usually agree in ORR and depend primarily only on the thermal flux. This difference may be due to an uncertainty in the cobalt concentration in the Co-V alloy (supplied by OWL). Checks are now in progress to compare this alloy with a Co-A1 alloy (NBS standard) during a simultaneous neutron activation analysis.

Fluence values were obtained using the STAYSL computer code, the four reaction rates in Table **2.1.3** and a neutronics calculation by T. A. Gabriel (ORNL). The fluxes listed in Table 2.1.4 are normalized to a 30 MW power level. The fluxes are about 30% lower than the neutronics calculations. The reason for this difference is not known and is under investigation. The thermal flux values are also uncertain since the neutron temperature distribution is not correct. An ambient (20°C) distribution was assumed to agree with the neutronics calculations. Raising the temperature to the correct value (600°C) would raise the thermal flux considerably. However, this would not change average thermal

TABLE 2.1.4

DOSIMETRY RESULTS FOR THE ORR-MFE4A EXPERIMENT

(Results normalized to 30 MW; accuracy ±2%)

Reaction	σφ(atom/atom-s)	Ratio to MFE2
$^{54}Fe(n,p)^{54}Mn$	1.02×10^{-11}	1.025
$^{46}Ti(n,p)^{46}Sc$	1.40×10^{-12}	1.022
$^{58}Fe(n,\gamma)^{59}Fe$	1.79×10^{-10}	1.053
$^{59}Co(n,\gamma)^{60}Co$[a]	7.17×10^{-9}	1.203[a]

[a]Burnup correction of 6% included; concentration of cobalt in Co-V alloy may be uncertain.

TABLE 2.1.5

FLUX AND FLUENCE VALUES FOR ORR-MFE4A

(5471 MWD, 222 days, normalized to 30 MW)

Reaction	Flux (30 MW) ($\times 10^{14}$ n/cm^2-s) ANL	Flux (30 MW) ($\times 10^{14}$ n/cm^2-s) ORNL[a]	Ratio	Fluence ($\times 10^{21}$ n/cm^2)	Error (%)
Total	(5.39)	7.85	(0.69)	(8.45)	10
Thermal[b] (<.5 eV)	(1.72)	2.51	(0.69)	(2.70)	15
0.5 eV-0.11 MeV	1.88	2.73	0.69	2.95	22
>0.11 MeV	1.79	2.61	0.69	2.81	15
>1 MeV	0.96	1.39	0.69	1.50	14
>2 MeV	0.51	0.75	0.68	0.80	12
>5 MeV	0.072	0.107	0.67	0.11	15

[a]T. G. Gabriel (ORNL).

[b]Thermal temperature distribution not correct (ambient assumed).

reaction rates (e.g., helium production from nickel) since most thermal cross sections have the same 1/V energy dependence. Hence, care must be taken to use thermal fluxes properly at elevated temperatures. We are now attempting to obtain the proper temperature and will revise our thermal fluxes accordingly.

Preliminary estimates can be made for displacement damage and helium production. Using our recently revised (ENDFIB-V) cross sections, we estimate DPA values of 2.6(Ni), 2.4(Fe), and 2.5(316 SS). Helium rates are estimated to be 122 appm(Ni), 0.63 appm(Fe), and 12.7 appm(316 SS). The nickel values for helium assume a thermal fluence of 2.7×10^{21} n/cm^2 and the equations in ORNL/TM-6361 (1979). This procedure worked well for the MFEl experiment and agreed with helium measurements by Rockwell International. Some nickel samples from the present experiments were also analyzed by D. Kneff and H. Farrar IV, and their measurements are in excellent agreement with our calculations.

One nickel wire was cut into short segments to determine the gradient. The ^{58}Ni(n,p) and ^{60}Ni(n,p) reactions show an unusually fine pattern of thermal flux variations that are also confirmed by helium measurements at Rockwell International. The fast flux shows only a smooth variation. Hence, we conclude that some material in the experimental packages is producing some thermal neutron shadowing effect. However, these variations are only a few percent and will be further investigated.

2.1.5 Future Work

Data has been analyzed for the X287 experiment in EBR II and the HEDL1 experiments in the Omega West Reactor at Los Alamos. The new Intense Pulsed Neutron Source at ANL has also been characterized. All of these results will be reported in the next ADIP Report. Samples are now being gamma-counted from the CTR 32 irradiation in HFIR.

2.1.6 References

1. L. R. Greenwood, DOE/ET-0065/6, p. 13 (June 1979).

2.1.7 Publications

1. L. R. Greenwood, "Neutron Source Characterization for Fusion Materials Studies," Proceedings of Second Topical Meeting on Fusion Reactor Materials, Seattle, August 1981.

2.2 NEUTKONIC CALCULATIONS IN SUPPORT OF THE ORR-MFE-4 SPECTRAL TAILORING EXPEKIMENTS — R. A. Lillie, R. L. Childs, and T. A. Gabriel (Oak Ridge National Laboratory)

2.2.1 ADIP Task

ADIP Task I.A.2, Define Test Matrices and Test Procedures.

2.2.2 Objective

The objective of this work is to provide the neutronic design for materials irradiation experiments in the Oak Kidge Research Kenctor (ORR). Spectral tailoring to control the fast and thermal neutron fluxes is required to provide the desired displacement and helium production rates in alloys containing nickel.

2.2.3 Summary

Three-dimensional neutronics calculations[1,2] are being carried out to follow the irradiation environment of the ORR-MFE-4A and -4B experiments. These calculations currently cover the 30 ORR cycles completed for the -4A experiment and 9 ORK cycles completed for the -4B experiment, which correspond to 221,178 MWh and 83,634 MWh, respectively. At these exposures, the calculations yield 6.66 $\times 10^{25}$ neutrons/m^2 in thermal fluence, 1.99 $\times 10^{26}$ neutrons/m^2 in total fluence, 5.05 dpa in type 316 stainless steel, and 51.78 at. ppm He in type 316 stainless steel (nut including 2.0 at. ppm from ^{10}B) for the -4A experiment. The -4B experiment has achieved 2.52 $\times 10^{25}$ neutrons/m^2 in thermal fluence, 7.52 $\times 10^{25}$ neutrons/m^2 in total fluence, 1.91 dpa and 8.13 at. ppm He in type 316 stainless steel.

The nuclear analysis of the hafnium corepiece for the ORR-MFE-4A experiment has been completed.[3-5] The results of this analysis indicate acceptable helium production to displacement damage ratios over the lifetime (>50 dpa) of the experiment may be obtained using solid aluminum corepieces containing a 0.65-mm-thick hafnium annulus.

2.2.4 Progress and Status

The real time projections of the helium production and displacement damage levels based on current calculated data are given in Figs. 2.2.1 and 2.2.2 for the ORR-MFE-4A and -4B experiments, respectively. These

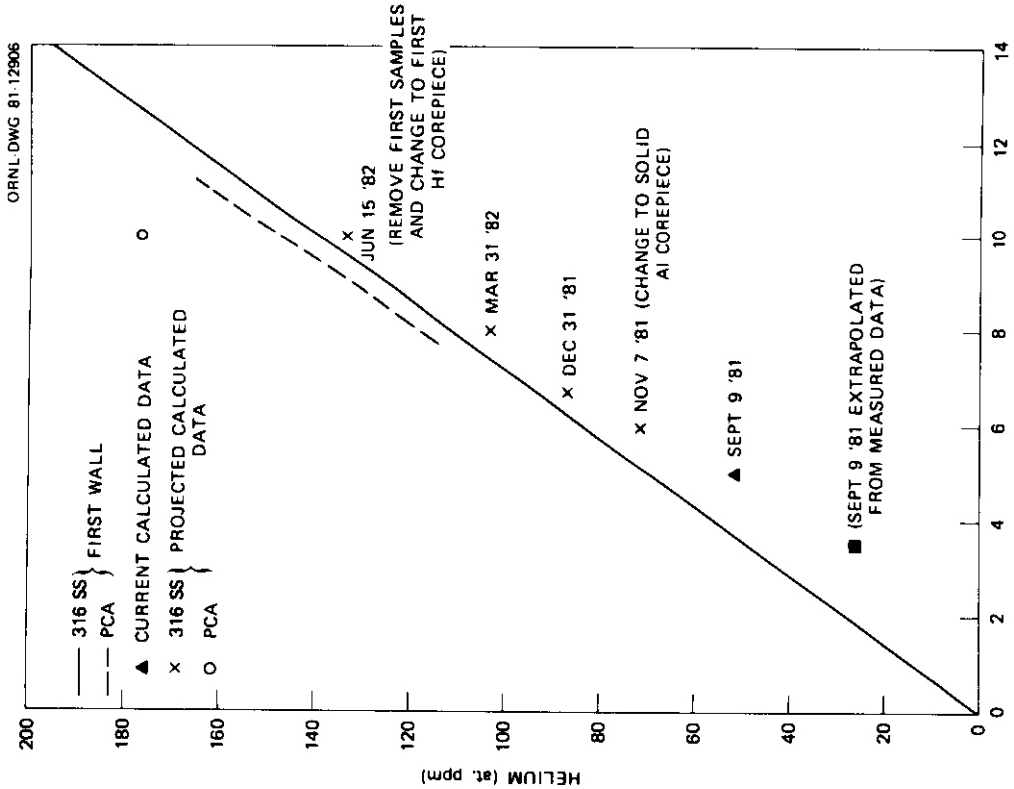

Fig. 2.2.1. Current and Projected Helium Production and Displacement Damage Levels Expected in the ORR-MFE-4A Experiment.

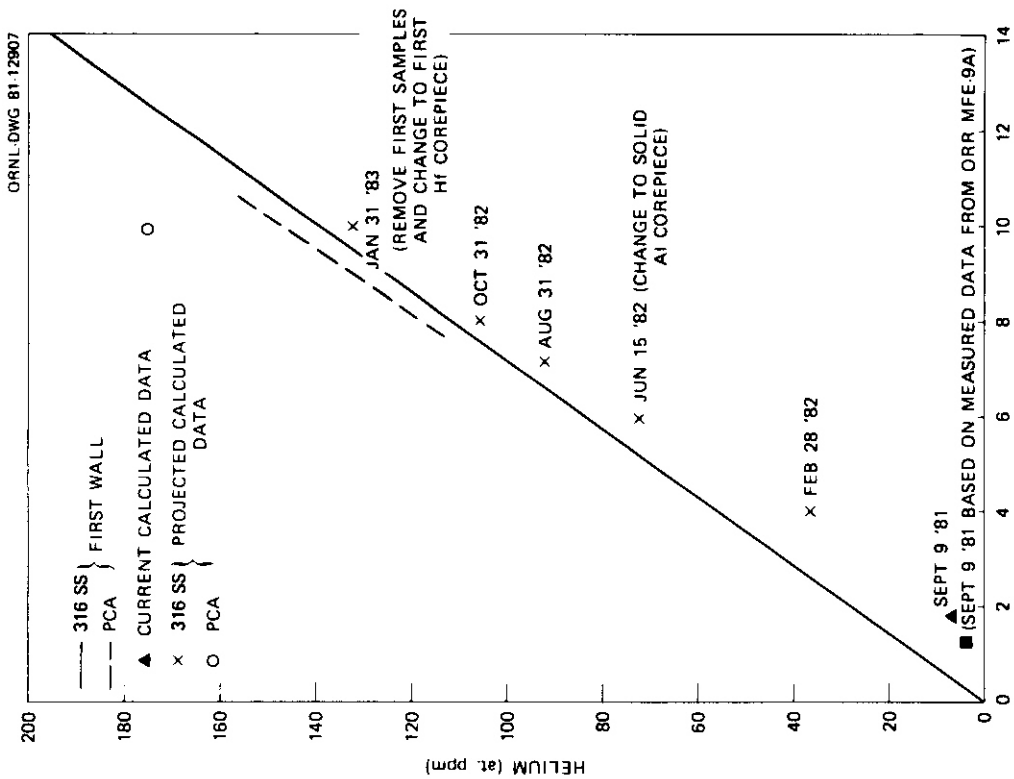

Fig. 2.2.2. Current and Projected Helium Production and Displacement Damage Levels Expected in the ORR-MFE-4B Experiment.

data reflect all refueling and extended shutdown times as of September 9, 1981. However the projected dates for the -4A experiment do not take into account that this experiment was removed from the reactor September 9, 1981. In addition to the calculated and projected calculated data in Figs. 2.2.1 and 2.2.2, the helium production and displacement levels as of September 9, 1981, projected from -4A measured fluence data are also shown.

The measured data were obtained from dosimeters that were removed from the ORR-MFE-4A experiment after 131,304 MWh exposure.[6] The dosimetry data yield 2.71 $\times 10^{25}$ neutrons/m^2 in thermal fluence and 8.49 $\times 10^{25}$ neutrons/m^2 in total fluence, whereas the corresponding fluences after 131,304 MWh based on the neutronics calculations are 3.93 $\times 10^{25}$ and 1.23 $\times 10^{26}$ neutrons/m^2, respectively. The discrepancy between the experimentally obtained fluences and those obtained from the neutronics calculations is currently under investigation. Based on preliminary results, it appears that approximately 40% of the discrepancy may be due to the geometric model of the ORR-MFE-4A experimental capsule employed in the three-dimensional neutronics calculations. However, since these results are preliminary, the calculated and calculated projected data in Figs. 2.2.1 and 2.2.2 have not been modified to account for the discrepancy between the experimentally determined and calculated fluences.

The nuclear analysis of the hafnium corepiece for the ORR-MFE-4A experiment has been completed. The results of this analysis indicate acceptable helium production to displacement levels may be obtained over the lifetime (>50 dpa) of the experiment using solid aluminum corepieces containing a 0.65-mm-thick hafnium annulus surrounding the experimental capsule. It is anticipated, based on hafnium burn-up considerations, that each hafnium corepiece will perform satisfactorily for approximately 227,000 MWh, and the gamma heating rates will range from 70 to 80% of the corresponding heating rates with the current (63% H_2O-37% Al) corepiece in place.

The paper entitled "Spectral Tailoring for Fusion Reactor Damage Studies: Where Do We Stand?," which will be published in the *Journal of Nuclear Materials*, was presented at the Second Topical Meeting on Fusion Reactor Materials, August 9-12, 1981, at Seattle, Washington.

2.2.5 Future Work

The investigation to determine the apparent discrepancy between the experimentally determined and calculated fluences will be continued. If this discrepancy is attributed to the calculational procedures, the three-dimensional neutronics calculations that monitor the radiation environment of the ORR-MFE-4A and -4B experiments during each cycle will be revised accordingly.

2.2.6 References

1. D. R. Vondy, T. B. Fowler, and G. W. Cunningham, *VENTURE, A Code Block for Solving Multigroup Neutron Problems Applying Fine-Diffusion-Theory Approximations to Neutron Transport,* ORNL-5062, Oak Ridge National Laboratory, Oak Ridge, Tennessee, 1975.
2. T. A. Gabriel, R. A. Lillie, B. L. Bishop, and R. L. Childs, "Neutronic Calculations in Support of the ORR-MFE-4A Spectral Tailoring Experiment," *ADIP Quart. Prog. Rep. June 30, 1980,* DOE/ER-0045/3, pp. 7-9.
3. W. W. Engle, Jr., *A User's Manual for ANISN, A One-Dimensional Discrete Ordinates Code with Anisotropic Scattering,* K-1693, Oak Ridge Gaseous Diffusion Plant, Oak Ridge, Tennessee, 1967.
4. T. A. Gabriel, R. A. Lillie, B. L. Bishop, and R. L. Childs, "Neutronic Calculations in Support of the ORR-MFE-4A Spectral Tailoring Experiment," *ADIP Quart. Prog. Rep. Sept. 30, 1980,* DOE/ER-0045/4, pp. 14-19.
5. R. A. Lillie, R. L. Childs, and T. A. Gabriel, "Neutronic Calculations in Support of the ORR-MFE-4A Spectral Tailoring Experiment," *ADIP Quart. Prog. Rep. Dec. 31, 1980,* DOE/ER-0045/5, pp. 15-18.
6. Letter from L. Greenwood, Argonne National Laboratory, Argonne, Illinois, to M. L. Grossbeck dated July 21, 1981.

2.3 OPERATION OF THE ORR SPECTRAL TAILOKING EXPERIMENTS ORR-MFE-4A AND ORR-MFE-4B — I. T. Dudley (Oak Ridge National Laboratory)

2.3.1 ADIP Task

ADIP Task I.A.2, Define Test Matrices and Test Procedures.

2.3.2 Objectives

Experiments ORR-MFE-4A and -4B irradiate austenitic stainless steels, using neutron spectrum tailoring to achieve the same helium-to-displacement-per-atom (He/dpa) ratio as predicted for fusion reactor first-wall service. Experiment ORR-MFE-4A contains mainly type 316 stainless steel and the Path A Prime Candidate Alloy (PCA) at irradiation temperatures of 330 and 400°C. Experiment ORR-MFE-4B contains similar materials at irradiation temperatures of 500 and 600°C.

2.3.3 Summary

The ORR-MFE-4A experiment, described previously,[1] was installed in the Oak Ridge Research Reactor (ORR) on June 10, 1980, and as of September 10, 1981, it had operated for an equivalent 330 d at 30 MW reactor power, with maximum specimen temperatures in each region of 330 and 400°C, respectively. On September 8, 1981, two of the multijunction thermocouples located in the lower region of the capsule, as previously described,[2] indicated sharp drops in temperatures of about 90°C on each. The capsule was removed from the reactor for investigation. Tests have indicated that there are no leaks in the secondary system and no leaks between the thermocouple well and primary system. The possibility of rearranging primary and secondary system boundaries to permit continuation of the capsule irradiation is under investigation.

The ORR-MFE-4B experiment, installed in the ORR on April 23, 1981, is essentially identical to ORR-MFE-4A. Its upper region operates at 600°C, and its lower region operates at 500°C. As of September 30, 1981, it has operated for an equivalent 136 d at 30 MW reactor power.

2.3.4 Progress and Status

The ORR-MFE-4A capsule has a history of apparently unrelated difficulties. After approximately 4000 h operation in the reactor, all six thermocouples used to monitor specimen temperatures failed during a two-week period. A new multijunction thermocouple was installed in what was originally a flux monitor well, positioned in the center of the capsule.[2] Operation of the capsule was then resumed, using these thermocouples for monitoring the specimen temperatures.

In July 1981 a small leak developed in the secondary gas system. Pressure leak tests made on the capsule after it was removed from the reactor indicated no leakage in the secondary system of the capsule. Leak tests on the lines outside of the pool also indicated no significant leakage. Based on the results of those tests, the leak probably occurred at one of the three connections between the capsule proper and the lines to the system outside of the pool. The connections are made with compression-type tube fittings within a junction box located in the reactor pool. Routine helium leak tests made at the connections may have failed to detect the leak. Irradiation was resumed after this testing.

On September 8, 1981, two of the multijunction thermocouples located in the lower region of the capsule indicated a rapid drop in temperature of approximately 90°C. This temperature drop is equal to the drop that would be expected if the annulus surrounding the well containing the multijunction thermocouple were partially filled with NaK. This indicates that a leak may have developed in the inner cylindrical primary boundary and allowed some NaK to enter that annulus.

The investigation to date has indicated that there are no leaks between the secondary system and the primary system. There are no leaks from the secondary system of the capsule proper. There is no leakage from the thermocouple well into the primary portion of the capsule. It is not possible to leak test the area of the primary system suspected of leaking NaK into the annulus around the thermocouple well.

The possibility of rearranging the primary and secondary boundaries by changing system pressures and some controls to permit continuation of the capsule irradiation testing is under investigation.

Capsule ORR-MFE-4A was operated until removed from temperatures indicated by the multijunction thermocouple. Actual temperatures in the upper and lower capsule zones were controlled at the desired levels by use of relationships established by heat transfer analyses.[2] The upper region of the capsule operated at the desired 400°C and the lower region at the desired 330°C.

The ORR-MFE-4B capsule has operated, as planned, since it was installed in the reactor on April 23, 1981. As of October 1, 1981, it has accumulated an equivalent of 136 d at 30 MW reactor power with maximum specimen temperatures in the upper region of 600°C and in the lower region of 500°C. A schematic representation of the capsule is shown in Fig. 2.3.1. Plots of the temperature history for the period covered by this report are shown in Figs. 2.3.2 and 2.3.3. Curve TE-1 shows the temperature of the upper region of the capsule, and TE-4 shows the temperature of the lower region.

2.3.5 References

1. K. R. Thoms and M. L. Grossbeck, "Operation of the ORR Spectral Tailoring Experiment ORR-MFE-4A," *ADIP Quart. Prog. Rep. Sept. 30, 1980,* DOE/ER-0045/4, pp. 20–24.
2. K. R. Thoms, "Operation of the ORR Spectral Tailoring Experiment ORR-MFE-4A," *ADIP Quart. Prog. Rep. Mar. 31, 1981,* DOE/ER-0045/6, pp. 18–21.

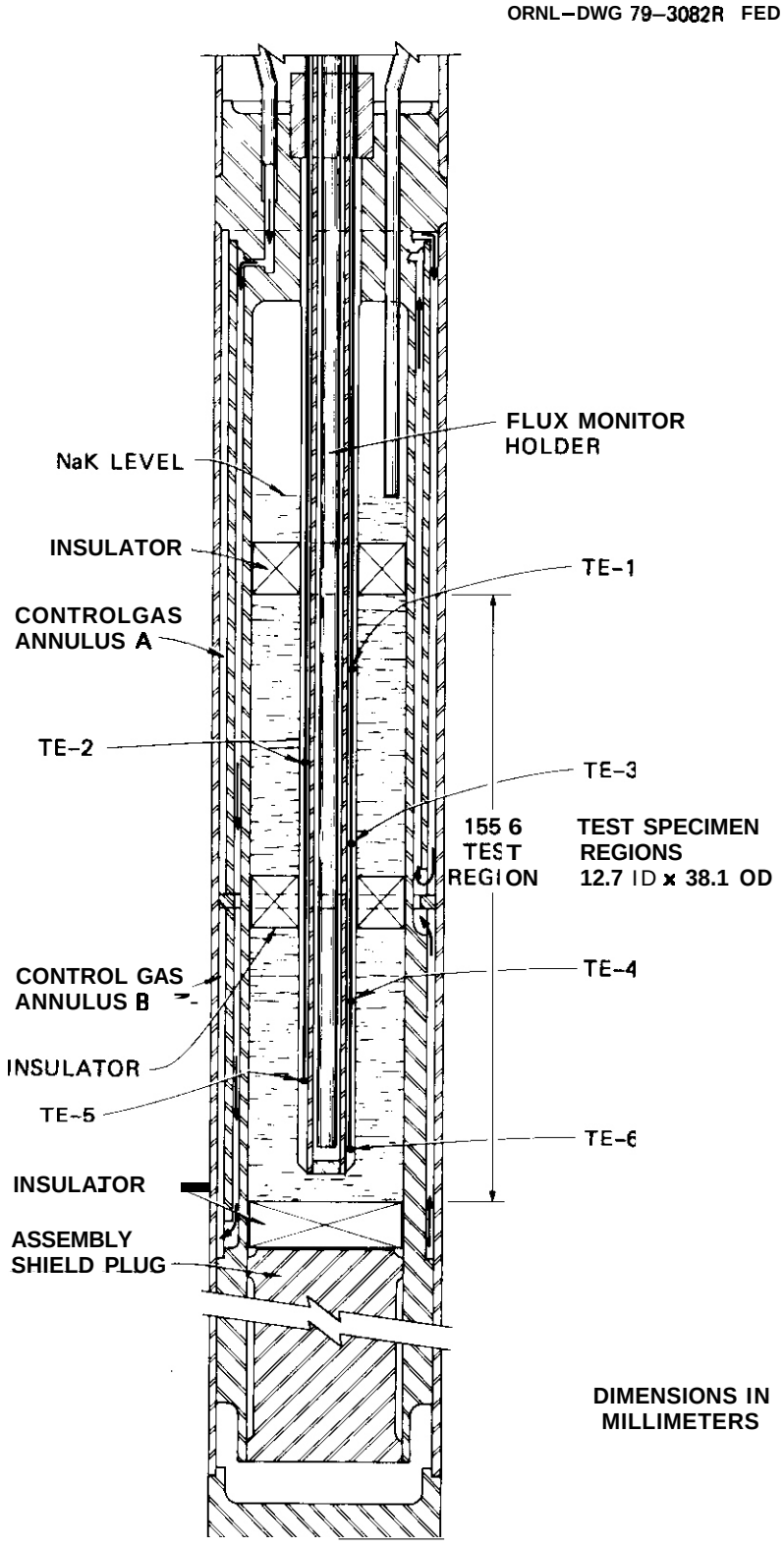

Fig. 2.3.1. Schematic of ORR-MFE-4B Irradiation Capsule Design. Thermocouple locations are indicated by TE.

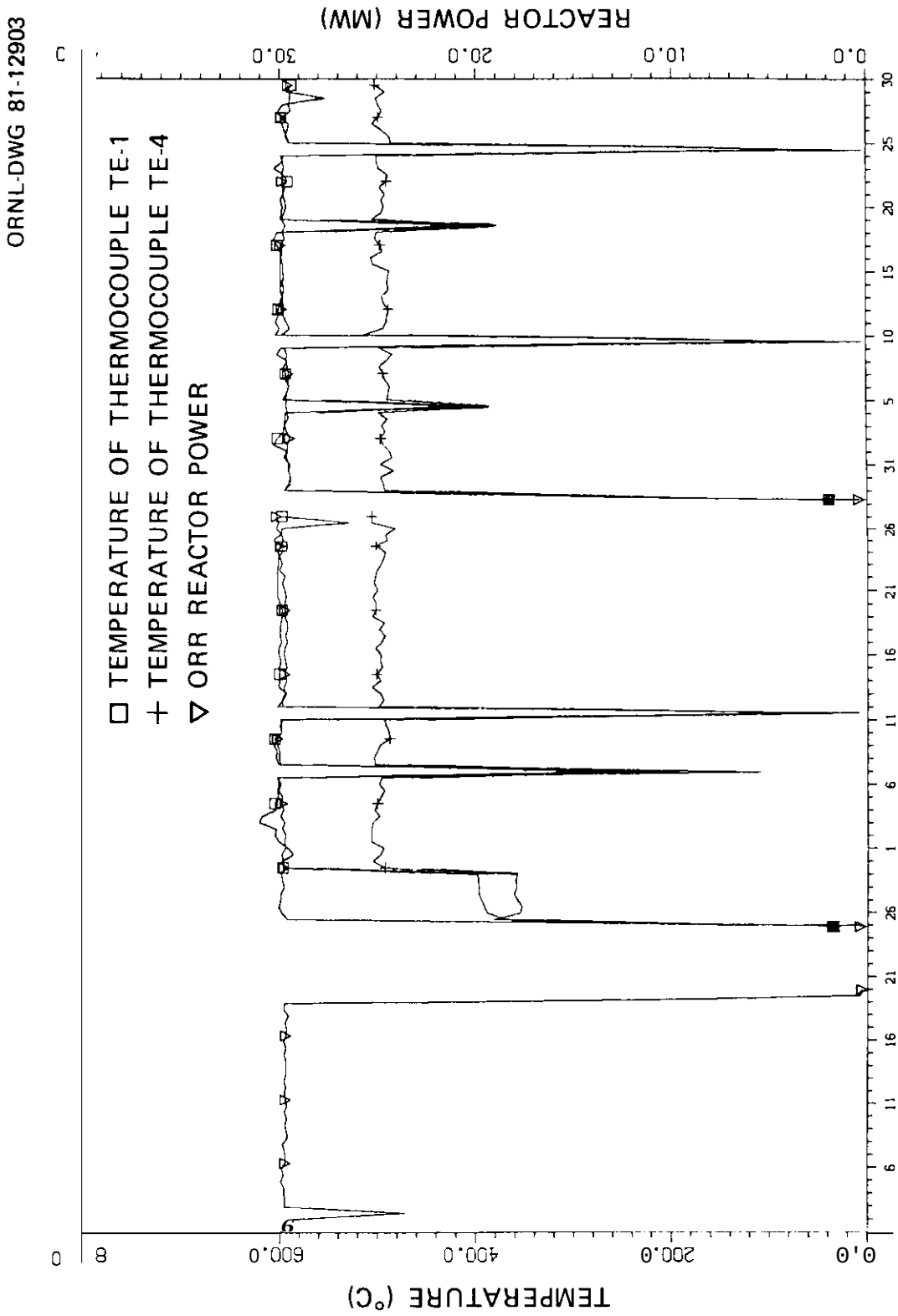

Fig. 2.3.2. Operating History of the ORR and Experiment ORR-MFE-4B From April 1981 Through June 1981.

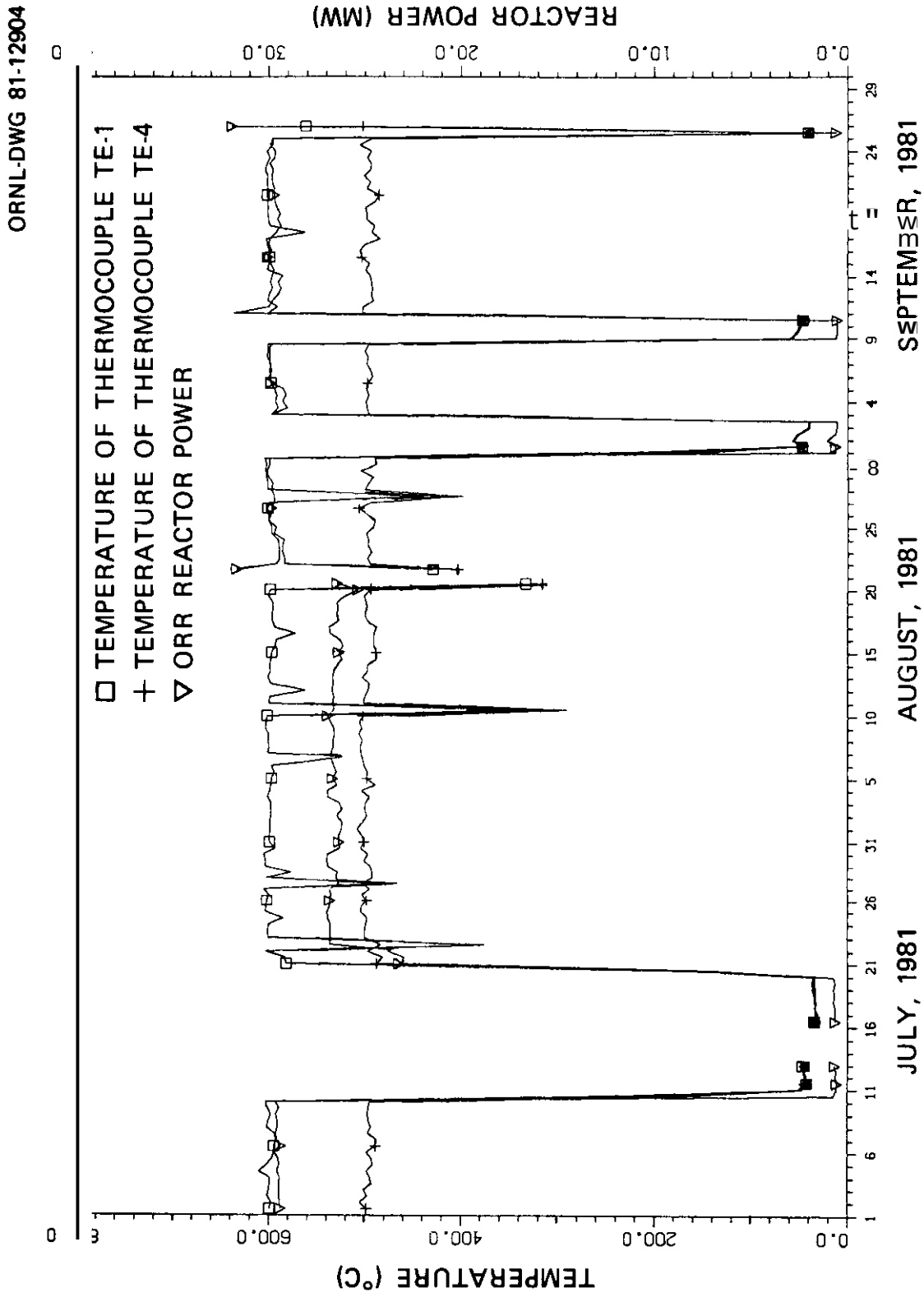

Fig. 2.3.3. Operating history of the ORR and experiment ORR-MFE-4B From July 1981 Through September 1981.

2.4 EXPEKIMENTS HFIR-MFE-RBl, -RB2, AND -RB3 FOK LOW-TEMPERATUPS IRRADIATION OF PATH E FEKKITIC STEELS — J. M. Vitek and J. W. Woods (Oak Ridge National Laboratory)

2.4.1 ADIP Task

ADIP Task I.A.2, Define Test Matrices and Test Procedures.

2.4.2 Objective

The objective of these experiments is to acquire data on the effects of low-temperature irradiation on the properties of ferritic steels. Irradiation in a beryllium reflector position of the High Flux Isotope Reactor (HFIK) will result in concurrent production of helium and displacement damage. A broad range of sample types is to be irradiated, including some larger specimens that cannot be accommodated in irradiation experiments in the HFIK target region.

2.4.3 Summary

The HFIR-MFE-RBl, -RB2, and -RB3 experiments are planned for low-temperature irradiation of a variety of specimen types of ferritic steels to approximately 10 and 20 dpa. The final specimen matrices for RBl and RB2 are given, along with a preliminary matrix for RB3. Also given are details on the alloys included and their conditions. Assembly of the RBl and RB2 capsules is presently under way. Irradiation of the RBl capsule is planned to start in November 1981, and irradiation of RB2 is expected to begin about January 1982.

2.4.4 Progress and Status

2.4.4.1 Introduction

The HFIR-MFE-RBl experiment was described in detail in an earlier quarterly report.[1] Since that time, the experiment plan has been expanded to include three capsules, RBl, RB2, and RB3. These experiments will be located in the beryllium reflector positions of HFIK. They will be able to accommodate a wide variety of samples, including larger samples that

cannot be irradiated in any other HFIR locations. The RB capsules will provide the first data for several properties under the HFIR irradiation conditions of simultaneous displacement damage and helium production. This contribution updates the RB experiment plan and includes the revised test matrices. Insertion of RB1 into HFIK is expected in November of 1981, with RB2 to follow by January 1982. The RB3 experiment will be a reconstruction of the RB1 capsule and will be inserted after October 1982.

2.4.4.2 Experimental Design

The RB capsules will be irradiated at the reactor coolant temperature of 50°C. Samples will be enclosed in evacuated and collapsed aluminum tubing in order to avoid excessive corrosion. The encapsulation procedure is described elsewhere.[1] Temperature increases within the tube due to gamma heating are expected to be less than 25°C.

Seven different sample geometries are to be used: sheet tensile (ST), fatigue initiations (FI), Grodzinski fatigue (GF), miniature Charpy (MC), compact tension (CT), crack growth (CG), and transmission electron microscopy (TEM). A brief description of these samples is given in Table 2.4.1. Further details and drawings of the specimens are presented elsewhere.[1,2] The miniature Charpy samples from HEDL and ORNL differ slightly in length; HEDL specimens are 23.6 mm long whereas ORNL specimens are 25.4 mm long.

Table 2.4.1. Specimen Geometries to be Used

Specimen designation	Specimen	Material stack	Dimensions, mm			
			Thickness	Length	Width	Diameter
ST	Sheet tensile	Sheet	0.762	44.4	4.95	
FI	Fatigue initiation	Rod, plate		45.2		6.35
GF	Gradzinski fatigue	Sheet	0.762	44.4	4.95	
MC	Miniature Charpy (ORNL)	Plate	5.0	25.4	5.0	
MC	Miniature Charpy (HEDL)	Plate	5.0	23.6	5.0	
CT	Compact tension	Plate	2.54			16.0
CG	Crack growth	Sheet	0.762	12.7	25.4	
TEM	TEM disks	Sheet	0.25			3.0

A SiC temperature monitor was inserted in a dummy sample and is included in the chain of sheet tensile and Grodzinski fatigue samples. Flux monitors have been included in both the compact tension and sheet tensile–Grodzinski fatigue sample trains.

2.4.4.3 HFIR-MFE-RB1, -RB2, and -RB3 Test Matrices and Irradiation Conditions

All three Path E alloys, 12 Cr-1 MoVW, 9 Cr-1 MoVNb, and 2 1/4 Cr-1 Mo are to be included in these experiments, as both base metal and welds. In addition, alloy variations of the 12 Cr-1 MoVW and 9 Cr-1 MoVNb alloys, with supplemental nickel, will be inserted. These nickel–doped alloys are being used to determine the effect of helium on the microstructure and properties, since a transmutation of nickel in HFIR produces helium. The nickel–doped alloys have been characterized earlier.[3] A few samples of type 316 stainless steel will also be irradiated. Table 2.4.2

Table 2.4.2. Alloy Heats and Heat Treatment Conditions[a]

Alloy	Heat	Temperature, °C/time, h	
		Normalizing treatment[b]	Tempering treatment[b]
2 1/4 Cr-1 Mo	56447	900/0.5	700/1
2 114 Cr-1 Mo, weld	56447	As welded	78011
9 Cr-1 MoVNb	30176	1038/0.5	760/0.5
9 Cr-1 MoVNb, weld	30176	As welded	780/1
9 Cr-1 MoVNb	XA–3590	1040/0.5	760/1
9 Cr-1 MoVNb-2 Ni	XA–3591	1040/0.5	700/5
12 Cr-1 MoW plate	91353	1038/0.16	76010.5
12 Cr-1 MoVW sheet	91353	1038/0.067	760/0.5
12 Cr-1 MoW weld	91353	As welded	78011
12 Cr-1 MoW	XAA–3587	1050/0.5	780/2.5
12 Cr-1 MoVW-1 Ni	XAA-3588	1050/0.5	780/2.5
12 Cr-1 MOVW–2 Ni	XAA-3589	1050/0.5	70015
Type 316 stainless steel, 20% CW	X–15893	As worked	

[a] Not including TEM disk conditions.

[b] Air cooled.

lists the alloys, their heat numbers, and their conditions. This table does not include all of the alloys and conditions of the TEM disks, which are too numerous to mention in this contribution.

Two fluence levels for the specimens are targeted to yield displacement levels of 10 and 20 dpa (these values are for the capsule midplane). With the reduced flux available in the HFIR reflector positions, irradiations are projected to take 10 and 20 months, respectively. The RB1 capsule will be irradiated to 10 dpa. Upon completion, the capsule will be disassembled, reconstituted, and reinserted as RB3 for a further 10 dpa irradiation. The RB2 capsule will be irradiated to 20 dpa. Due to space limitations, all of the 20 dpa specimen matrix cannot be included in RB2. Consequently, some of the specimens with a planned 20 dpa exposure will be irradiated in both the RB1 and RB3 capsules. The 10 dpa matrix will be divided between the RB1 and RB3 capsules. The specimen matrices are given in Tables 2.4.3 through 2.4.5 for 10 and 20 dpa irradiations.

Table 2.4.3. Specimen Matrix to be Irradiated to 10 dpa[a] in Experiment HFIR-MFE-RB1

Alloy	Heat	Number of specimens of each type						
		ST	FI	GF	MC	CT	CG	TEM[b]
2 1/4 Cr-1 Mo	56447	2		2	4		3	16
2 1/4 Cr-1 Mo, weld	56447				4		2	
2 1/4 Cr-1 Mo	72768							9
9 Cr-1 MoVNb	30176	4			7	7	3	24
9 Cr-1 MoVNb, weld	30176				4		2	
9 Cr-1 MoVNb	XA-3590		3	3	6		3	18
9 Cr-1 MoVNb-2 Ni	XA-3591			3	6		3	18
9 Cr-1 MoVNb-2 Ni, adj	XA-3593							18
12 Cr-1 MoVW	91353	4		3	7	7	3	31
12 Cr-1 MoVW, weld	91353				4		2	8[c]
12 Cr-1 MoVW	XAA-3587		3	3	4	5	3	18
12 Cr-1 MoVW-1 Ni	XAA-3588			3	5	4	3	18
12 Cr-1 MoVW-2 Ni	XAA-3589		3	3	3	4	3	18
12 Cr-1 MoVW-2 Ni, adj	XAA-3592							18

[a] At experiment midplane.

[b] ADIP, Path E alloys only.

[c] From heat-affected zone simulation.

Table 2.4.4. Specimen Matrix to be Irradiated to 10 dpa[a] in Experiment HFIR–MFE–RB3

Alloy	Heat	Number of specimens of each type	
		FI	CT
2 1/4 Cr-1 Mo	56447		4
2 1/4 Cr-1 Mo, weld	56447		
9 Cr-1 MoVNb	30176		
9 Cr-1 MoVNb, weld	30176		5
9 Cr-1 MoVNb	XA-3590		3
9 Cr-1 MoVNb-2 Ni	XA-3591	4	4
12 Cr-1 MoVW	91353		
12 Cr-1 MoVW, weld	91353		5
12 Cr-1 MoVW	XAA-3587	1	
12 Cr-1 MoVW-1 Ni	XAA-3588	4	
12 Cr-1 MoVW-2 Ni	XAA-3589	1	
Type 316 stainless steel	x-15893		6

[a]At experiment midplane.

Table 2.4.5. Specimen Matrix to be Irradiated to 20 dpa[a] in Experiment HFIR–MFE–RB2

Alloy	Heat	Number of specimens of each type						
		ST	FI	GF	MC	CT	CG	TEM[b]
2 1/4 Cr-1 Mo	56447		2	3		2	3	16
2 1/4 Cr-1 Mo, weld	56447						2	
2 1/4 Cr-1 Mo	72768							9
9 Cr-1 MoVNb	30176		4	3	8[c]	8	3	24
9 Cr-1 MoVNb, HAZ	30176					4		
9 Cr-1 MoVNb, weld	30176				4	4	2	
9 Cr-1 MoVNb	XA-3590	4			4	3	3	18
9 Cr-1 MoVNb-2 Ni	XA-3591	4			4[c]	4	3	18
9 Cr-1 MoVNb-2 Ni, adj	XA-3593							18
12 Cr-1 MoVW	91353		5	4	8[c]	8	3	31
12 Cr-1 MoVW, HAZ	91353				8[c]			8[d]
12 Cr-1 MoVW, weld	91353				4[c]	4	2	
12 Cr-1 MoVW	XAA-3587	4	3		5[c]	5	3	18
12 Cr-1 MoVW-1 Ni	XAA-3588	4	3		4	4	3	18
12 Cr-1 MoVW-2 Ni	XAA-3589	4	3		5[c]	4	3	18
12 Cr-1 MoVW-2 Ni, adj	XAA-3592							18
Type 316 stainless steel	x-15893					4		

[a]At experiment midplane.

[b]ADIP, Path E alloys only.

[c]Some samples to be irradiated to 10 dpa in each of capsules HFIR-MFE-RB1 and -RB3, to achieve the 20 dpa goal.

[d]From heat-affected zone simulation.

Only a partial loading matrix is given for the RB3 capsule, and this matrix will be supplemented at a later date. All samples have been prepared for the HFIR-RB experiments as outlined, and assembly and insertion of the RB1 and RB2 capsules is presently under way.

2.4.5 References

1. J. M. Vitek, R. L. Klueh, M. L. Grossbeck, and J. W. Woods, "HFIR-MFE-T1, -T2, and -RB1: Experiments to Evaluate the Effects of Low-Temperature Irradiation on Ferritic Steels," *ADIP Quart. Prog. Rep. Sept. 30,* 1980, DOE/ER-0045/4, pp. 26-35.
2. R. J. Puigh and N. F. Panayotou, "Specimen Preparation and Loading for the *AD-2* Ferritics Experiment,,, *ADIP Quart. Prog. Rep. June 30, 1980,* DOE/ER-0045/3, pp. 278-79.
3. R. L. Klueh and J. M. Vitek, "Characterization of Ferritic Steels for HFIK Irradiation," *ADIP Quart. Prog. Rep. June 30, 1980,* DOE/ER-0045/3, pp. 294-308.

2.5 EXPERIXENT HFIR-MFE-T3 FOK LOW-TEMPERATURE IRRADIATION OF MINIATUKIZED CHARPY V-NOTCH SPECIMENS OF NICKEL-DOPED FERRITIC STEELS — J. M. Vitek and J. W. Woods (Oak Ridge National Laboratory)

2.5.1 ADIP Task

ADIP Task I.A.2, Define Test Matrices and Test Procedures.

2.5.2 Objective

The objective of this experiment is to provide data on the effect of transmutation produced helium on the impact properties of ferritic steels following low-temperature irradiation. The irrddiation will be done in the target region of the High Flux Isotope Reactor (HFIK). The 12 Cr-1 XoVW alloys (HT9 type) with different nickel contents will be employed using the transmutation of nickel to iron and helium to produce different levels of helium in the irradiated samples.

2.5.3 Summary

The HFIR-MFE-T3 experimental capsule is described. This experiment consists of miniature Charpy V-notch specimens of 12 Cr-1 MoVW and 12 Cr-1 MoVW-2 Ni alloys. The different levels of nickel will result in different helium levels generated during irradiation, and thus will allow for an evaluation of the effect of helium on impact properties. Irradiation of the capsule has started with projected fluence at midplane that will produce 10 dpa expected by January 1982.

2.5.4 Progress and Status

2.5.4.1 Introduction

By taking advantage of the two-step transmutation reaction of nickel, which results in helium production, increasing levels of helium can be generated during irradiation by increasing the initial nickel content of the alloy. Nickel-doped ferritic alloys,[1] with 1/2, 1, and 2% Ni are being studied in order to ascertain the effect of helium at levels expected in fusion environments on various material properties. The HFIR-MFE-T3 experiment is designed to evaluate the effect of helium on the impact properties of 12 Cr-1 MoVW ferritic steels. This experiment will

also provide the necessary baseline information needed to properly evaluate the impact property results from the HFIK–MFE–RBI experiment,[2] in which more alloys are being irradiated but fewer samples of each alloy are available. Finally, inclusion of different heats of 12 Cr-1 MoVW will allow for a proper comparison of the Combustion Engineering heats with the breeder program reference heat.

2.5.4.2 Experimental Design

The HFIR-MFE-T3 capsule is being irradiated at the reactor coolant temperature of 50°C. Samples are enclosed in evacuated and collapsed aluminum tubing to protect them from excessive corrosion while maintaining good thermal contact with the coolant. This technique has been described earlier.[3] The irradiation is in one of the outermost target positions of the HFIK flux trap region.

The experiment consists of a single column of miniature Charpy V-notch impact specimens. The samples are 5 by 5 mm in cross section, and 25.4 mm in length. The notch has a root radius of 0.05 to 0.10 mm and the remaining sample ligament is 4.24 mm in length. The samples were not precracked. The specimens were cut from 5.3-mm-thick plate with the length parallel to the rolling direction and the notch running through the thickness of the plate.

A SiC temperature monitor was inserted in a 12 Cr-1 MoVW spacer to determine the amount of heating during irradiation. A flux monitor was also included in the irradiation capsule.

2.5.4.3 HFIR-MFE-T3 Test Matrix and Irradiation Conditions

Three alloys are included in the HFIR-MFE-T3 capsule: 12 Cr-1 MoVW (breeder heat), 12 Cr-1 MoVW (Combustion Engineering heat), and 12 Cr-1 MoVW-2 Ni (Combustion Engineering heat). The bulk of the samples are from the Combustion Engineering heats, in order to determine the effect of helium (by way of the nickel transmutation reaction) on the impact properties. The breeder reference heat is included in order to compare different heats of 12 Cr-1 MoVW steel. Table 2.5.1 lists the alloys and their heat treatments. The alloy compositions were reported previously.[1] The specimen matrix is given in Table 2.5.2.

Table 2.5.1. Alloys Irradiated in HFIR-MFE-T3

Alloy	Heat	Normalizing		Tempering	
		(°C)	(h)	(°C)	(h)
12 Cr-1 MoVW	91353 (Breeder)	1050	0.5	780	2.5
12 Cr-1 MoVW	XAA-3587 (Combustion Engineering)	1050	0.5	780	2.5
12 Cr-1 MoVW-2 Ni	XAA-3589 (Combustion Engineering)	1050	0.5	700	5

Table 2.5.2. Specimen Matrix for HFIR-MFE-T3

Position	Distance from midplane (mm)	Alloy	Heat
1 (Top)	184	12 Cr-1 MoVW	91353
2	159	12 Cr-1 MoVW	91353
3	133	12 Cr-1 MoVW-2 Ni	XAA-3589
4	108	12 Cr-1 MoVW-2 Ni	XAA-3589
Aluminum spacer			
5	76	12 Cr-1 MoVW-2 Ni	XAA-3589
6	51	12 Cr-1 MoVW-2 Ni	XAA-3589
7	25	12 Cr-1 MoVW-2 Ni	XAA-3589
8	0	12 Cr-1 MoVW-2 Ni	XAA-3589
9	−25	12 Cr-1 MoVW-2 Ni	XAA-3589
Flux monitor			
10	−51	12 Cr-1 MoVW	XAA-3587
11	−76	12 Cr-1 MoVW	XAA-3587
Temperature monitor			
12	−108	12 Cr-1 MoVW	XAA-3587
13	−133	12 Cr-1 MoVW	XAA-3587
14	−159	12 Cr-1 MoVW	XAA-3587
15	−184	12 Cr-1 MoVW	XAA-3587
16	−210	12 Cr-1 MoVW	XAA-3587
17	−235	12 Cr-1 MoVW	XAA-3587
18	−260	12 Cr-1 MoVW	91353

The goal fluence for the experimental midplane will produce a displacement level of 10 dpa. The fluence decreases towards the end of the capsule, falling to approximately 50% of the midplane values. Expected helium levels at the midplane are 20 at. ppm in the base alloy and 85 at. ppm in the 2% Ni doped alloy. The capsule was inserted into HFIK in early September 1981, and will be removed in January 1982.

2.5.5 References

1. R. L. Klueh and J. M. Vitek, "Characterization of Ferritic Steels for HFIR Irradiation," *ADIP Quart. Prog. Rep. June 30, 1980,* DOE/ER-0045/3, pp. 294–308.
2. J. M. Vitek and J. W. Woods, "Experiments HFIR–MFE–RB1, -RB2, and -RB3 for Low–Temperature Irradiation of Path E Ferritic Steels," Sect. 2.4 in this report.
3. J. M. Vitek, R. L. Klueh, M. L. Grossbeck, and J. W. Woods, "HFIK–MFE–T1, -T2, and -RB1: Experiments to Evaluate the Effects of Low–Temperature Irradiation on Ferritic Steels," *ADIP Quart. Prog. Rep. Sept. 30, 1980,* DOE/ER-0045/4, pp. 26–35.

3. PATH A ALLOY DEVELOPMENT — AUSTENITIC STAINLESS STEELS

3.1 RESULTS OF THE MFE-5 IN-REACTOR FATIGUE CRACK GROWTH EXPERIMENT - A. M. Ermi (Hanford Engineering Development Laboratory)

3.1.1 ADIP Task

ADIP Task I.B.l, "Fatigue Crack Growth in Austentic Alloys" (Path A).

3.1.2 Objectives

An in-reactor fatigue machine has been developed to conduct a fatigue crack propagation experiment in the ORR on the Path A Reference Alloy. Effects of dynamic irradiation on crack growth behavior will be evaluated by comparing the results with those of an unirradiated test.

3.1.3 Summary

Examination of the crack growth specimens from the ORR-MFE-5 in-reactor fatigue test and from the HEDL thermal control test has been completed. Results indicated that there were no effects of dynamic irradiation on crack growth at a fluence of 1.5×10^{21} n/cm^2 (E > 0.1 MeV). Furthermore, the crack growth rates in elevated temperature sodium were a factor of 3 to 4 lower than in room temperature air.

3.1.4 Progress and Status

3.1.4.1 Introduction

Fatigue crack propagation (FCP) in the first wall of a magnetic fusion reactor may be a limiting quantity governing reactor lifetimes. Previous studies of irradiation effects on FCP have all been conducted out of reactor on materials preirradiated in the unstressed condition. The ORR-MFE-5 experiment was designed to investigate FCP during irradiation, where dynamic irradiation may effect crack growth characteristics.

3.1.4.2 Specimen Examination and Results

As reported previously, the in-reactor fatigue machine[1,2] was removed from the ORR after ~60,000 cycles when an apparent specimen

chain lengthening caused the bellows to reach its stop before the full load could be transmitted to the specimens.[3] The thermal control test at **HEDL** was also terminated after it had accumulated the same number of cycles. Both assemblies were sectioned and inserted into a specially designed furnace apparatus where the sodium was removed from around the specimens.

Crack length measurements on the thermal control specimens were made with a travelling microscope, while the irradiated specimens were measured from a calibrated television screen. Because of (1) the lower than expected growth rates in sodium; and (2) the shortened duration of the test (the planned duration was 200,000 cycles), nine of the sixteen specimens exhibited crack growths which measured less than 0.125 mm (0.005 in). These data were discarded since the growth was not considered adequate for a reliable result. Based on the experience of previous chain testing,[4] only crack extensions greater than 0.125 mm were used in the determination of crack growth rates. (The ASTM Standard actually specifies 0.250 mm as the minimum crack growth criterion.[5])

The crack growth results for both the in-reactor and thermal control tests are given in Figure 1. A room temperature air data band is included for comparison. The temperatures across the two specimen chains (detailed elsewhere[7]) varied from 315°C at the bottoms to 460°C near the centers. Since the tests were conducted in sodium, the direct effects of temperature on growth rate should be minimal since FCP in sodium is not strongly thermally activated up to about $0.5\ T_m$.[8,9]

The results indicated that there were no significant effects of dynamic irradiation on fatigue crack growth for a fluence of 1.5×10^{21} n/cm^2, E > 0.1 MeV. Secondly, the crack growth rates in the sodium environment were a factor of 3 to 4 lower than that for a temperature air environment. There was some question as to whether the lower growth rates observed were a true representation of the crack

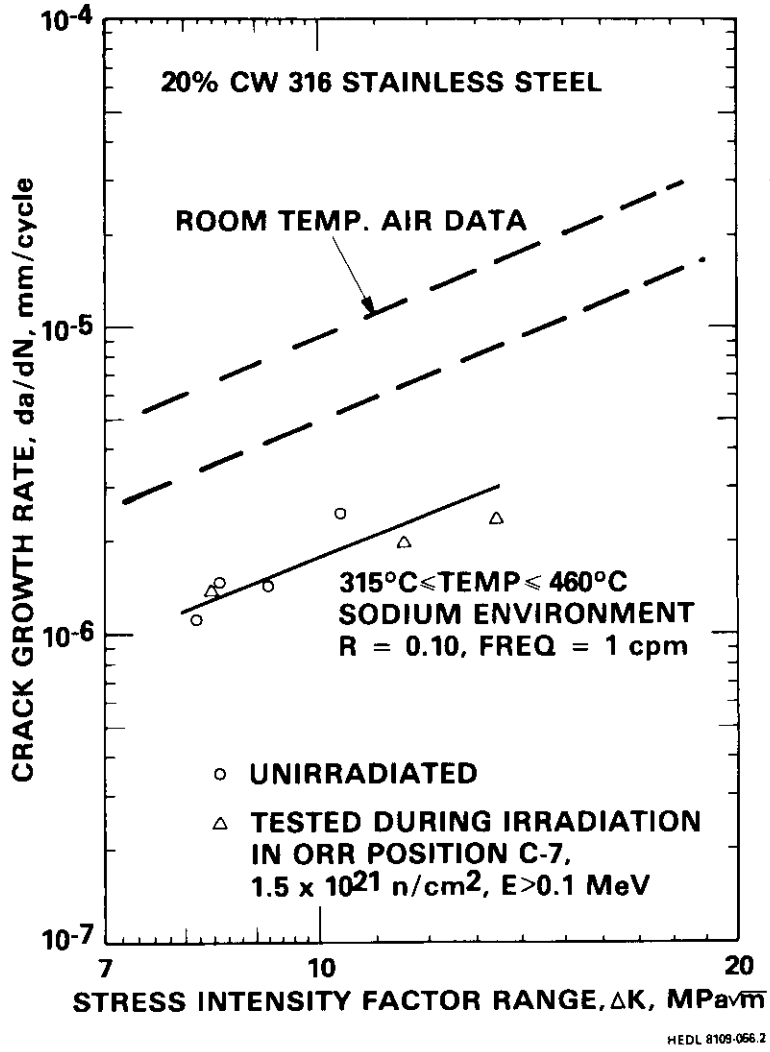

Figure 3.1.1 Comparison of fatigue crack growth behavior of unirradiated and in-reactor tested 20% cold-worked 316 stainless steel (Room temperature data from ref. 6).

growth behavior or whether the growth rates were affected in some way by the several test shutdowns and thermal cycles common in such reactor type tests. To investigate this, two specimens were individually cycled in helium on laboratory hydraulic fatigue testers, duplicating the test conditions and shutdown history of the in-reactor and thermal control tests. The crack lengths of these two specimens were continuously monitored using an electropotential technique.(6)

The crack length **vs.** cycles results of one of the tests is shown in Figure 2. Despite twelve test interruptions, including five temperature shutdown cycles, the crack lengths increased smoothly; there was no evidence of crack growth retardation after any of the shutdowns.

3.1.5 Conclusions

An in-reactor fatigue crack propagation experiment was conducted in the ORR on 20% cold-worked **316** stainless steel. The test was conducted in sodium at a peak temperature of 460°C and at a frequency of **1** cpm. Comparison of the results with a laboratory control test indicated that:

(1) There were no effects of dynamic irradiation for a fluence of 1.5×10^{21} n/cm^2, E > 0.1 MeV.

(2) Crack growth rates were a factor of *3* to 4 lower than in room temperature air.

3.1.6 Future Work

Plans are underway to conduct a second in-reactor FCP experiment on the same heat of material using a newly designed fatigue machine. The new test matrix includes extension of the test to a year, or a fluence of $\sim 10^{22}$ n/cm^2, E > 0.1 **MeV.**

3.1.7 References

1. **A.** M. Ermi, "Status of an In-Reactor Fatigue Crack Growth Experiment", *ADIP Quarterly* ***Progress*** *Report,* ***June*** *30, 1979,* DOE/ET-0058/6 (1979) 28.

2. **A. M.** Ermi, "Results of Prototypic Testing for the MFE-5 In-Reactor Fatigue Crack Propagation Experiment", *ADIP Quarterly*

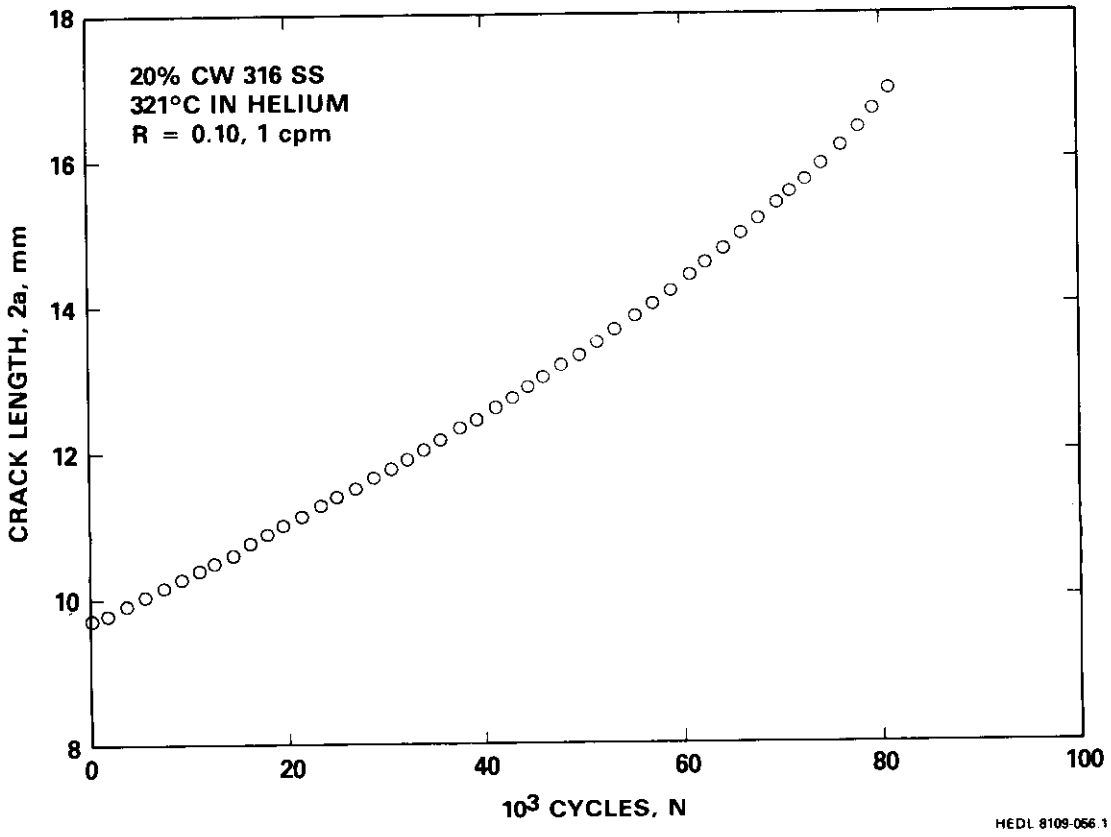

Figure 3.1.2 Crack length vs. cycles from a laboratory test which duplicated the shutdown history of the in-reactor experiment.

Progress Report, September 30, 1979, DOE/ET-0058/7 (1979) 50.

3. A. M. Ermi, "Status of MFE-5 In-Reactor Fatigue Crack Growth Experiment, *ADIP Quarterly Progress Report, March 31, 1981*, DOE/ER-0045/6 (1981) 6.
4. A. M. Ermi, R. E. Bauer, B. A. Chin, and J. L. Straalsund, "Multispecimen Fatigue Crack Propagation Testing", Journal of Eng. Mat. and Tech., 103 (1981) 240.
5. ASTM Designation: E647-78T, Annual Book of ASTM Standards, Part 10 (1979) 707.
6. D. A. Mervyn and A. M. Ermi, "Miniature Specimen Technology for Postirradiation Fatigue Crack Growth Testing", Proceedings of the 8th Symposium on Engineering Problems of Fusion Research, Vol. IV (November 1979) 1832.
7. A. M. Ermi, "Status of MFE-5 In-Reactor Fatigue Crack Growth Experiment, *ADIP Quarterly Progress Report, December 31, 1980*, DOE/ER-0045-5 (1980) 6.
8. L. A. James and R. L. Knecht, "Fatigue Crack Propagation Behavior of Type 304 Stainless Steel in a Liquid Sodium Environment", Met. Trans., 6A (1975) 109.
9. L. A. James, "Fatigue Crack Propagation in Austenitic Stainless Steels", Atomic Energy Review, 14 (1976) 53.

3.2 EFFECT OF PREINJECTEO HELIUM ON SWELLING AND MICKOSTKUCTURE OF NEUTKON IKRADIATEU STRESSED TYPE 316 STAINLESS STEEL —

A. Hishinuma* and J. M. Vitek (Oak Ridge National Laboratory)

3.2.1 ADIP Tasks

ADIP Tasks I.C.1., Microstructural Stability, and I.C.2., Microstructure and Swelling in Austenitic Alloys.

3.2.2 Objective

The objective of this work is to characterize the effect of helium on the swelling and microstructure of pressurized tubes of cold worked type 316 stainless steel after irradiation in EBR-II. This was accomplished by preinjecting helium in only a fraction of the total specimen length in pressurized tube samples, thereby allowing a comparison of regions with and without helium from the same specimen. The helium levels, stress, and irradiation temperatures were varied to determine their influence.

3.2.3 Summary

In this period, examination was performed on pressurized tubes of 22%-cold-worked type 316 stainless steel after irradiation at 525°C. The hoop stress was 31.7 MPa and the fluence was 5×10^{26} neutrons/m^2 (>0.1 MeV) producing 23 dpa. Helium was preinjected into the center portion of the tube specimen to levels of 20 and 60 at. ppm.

Diameter measurements, which include both swelling and creep effects, show that a 20 at. ppm He preinjected region expanded about 30% less than the uninjected regions. For a sample with 60 at. ppm He, a 60% lower expansion was found.

The microstructure of a 60 at. ppm He preinjected region shows a bimodal cavity distribution. An inhomogeneous distribution of voids less than 50 nm in diameter is accompanied by a homogeneous population of tiny cavities, with a concentration near $10^{21}/m^3$. In the uninjected region, a single distribution of cavities was observed with a number density of

---

* On assignment from the Japanese Atomic Energy Research Institute, Tokai-Mura, Japan.

about $1 \times 10^{20}/m^3$ and an average diameter of about 100 nm. Precipitates were observed in both regions. Almost all were eta-phase, with a number density of about $5 \times 10^{19}/m^3$.

3.2.4 Progress and Status

3.2.4.1 Experimental Procedure

The specimens examined in this study were thin-walled helium filled capsules produced from drawn tubing with welded end caps. They were 51 mm in length, with an outer diameter of 4.57 mm and a wall thickness of 0.25 mm. These specimens were internally pressurized, producing biaxial loading on the tube wall with a hoop stress of 31.7 MPa at temperature. The specimens were preinjected with helium into the center 13-mm section along the length, using the Oak Ridge Isochronous Cyclotron (ORIC). The beam of 60 MeV alpha particles was degraded to yield a variable energy at the tube specimen, resulting in a uniform distribution of helium through the tube wall thickness. Injection at 20°C achieved helium levels of 20 and 60 at. ppm.[1] Both ends of the tubes were free of any preinjected helium.

The tube specimens were irradiated in EBR-II at 525°C (nominal temperature) to a fluence of 5×10^{26} neutrons/m^2 (>0.1 MeV), producing 23 dpa. The diameters of the specimens were measured after helium filling and after neutron irradiation. These measurements were carried out at Hanford Engineering Development Laboratory.[2] The disk specimens for microstructure characterization were prepared by cutting the tubes as shown schematically in Fig. 3.2.1. Sections of these hoops were electropolished in a solution of CH_3OOH and H_2SO_4 (7:1) at −10°C and with a voltage of 12 to 15 V.

3.2.4.2 Results

The diameter measurements on a 60 at. ppm He preinjected specimen (S-22) are shown in Fig. 3.2.2. The letters A, B, C, D, and E on the abscissa correspond to the specimen positions in Fig. 3.2.1. The center region, containing preinjected helium, shows a much smaller diameter change

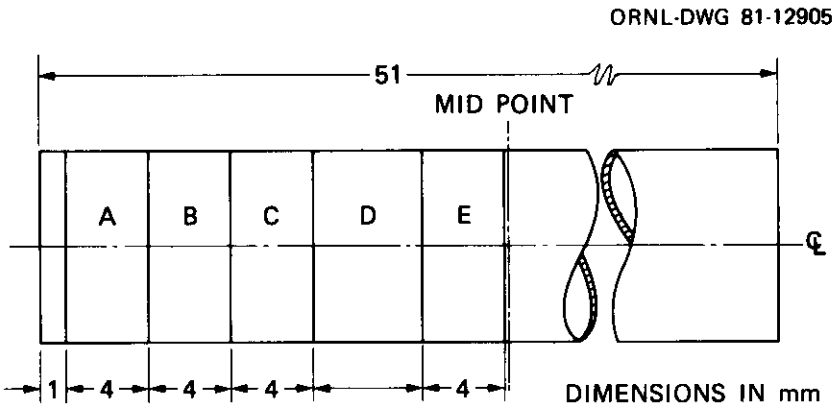

Fig. 3.2.1. Schematic Diagram of Segmented Pressurized Tube Samples for Microstructural Analysis.

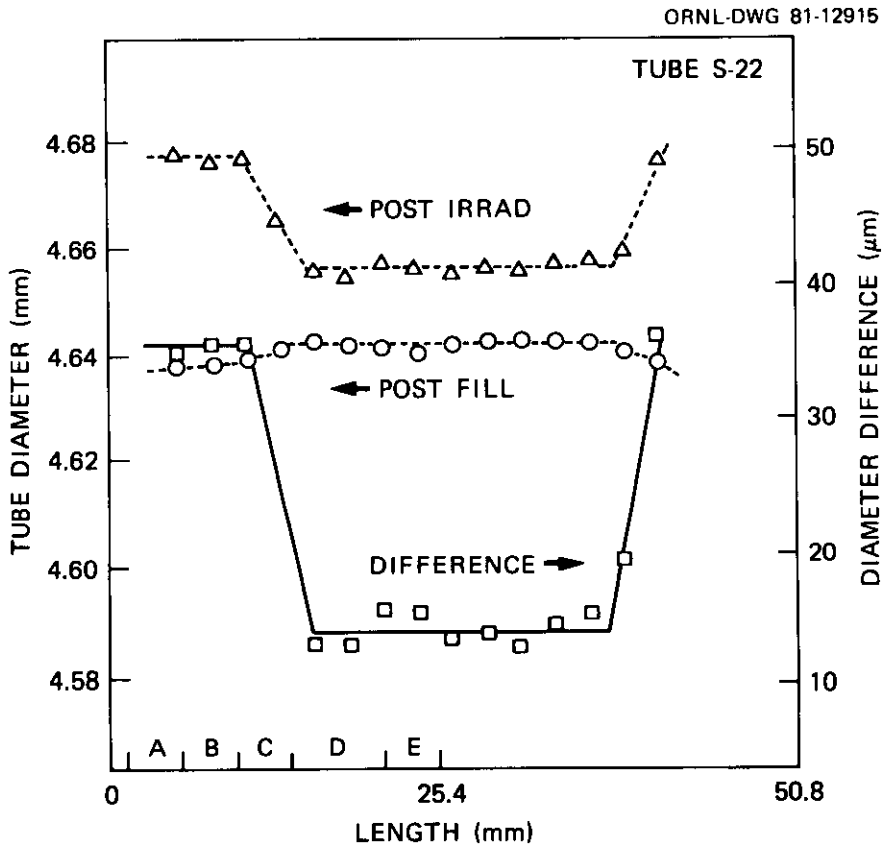

Fig. 3.2.2. Diameter Measurements Versus Specimen Length for Tube S-22 Preinjected with 60 at. ppm He in the Center Section and then Irradiated to 23 dpa at 525°C in EBR-II.

due to the irradiation than that found in the uninjected outer region. The diameter change was about 14 μm in the center section and 36 μm in the outer region. Thus, the helium preinjection suppressed the expansion (composed of both swelling and irradiation creep) by about 60%. The degree of suppression decreases with decreasing preinjected helium levels. This is shown in Table 3.2.1, where diameter measurement results of specimens examined are summarized.

The microstructure of specimen S-22 is shown in Figs. 3.2.3 and 3.2.4. Figure 3.2.3(a) shows the microstructure of the uninjected region. This region contains a relatively homogeneous distribution of cavities. The cavity number density and average diameter are about $1 \times 10^{20}/m^3$ and about 100 nm, respectively. In contrast, the cavity distribution in the helium preinjected region was inhomogeneous and bimodal; heterogeneous cavity distributions with average diameter of less than about 50 nm were observed as shown in Fig. 3.2.3(b), accompanied by homogeneous tiny cavities, shown in Fig. 3.2.4. The number density and average diameter of these smaller cavities are about $10^{21}/m^3$ and about 3 nm, respectively.

Table 3.2.1. Diameter Changes after Neutron Irradiation in EBR-II to 23 dpa at 525°C

Sample	Helium content (at. % ppm)	Diameter increase (nm)	Decrease in tube expansion in the helium preinjected region (%)
s-22			
Uninjected	0	0.036	61
Helium preinjected	60	0.014	
S-23			
Uninjected	0	0.052	62
Helium preinjected	60	0.020	
s-44			
Uninjected	0	0.064	22
Helium preinjected	20	0.050	
s-45			
Uninjected	0	0.047	30
Helium preinjected	20	0.033	

[a]Hoop stress was 31.7 MPa.

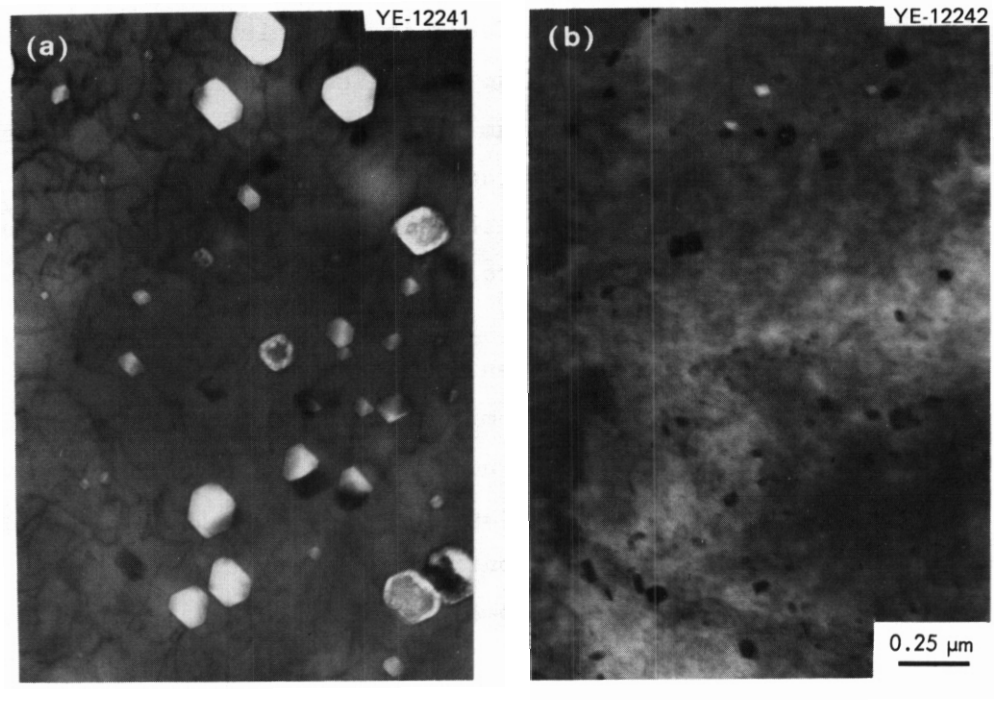

Fig. *3.2.3.* Transmission Electron Microscopy Micrographs of Specimen *S-22* After Irradiation in the (a) Uninjected and (b) Helium Preinjected (60 at. ppm He) Regions. Sample was irradiated to *23* dpa at 525°C.

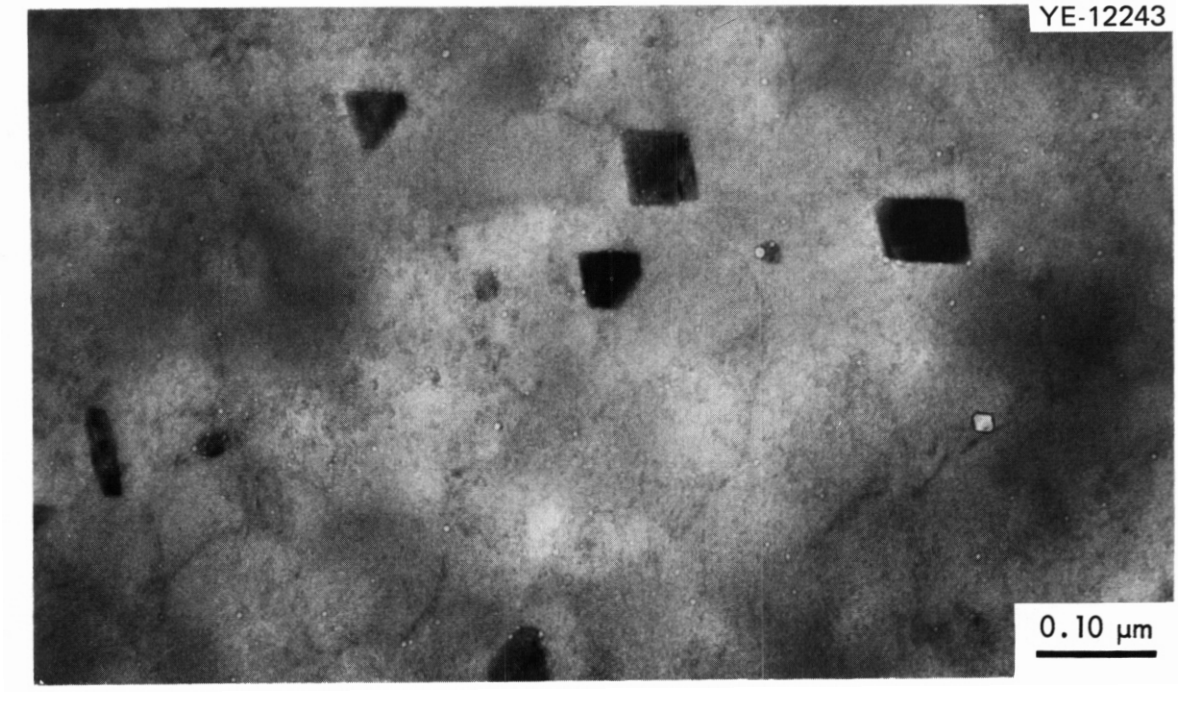

Fig. *3.2.4.* Transmission Electron Microscopy Micrographs of Preinjected Helium (60 at. ppm He) Region of Specimen *S-22* Showing the Fine Distribution of Cavities. Sample was irradiated in EBR-II to *23* dpa at *525°C.*

Although the larger cavities in the preinjected helium region are inhomogeneously distributed, their average density is smaller than that found in the uninjected region. In addition, the size of the cavities in the helium injected region are significantly smaller than those found in the helium-free region. These two observations account for the smaller swelling found in the helium preinjected region. These micrographs also show a large concentration of precipitates, about $5 \times 10^{19}/m^3$, in both regions. Some cavities are attached to the precipitates, but this is not always true. These precipitates were identified as eta phase by using convergent beam electron diffraction (CBED).

3.2.5 Conclusions

The present results may be summarized as follows:

1. Preinjected helium at levels of 20 to 60 at. ppm suppresses the swelling in neutron irradiated cold-worked type 316 stainless steel at 525°C.

2. The degree of suppression increases with increasing preinjected helium levels.

3. The preinjected helium results in a bimodal distribution of cavities after neutron irradiation. All of these cavities are smaller than the cavities found in the uninjected areas of the same tube.

3.2.6 References

1. J. A. Horak, "Helium Implantation in Potential CTK Structural Materials," *Controlled Thermonuclear Materials Technology Program Annu. Prog. Rep. June 30, 1975, ORNL-5082*, pp. 40-42.

2. E. R. Gilbert and B. A. Chin, "Irradiated Materials Measurement Technology," pp. 665-80 in *Effects of Radiation a Materials, ASTM Spec. Tech. Publ. 725*, American Society for Testing and Materials, Philadelphia, 1981.

3.3 MICROSTRUCTURAL DEVELOPMENT ON 20%-COLD-WORKED TYPES 316 AND 316 + Ti STAINLESS STEELS IRRADIATED IN HFIK: TEMPEKATURE AND FLUENCE DEPENDENCE OF THE DISLOCATION COMPONENT — P. J. Maziasz (Oak Ridge National Laboratory)

3.3.1 ADIP Tasks

ADIP Task I.C.1, Microstructural Stability, and I.C.2, Microstructure and Swelling in Austenitic Alloys.

3.3.2 Objective

The objective of this work is to characterize the microstructural development in standard and titanium modified type 316 stainless steels irradiated in the High Flux Isotope Reactor (HFIK). This report describes the dislocation component of this microstructure. The total microstructure is used for swelling determination, mechanical properties correlation, and input to alloy development. The extensive analysis is aimed at better understanding relationships, mechanisms, and important variables controlling microstructural evolution during irradiation.

3.3.3 Summary

The dislocation structures of ZOX-cold-worked type 316 stainless steel (CW 316) and CW 316 + Ti are investigated and compared after thermal aging, HFIR irradiation at 55 to 750°C at fluences producing up to 16 dpa and 1020 at. ppm He, and EBR-II irradiation to 8.4 and 36 dpa at 500 to 630°C. The CW 316 shows dislocation recovery on aging in the range 550 to 700°C, with recovery increasing as temperatures increase. By comparison, CW 316 + Ti exhibits MC formation and resists dislocation recovery for *4400* h at 700°C. Dislocation recovery and precipitation are uncoupled in CW 316 after EBR-II irradiation. Recovery is enhanced and precipitation is retarded. The DO heat of CW 316 does not form Frank loops in the 500 to 630°C range. Network dislocation concentrations tend toward a steady value of 1 to $3 \times 10^{14} m/m^3$, with only slight temperature and fluence variations. During HFIK irradiation, CW DO heat 316 shows dislocation recovery after 7 to 10 dpa, with moderate temperature dependence from

55 to 450°C and stronger temperature dependence above 450°C. Between 55 and 550°C the dislocation recovery is strongly coupled to other microstructural features. Frank loops are found for irradiation at 450°C and below, cavities at 350°C and above, and precipitation at 450°C and above. The dislocation structure recovers to similar values in HPIR and EBR-II at 500 to 630°C.

The dislocation microstructure in CW 316 + Ti is similar to CW 316 after HFIR irradiation from 55 to 750°C, but the coupling of network recovery, Frank loop behavior, and other microstructural phenomena is different from those in CW 316. The greatest differences reflect MC dislocation pinning and reduced phase instability. Dislocation concentrations are 3 to 5 times higher in the CW 316 + Ti than in the CW 316.

3.3.4 Progress and Status

3.3.4.1 Introduction

This is the second part of a series on the development of the total microstructure in 20%-cold-worked types 316 stainless steel (CW 316) and 0.23 wt % Ti-modified 316 stainless steel (CW 316 + Ti) during irradiation in HFIR. The cavity component was reported previously,[1] and that portion of the microstructure reflects the most direct effect of the increased helium generation relative to a fast breeder reactor (FBR) like Experimental Breeder Reactor (EBR)-II.

The HFIR dislocation data on CW 316 and CW 316 + Ti covers the temperature range 55 to about 750°C for neutron fluences producing up to 16 dpa and 1020 at. ppm He. Thermally aged control samples of CW 316 and CW 316 + Ti have also been examined. [There is but little data on the thermal recovery of CW 316 (refs. 2 and 3) and none on CW 316 + Ti.] EBR-II data on CW 316 is also included to give a baseline for recovery under irradiation with low helium production.

Bloom and Stiegler described dislocation changes produced by EBR-II irradiation of the same heat of CW 316 (DO heat) examined in this work.[4] Brager and Garner have recently reported dislocation data on the same material irradiated to higher fluences in EBR-II (refs. 5 and 6).

Quantitative dislocation information on other heats of CW 316 have been reported by Bramman et al.[7] after irradiation in the Dounreay Fast Reactor (DFR) and by Brager et al.[8,9] after EBR-II irradiation. There is no literature data on the effect of EBR-II irradiation on dislocations in the heat of CW 316 + Ti (R1 heat) presently reported.

3.3.4.2 Experimental

The compositions of two steels, CW 316 (DO heat) and CW 316 + Ti (R1 heat) are given in Table 3.3.1. Rod stock of each material was annealed for 1 h at 1150°C, cold swaged to 50% reduction in area, annealed 1 h at 1050°C, and then swaged an additional 20%. Buttonhead tensile specimens were machined from a portion of the rod and irradiated in experiments HFIR-CTR-9 through -13. Many of the details of irradiation history and conditions, including neutron spectra, temperature, and helium generation, were reported previously.[1,10]

Table 3.3.1. Composition of Two Austenitic Stainless Steels

Alloy	Heat identification	Content,[a] wt %										
		Cr	Ni	Mo	Mn	C	Ti	Si	P	S	N	B
316	DO	18.0	13.0	2.58	1.90	0.05	0.05	0.80	0.013	0.016	0.05	0.0005
316 + Ti	R1	17.0	12.0	2.50	0.5	0.06	0.23	0.40	0.01	0.013	0.0055	0.0007

[a]Balance iron.

Other segments of these same rods were wrapped in tantalum foil encapsulated in evacuated quartz tubes, backfilled with high-purity argon, and then sealed. The encapsulated specimens were isothermally'aged at 275, 375, 475, 560, 600, and 700°C for 2770 and 4400 h to equal the HFIR irradiation times.

Sheet samples of CW 316 were irradiated in experiment X-264, in row 8 of EBR-II at 500 and 625°C to 8.4 dpa (ref. 11). Samples of CW 316 DO heat were also cut from stress-free sample holders from experiments X-100 and X-100A. This material had been irradiated in row 2 of EBR-II at average temperatures of about 525 and 630°C, to neutron

fluences producing 36 dpa. Several papers report experimental details of this last experiment, particularly the fact that start and finish temperatures were different, increasing by about 50°C during the course of the irradiation.[4] Data is also included from Brager and Garner.[5,6] They examined pieces of these holders that were irradiated in a reconstituted experiment in EBR-II for an additional 33 dpa at 510°C for the piece initially irradiated at about 525°C, and an additional 38 dpa at about 620°C for the piece initially irradiated at about 630°C.

Only those details of the HFIK irradiations pertinent to the dislocation information and not treated previously will be given here. Transmission electron microscopy (TEM) disks were sliced from the shoulders of buttonhead tensile specimens. The irradiation temperature was nearly constant along both gage and shoulders, as shown in ref. 10, unlike older HFIR experiments.[12] As noted previously,[1,13] the actual HFIR irradiation temperature for experiments HFIR-CTR-9 through -13 are probably 50 to 75°C higher than calculated. Recent TEM microstructure matching after about 8 to 10 dpa HFIR irradiation of a sample with an irradiation temperature measured using melt-capsule monitors also indicate this 50 to 75°C higher than design temperature. To improve the comparison with thermally aged and EBR-II irradiated materials, the old calculated HFIR temperatures will be replaced by nominal irradiation temperatures that are 50 to 75°C higher than previously reported. This is consistent with a recent similar treatment of the microstructural data in ref. 14. Final temperature calculations are still pending.

Most TEM disks were cut from the shoulder of specimens that were tensile tested at 75 to 100°C below the revised irradiation temperature. While these samples should contain the as-irradiated microstructure, several disks were removed before tensile testing from a sample irradiated at 525 to 550°C to 10 dpa to confirm this.

Transmission electron microscopy disks were thinned using either a standard two-stage method or using an automatic dual-jet Tenupole thinning unit with cooling attachment.

Dislocation analysis methods similar to those reported by Barton et al. were used.[15] JEM 100 C and 100 CX microscopes were primarily used,

with some supplementary examination using a Philips *EM–400* with field emission gun. All were operated at 120 kV. Thickness was estimated from g_{111} or g_{200} dynamical ($s = 0$) thickness fringes, with the diffraction condition set by observing maximum spacing of fringes while rocking the crystal. Values of extinction distance, ξ_g, of 27.8 nm for g_{111} and 32.0 nm for g_{200} were taken from Muir[16] and values agree well with those used by Barton et al.[15] Network concentrations were usually measured several fringes from the edge in regions about 100 to 200 nm thick with two–beam, $s > 0$, kinematical conditions for g_{111} (usually 10 to 15° away from a $(0\bar{1}1)$ or $(0\bar{1}2)$ foil normal orientation) or g_{200} (usually 10 to 15" away from (001) or $(0\bar{1}1)$ foil normal orientations). The length per unit volume dislocation concentration parameter, A, was measured by counting intersections of the network with a set of concentric circles inscribed on a transparent overlay. Values measured in bright field were multiplied by 1.5 for g_{200} and 2.0 for g_{111} to account for invisibilities of an isotropic distribution of dislocations with $\langle 110 \rangle$ type Burgers vectors. When network concentrations exceeded approximately 10^{15} m/m^3, or when faulted loops were present, weak beam imaging with g_{200} in a g/3g diffraction condition was used for the network with foils oriented near (001) or $(0\bar{1}1)$ poles. Frank faulted loops were imaged separately from the network, using high resolution dark field with $\langle 111 \rangle$ kinematical satellite streaks around g_{200} type matrix reflections.[17] Loop size distributions were measured using a Zeiss particle size analyzer, and at least two sets of loops on different $\{111\}$ planes were analyzed. In several cases, all four sets were analyzed and their size distributions found to exactly superimpose, consistent with the samples being unstressed. The loop contribution to the total dislocation density was then added to the network component. Given the above precautions and techniques, the expected accuracies are[15] total dislocation concentration, A, $^{+100}_{-50}$%; average loop diameter, d_L, ±25%; and loop concentration, N_L, ±30%.

3.3.4.3 Results

The measured dislocation parameters for all samples in all exposure environments are given in Table 3.3.2 for CW 316 and in Table 3.3.3 for CW 316 + Ti.

Table 3.2 Dislocation Statistics for 20%-Cold-Worked Type 316 Stainless Steel After Thermal Aging, EBR-II or HFIR Irradiation

Exposure conditions					Dislocation information			
						Loops		
Design temperature (°C)	Probable temperature (°C)	Neutron fluence (E > 0.1 MeV, neutrons/m^2)	Displacement damage (dpa)	Helium (at. ppm)	Average network concentration (m/m^3)	Average diameter (nm)	Concentration (loops/m^3)	Total dislocation concentration (m/m^3)
		As cold worked			3–5 × 10^{15}			3–5 × 10^{15}
				Thermally aged (4400 h)				
	470				3–5 × 10^{15}			3–5 × 10^{15}
	560				0.8–1 × 10^{15}			0.8–1 × 10^{15}
	600				5–6 × 10^{14}			5–6 × 10^{14}
	700				1 × 10^{14}			1 × 10^{14}
				Irradiated in EBR-II (3300 to 9000 h)				
	500	1.6 × 10^{26}	8.4	~5	3 × 10^{14}			3 × 10^{14}
	525	6.6	36	~22	2 × 10^{14}			2 × 10^{14}
	625	1.6 × 10^{26}	8.4	~5	2 × 10^{14}			2 × 10^{14}
	630	6.6	36	~22	1 × 10^{14}			1 × 10^{14}
				Irradiated in HFIR (2770 to 4400 h)				
55	55[a]	1.4 × 10^{26}	10.8	520	5 × 10^{14}	23[b]	1.0 × 10^{21}	1.4 × 10^{15}
285	325–350[a]	1.0	7.7	390	5 × 10^{14}	3.5[c]	7.7 × 10^{22}	6 × 10^{14}
375	425–450[a]	1.1	8.5	380	1 × 10^{15}	24[b]	1 × 10^{21}	1.5 × 10^{15}
375	425–450[a]	1.7	13.0	740	2.5 × 10^{14}	19[b]	9 × 10^{21}	2.5 × 10^{14}
475	525–550[a]	0.9	6.9	290	4 × 10^{14}	[d]		4 × 10^{14}
475	525–550[a]	1.3	10.0	500	1 × 10^{14}	[d]		1 × 10^{14}
475	525–550[e]	1.3	10.0	500	1.5 × 10^{14}	[d]		1.5 × 10^{14}
475	525–550[a]	2.1	16.0	1020	3 × 10^{14}	[d]		3 × 10^{14}
565	620–645[a]	1.2	9.2	440	1 × 10^{14}	[d]		1 × 10^{14}
565	620–645[a]	2.0	15.0	880	8 × 10^{13}	[d]		8 × 10^{13}
620	670–700[a]	2.1	16.0	1020	4 × 10^{12}	[d]		4 × 10^{12}

[a]Taken from shoulder samples that saw little or no stress during postirradiation tensile testing 25 to 75°C below the irradiation temperature.

[b]Frank-faulted interstitial loops.

[c]Small defect clusters, tenatively identified as loops, but nature not yet determined.

[d]No faulted loops observed.

[e]As-irradiated microstructure from duplicate specimen irradiated at exactly the same condition as the transmission electron microscopy disk out before tensile testing.

Table 3.3.3. Dislocation Statistics for 20%-Cold-Worked Type 316 + Ti Stainless Steel After Thermal Aging and HFIR Irradiation

Exposure conditions					Dislocation information			
Design temperature (°C)	Probable temperature (°C)	Neutron fluence (E > 0.1 MeV, neutrons/m^2)	Displacement damage (dpa)	Helium (at. ppm)	Average networ concentration (m/m^3)	Average diameter (nm)	Concentration (loops/m^3)	Total dislocation concentration (m/m^3)
		As cold worked			5 × 10[illegible]			5 × 10[illegible]
				Thermally aged (4400 h)				
	470				5 × 10^{15}			5 × 10^{15}
	560				5 × 10^{15}			5 × 10^{15}
	600				5 × 10^{15}			5 × 10^{15}
	700				5 × 10^{15}			5 × 10^{15}
				Irradiated in HFIR (2770 to 4400 h)				
55	55	1.3 × 10^{26}	10.5	490	2.7 × 10^{15}	3.5[a]	3.5 × 10^{23}	6.6 × 10^{15}
285	325–350	1.0	7.7	390	1.5 × 10^{15}	13[b]	4.2 × 10^{22}	3.2 × 10^{15}
375	425–450	1.1	8.5	380	1.5 × 10^{15}	25[b]	9.2 × 10^{21}	2.2 × 10^{15}
375	425–450	1.7	13.0	740	6 × 10^{14}	50[b]	1 × 10^{21}	7.6 × 10^{14}
475	525–550	1.3	10.0	500	5 × 10^{14}	[c]		5 × 10^{14}
475	525–550	2.1	16.0	1020	5 × 10^{14}	[c]		5 × 10^{14}
565	620–645	1.2	9.2	440	3 × 10^{14}	[c]		3 × 10^{14}
565	620–645	2.0	15.0	880	3 × 10^{14}	[c]		3 × 10^{14}
620	670–700	1.3	10.0	500	3 × 10^{14}	[c]		3 × 10^{14}
670	720–745	1.3	10.0	500	1.5–3 × 10^{14}	[c]		1.5–3 × 10^{14}

[a]Small defect clusters, tenatively identified as loops, but nature not yet determined.

[b]Frank faulted interstitial loops.

[c]No loops observed.

3.3.4.3.1 Thermal Aging in CW *316*. The dislocation microstructure of CW *316* after aging at 470°C for *4400* h is shown in Fig. 3.3.1. The microstructure is unchanged from the as-cold-worked structure. The network shows a somewhat cellular arrangement of tangles with linear arrays or clusters (usually parallel to <111> type directions). Image overlap, and hence blackness, will occur at local concentrations of *5* to 7×10^{15} m/m^3. The cell widths range from several hundred nanometers to about 0.5 μm and are characteristic of cold or warm deformed materials. Only the dislocation statistics for aging times of *4400* h are reported in Table *3.3.2*, because no change occurred between *2770* and *4400* h. The dislocation concentrations are shown as a function of aging temperature in Fig. *3.3.2*. Dislocation recovery and precipitation apparently both begin

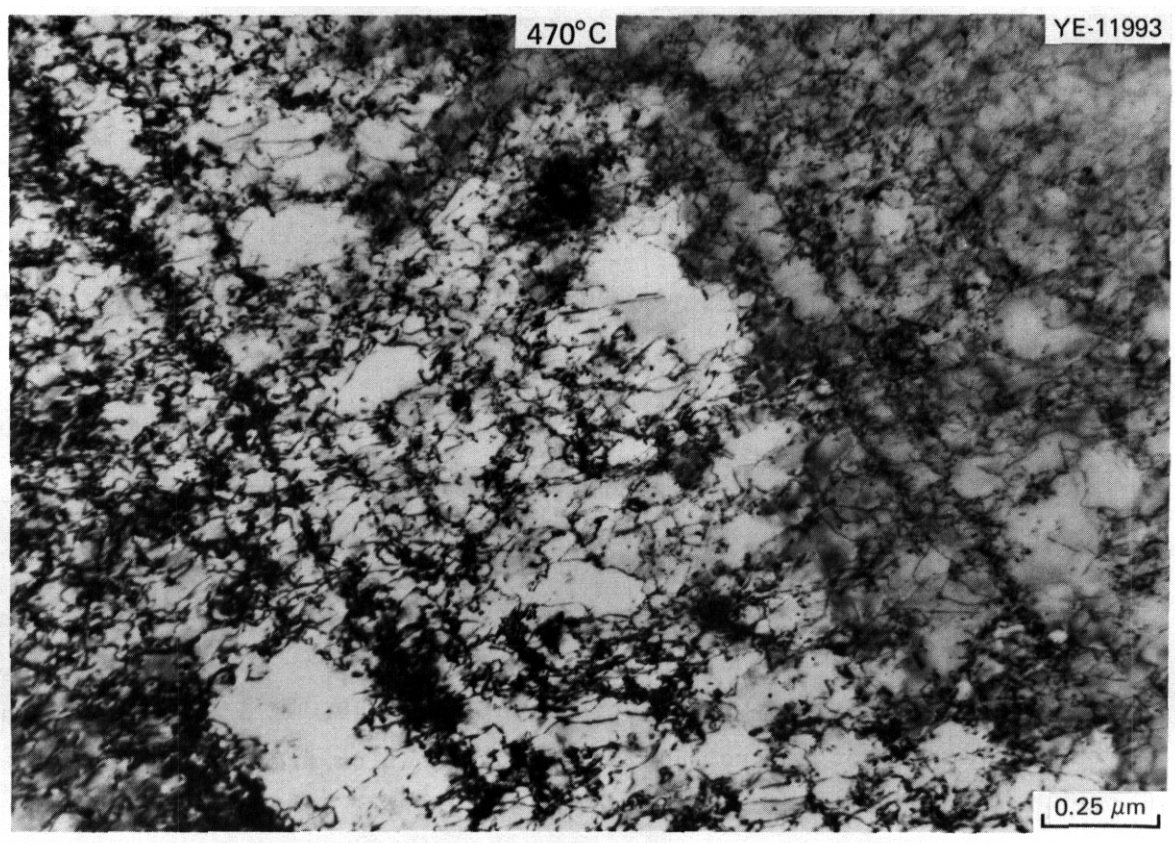

Fig. *3.3.1*. Dislocation Structure of CW *316* After Aging at 470°C for *4400* h. The structure is unchanged from the as-cold-worked structure.

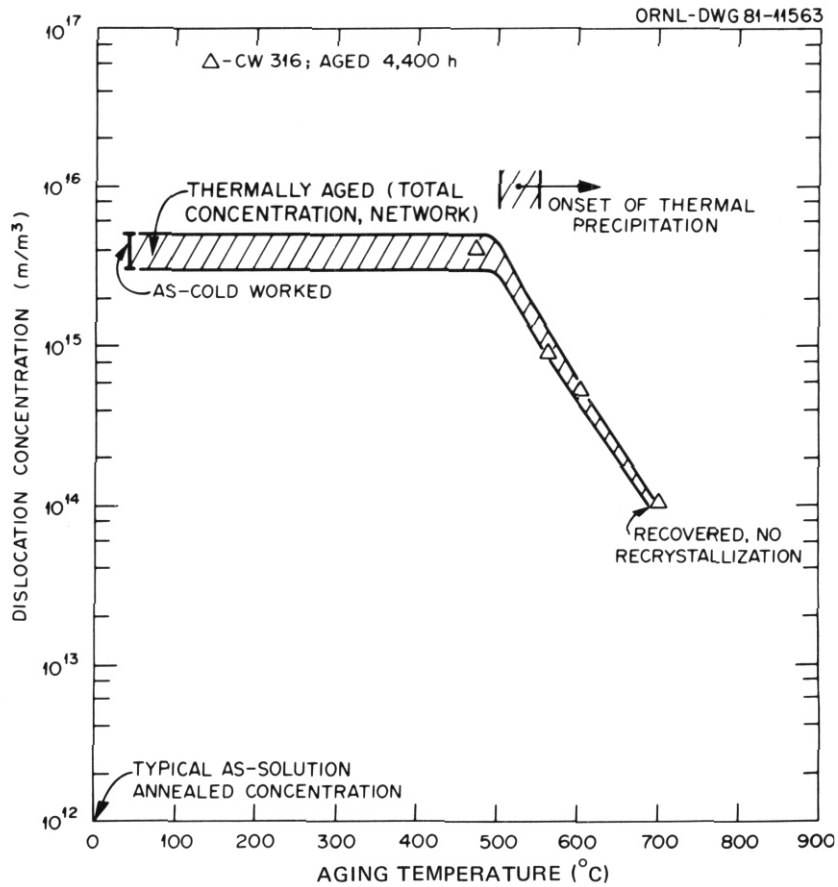

Fig. 3.3.2. Dislocation Concentration in CW 316 as a Function of Thermal Aging Temperature, for Aging Times of 2770 and 4400 h.

at about 500°C, and then dislocation recovery increases with increasing temperature. The microstructures after aging for 2770 h at 600 and 700°C are shown in Fig. 3.3.3. The network recovers to about 1×10^{14} m/m^3 at 700°C. At a given temperature, precipitation and dislocation recovery are completed within 2770 h, because no changes are observed between 2770 and 4400 h. In related work[18] 10,000 h at 600°C did not result in recrystallization, but after 10,000 h at 650°C a small volume fraction of recrystallization (dislocation free grains) can be seen. Recrystallization was also observed after 1000 h at 750°C. In this work no recrystallization was observed for aging up to 4400 h at 700°C.

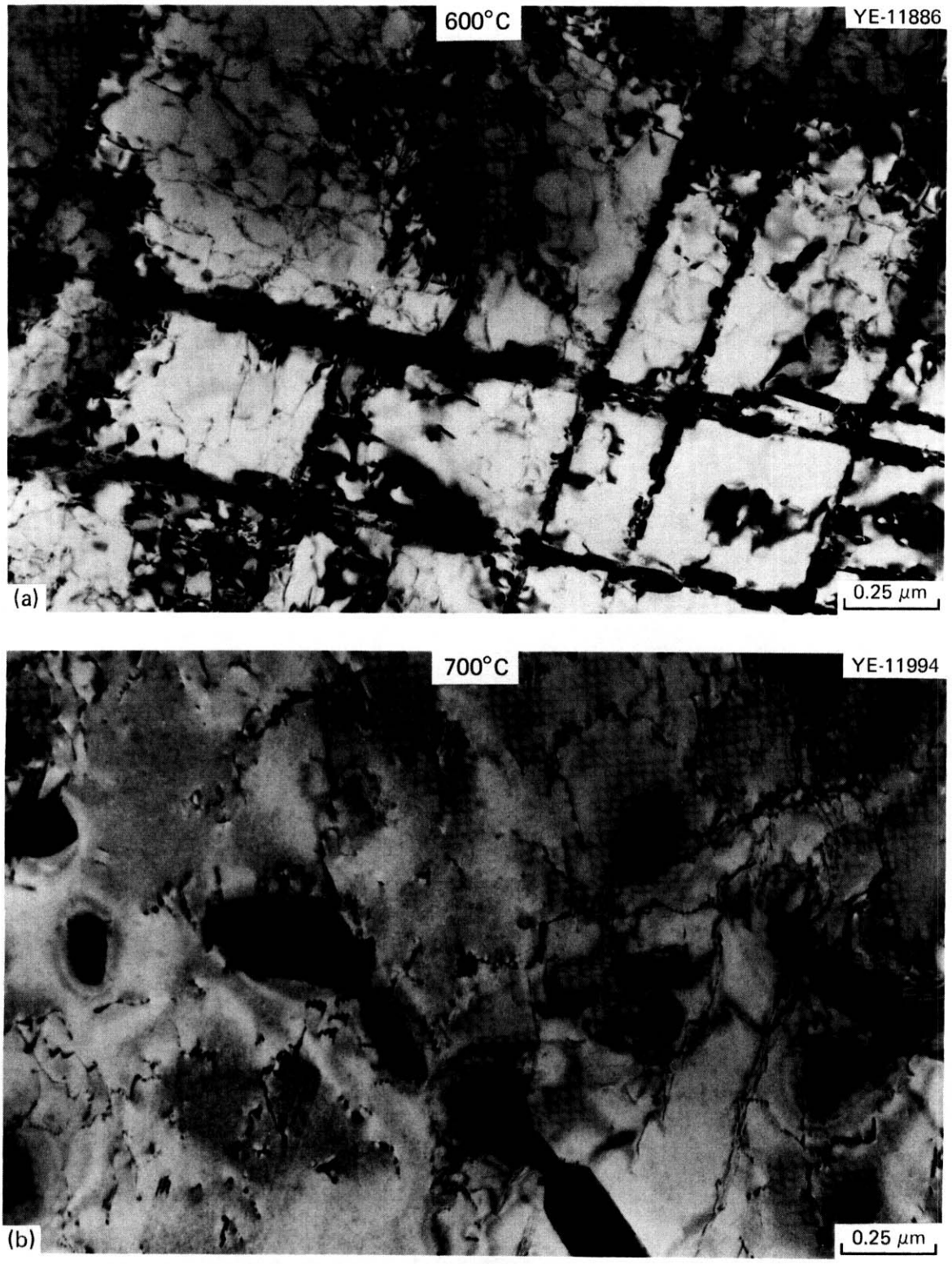

Fig. 3.3.3. Dislocation and Precipitation Microstructure of CW 316 After Aging for 2770 h at (a) 600°C and (b) 700°C.

3.3.4.3.2 Thermal Aging in *CW* 316 + Ti. The as-cold-worked microstructure of *CW 316* + Ti is essentially the same as that of *CW 316*, with possibly a slightly higher tangle density in the cell walls. The microstructural statistics are given in Table *3.3.3.* In contrast to the *CW 316*, *CW 316* + Ti shows virtually no hint of recovery after aging at 700°C for *4400* h. The microstructure of CW 316 + Ti after *2770* h at *600°C* is shown in Fig. *3.3.4*, and the temperature dependence of the dislocation concentration after *4400* h is shown in Fig. *3.3.5.* Figure 3.3.4 is representative of all the *CW 316* + Ti microstructures observed at *700°C* and below. The dark-field inlay shows the fine *MC* precipitation distributed along dislocation lines. The precipitation is representative of all the

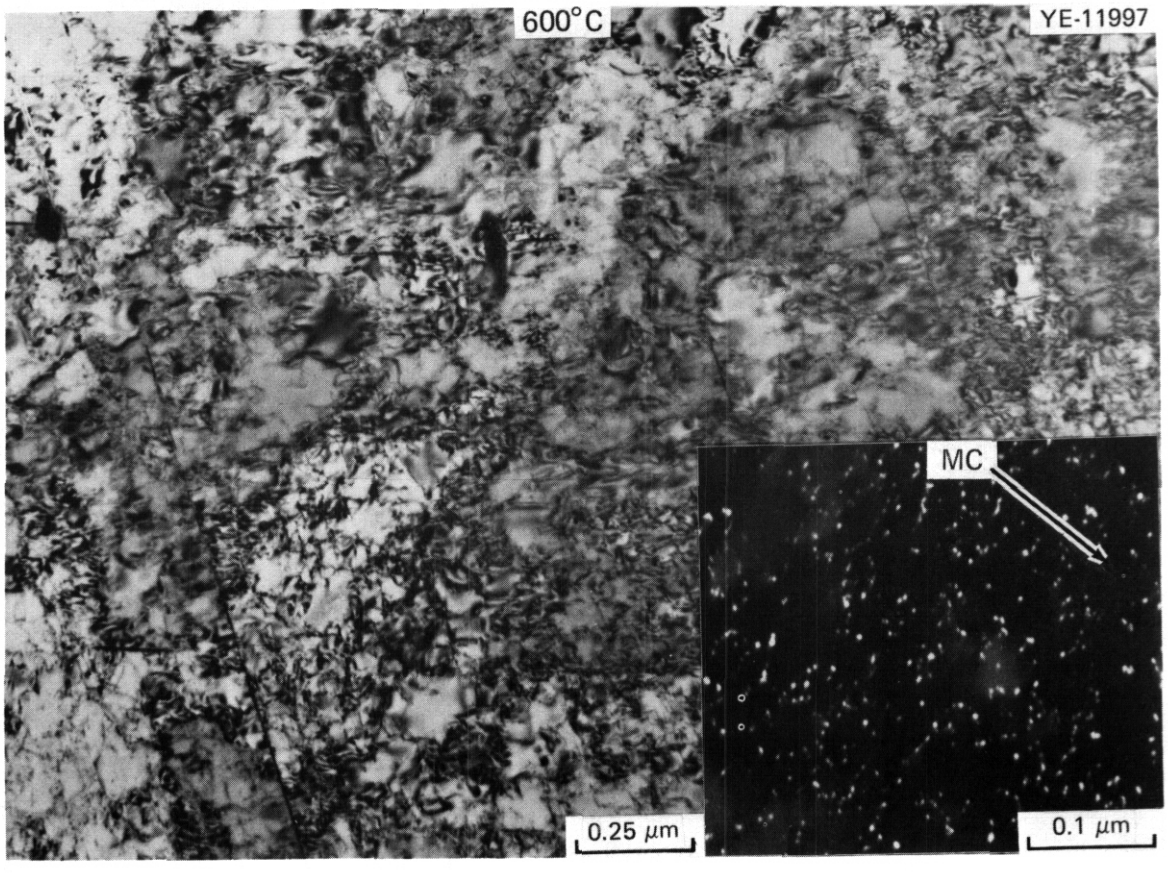

Fig. *3.3.4.* Dislocation Structure of *CW 316* + Ti After Aging for *2770* h at 600°C. No recovery of the as-cold-worked structure is observed. The high magnification, dark field inlay, shows *MC* precipitation that has formed along dislocations.

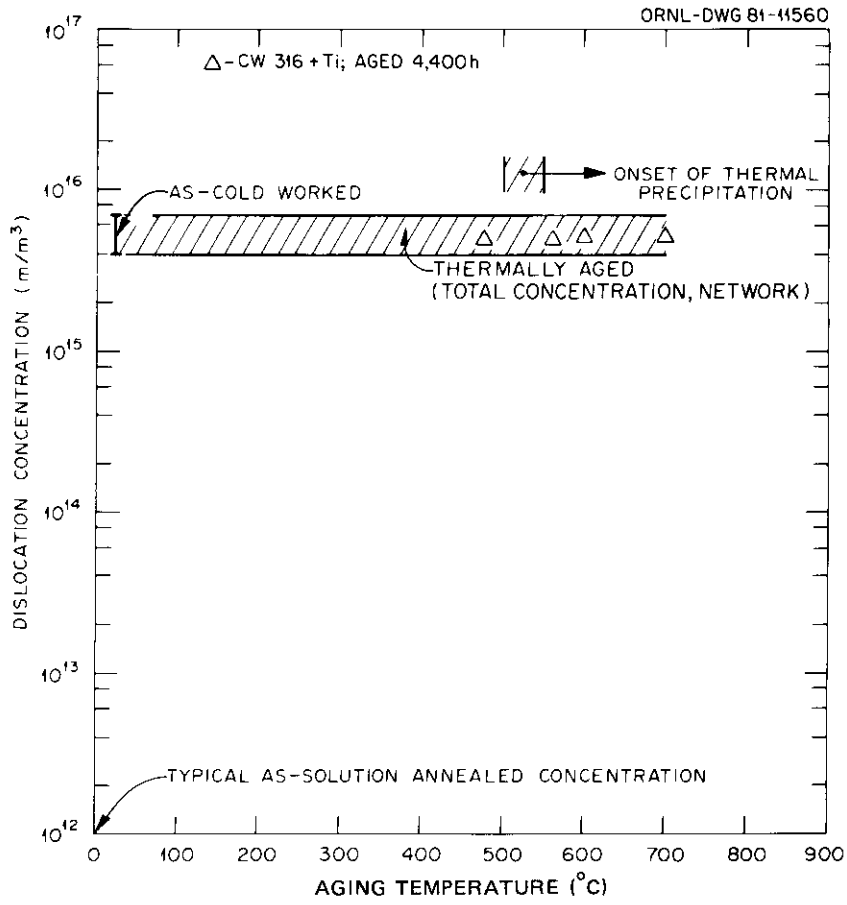

Fig. 3.3.5. Dislocation Concentration in CW 316 + Ti as a Function of Thermal Aging Temperature for 4400 h of Aging.

samples and at least partly responsible for the resistance to thermal recovery. The MC formation also drastically reduces the formation of coarse particles of $M_{23}C_6$, M_6C, and Laves phases in CW 316 + Ti, compared to their formation in CW 316 (ref. 19).

The microstructures of specimens of CW 316 and CW 316 + Ti after tensile testing at 350°C are compared in Figs. 3.3.6 and 3.3.7 (ref. 20). Figure 3.3.6 shows low-magnification bright-field images of each steel to indicate the thicker walled, cellular network structure that has resulted from the deformation during testing. (Compare Fig. 3.3.6 to the microstructures of untested steels in Figs. 3.3.1 and 3.3.4.) Figure 3.3.7 shows higher magnification weak-beam dark-field (WBDF) images (g_{200}, g/3g) of each steel in nearly the same crystallographic orientation, 10 to 15° off a (001) pole. Both areas are of similar

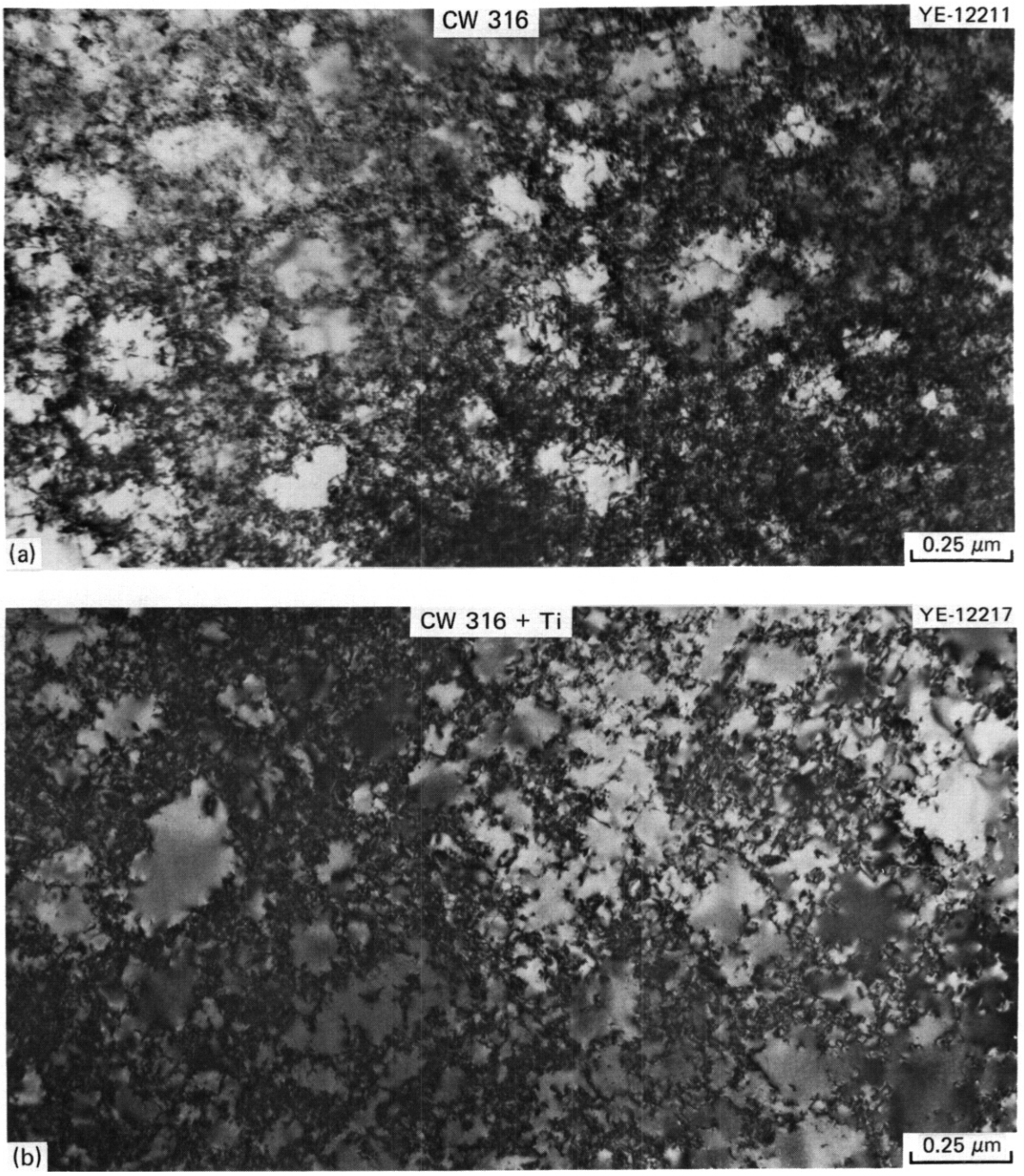

Fig. 3.3.6. Dislocation Microstructure of Deformed Tensile Specimens After Testing at 350°C. (a) CW 316. (b) CW 316 + Ti. Note cellular dislocation texture in both.

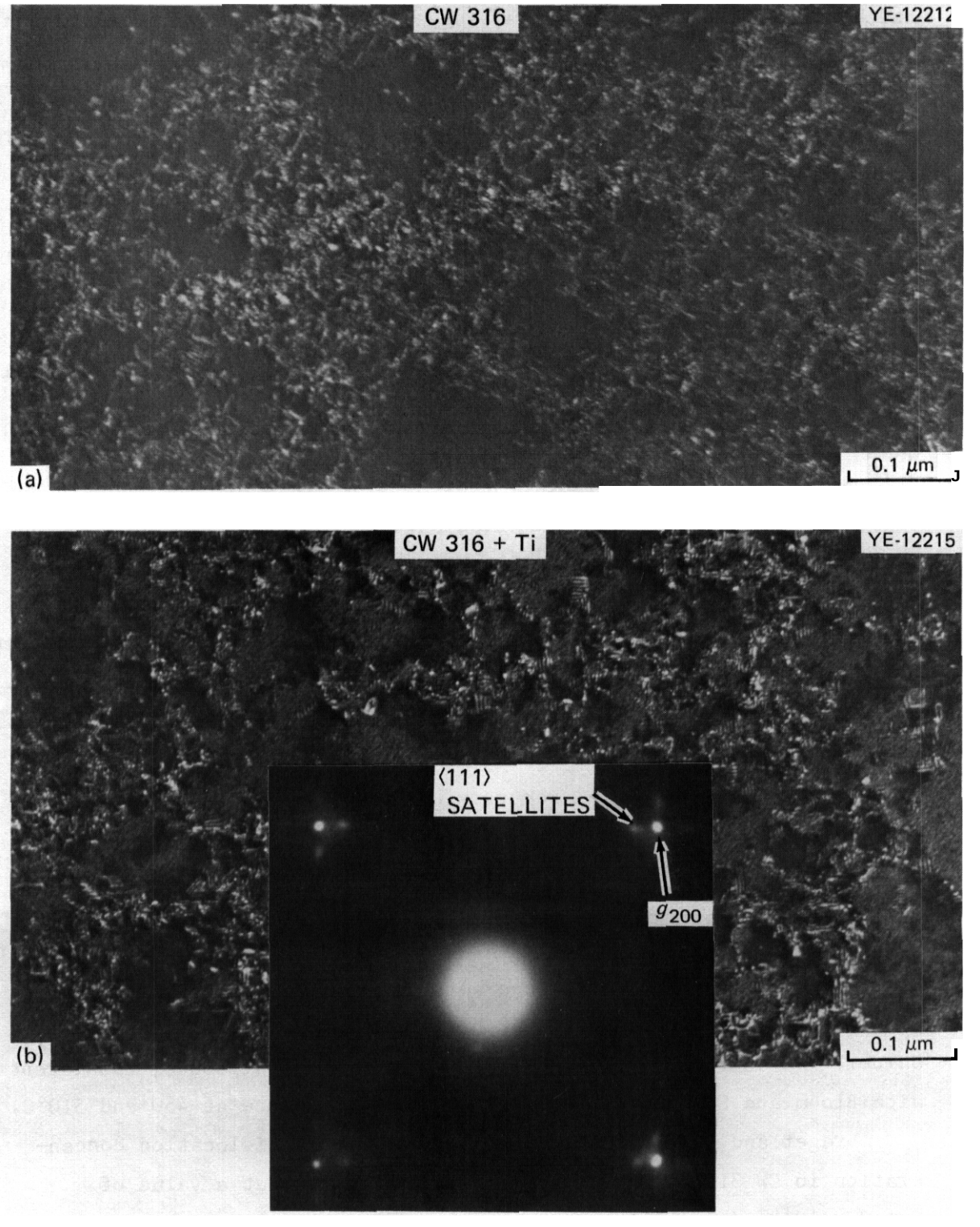

Fig. 3.3.7. High Magnification of Dislocation Structure in Samples Tested at 350°C. The WBDF image uses g_{200}, +g/+3g with foil orientation less than 10° from an 001 pole. (a) CW 316. (b) CW 316 + Ti. Inlay of diffraction pattern in (b) is corrected for rotation with respect to image and shows streaks in ⟨111⟩ directions that are parallel to the stacking faults of extended dislocations.

thickness. These microstructures suggest a slightly higher dislocation concentration in the CW 316, primarily due to thicker cell walls. However, tensile properties of these samples show that the CW 316 + Ti is about 40% stronger with about one-third the ductility of the CW 316 (ref. 20). The WBDF images of the CW 316 + Ti in Fig. 3.3.7 show much more frequent dislocation extension, evidenced by the relaxed stacking faults on {111} planes near the foil surface, than those of the CW 316 for the same imaging conditions. These results suggest that titanium in solution lowers the stacking fault energy of type 316 stainless steel. This is also consistent with much greater strength in the CW 316 + Ti, compared with CW 316, for similar dislocation structures.

3.3.4.3.3 EBR-II Irradiation of CW 316. Data are included in Table 3.3.2 for CW 316 DO heat irradiated in EBR-II at 500 to 525°C and 625 to 630°C to fluences producing 8.4 and 36 dpa. These data and the high fluence data of Brager and Garner[5,6] are plotted as a function of fluence together in Fig. 3.3.8. Table 3.3.2 and Fig. 3.3.8 show similar dislocation recovery at both temperatures with a slightly lower network concentration at the higher irradiation temperature after 8.4 and 36 dpa. The 69-to-75-dpa data shows apparent saturation at about 1.5 to 3×10^{14} m/m^3. Substantial recovery has occurred by the time a fluence producing about 10 dpa is achieved and continues slowly up to 20 to 30 dpa. Figure 3.3.9 shows the dislocation microstructures of CW 316 after 36 dpa at 525 and 625°C. Although similar, the lower temperature sample shows a slightly higher dislocation content in the otherwise fairly uniform networks. No Frank loops were observed at either temperature after 36 dpa, as also reported at higher damage level by Brager and Garner.[5,6] There were also no loops after 8.4 dpa at 500°C, consistent with Bloom and Stiegler's results[4] at similar fluence at 450 and 510°C.

Brager and Garner[21] suggest that the network dislocation concentration in CW 316 stainless steel rapidly saturate at a value of $6 \pm 3 \times 10^{14}$ m/m^3. This saturation density is claimed to be fairly independent of irradiation temperature under zero- or low-stress conditions. Their data apparently do not include loop contributions.[8]

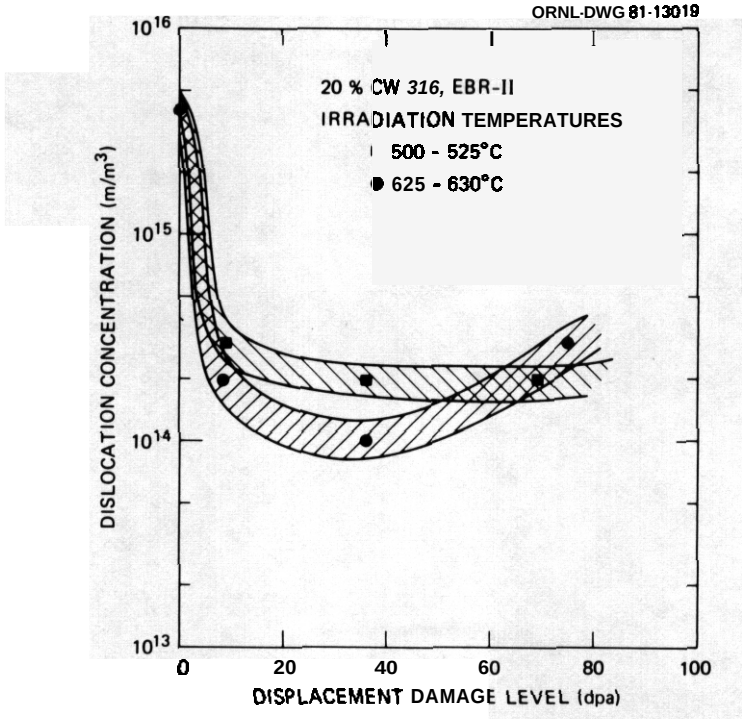

Fig. 3.3.8. Dislocation Concentration of CW 316 (DO heat) as a Function of Fluence for EBR-II Irradiation at 500 to 630°C. Data at 69 and 75 dpa are taken from H. R. Brager and F. A. Garner, "Comparison of the Swelling and the Microstructural/Microchemical Evolution of AISI 316 Irradiated in EBR-II and HFIR," paper presented at Second Topical Meeting on Fusion Reactor Materials, Seattle, Wash., Aug. 9–12, 1981, to be published in the *Journal* of *Nuclear Materials* and H. R. Brager and F. A. Garner, "Microstructural Development of 20%–Cold–Worked 316 Irradiated in EBR-II," DAFS *Quart. Prog. Rep. Dec. 1980*, DOE/ER-0046/4, vol. 1, pp. 81-87.

British data by Bramman et al.[7] include faulted loops in reporting their total dislocation concentration. In the present work both the line network and loop component are shown to be sensitive to irradiation conditions, decreasing with increasing irradiation temperature. The British values for the dislocation concentration in the line network are 8.6×10^{14} m/m^3 at 480°C and about 6.6×10^{14} m/m^3 at 548°C, for irradiation to about 36 dpa in DFR. These values are higher than network dislocation concentrations for the DO heat 316 (see Table 3.3.2). Loops add an additional 25% to the dislocation concentration data reported by Bramman for 480°C and contribute little or nothing at 510°C and above. The concept of a rapidly achieved, terminal saturation dislocation density that is the same for all temperatures may be too broad a generalization.

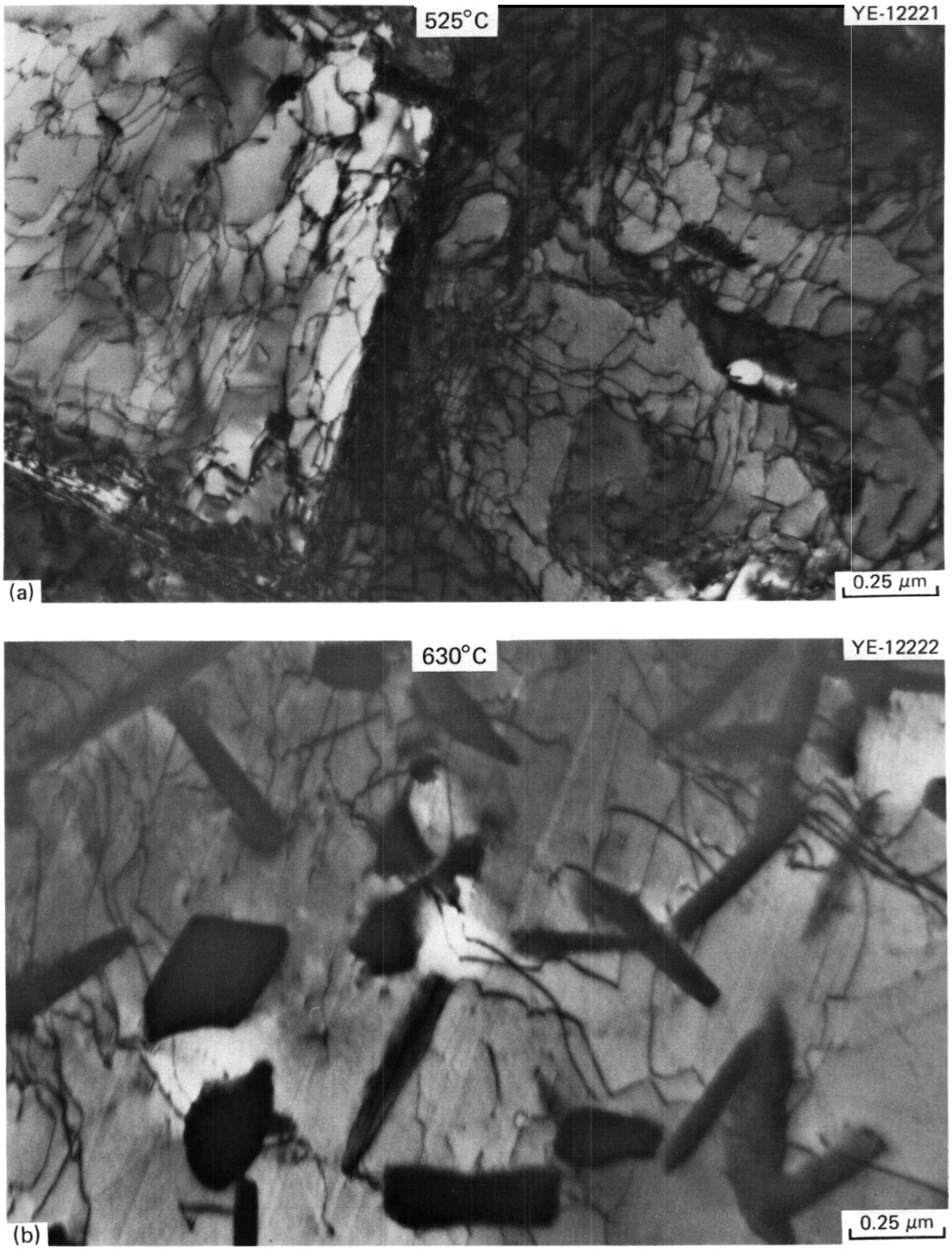

Fig. 3.3.9. Dislocation Structures of CW 316 After EBR-II Irradiation to 36 dpa at (a) 525°C and (b) 630°C. (a) is imaged near a 001 pole with two orthogonal g_{200} type reflections excited and hence shows the structure without invisibility of any dislocations. (b) is a normal g_{111}, two-beam picture and only half the dislocations are visible.

This is particularly true if that concentration neglects an important component like Frank loops, which appear to be sensitive to both irradiation temperature and the composition of a particular heat of steel.

3.3.4.3.4 HFIR Lrradition of CW 316 and CW 316 + Ti.

CW 316, Temperature Dependence. The dislocation statistics for CW **316** DO heat irradiated in HFIR are also given in Table **3.3.2.** Total and line network concentrations are plotted as a function of temperature for several fluence ranges in Fig. **3.3.10.** This figure also indicates

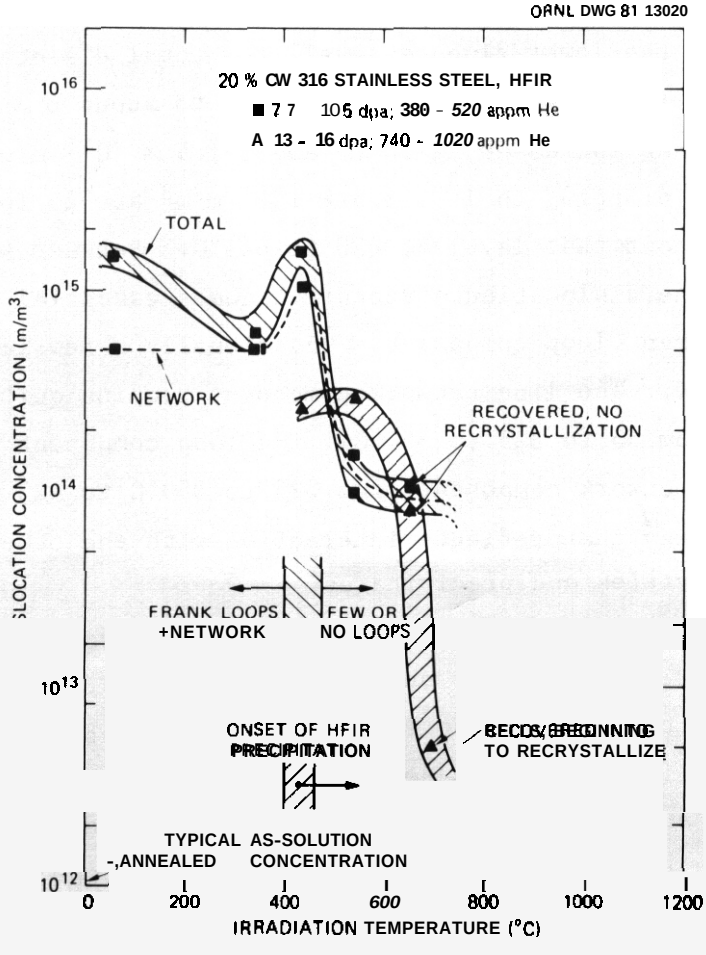

Fig. **3.3.10.** Dislocation Concentration of CW **316** Irradiated in **HFIR** as a Function of Irradiation Temperature. ***Also*** indicated are the temperature ranges at which other important microstructural components are changing.

other microstructural phenomena, such as the beginning of general precipitation and the transition from many to few or no Frank loops. Some information on the dislocation behavior of these samples irradiated in HFIR has been published previously in a more qualitative and preliminary form.[19] The data in this report represent more complete measurements and include the loop parameters. The revised nominal irradiation temperatures are used throughout.

Figure 3.3.10 shows considerable temperature dependence of the dislocation concentration over the range 55 to 650°C. This reflects changes in both the line network and in the loop component. Figure 3.3.11 shows the dislocation microstructure from 55 to 525 to 550°C at the lower fluence level, and Fig. 3.3.12 shows the microstructure at 620 to 700°C after 15 to 16 dpa. At the lower fluence level, the total dislocation concentration decreases from 1.5×10^{15} m/m^3 at 55°C to about 6×10^{14} m/m^3 at 325 to 350°C and then increases again to about 1.5×10^{15} m/m^3 at 425 to 450°C before sharply dropping to 1 to 1.5×10^{14} m/m^3 at 525 to 550°C and remaining at about that level at 620 to 645°C. Between 425 to 450°C and 525 to 550°C the dislocation structure becomes essential line network with little or no Frank loop component. Occasionally a few large prismatic loops are found. The line network component remains quite constant with temperature from 55 to 325 to 350°C. The loop component from 55 to 425 to 450°C and the network component from 325 to 350°C to 425 to 450°C vary in a complicated way that reflects interaction with the other microstructural components; cavities and precipitates.

High-magnification examination of the CW 316 after irradiation to 7.7 dpa at 55°C, Fig. 3.3.13, shows a high concentration of fine black spot damage in the dislocation structure shown in Fig. 3.3.11(a). This type of damage is observed in several materials in both the solution-annealed (SA) and CW conditions but appears confined to about 55°C for irradiation in HFIR.[22,23] These were counted as loops because of their image contrast behavior and the fact that the material becomes so much stronger in spite of network recovery. The details of their vacancy or interstitial nature is not yet known and is still under investigation. Bloom et al.[24] observed similar damage in SA type 304 stainless steel

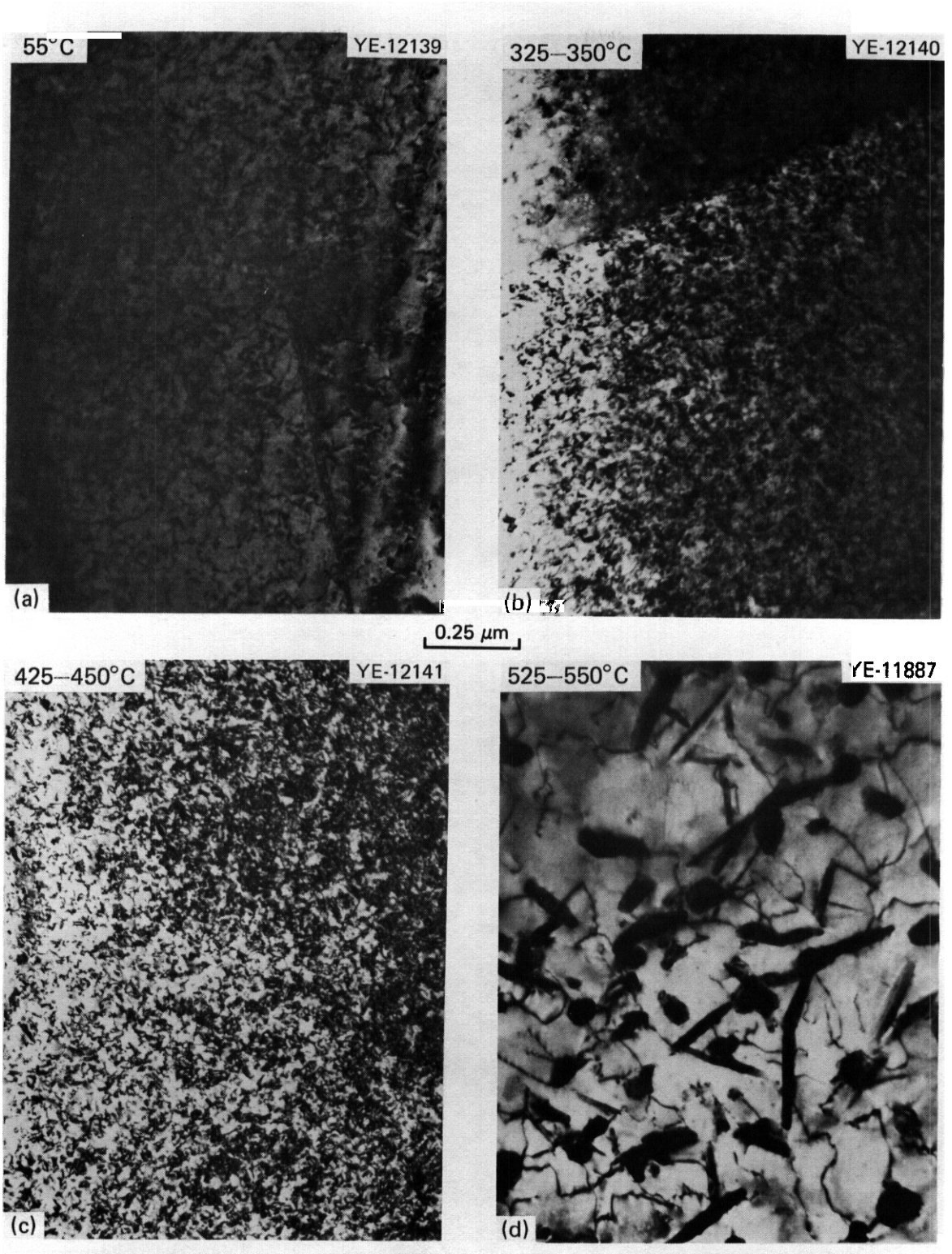

Fig. 3.3.11. Dislocation Microstructures of CW 316 After HFIR Irradiation to 7.7 to 10.8 dpa and 380 to 520 at. ppm He at Nominal Temperatures of (a) 55°C, (b) 325 to 350°C, (c) 425 to 450°C, and (d) 525 to 550°C.

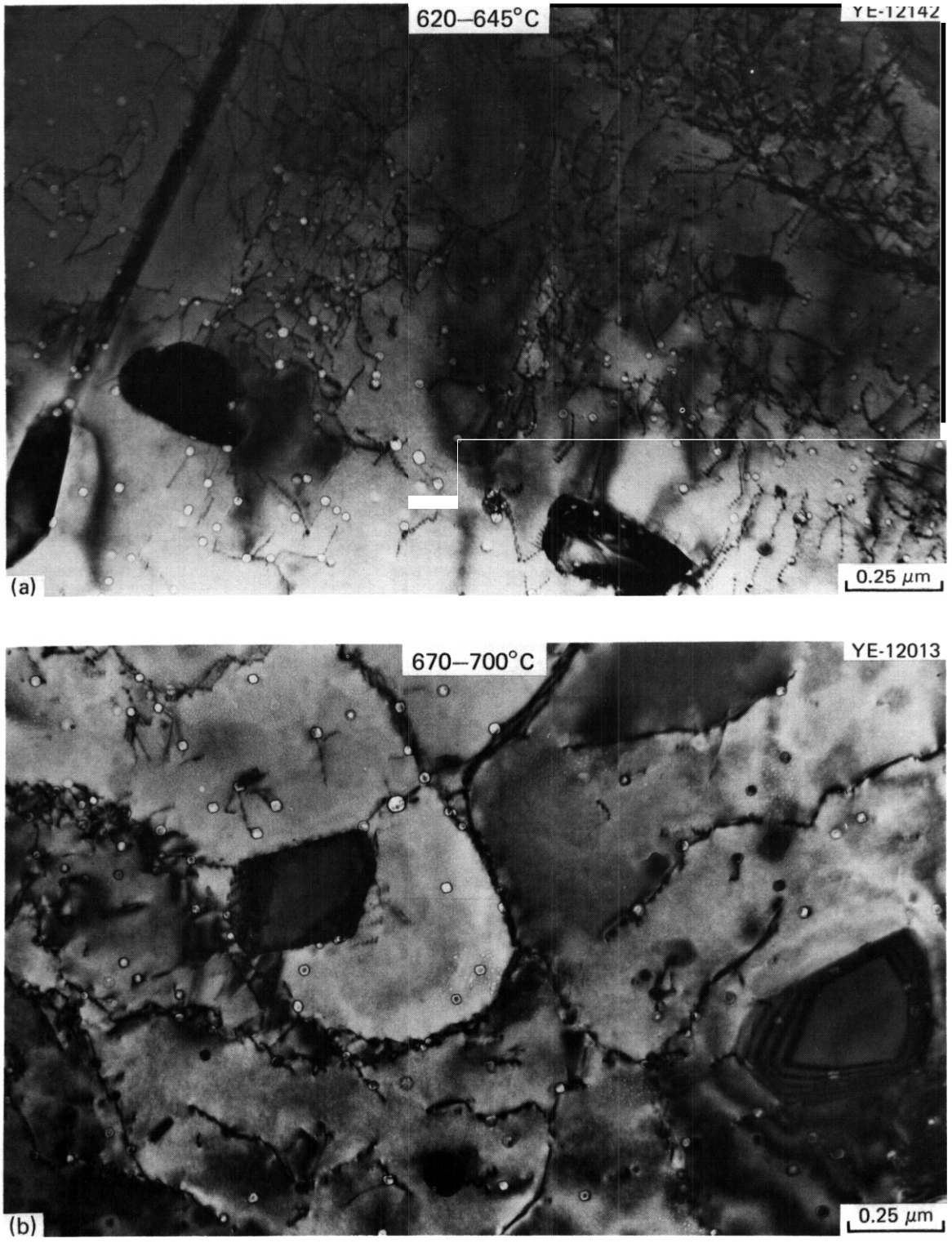

Fig. 3.3.12. Dislocation Microstructures of CW 316 After HFIR Irradiation to 15 to 16 dpa and 880 to 1020 at. ppm He at Nominal Temperatures of (a) 620 to 645°C and (b) 670 to 700°C.

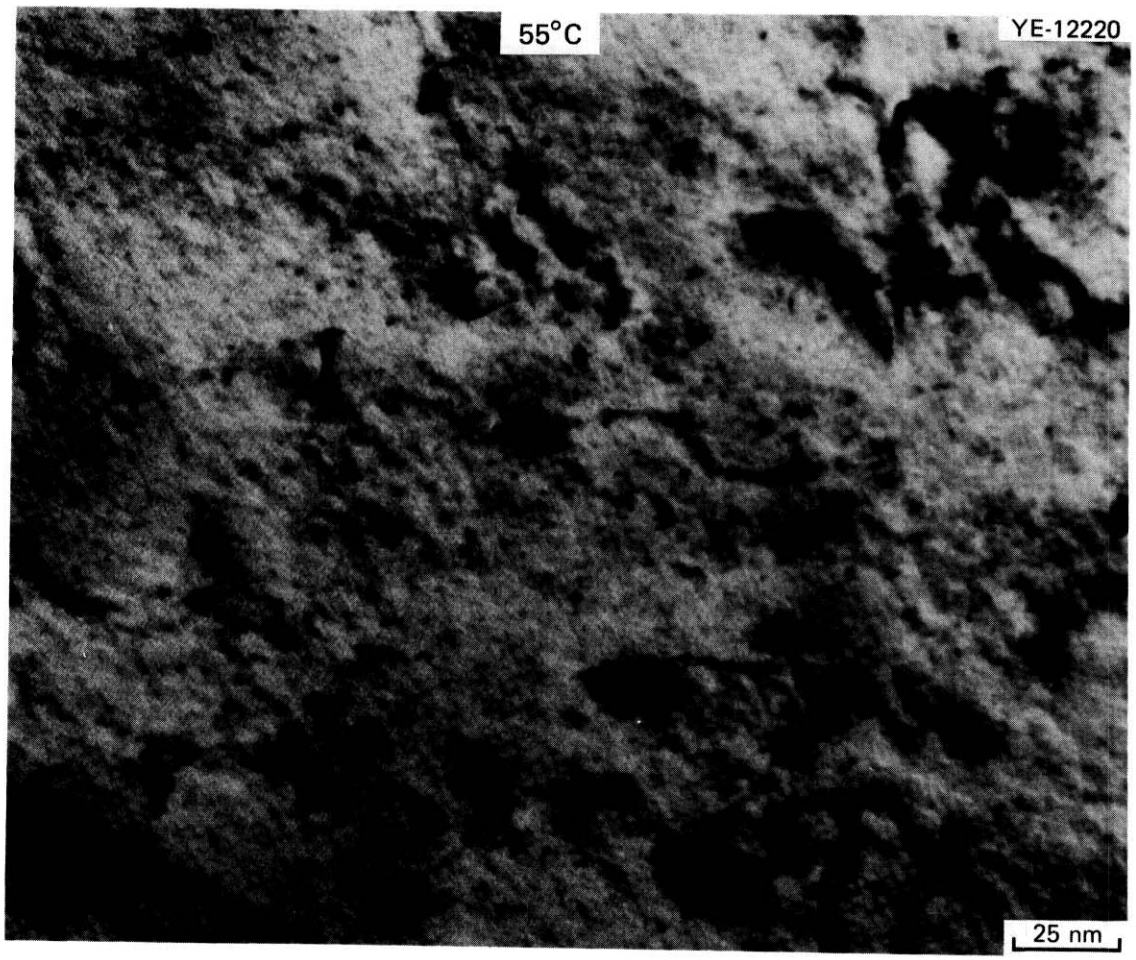

Fig. 3.3.13. Dislocation and Fine Structure Suspected of Being Loops in CW 316 After HFIR Irradiation at 55°C to 10.8 dpa and 520 at. ppm He. Imaging conditions are g_{200}, $s > 0$ off an 011 pole.

irradiated to low fluence at temperatures of 90 to 300°C. Figure 3.3.14 again shows the 55°C sample but now imaged in high-resolution dark field using the <111> satellite streaks about g_{200} matrix reflections to show Frank loops. There are very few found in the matrix at 55°C compared to the higher temperatures, similar to the findings of Bloom et al. The Frank loops that are found appear to be arranging in planar arrays parallel to the (111) planes and appear similar to thick stacking fault bands. This behavior has been observed several times on other samples by this author and is not understood.

As the irradiation temperature increases at the fluence level of 7.7 to 10.5 dpa, the black spot damage is no longer observed at 325 to 350°C and the dislocation structure consists of larger Frank loops plus network.

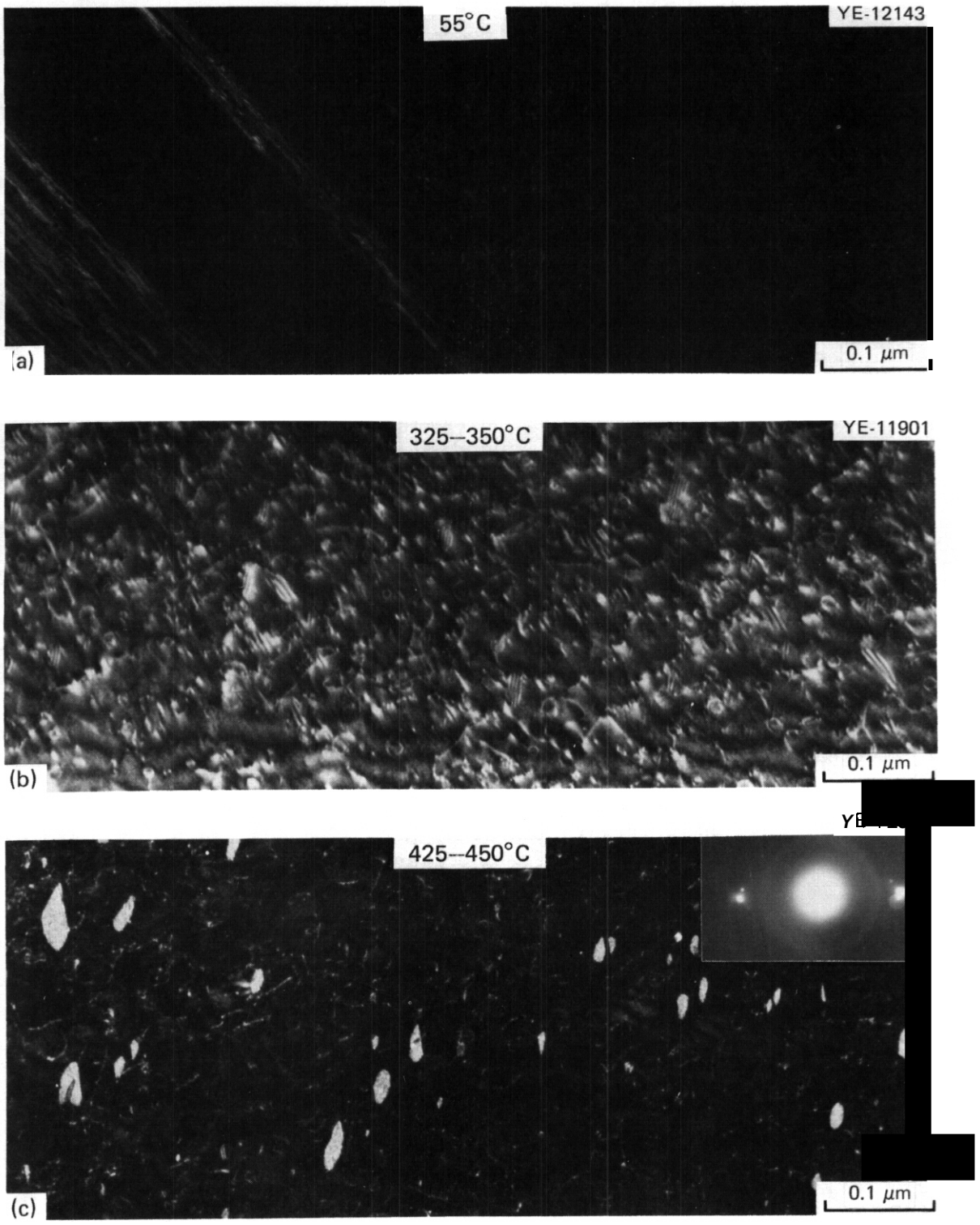

Fig. 3.3.14. Frank Loop Structure in CW 316 Irradiated in HFIR to 7.7 to 10.8 dpa and 380 to *520* at. ppm He at Nominal Irradiation Temperatures of (a) 55°C, (b) *325* to 350°C, and (c) *425* to 450°C. (a) and (c) are images of the faults using satellite streaks about g_{200} as shown in the diffraction inlay in (c). (b) is a WBDF with g_{111}, +g/+3g.

The size (~23–24 nm diam) and number density ($\sim 1 \times 10^{21}$ loops/m^3) of Frank loops are similar at 55 and 325 to 350°C, but they are more uniformly distributed at the higher temperature. The size distribution of the Frank loops is shown in Fig. 3.3.15. The distributions determined for

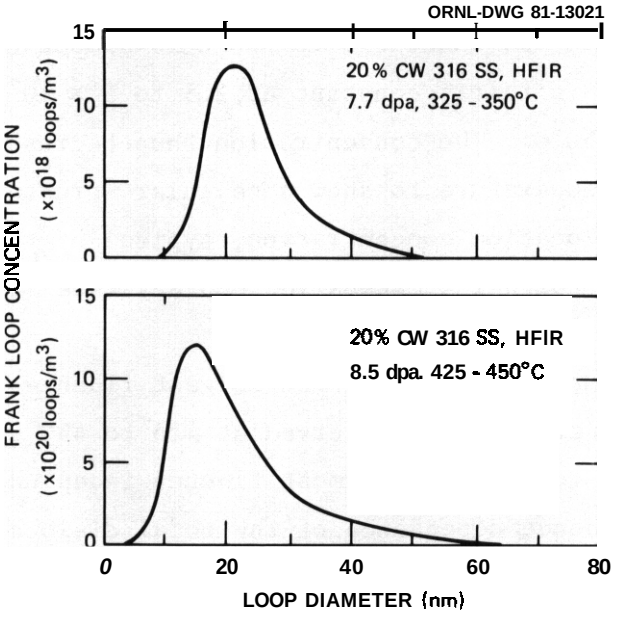

Fig. 3.3.15. Size Distribution of Frank Loops for CW 316 Irradiated in HFIR to the Conditions Shown.

different (111) planes exactly superimpose, consistent with stress-free loop formation. The drop in total dislocation concentration in Fig. 3.3.10 is due to the absence of fine loop structure. At 425 to 450°C both Frank loop and line network components of the dislocation structure increase relative to 325 to 350°C. The Frank loops are shown in Fig. 3.3.14 for both temperatures. Figure 3.3.15 reveals that the loop size distribution at 425 to 450°C is extended to both larger and smaller sizes, whereas the average size of the population is decreased, compared to 325 to 350°C, due to much larger relative fraction at smaller sizes. The loop number density is almost a factor of 10 greater at the higher temperature. The size distribution and density of loops would indicate that more Frank loops are being nucleated and are growing longer before adding to the network at 425 to 450°C compared to 325 to 350°C. This behavior correlates with fine gamma-prime precipitation (Ni_3Si type)

observed along the line network component of the dislocation structure at *425* to 450°C (ref. *19)* and no precipitation at *325* to 350°C. The line network concentration is a factor of 5 greater at the higher temperature. Cavity formation is observed at both temperatures, but the cavities at the lower temperature are coarser.[1]

At the higher fluence level of *13* to *16* dpa, the dislocation structure between *425* to *450°C* and *670* to *700°C* is almost exclusively network. The concentration is fairly constant at *2.5* to *3* x 10^{14} m/m^3 from *425* to 450°C to *525* to 550°C. The concentration then begins to fall off rapidly with increasing temperature to show a cellular structure with very low intracellular dislocation concentration, typical of the onset of recrystallization following extensive recovery (see Fig. *3.3.12).*

CW 316, Fluence Dependence. The largest fluence dependence of the dislocation microstructure is observed at *425* to 450°C, with only a small dependence at *525* to *550°C* and almost fluence independent behavior at *620* to 645°C. The fluence dependence of the total dislocation concentration at these temperatures is shown in Fig. *3.3.16.* The fluence dependence of the microstructure at *425* to *450°C* and 525 to 550°C is shown in Figs. 3.3.17 and *3.3.18,* respectively.

At *425* to *450°C* the total dislocation concentration recovers nearly an order of magnitude between *8.4* and *16* dpa as shown in Figs. *3.3.10* and *3.3.16.* This is due both to line network recovery (Table *3.3.2)* and the complete disappearance of Frank loops at the higher fluence (Fig. *3.3.17).* Major changes in the precipitation component of the microstructure occur between these fluences, with only small changes occurring in the cavity component.[1,19] The fine γ' found pinning the network at *8.4* dpa is absent at *13* dpa and appears to have been replaced by much coarser eta (M_6C type) phase precipitation along stacking faults and in the matrix. This is consistent not only with the sharp dislocation recovery, but also with the sharp change in yield strength observed after postirradiation tensile testing of these same samples.[20,25] The precipitation change at low fluence is then consistent with the precipitate and cavity structures found to develop after irradiation to 49 dpa at this nominal temperature of *425* to 450°C (refs. *1, 12,* and 18).

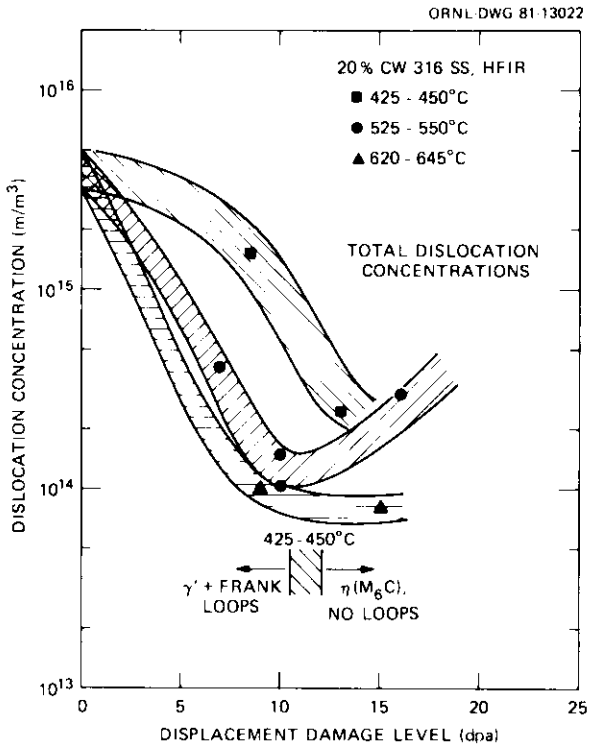

Fig. 3.3.16. Total Dislocation Concentration as a Function of Fluence for CW 316 Irradiated in HFIR at Several Temperatures.

For irradiation at 525 to 550°C in HFIR, Figs. 3.3.16 and 3.3.18 show the dislocation development from 6.9 to 16 dpa. Networks are observed for all fluences, with no Frank loops at any fluence and a few large prismatic loops at the highest fluence. At 6.9 dpa, the network has recovered to about 4×10^{14} m/m^3. There is also a small amount of tau ($M_{23}C_6$ type) and/or eta precipitate formed at stacking faults and grain boundaries. Some cavities can also be seen. At 10 dpa network recovery continues to 1 to 1.5×10^{14} m/m^3, considerable precipitation of eta and Laves has developed in the matrix, and the cavity microstructure coarsens.[1,19] At 16 dpa, the network concentration increases slightly and the prismatic loops contribute to the small total increase shown in Fig. 3.3.16. Attendant with this dislocation change is a refinement in the cavity structure and a reduction in the amount of precipitation. The cavities are spacially clustered,[1] and precipitates are partially dissolved.[19] Parallel to the matrix precipitation changes and adjustments, the precipitation along the stacking faults (observed at 10 dpa also) dissolves, as does a significant amount of the grain boundary precipitation. This is also coincident with formation of many small

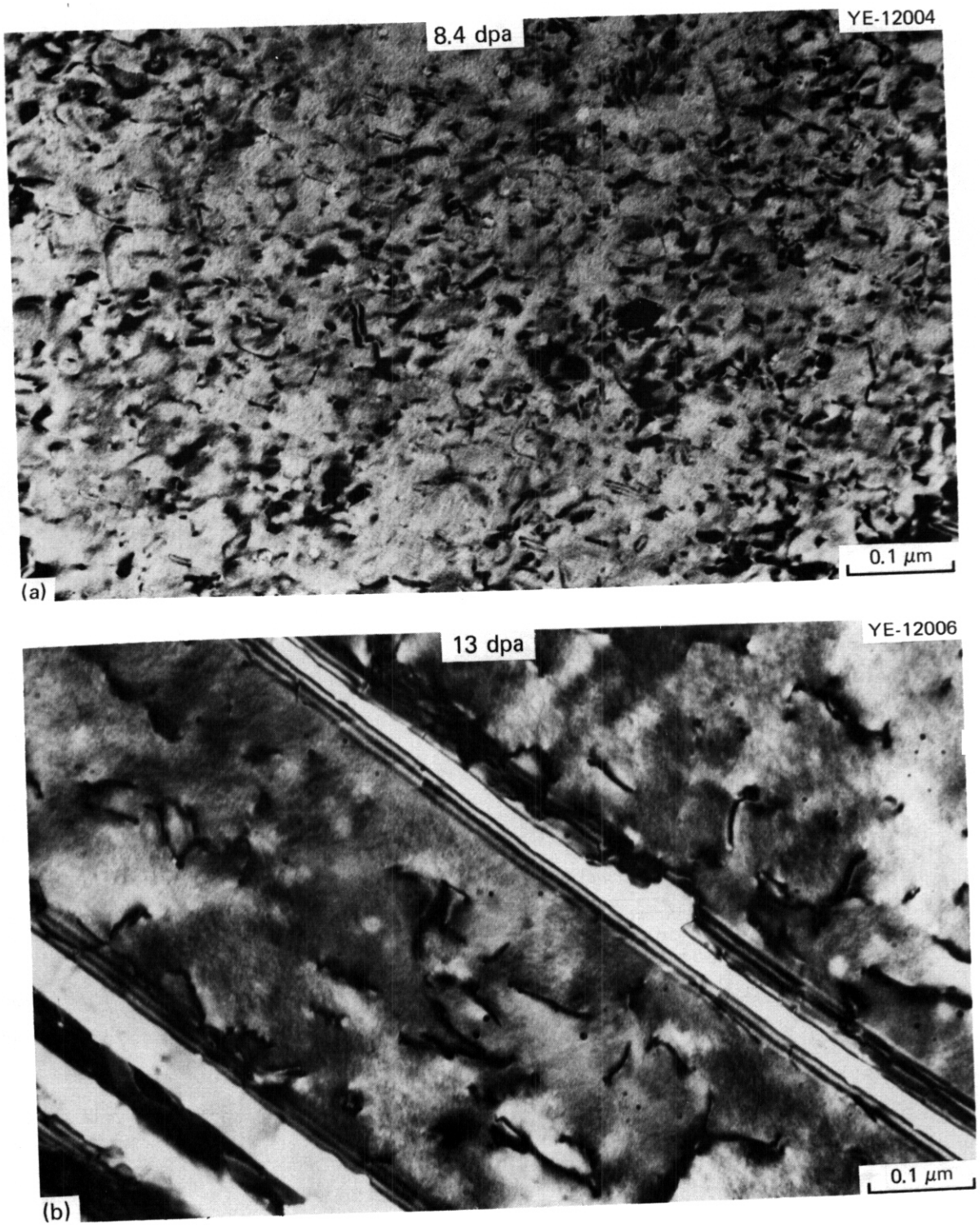

Fig. 3.3.17. Dislocation Microstructures of CW 316 Irradiated in HFIR at Nominally *425* to 450°C to Fluences Producing (a) 8.5 dpa and 380 at. ppm He and (b) 13 dpa and *740* at. ppm He. No Frank loops are observed in (b).

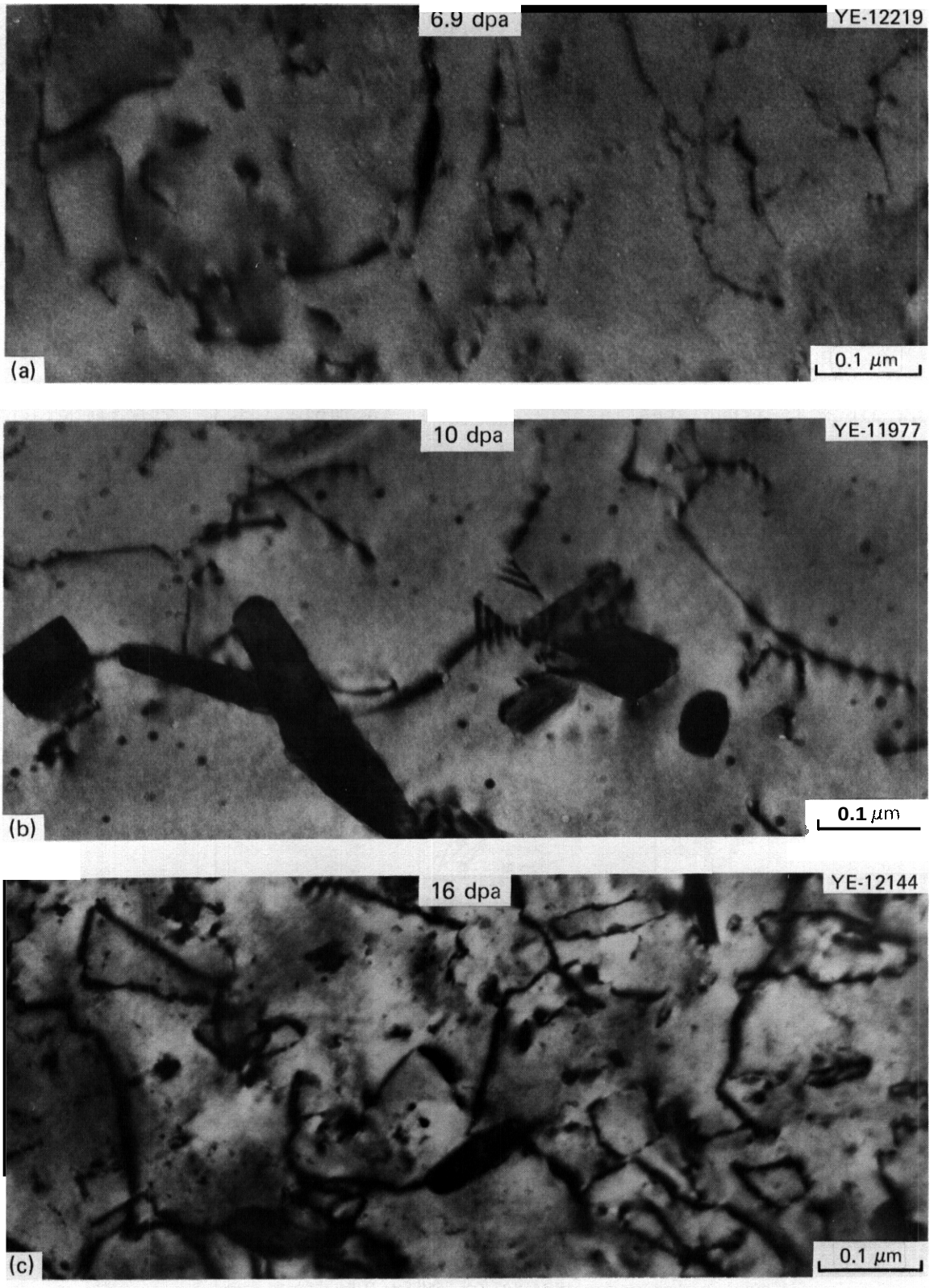

Fig. 3.3.18. Dislocation Microstructures of CW 316 Irradiated in HFIR at Nominally 525 to 550°C to Fluences Producing (a) 6.9 dpa and 290 at. ppm He, (b) 10 dpa and 500 at. ppm He, and (c) 16 dpa and 1020 at. ppm He. A few large prismatic loops are observed in (c).

grain boundary cavities[1] and corresponding changes in tensile test fracture mode.[25] Examination of a second identical sample at 10 dpa confirmed the microstructure shown in Fig. 3.3.18(b).

The microstructure of the duplicate sample at 10 dpa and 525 to 550°C also confirms that HFIR irradiation temperatures are reproducible. Since the duplicate specimen was segmented without postirradiation tensile testing, it also indicated that the testing does not significantly perturb the shoulder microstructure from the as-irradiated condition.

CW 316 + Ti, Temperature Dependence. The dislocation statistics for CW 316 + Ti irradiated in HFIR are given in Table 3.3.3. The temperature dependence of the total dislocation concentration and the line network component after irradiation to 7.7 to 10.5 dpa are shown in Fig. 3.3.19. Many of the observations are qualitatively similar to CW 316 so that the data will be presented to emphasize the differences.

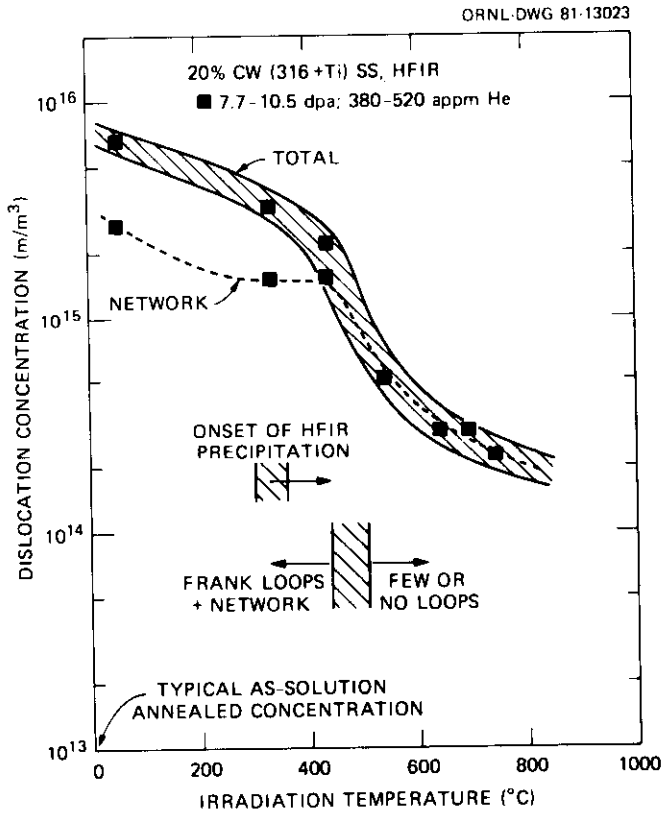

Fig. 3.3.19. Dislocation Concentration of CW 316 + Ti Irradiated in HFIR as a Function of Irradiation Temperature. The irradiation produced 7.7 to 10.5 dpa and 380 to 520 at. ppm He.

In general the total dislocation concentration decreases monotonically with increasing irradiation temperature and does not exhibit the same degree of anomalous behavior as does CW 316. The microstructures for irradiation at 55°C to nominally 525 to 550°C are shown in Fig. 3.3.20 and at 620 to 645°C to 720 to 745°C in Fig. 3.3.21. The total concentration declines slowly from 6.6 $\times 10^{15}$ m/m^3 at 55°C to 2.2 $\times 10^{15}$ m/m^3 at 425 to 450°C. The total concentration declines more rapidly between 425 to 450°C and 525 to 550°C, when, as in CW 316, the material undergoes a transition from Frank loops plus network to network alone as temperature increases. From 525 to 550°C to 720 to 745°C, the total concentration again declines more slowly with temperatures ana continues recovery into a network rather than falling off into a cellular structure leading to recrystallization, as observed in the CW 316 (see Fig. 3.3.10). Comparison of Figs. 3.3.11 and 3.3.21 shows the general similarity between the two steels, particularly with respect to the temperatures of loop disappearance. Comparing Figs. 3.3.10 and 3.3.19 also shows that the dislocation concentrations are generally a factor of 3 to 5 higher in CW 316 + Ti than in CW 316 after identical irradiations. At 525 to 550°C, this reflects resistance to dislocation recovery in the network, but at lower temperatures it also reflects differences in the loop component. For irradiation at 325 to 350°C and above, the differences in dislocation structure are largely due to the several beneficial effects of formation of fine-scale titanium-rich MC, which include reduced phase instability with respect to $M_{23}C_6$, M_6C, and Laves phases and MC-dislocation pinning.

At 55°C, the line network is a factor of 5 denser in CW 316 + Ti than in CW 316 and the "black spot" loops contribute greater than 50% to the total dislocation concentration. The black spot damage is considerably denser in the CW 316 + Ti, and the larger Frank loops observed in CW 316 are not found in the CW 316 + Ti. Figure 3.3.22 shows the temperature dependence of the loop component (compare with Fig. 3.3.14), and in particular the WBDF images show the fine loops formed at 55°C. Figure 3.3.23 shows the size distributions of Frank loops at 325 to 350°C and 425 to 450°C and can be compared to Fig. 3.3.15 for CW 316.

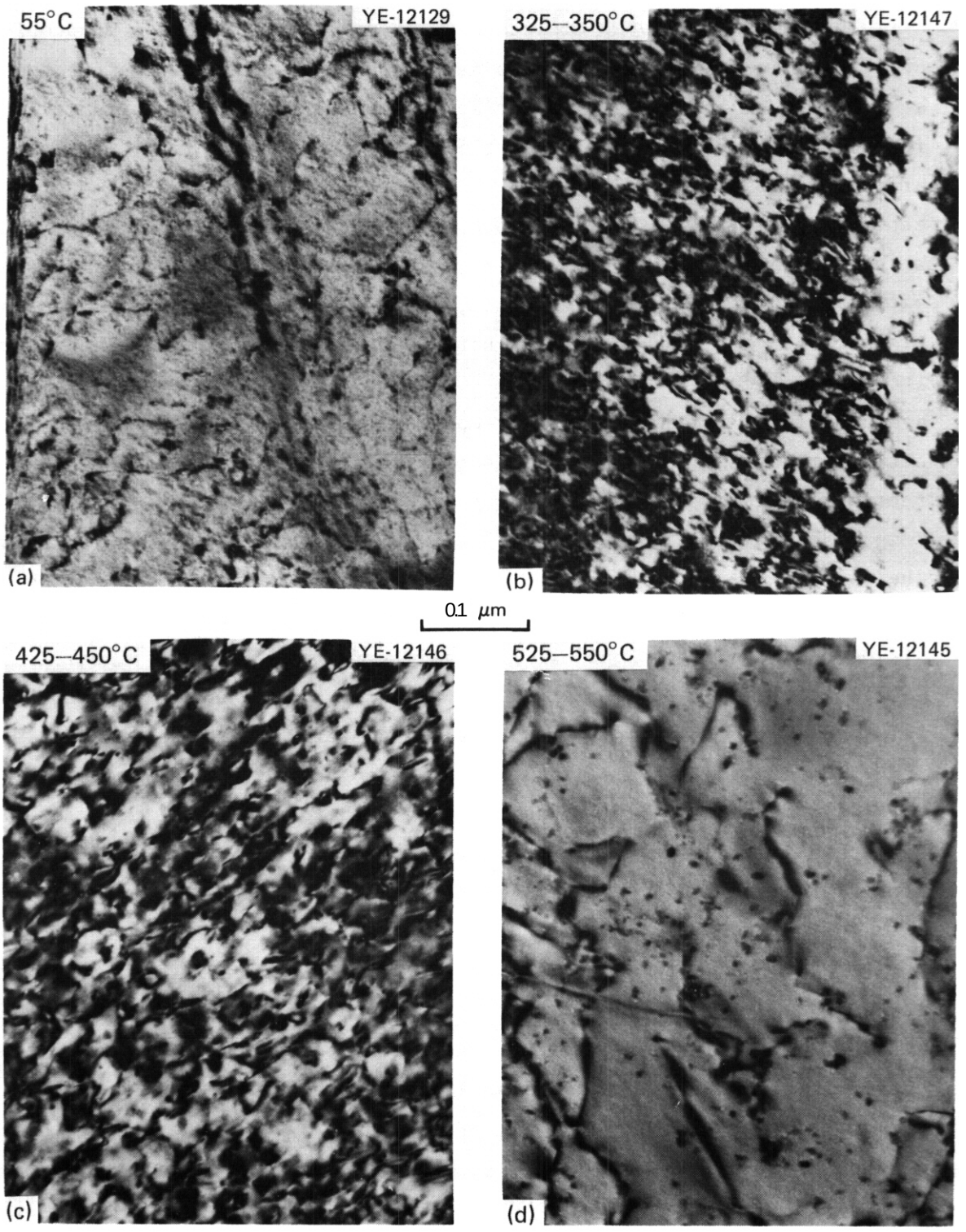

Fig. 3.3.20. Dislocation Microstructures of CW 316 + Ti Irradiated in HFIK to 7.7 to *10.5* dpa and *380* to *520* at. ppm He at Nominal Temperatures of (a) 55°C, (b) *325* to 350°C, (c) *425* to 450°C, and (d) *525* to 550°C.

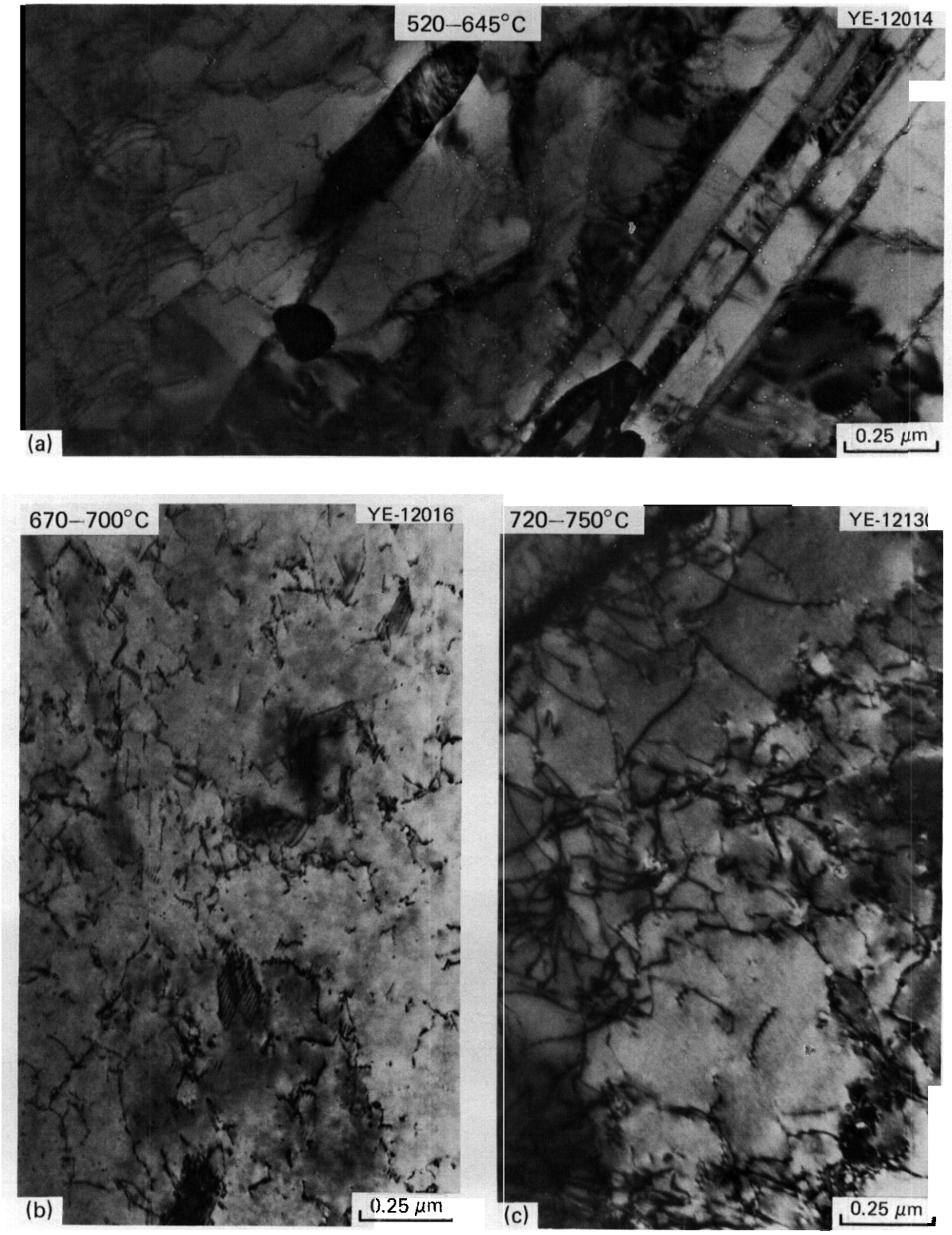

Fig. 3.3.21. Dislocation Microstructures of CW 316 + Ti Irradiated in HFIR to 9.2 to 10 dpa and *400* to 500 at. ppm He at Nominal Temperatures of (a) 620 to 645°C, (b) 670 to 700°C, and (c) 720 to 750°C.

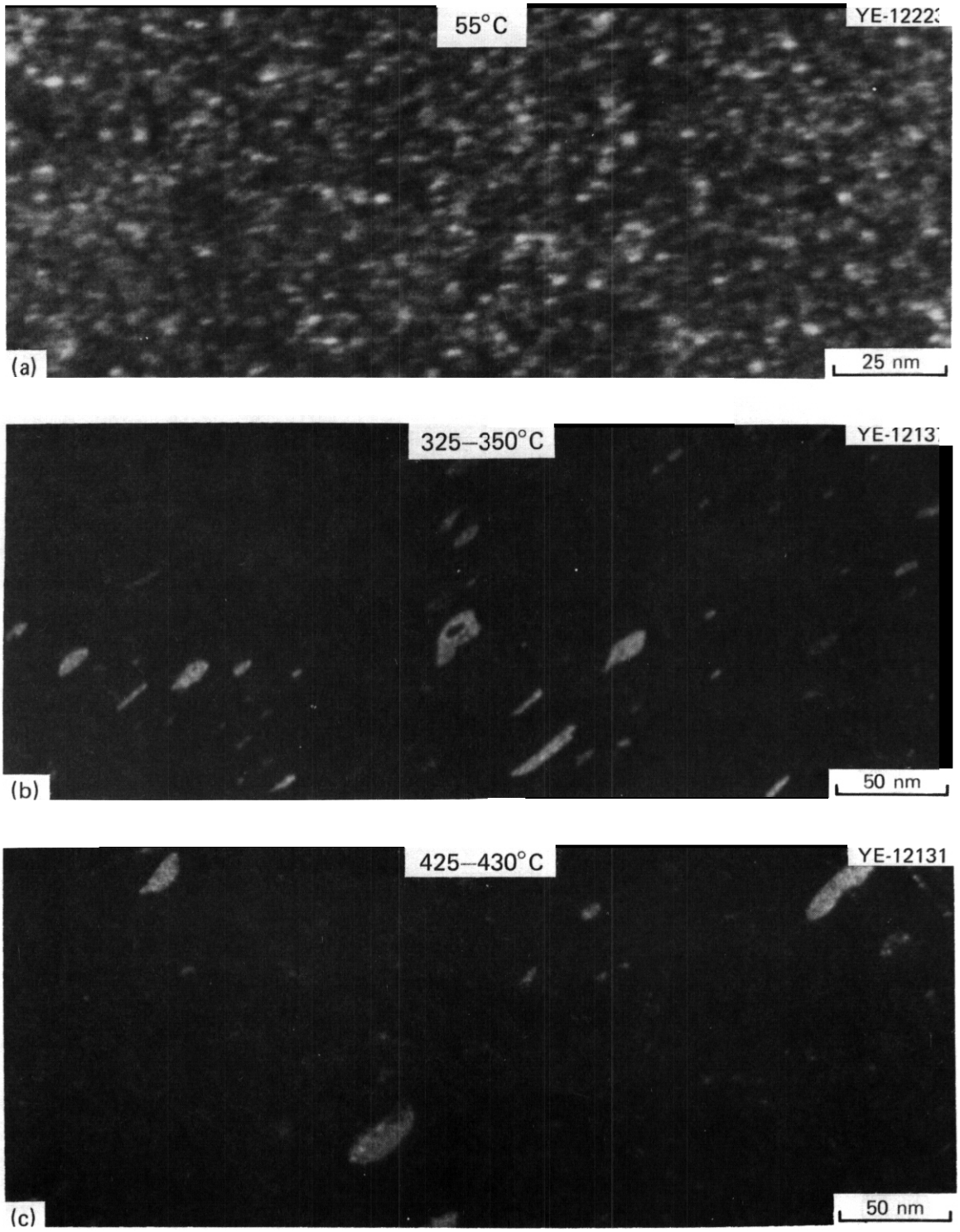

Fig. 3.3.22. Frank loop Structures of CW *316* + Ti Irradiated in HFIR to 7.7 to 10.5 dpa and *380* to *490* at. ppm He at Nominal Temperatures of **(a)** 55°C, **(b)** ***325* to 350°C, and (c) *425* to *450°C.***

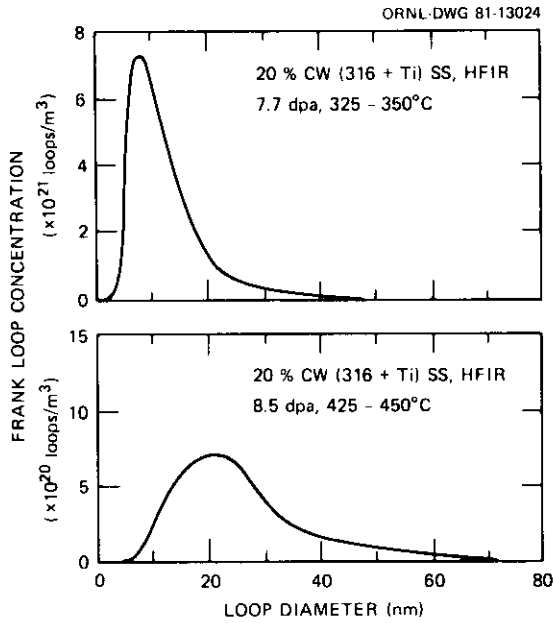

Fig. 3.3.23. Size Distribution of Frank Loop Concentration for CW 316 + Ti Irradiated in HFIR to the Conditions Indicated.

Figure 3.3.24 illustrates separation of the complex microstructure at 425 to 450°C into network (WBDF), Frank loops [two sets of (111) planes shown using satellite streaks], and fine MC precipitation [using precipitate-centered dark field (CDF)].

Frank faulted loops and fine MC precipitation are observed at 325 to 350°C, whereas precipitation does not begin until 425 to 450°C at the same fluence in CW 316 (ref. 19). The network dislocation concentration in the CW 316 + Ti is a factor of 3 higher than in CW 316 at 325 to 350°C, and the loop contribution to the total concentration is greater by at least a factor of 10 compared to the CW 316. The Frank loop size in CW 316 + Ti is about one-half and loop concentration about 40 times that found in CW 316 at 325 to 350°C (compare Figs. 3.3.15 and 3.3.23). The network remains constant for irradiations at 325 to 350°C and 425 to 450°C, in contrast to the sharp increase in CW 316. The network concentrations in the two alloys are similar at the higher temperature. The Frank loop component for CW 316 + Ti shows a more expected temperature behavior in this range than did CW 316, with size increasing by a factor of 2 and loop density decreasing by a factor of about 5 with increasing temperature. Figure 3.3.23 shows that the loop size distribution broadens and that the average size increases with increased temperature. The Frank loop density

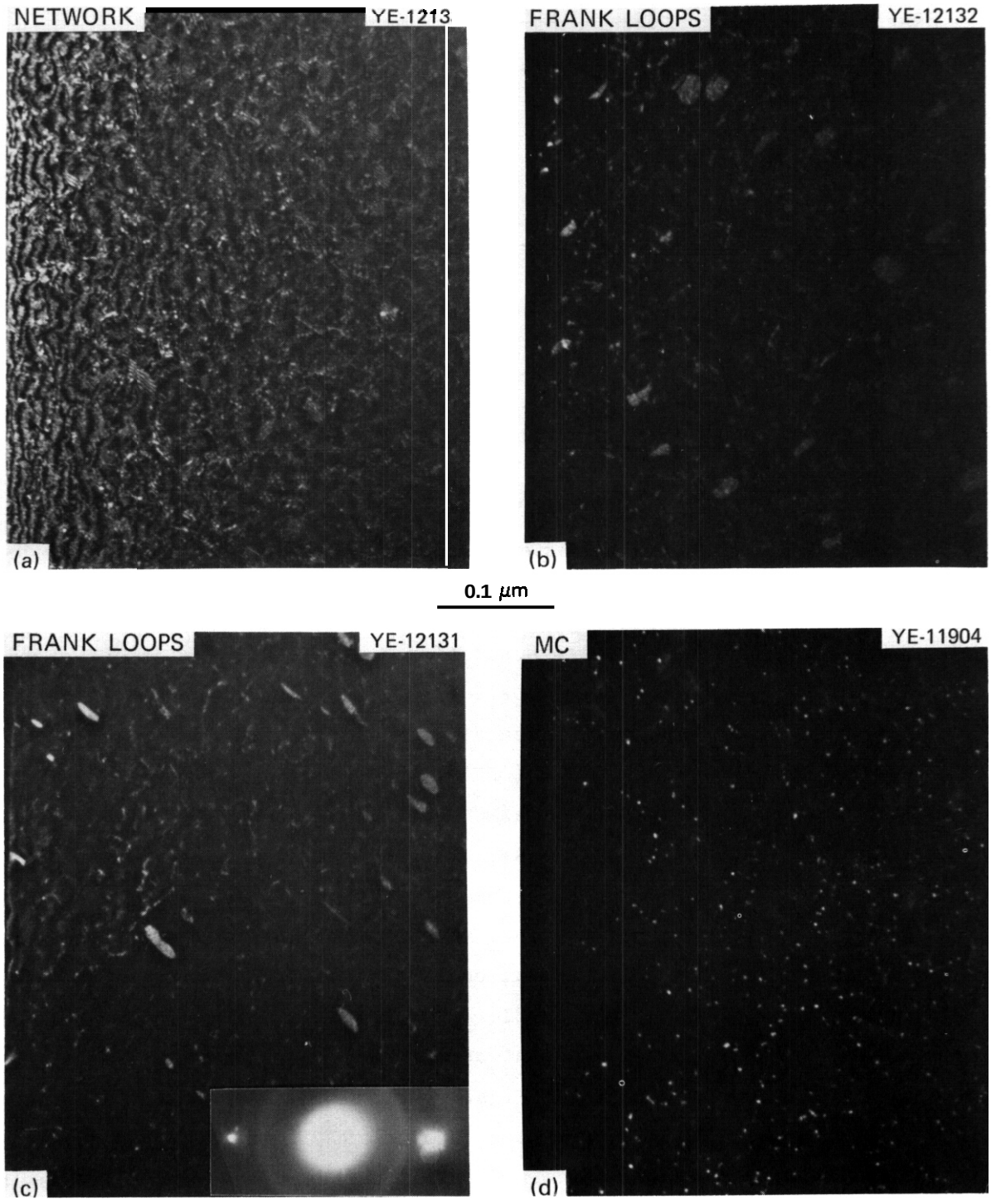

Fig. 3.3.24. An Example of the Imaging Necessary to Isolate the Various Components of the Complex Microstructure of CW 316 + Ti After HFIR Irradiation at Nominally 425 to 450°C to 8.5 dpa and 380 at. ppm He. (a) WBDF, g_{200}, +g/3g that images both network and Frank loops. (b) and (c) DF with two different <111> satellite streaks around g_{200} reflection (as shown in diffraction inlay of (c). (d) MC precipitate DF.

in CW 316 + Ti is similar to CW 316 at 425 to 450°C, but loop size is greater in the former. The MC precipitation is observed to coarsen slowly with increasing irradiation temperature from 325 to 350°C to 720 to 745°C. This is consistent with the similar dependence of recovery on irradiation temperature and in contrast to the temperature independent MC distribution[19] and dislocation recovery behavior (Fig. 3.3.5) after thermal aging.

CW 316 + Ti, Fluence Dependence. The fluence dependence of the total dislocation concentrations at 425 to 450°C to 620 to 645°C is shown in Fig. 3.3.25. The only significant fluence dependence in CW 316 + Ti is observed at the temperature of 425 to 450°C, where Frank loops are observed, and none at temperatures of 525 to 550°C and 620 to 645°C, where Frank loops are not observed. The fluence dependence of the microstructures at 425 to 450°C and 525 to 550°C are also shown in Fig. 3.3.26 to illustrate this point. The dislocation concentrations appear to saturate with fluence for irradiation temperatures above 425 to 450°C, in contrast

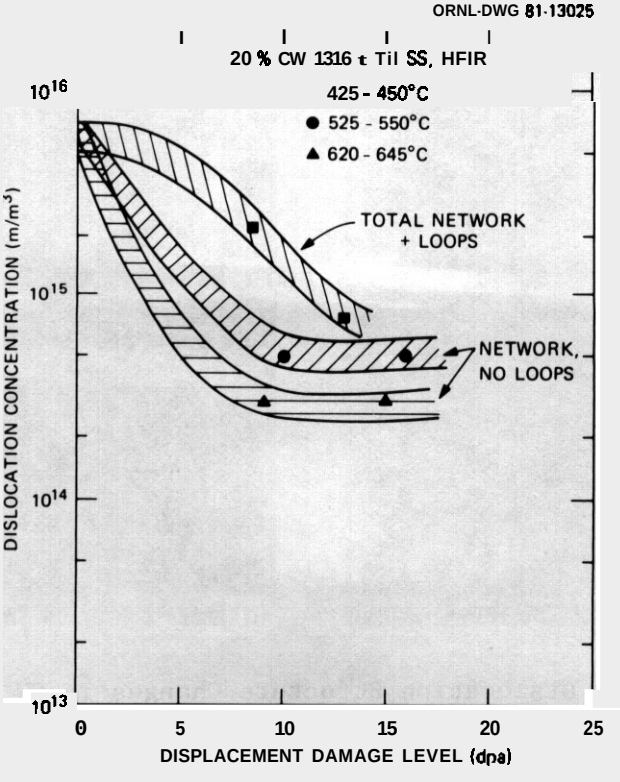

Fig. 3.3.25. Total Dislocation Concentration in CW 316 + Ti as a Function of Fluence for HFIR Irradiation at Several Temperatures.

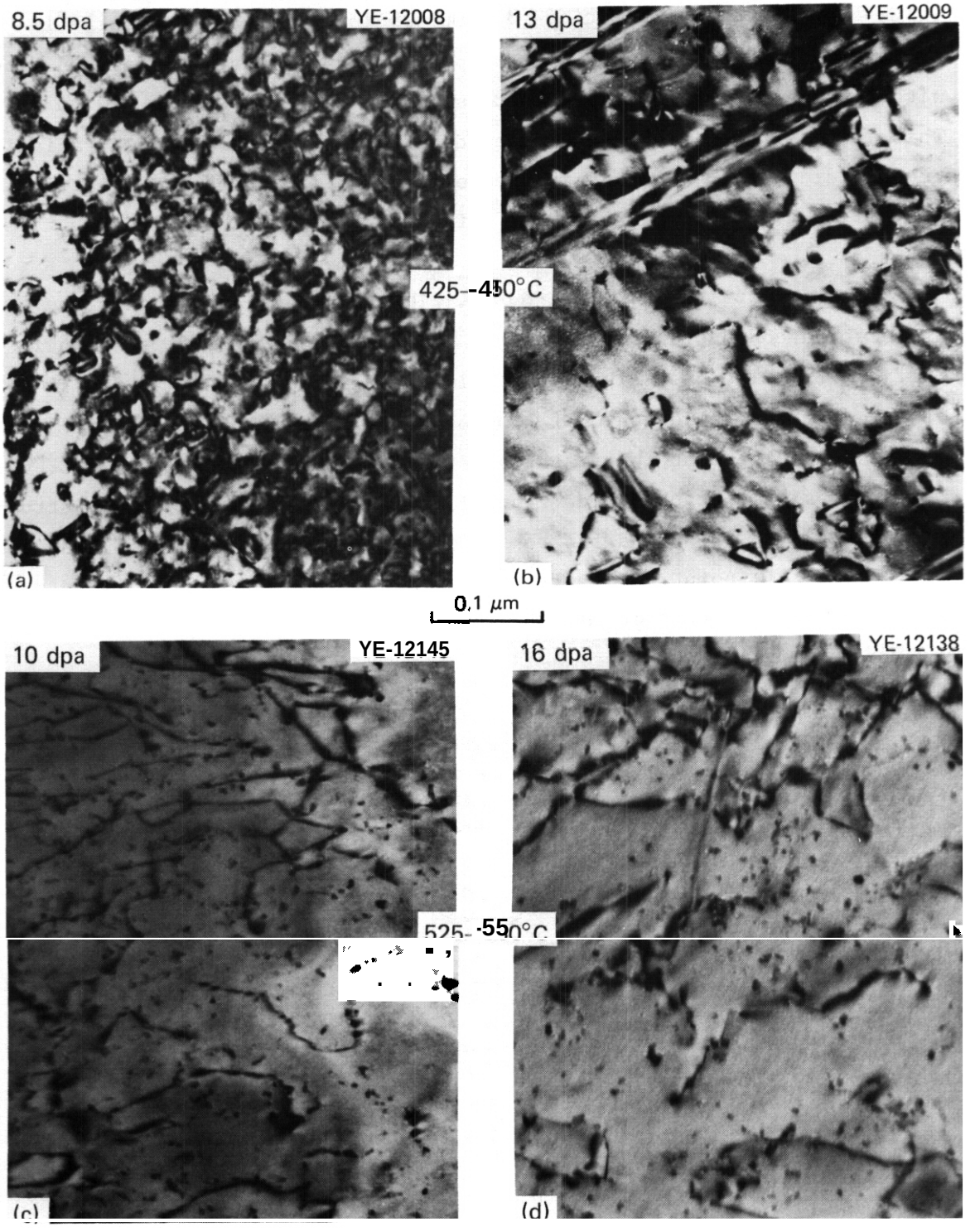

Fig. 3.3.26. Dislocation Structure Changes in CW 316 + Ti After HFIR Irradiation at Nominally *425* to 450°C to (a) 8.5 dpa and (b) 13 dpa and at nominally 525 to 550°C to (c) 10 dpa and (d) 16 dpa. Frank loops are still observed in (b) but considerably reduced from (a) and none are found in (c) and (d).

to variations shown in CW 316 (compare Figs. 3.3.16 and 3.3.25). The saturation levels decrease with increasing temperature and are at least a factor of 5 higher than the network levels found in CW 316 at the same conditions. The MC precipitate distributions at 525 to 550°C and 620 to 645°C show saturation with fluence as well,[19] whereas the MC precipitation coarsens with increasing fluence, following the network recovery, at 425 to 450°C.

The Frank loop component contributing to the total dislocation concentration at 425 to 450°C is reduced as fluence increases from 8.5 to 13 dpa but does not disappear, as observed in CW 316. The Frank loops are a factor of 2 larger and almost a factor of 10 less numerous at the higher fluence. The total concentration at 13 dpa remains at least a factor of 7 greater in CW 316 + Ti than in CW 316, and these differences are reflected in the postirradiation mechanical behavior of the CW 316 + Ti and CW 316 (ref. 20).

3.3.4.4 Discussion

Dislocation microstructures in irradiated stainless steels have received much **less** consideration and experimental attention than bubble or void swelling. They do not bear the direct relationship to volume change and swelling that cavities do, **but** do very much influence the development of the cavity component. Dislocation information is required for a mechanistic understanding that is important for modeling effort[26] and bears directly on mechanical properties.

The thermal aging data for CW **316** and CW 316 + Ti reveals the strong influence of MC formation on both dislocation recovery and precipitation of other phases. The small addition of titanium makes the type 316 alloy a phase stable and potentially precipitation-hardenable alloy. The result of this is seen in improved tensile and creep properties. The lower stacking fault energy in the titanium-modified material may also infer better irradiation creep properties, through mechanisms recently considered by Reiley.[27]

The range of irradiation temperatures in this work is among the broadest examined for neutron irradiated steels. The revision of HFIR

irradiation temperatures by an increase of 50 to 75°C results in satisfactory alignment of many of the general aspects of microstructural behavior between irradiation in HFIR or EBR-II and thermal aging.

The saturation dislocation concentration in CW 316 for irradiation at 500 to 625°C is the same whether the irradiation is in HFIR or EBR-II. However, this similarity may only hold for this narrow temperature range. If it is truly temperature independent in EBR-II over a wider temperature range, then it is quite different in HFIR at temperatures above and below 500 to 625°C. The precipitation differences for CW 316 irradiated in these two reactors, reported in more detail elsewhere,[14,18,19,26] support this possibility. It is also possible that temperature-independent saturation does not in fact occur.

The data on CW 316 + Ti irradiated in HFIR demonstrates the shift in controlling mechanisms of microstructural development that results from titanium-rich MC formation. This is consistent with the role of helium identified in earlier work[1,14,18,19,28,29] as being microstructure determining. The CW 316 + Ti demonstrates a reduced dependence of the dislocation structure on temperature and fluence compared to the CW 316 for irradiation in HFIR. The higher and more stable dislocation contents in the CW 316 + Ti are consistent with both the increased phase stability[19] and the considerably refined cavity microstrucutres[1,10] compared to CW 316 irradiated in HFIR. These same benefits are expected to carry over to the 14 Cr-16 Ni-0.25 Ti first-generation prime candidate austenitic alloy, which is more phase stable than 316 + Ti and is being investigated in current irradiation experiments.

3.3.5 Conclusions

1. During long-term (2770-4400 h) aging, the DO heat of CW 316 shows no recovery of the as-cold-worked dislocation structure for temperatures up to 470°C. The dislocation structure begins to recover between 470 and 560°C, concurrent with precipitation of $M_{23}C_6$, Laves, and M_6C phases. The network then recovers continuously with temperature, and at 700°C reaches a value that is a factor of 30 to 50 less than the starting line network concentration of 3 to 5 x 10^{15} m/m^3.

2. The Rl heat of CW 316 + Ti shows virtually no recovery up to at least 700°C for long-term thermal aging. Very fine MC precipitation begins between 470 and 560°C, and the distribution remains unchanged with increasing temperature up to at least 700°C. The MC particles pin the dislocation structure and prevent or significantly reduce $M_{23}C_6$, Laves, and M_6C precipitation.

3. During EBR-II irradiation, the dislocation structure of CW 316 recovers rapidly to a uniform network concentration that is about 2 to 3 x 10^{14} m/m^3 after 8.4 dpa and then reduces slightly to 1 to 2 x 10^{14} m/m^3 after 36 dpa at 500 to 630°C. No Frank loops are observed, and the network shows only a slight temperature dependence with the higher concentrations at the lower temperatures.

4. Network dislocation recovery occurs in CW 316 during HFIR irradiation at 55 to 670 to 700°C at 6.9 dpa and above. The least amount of network recovery occurs at 425 to 450°C when fine γ' precipitate pins the dislocation structure at 8.5 dpa. Recovery accelerates when the γ' dissolves at higher fluence. The total dislocation concentration shows the greatest temperature and fluence dependence in the range between 325 to 350°C and 525 to 550°C and reflects complicated interactions with loop, precipitate, and possibly cavity components of the microstructure. Frank loops are found below 425 to 450°C but not above. In the range 425 to 640°C the network dislocation concentration may saturate or remain in the 1 to 3 x 10^{14} m/m^3 range but drops to very low levels at higher temperatures.

5. The dislocation changes in CW 316 (DO heat) irradiated in HFIK align quite well with material irradiated in EBR-II. The coupling between cavity and precipitate formation and dislocation recovery is altered, with those components accelerated and enhanced in HFIK. Recovery is also accelerated in HFIR, but, in the range of 500 to 630°C, dislocation concentrations are 1 to 3 x 10^{14} m/m^3 for both reactors with only subtle changes with temperature.

6. Dislocation behavior in CW 316 + Ti irradiated in HFIK is qualitatively similar to CW 316 with regard to transitions from fine loops to Frank loops and from loops plus network to network only. However,

quantitative differences in temperature and fluence dependence reflect a strong coupling between dislocation and MC precipitation behavior. As in CW 316, Frank loops are found only at 425 to 450°C and below. Dislocation concentrations are 3 to 5 times higher in CW 316 + Ti than in CW 316. There is considerable difference between the two alloys in the amount, temperature, and fluence dependence of loop formation. There are more loops, they contribute more to the total dislocation concentration, and they persist to higher fluence in the CW 316 + Ti than in the CW 316.

3.3.6 Future Work

This project will continue with presentation of the detailed precipitation behavior for these same samples. The various microstructural components will then be correlated and will in turn be correlated with swelling and tensile properties to understand the property changes. This will facilitate predicting properties for the fusion environment and will help guide further alloy development and alloy selection for fusion.

3.3.7 References

1. P. J. Maziasz and M. L. Grossheck, "Microstructural Development in 20%-Cold-Worked Type 316 Stainless Steel and Titanium-Modified Type 316 Stainless Steel Irradiated in the HFIR: Fluence Dependence of the Cavity Component," *ADIP Quart. Prog. Rep. March 31, 1981*, DOE/ER-0045/6, pp. 28–56.
2. B. Weiss and R. Stickler, "Phase Instabilities During High Temperature Exposure of 316 Austenitic Stainless Steel," *Metall. Trans.* 3: 851–66 (1972).
3. J. E. Spruiell, J. A. Scott, C. S. Avy, and R. L. Hardin, "Microstuctural Stability of Thermal-Mechanically Pretreated Type 316 Austenitic Stainless Steel," *Metall. Trans.* 4: 1533–34 (1973).
4. E. E. Bloom and J. O. Stiegler, "Effect of Irradiation on the Microstructure and Creep-Rupture Properties of Type 316 Stainless Steel," pp. 360–82 in *Symposium a Effects of Radiation a Substructure and Mechanical Properties of Metals and Alloys*, ASTM STP 529, American Society for Testing and Materials, Philadelphia, 1973.

5. H. R. Brager and F. A. Garner, "Comparison of the Swelling and the Microstructural/Microchemical Evolution of AISI 316 Irradiated in EBR-II and HFIR," paper presented at Second Topical Meeting on Fusion Reactor Materials, Seattle, Wash., Aug. 9–12, 1981, to be published in the *Journal* of *Nuclear Materials*.

6. H. R. Brager and F. A. Garner, "Microstructural Development of 20%-Cold-Worked 316 Irradiated in EBR-II," *DAFS Quart. Prog. Rep. Dec. 1980,* DOE/ER-0046/4, vol. 1, pp. 81-87.

7. J. I. Bramnan, C. Brown, J. S. Watkin, C. Cawthorne, E. J. Fulton, P. J. Barton, and E. A. Little, "Void Swelling and Microstructural Changes in Fuel Pin Cladding and Unstressed Specimens Irradiated in DFR," *Radiation Effects in Breeder Reactor Structural Materials,* M. L. Blieberg and J. W. Bennett, eds., The Metallurgical Society of AIME, New York, 1977, pp. 479–507.

8. H. R. Brager, "The Effects of Cold Working and Pre-Irradiation Heat Treatment on Void Formation in Neutron-Irradiated Type 316 Stainless Steel," *J. Nucl. Mater.* 57: 103–18 (1975).

9. H. R. Brager, E. R. Gilbert, and J. L. Straaslsund, "The Effect of Stress on the Microstructure of Neutron Irradiated Cold Worked Type 316 Stainless Steel," *Radiat. Eff.* 21: 37–50 (1974).

10. P. J. Maziasz and M. L. Grossbeck, "Swelling and Microstructure of HFIR-Irradiated 20%-Cold-Worked Types 316 Stainless Steel and 316 + 0.23 wt % Ti," *ADIP Quart. Prog. Rep. Dec. 31, 1980,* DOE/ER-0045/5, pp. 43–69.

11. P. J. Maziasz, B. L. Cox, and J. A. Horak, "The Properties of Preinjected Helium on the Microstructure and Tensile Properties of EBR-11-Irradiated 20%-Cold-Worked Type 316 Stainless Steel," *ADIP Quart. Prog. Rep. Mar. 31, 1980,* DOE/ER-0045/2, pp. 35–57.

12. P. J. Maziasz, F. W. Wiffen, and E. E. Bloom, "Swelling and Microstructural Changes in Type 316 Stainless Steel Irradiated Under Simulated CTR Conditions," pp. 259–88 in *Radiation Effects and Tritium Technology for Fusion Reactors,* CONF-750989, vol. 1 (March 1976).

13. P. J. Maziasz, M. L. Grossbeck, and F. W. Wiffen, "The Microstructure and Mechanical Properties of 20%-Cold-Worked Type 316 Stainless Steel and 316 + 0.23 wt % Ti After HFIU Irradiation at 55 to 375°C," *ADIP* ***Quart. Prog. Rep. June 30, 1980,*** DOE/ER-0045/3, pp. 48-74.

14. G. R. Odette, P. J. Maziasz, and J. A. Spitznagel, "Fission-Fusion Correlations for Swelling and Microstructure in Stainless Steels: Effect of Helium to Displacement per Atom Ratio," paper presented at Second Topical Meeting on Fusion Reactors, Seattle, Wash., Aug. 9-12, 1981, to be published in the ***Journal*** of ***Nuclear*** *Materials.*

15. P. J. Barton, B. L. Eyre, and D. A. Stow, "The Structure of Fast-Reactor Irradiated Solution-Treated AISI Type 316 Steel," ***J. Nucl. Mater.*** 67: 181-97 (1977).

16. L. E. Murr, ***Electron Optical Applications in Materials Science,*** McGraw-Hill, New York, 1970, p. 517.

17. P. R. Okamoto and S. **D. Harkness,** "Stress-Biased Loop Nucleation in Irradiated Type 316 Stainless Steel," ***J. Nucl. Mater.*** 48: 204-06 (1973).

18. P. J. Maziasz, "The Precipitation Response of 205-Cold-Worked Type 316 Stainless Steel to Simulated Fusion Irradiation," ***J. Nucl. Mater.*** 85&86: 713-17 (1979).

19. P. J. Maziasz, J. A. Horak, and B. L. Cox, "The Influence of Both Helium and Neutron Irradiation on Precipitation in 20%-Cold-Worked Austenitic Stainless **Steel,**" pp. 271-92 in ***Phase Stability During Irradiation,*** (Proc. Symp. Pittsburgh, Pa., Oct. 5-9, 1980), J. R. Holland, L. K. Mansur, and D. I. Potter, eds., **The** Metallurgical Society of AIME, Warrendale, Pa., 1981.

20. M. L. Grossbeck and P. J. Maziasz, "Tensile Properties of 205-Cold-Worked Titanium-Modified Type 316 Stainless Steel Irradiated in HFIR," paper presented at Second Topical Meeting **on** Fusion Reactor Materials, Seattle, Wash., Aug. 9-12, 1981, to be published in the ***Journal of Nuclear Materials.***

21. H. R. Brager and F. A. Garner, "Dependence of Void Formation on Phase Stability in Neutron-Irradiated Type 316 Stainless Steel," pp. 207-32 in ***Effects*** of ***Radiation a Structural Materials,*** J. A. Sprague and P. Krams, eds., ASTM-STP 683, American Society for Testing and Materials, Philadelphia, 1979.

22. F. W. Wiffen and P. J. Maziasz, "The Influence of Neutron Irradiation at 55°C on the Properties of Austenitic Stainless Steels," paper presented at Second Topical Meeting on Fusion Reactor Materials, Seatttle, Wash., Aug. 9–12, 1981, to be published in *Journal of Nuclear Materials.*

23. P. J. Maziasz, "Microstructures Developed in Austenitic Stainless Steels Irradiated in HFIK at 55°C," (Summary) *Trans. Am. Nucl. Soc.* 39 (TANSAO 39): 433–35 (November–December 1981).

24. E. E. Bloom, W. K. Martin, J. O. Stiegler, and J. R. Weir, "The Effect of Irradiation Temperature on Strength and Microstructure of Stainless Steel," *J. Nucl. Mater.* 22: 68–76 (1967).

25. M. L. Grossbeck and P. J. Maziasz, "Tensile Properties of Type 316 Stainless Steel Irradiated in a Simulated Fusion Reactor Environment," *J. Nucl. Mater.* 85&86: 883–87 (1979).

26. R. E. Stoller and G. R. Odette, "A Model Based Fission–Fusion Correlation of Cavity Swelling in Stainless Steel," paper presented at Second Topical Meeting on Fusion Reactor Materials, Seattle, Wash., Aug. 9–12, 1981, to be published in the *Journal of Nuclear Materials.*

27. T. C. Keiley, "On the Stacking Fault Energy Dependence of Irradiation Creep," *Scr. Metall.* 15: 313–18 (1981).

28. P. J. Maziasz and M. L. Grossbeck, "Swelling, Microstructural Development and Helium Effects in Type 316 Stainless Steel Irradiated in HFIR and EBR-II," paper presented at Second Topical Meeting on Fusion Reactor Materials, Seattle, Wash., Aug. 9–12, 1981, to be published in the *Journal of Nuclear Materials.*

29. P. J. Maziasz, "Micorstructural Development and the Effects of Helium in Type 316 Stainless Steel Irradiated in HFIR and in EBR-II," *ADIP Quart. Prog. Rep. Mar. 31, 1981,* DOE/ER-0045/6, pp. 70–92.

3.4 EQUATIONS TO DESCRIBE THE SWELLING OF 20%-COLD-WORKED TYPE 316 STAINLESS STEEL IRRADIATED IN HFIR — P. J. Maziasz and M. L. Grossbeck (Oak Ridge National Laboratory)

3.4.1 ADIP Task

ADIP Task I.C.2, Microstructure and Swelling in Austenitic Alloys.

3.4.2 Objective

The objective of this work is to develop equations giving the temperature and fluence dependence of swelling in 20%-cold-worked type 316 stainless steel during irradiation in HFIR. These equations are needed to (1) describe swelling for use in fusion reactor design, (2) compare with similar equations for EBR-II data, in an effort to develop design swelling equations for fusion, on the basis of correlation between fission reactors, and (3) provide a microstructurally based description of swelling.

3.4.3 Summary

Equations describing cavity volume fraction swelling are developed for 20%-cold-worked type 316 stainless steel (CW 316) irradiated in HFIR. These equations are based on the physical phenomena observed in the microstructure, such as matrix void swelling, matrix bubble swelling, grain boundary cavity swelling, and precipitate-assisted void swelling. The temperature and fluence dependence of each component is considered, and microstructural information is interpolated to provide a description of the swelling behavior within the limits of the data set (up to 50–60 dpa). The data base is for the D0 heat of CW 316. Some facets of the swelling behavior, such as void attachment to eta (M_6C) phase particles at lower temperature, may vary between heats of type 316 stainless steel. Other components, such as bubbles in the matrix and grain boundary cavities, may be more general. The expression of total swelling as the sum of distinct, microstructurally related components allows flexibility in describing other heats of steel having generally similar behavior but with some differences in precipitate response, for example. It also permits separate comparison of components of the swelling, such as bubbles or

void formation, with these same phenomena observed under different irradiation conditions. Comparison of the overall swelling in HFIR with that observed in EBR-II indicates substantial differences in the temperature and fluence dependence of swelling in these reactors. The microstructural information shows that the differences are due to the helium generation rate and its effect on various mechanisms responsible for development of the cavity microstructure. An understanding of these differences and development of physically based models that predict both EBR-II and HFIR data will be necessary to project the swelling behavior in a fusion reactor.

3.4.4 Progress and Status

3.4.4.1 Introduction

Since fusion irradiation environments do not exist, efforts to forecast the swelling behavior of fusion reactor components depend on results obtained in available fast-spectrum or mixed-spectrum (fast and thermal) fission reactors. Use of this data requires mechanistic understanding and descriptive equations. Extrapolation of the swelling behavior to a fusion first wall can then be based on the variable dependence of the known mechanisms of swelling. To date, HFIR and EBR-II have been used to explore the temperature and fluence dependence of swelling in 20%-cold-worked type *316* stainless steel (CW *316*).[1-8] The considerably different helium generation rates in the two reactors also provide a helium dependence in the data set. The swelling data for a single heat of CW *316* irradiated in both HFIR and EBR-II are being examined to develop the correlation and theoretical models necessary to extend the data to intermediate He/dpa ratios[9-11] more representative of fusion service. The first effort to achieve this extrapolated EBR-II data, with very little adjustment for the fusion case, on the assumption that helium had little effect on cavity swelling and that fusion irradiation would thus produce swelling similar to that found in EBR-II (ref. 9). That initial effort was restricted by limitations of the HFIR microstructural data. The

HFIR data that have recently been reported show clear differences in microstructural development and resultant swelling for irradiation in HFIR or EBR-II (refs. 2–4, 10, 12–15).

The current work seeks to express the HFIK swelling behavior via equations that contain the temperature and fluence dependence of the swelling. The equations are set up to represent the microstructural mechanisms to the best of our knowledge. They will also be compared with the well-established swelling equations for EBR-II irradiation.

If helium has little or no effect, the swelling behavior in HFIR should be similar to that found in EBR-II, and data from either would be applicable to fusion. If swelling in the two reactors is markedly different, neither may adequately represent fusion, and physically based modeling will be required to predict both microstructure and swelling.

3.4.4.2 Data Treatment and Equations

The following definitions are provided to clarify the use of the swelling equations:

$$\text{Fractional volume change} = \Delta V/V_0 = (V_f - V_0)/V_0 = (\rho_0 - \rho_f)/\rho_f \ , \qquad (1)$$

where

V_0 = initial volume,
V_f = final volume,
ρ_0 = initial density,
ρ_f = final density.

Swelling measurements are from transmission electron micrographs and include only the cavity volume fraction.[1-4] Density changes resulting from phase transformations must be included to determine net density changes. Primarily for the purpose of comparison with other swelling equations derived from immersion density data, the following definitions are given:

$$\Sigma = \text{negative fractional density change} = (\rho_f - \rho_0)/\rho_0 \ , \qquad (2)$$

and

$$\Delta V/V_0 = (V_f - V_0)/V_0 = \Sigma/(1 - \Sigma) \ . \qquad (3)$$

The method of development of these equations has been to assess and express separately the various microstructural contributions to the total swelling. The equation developed then contains the sum of these individual components to yield the total swelling behavior. The equations are justified only by their ability to fit the data and do not possess first principle theoretical significance.

The total volume change can be expressed as follows:

$$\left(\frac{\Delta V}{V_0}\right)_{\text{total}} = \left(\frac{\pm\Delta V}{V_0}\right)_{\text{precipitation}} + \left(\frac{\Delta V}{V_0}\right)_{\substack{\text{substitutional}\\ \text{helium}}} + \left(\frac{\Delta V}{V_0}\right)_{\substack{\text{cavity}\\ \text{swelling}}} \quad (4)$$

Precipitation can directly cause either densification or swelling of as much as ±0.5%; this phenomenon is treated elsewhere.[16] The substitutional helium contribution is simply a reflection of the fact that helium atoms can occupy lattice sites and therefore increase specimen volume. Swelling will increase linearly with increasing helium generation and give a value of $\Delta V/V_{0_{\text{subst He}}} = 0.1\%$ at 1000 at. ppm He. Data are available to indicate this type of behavior at HFIR irradiation temperatures of 55°C,[2,3,17] but this contribution will vanish when helium–vacancy complexes migrate to form cavities. Because of the limited range of applicability and the small magnitude, swelling due to this mechanism has not been explicitly included in the equation.

The cavity swelling is the dominant swelling component at higher temperatures. It can be expressed as the sum of the following components:

$$\left(\frac{\Delta V}{V_0}\right)_{\substack{\text{cavity}\\ \text{swelling}}} = \left(\frac{\Delta V}{V_0}\right)^{\text{voids}}_{\text{precipitates}} + \left(\frac{\Delta V}{V_0}\right)^{\text{voids}}_{\text{matrix}} + \left(\frac{\Delta V}{V_0}\right)^{\text{bubbles}}_{\text{matrix}} + \left(\frac{\Delta V}{V_0}\right)^{\text{bubbles}}_{\text{precipitates}} + \left(\frac{\Delta V}{V_0}\right)^{\text{bubbles}}_{\substack{\text{grain}\\ \text{boundaries}}} \quad (5)$$

Swelling attributable to voids on precipitates, $\frac{\Delta V}{V_0}^{\text{voids}}_{\text{precipitates}}$, is observed only for eta (η) phase particles at fluences greater than 13 dpa for temperatures of about 350 to 425°C (refs. 1, 3, 4). This component of swelling is expressed as:

$$\frac{\Delta V}{V_0}^{\text{voids}}_{\text{precipitates}} = 0.7 \exp[-0.001(T - 380)^2][0.028\, d - 0.36 + 0.36 \exp(-0.1\, d)] , \quad (6)$$

where T is temperature (°C) and d is atomic displacements (dpa).

The swelling component due to voids in the matrix is important at temperatures of 285°C and below;[2-4] decreases with increasing temperature and ≃0 at 400°C and above; and is assumed to increase with increasing fluence. This swelling is given by:

$$\frac{\Delta V}{V_0}^{\text{voids}}_{\text{matrix}} = 0.05 \exp\{-6.94 \times 10^{-5}(T - 250)^2\}\exp(-d^3/B) , \quad (7)$$

where $B = \exp(26 - 0.039\, T)$.

The swelling due to bubbles on precipitates is approximately zero for all conditions for CW 316.

$$\frac{\Delta V}{V_0}^{\text{bubbles}}_{\text{precipitates}} = 0 . \quad (8)$$

The swelling component due to bubbles in the matrix accounts for most of the cavities at 375°C and above. This component dominates swelling from about 400 to 700°C (refs. 1, 3, and 4), and can be expressed as:

$$\left(\frac{\Delta V}{V_0}\right)^{\text{bubbles}}_{\text{matrix}}$$

$$= 0.5\ [1 + \tanh(0.02(T - 100))]\{0.5[0.08(d + D) - 2.72][1 + \tanh(0.1(d + D - 40))] + 0.35\ \exp[-0.005(d + D - 40)^2]\}\ . \quad (9)$$

The contribution due to bubbles on the grain boundaries is essentially zero for temperatures below about 550°C, and then increases rapidly with increasing temperature at high fluences (refs. 1, 3, and 4). This is described by the equation

$$\left(\frac{\Delta V}{V_0}\right)^{\text{bubbles}}_{\text{grain boundaries}} = 0.033\ d\ \exp[0.025(T - 680)]\ . \quad (10)$$

These equations, giving the contributions for the various components of the swelling, can then be substituted into Eq. (5) to give total swelling. The combined and simplified total swelling equation, then, is

$$\left(\frac{\Delta V}{V_0}\right)_{\text{cavity swelling}} (\%) = 0.05\ A\ d\ \exp\ (-d^3/B) + C[0.028\ d - 0.36 + 0.36\ \exp(-0.1d)] + E\{0.5[0.08\ (d + D) - 2.72][1 + \tanh(0.1(d + D - 40))] + 0.35\ \exp[-0.005(d + D - 40)^2]\} + 0.033\ d\ \exp[0.025(T - 680)]\ ; \quad (11)$$

for the range $50 \leq T \leq 700$°C, $d \leq 60$ dpa. In the above equation

d = atomic displacements, dpa,

T = temperature (°C),

$A = \exp[-6.94 \times 10^{-5}(T - 250)^2]$,

$B = \exp(26 - 0.039\ T)$,

$C = 0.7\ \exp[-0.001(T - 380)^2]$,

$D = 0.041\ T - 15.3$,

$E = 0.5\{1 + \tanh[0.02(T - 100)]\}$,

The data used and the irradiation conditions are given in Table 3.4.1. These results have been presented in more detail in earlier reports.[1-4] The derived swelling equations are shown as functions of temperature and fluence in Figs. 3.4.1 and 3.4.2, respectively.

Table 3.4.1. Swelling and Cavity Statistics for Cold-Worked Type 316 Stainless Steel Irradiated in HFIR

Irradiation conditions				Swelling from immersion density (%)	Cavity parameters, %		
Temperature (°C)	Neutron fluence >0.1 MeV (neutrons/m^2)	Displacement damage (dpa)	Helium (at. ppm)		Matrix volume fraction	Grain boundary volume fraction	Total volume fraction
55	1.4×10^{26}	10.8	520	−0.03	0	*a*	0
285	1.0	7.7	390	0.04	0.46	*a*	0.46
375	1.1	8.5	380	0	0.12	*b*	0.12
375	1.7	13.0	740	0.36	0.03	*b*	0.03
380	7.05	49	3320	1.6	2.2 ± 0.4	*b*	2.2
475	1.4	10.0	500	−0.1	0.06 ± 0.01[c]	*b*	0.06
475	2.1	16.0	1020	0.03	0.02	0.005	0.02
460	7.69	54	3660	0.8	2.0 ± 0.4	0.01	2.0
565	1.2	9.2	440	0.1	0.04	0.02	0.06
565	2.0	15.0	880	0.37	0.13	0.02	0.15
550	6.18	42	2990	0.0	1.4 ± 0.1	0.03	1.4
620	2.1	16.0	1020	0.37	0.12	0.02	0.14
600[d]	8.71	60	4070	3.3	3.0 ± 0.5	0.4	3.4
680[e]	0.74	61	4140		6.0 ± 2.5	2.0	8.0

[a] None detected.

[b] Grain boundary precipitation of eta (M_6C) phase.

[c] Two separate disks with three areas analyzed in one disk and two areas analyzed in the other to show the area-to-area variation in swelling.

[d] Completely recrystallized, fine grains.

[e] Completely recrystallized, coarse grains.

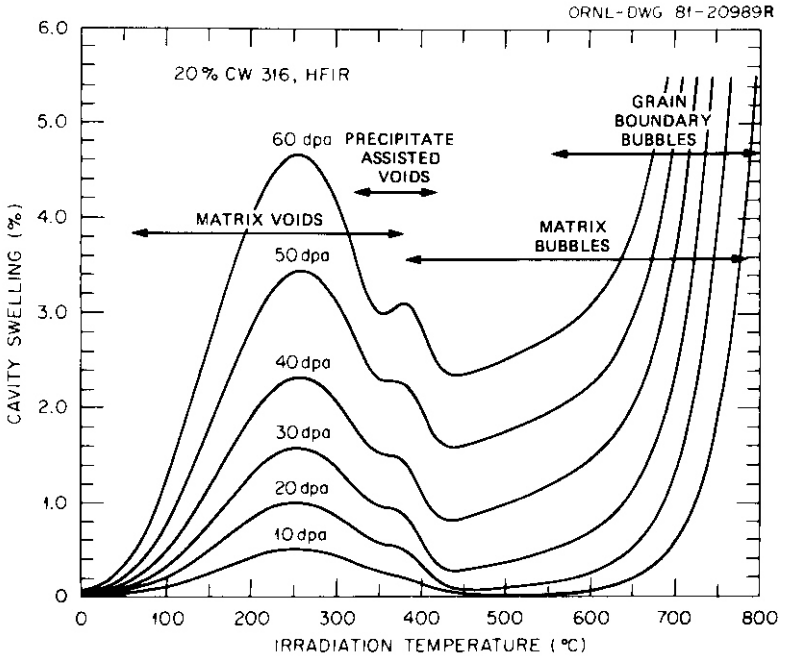

Fig. 3.4.1. Temperature Dependence of Equations Representing the Total Swelling Behavior of 20%-Cold-Worked (DO-Heat) Type 316 Stainless Steel After HFIR Irradiation at Various Fluence Levels.

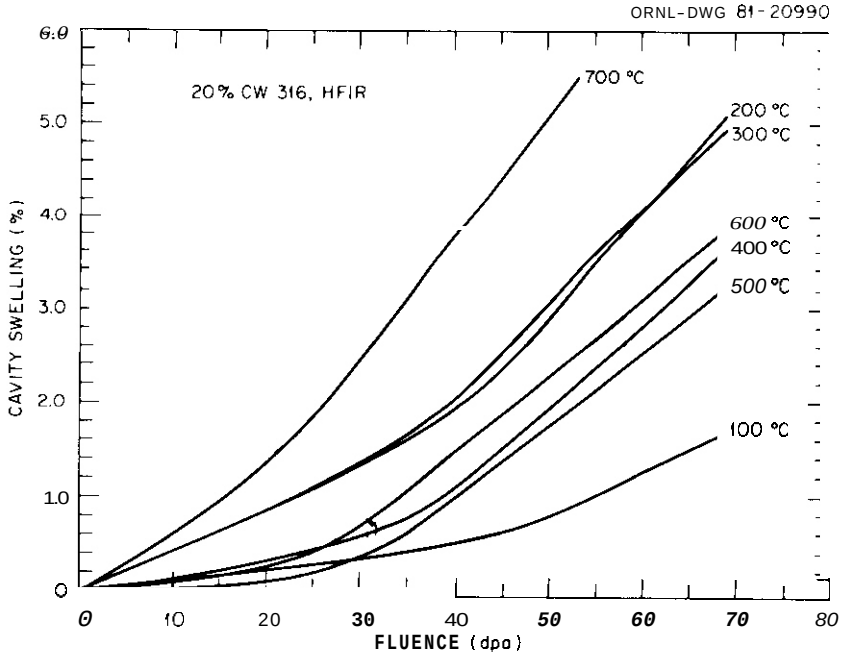

Fig. 3.4.2. Fluence Dependence of Equations Representing the Total Swelling Behavior of 20%-Cold-Worked (DO-Heat) Type 316 Stainless Steel After **HFIR** Irradiation at Various Temperatures.

3.4.4.3 Discussion

The swelling predictions for 20%-CW *316* in a fusion reactor, developed by Gamer, Maziasz, and Wolfer,[9] are shown in Fig. *3.4.3.* Comparison of Figs. *3.4.2* and 3.4.3 shows considerable differences between these predictions, which were based mainly on EBR-II data and the swelling observed in HFIR. Microstructural phenomena responsible for swelling are different in the two reactors. These differences relate to the increased helium generation rate in HFIR, as discussed in previous work.

The problem this comparison poses is that application of one or the other data set to fusion design without insight based on the physics of

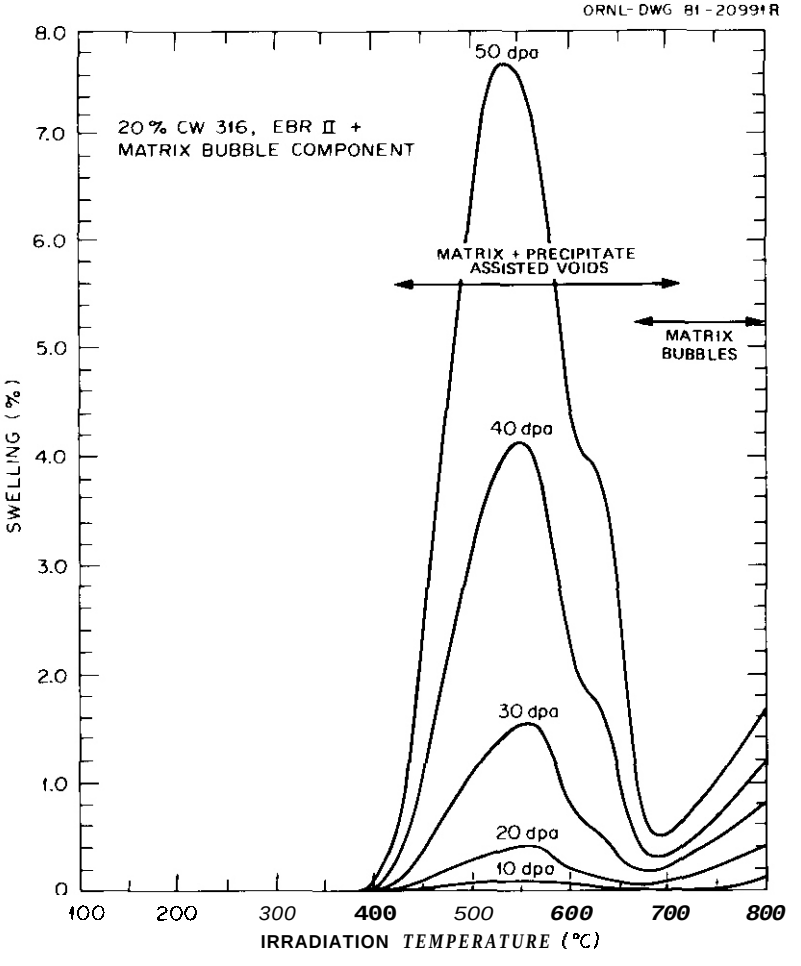

Fig. *3.4.3.* Temperature Dependence of Proposed Fusion Swelling for 20%-Cold-Worked Type *316* Stainless Steel at Various Fluence Levels for Void Swelling That is the Same as in EBR-II and a Superimposed Matrix Bubble Component. Source: F. A. Garner, P. J. Maziasz, and W. G. Wolfer, "Development of a Swelling Equation for 20%-CW *316* in a Fusion Device," ***DAFS Quart.*** *Prog.* ***Rep. Nov. 1980,*** DOE/ER-0046/3, pp. 159-77.

the swelling process may be seriously in error. Stoller and Odette have developed a swelling correlation model for CW 316 which is calibrated to both the EBR-II and HFIR data. However, extrapolation to fusion reactor service conditions requires assumption on the importance of precipitate-assisted void and matrix bubble components of the swelling. Further development of the model and additional experimental data are required before confident extrapolations can be made.

Sufficient data has recently become available to confirm that the actual HFIR irradiation temperatures are about 50 to 75°C higher than calculated, thus warranting the assignment of new nominal temperatures (see Sect. 3.1).[10] As a result, the equations in this work need to be updated. This task will be accomplished in the next progress report.

3.4.5 Conclusions and Future Work

The data for swelling of 20%-cold-worked type 316 stainless steel produced by HFIR irradiation can be represented by equations that depend only on temperature and fluence. These equations contain identifiable parts related to various microstructural mechanisms. The swelling is considerably different from swelling in EBR-II. The differences reflect the influence of helium on the microstructural evolution.

The HFIR swelling equation for cold-worked type 316 stainless steel will require revision to the adjusted irradiation temperatures.

3.4.6 References

1. P. J. Maziasz, F. W. Wiffen, and E. E. Bloom, "Swelling and Microstructural Changes in Type 316 Stainless Steel Under Simulated CTR Conditions," pp. 259–88 in *Radiation Effects and Tritium Technology for Fusion Reactors*, CONF-750989, vol. 1, March 1976.
2. P. J. Maziasz, M. L. Grossbeck, and F. W. Wiffen, "The Microstructure and Mechanical Properties of 20%-Cold-Worked Types 316 Stainless Steel and 316 + 0.23 wt % Ti After HFIR Irradiation at 55 to 375°C," *ADIP Quart. Prog. Rep. June 30, 1980,* DOE/ER-0045/3, pp. 48–74.
3. P. J. Maziasz and M. L. Grossbeck, "Swelling and Microstructure of HFIR-Irradiated 20%-Cold-Worked Types 316 Stainless Steel and 316 + 0.23 wt % Ti," *ADIP Quart. Prog. Rep. Dec. 31, 1980,* DOE/ER-0045/5, pp. 43-69.

4. P. J. Maziasz and M. L. Grossbeck, "Microstructural Development in 20%-Cold-Worked Type 316 Stainless Steel Irradiated in the HFIR: Fluence Dependence of the Cavity Component," *ADIP Quart. Prog. Rep. Mar. 31, 1981,* DOE/ER-0045/6, pp. 28–56.

5. J. J. Holmes and J. L. Straalsund, "Irradiation Sources for Fusion Materials Development," *J. Nucl. Mater.* 85&86: 447–51 (1979).

6. J. A. Spitznatel, F. W. Wiffen, and F. V. Nolfi, "Microstructures Developed in 'Simulated' Fusion Irradiations," *J. Nucl. Mater.* 85686: 629–46 (1979).

7. G. R. Odette, "Modeling of Microstructural Evolution Under Irradiation," *J. Nucl. Mater.* 85&86: 533–45 (1979).

8. F. A. Garner, "Development of Fission–Fusion Correlations," *DAFS Quart. Prog. Rep. May 1980,* DOE/ER-0046/1, pp. 119–32.

9. F. A. Garner, P. J. Maziasz, and W. G. Wolfer, "Development of a Swelling Equation for 20%-CW 316 in a Fusion Device," *DAFS Quart. Prog. Rep. Nov. 1980,* DOE/ER-0046/3, pp. 159–77.

10. G. R. Odette, P. J. Maziasz, and J. A. Spitznagel, "Fission–Fusion Correlations for Swelling and Microstructure in Stainless Steels: Effect of the Helium to Displacement Damage Per Atom Ratio," paper presented at Second Topical Meeting on Fusion Reactor Material, Seattle, Wash., Aug. 9–12, 1981, to be published in the *Journal of Nuclear Materials.*

11. R. E. Stoller and G. R. Odette, "A Model Based Fission–Fusion Correlation of Cavity Swelling in Stainless Steel," paper presented at Second Topical Meeting on Fusion Reactor Material, Seattle, Wash., Aug. 9–12, 1981, to be published in the *Journal of Nuclear Materials.*

12. P. J. Maziasz, "Microstructural Development and the Effects of Helium in Type 316 Stainless Steel Irradiated in HFIR and EBR-II," *ADIP Quart. Prog. Rep. Mar. 31, 1981,* DOE/ER-0045/6, pp. 70–92.

13. P. J. Maziasz and M. L. Grossbeck, "Swelling, Microstructural Development and Helium Effects in Type 316 Stainless Steel Irradiated in HFIR and EBR-II," paper presented at Second Topical Meeting on Fusion Reactor Materials, Seattle, Wash., Aug. 9–12, 1981, to be published in the *Journal of Nuclear Materials.*

14. H. R. Brager and F. A. Garner, "Microstructural Development of 20%-Cold-Worked 316 Irradiated in EBR-II," *DAFS Quart. Prog. Rep. Feb. 1980*, DOE/ER-0046/4, vol. 1, pp. 81-87.

15. H. R. Brager and F. A. Garner, "Comparison of the Swelling and the Microstructural/Microchemical Evolution of AISI 316 Irradiated in EBR-II and HFIR," paper presented at Second Topical Meeting on Fusion Reactor Materials, Seattle, Wash., Aug. 9-12, 1981, to be published in the *Journal of Nuclear Materials*.

16. F. A. Garner, W. V. Cummings, J. F. Bates, and E. R. Gilbert, *Densification-Induced Strains in 20%-Cold-Worked 316 Stainless Steel During Neutron Irradiation*, Hanford Engineering Development Laboratory, HEDL-TME 78-9 (June 1978).

17. P. J. Maziasz, "Microstructures Developed in Austenitic Stainless Steels Irradiated in HFIR at 55°C," *ANS Trans.* 39: 433-36 (1981).

3.5 WELD BEND TESTS ON IRRADIATED, 20% COLD-WORKED 316 STAINLESS STEEL - S. D. Atkin (Hanford Engineering Development Laboratory)

3.5.1 ADIP Task

Path A Alloy Development - Austenitic Stainless Steels.

3.5.2 Objective

This work is being conducted to investigate the feasibility of repair welding stainless steel components in a fusion reactor. The post-weld ductility and strength of irradiated 20% CW 316 SS will be determined.

3.5.3 Summary

Samples of 20% CW **316** SS were sectioned from various axial locations along an irradiated EBR-II duct. The bend samples were fabricated by Tungsten-Inert-Gas (TIG) welding two tabs together along the width. Bending was accomplished by centrally loading the **root** side of the weld while both ends of the specimen were supported by pins. The effects of sample fluence level, test temperature, and deflection rate on strength and ductility were investigated. A preliminary evaluation indicates the ductility of the welded material is much greater than expected. Helium produced in the metal during reactor service does not appear to cause embrittlement of the weld zone.

3.5.4 Progress and Status

3.5.4.1 Introduction

The ability to make repair welds on materials exposed to neutron radiation without adversely affecting their mechanical properties is of importance to the Fusion Program. Very little is known about the effects of neutron fluence on welding irradiated materials. The heat input associated with welding could act to anneal out radiation damage and cause **a** decrease in strength in the weld zone. Another possibility is severe embrittlement caused by the helium generated in service. This

is a critical concern for fusion reactors due to the inherent levels of helium production. Although helium production levels are lower in EBR-II, materials irradiated to 60 dpa in EBR-II produce approximately 30 appm helium.(1) These atoms normally remain in solution in the base metal, but welding could cause the helium to diffuse to the grain boundaries of the heat affected zone or coalesce and form large pores in the melt zone. Either of these would result in severe degradation of the mechanical properties.

Post-weld mechanical tests are necessary to investigate these effects and ultimately to define acceptable levels of fluence and helium generation for repair welds on components exposed to neutron radiation. An investigation is currently underway to determine the strength and ductility of weld samples fabricated from irradiated EBR-II material.

3.5.4.2 Procedure

The material was sectioned from a 20% CW 316 SS EBR-II duct. The duct was irradiated at approximately 400°C to a peak fluence of 12.6 x 10^{22} n/cm^2 (63 dpa) (E >.1 MeV). The six axial sections used in this work are indicated on the fluence profile (Figure 1).(2) The duct material was nominally 1.0 mm thick and was machined into tabs 25 x 13 mm. Two tabs from the same fluence level were butt welded together along the width (Figure 2) using pulsed TIG welding. The welding parameters had been defined through preliminary weld development work on unirradiated 316 SS duct material. All welds were visually inspected for evidence of cracks or other abnormalities prior to bend testing.

The bend test apparatus is illustrated in Figure 3. The procedure was based on ASTM E290 for three point bending tests. The weld samples were centered over the notch with the root side of the weld facing upward. The ends were freely supported by 3 mm diameter support rods. Bending was accomplished by centrally loading the sample across the width with a 6 mm diameter plunger until maximum load had been

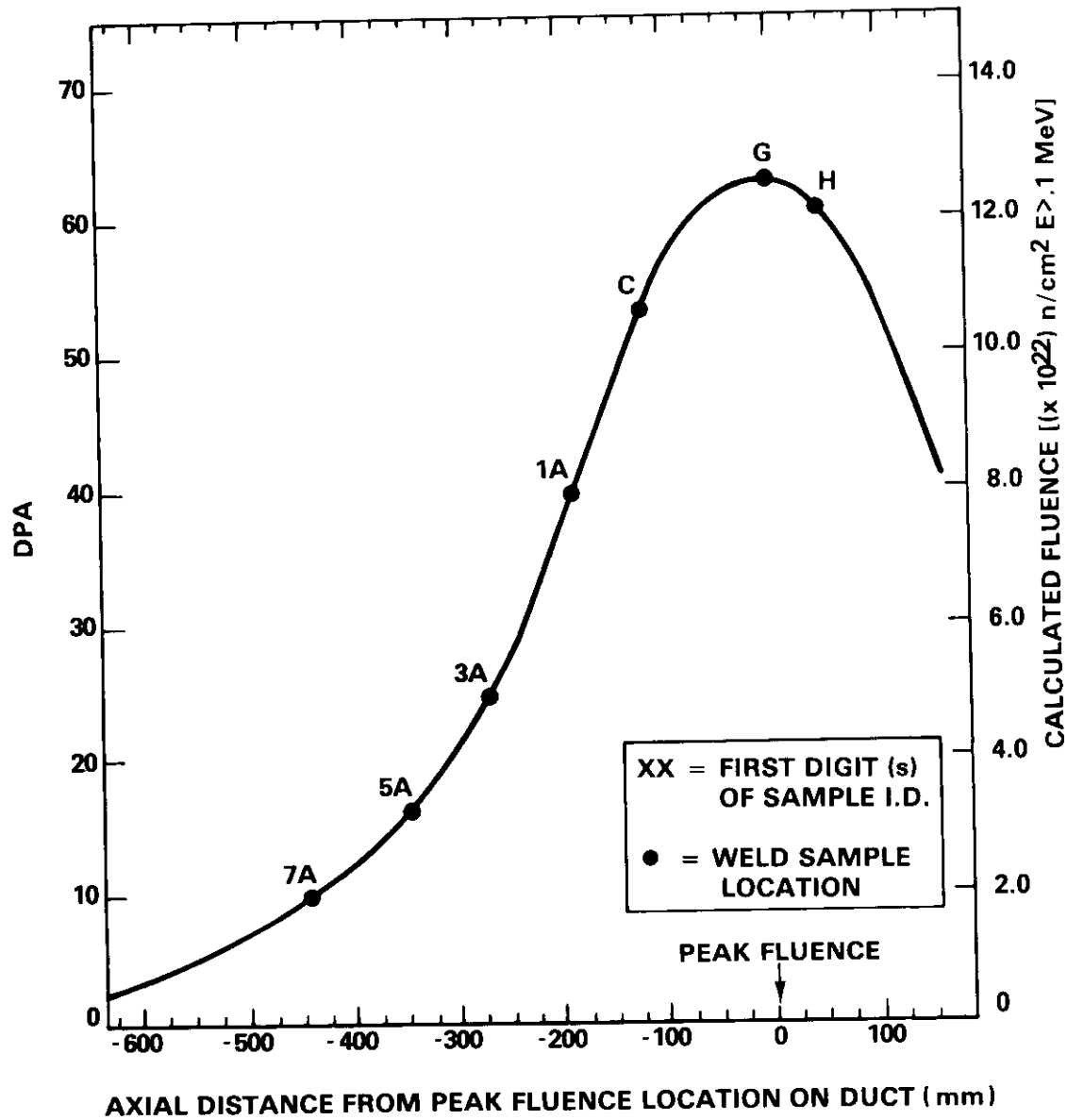

Figure 3.5.1 Axial Fluence Profile and Sample Location.

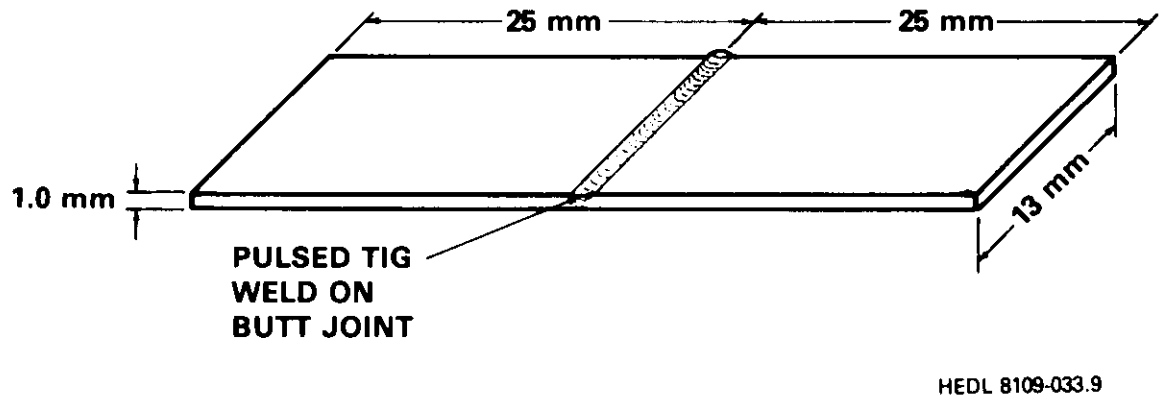

Figure 3.5.2 Weld Sample Configuration.

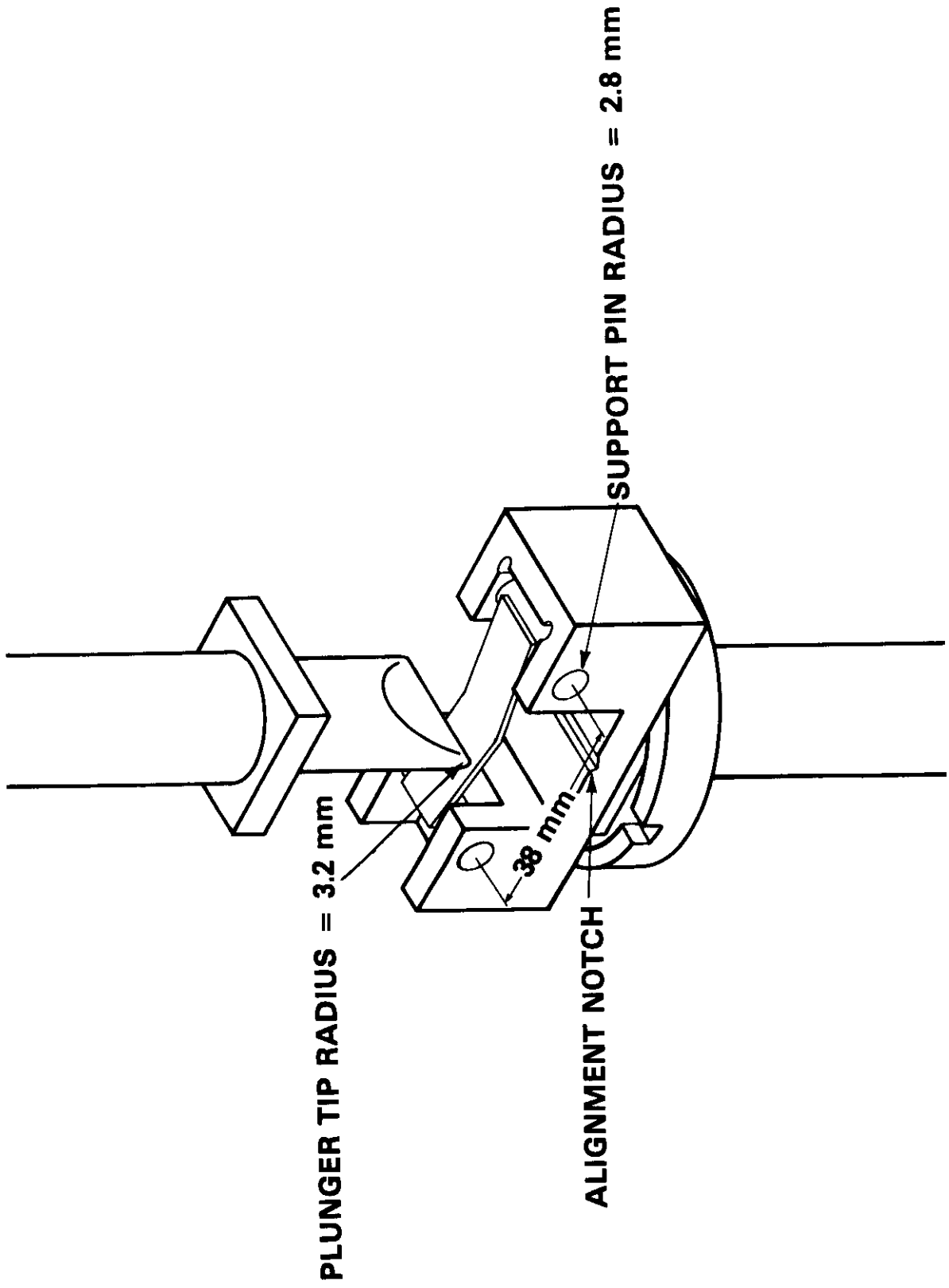

Figure 3.5.3 Bend Test Apparatus

attained. The tests were conducted at constant deflection rates of 8.5×10^{-4}, 8.5×10^{-3} and 8.5×10^{-2} mm/sec and temperatures of 400, 510. and 620°C. The different test conditions outlined in Table 1 were selected to determine the effects of sample fluence, test temperature and deflection rate on strength and ductility.

3.5.5 Results and Discussion

Weld bend testing of all 23 samples (Table 1) has been completed. Welds on samples from all fluence levels appeared sound and free from cracks. Bend testing of the weld samples produced bend angles greater than 90 degrees and no failures occured. The samples exhibit good ductility in tests both at the irradiation temperature and 100°C above the irradiation temperature. A quantitative analysis of the data is currently in progress.

3.5.6 Conclusions

Irradiated 20% CW 316 SS material can be welded even to high peak fluence levels of 12.6×10^{22} n/cm^2 (63 dpa) (E >.1 MeV). Bending of the weld samples through angles greater than 90 degrees did not produce any failures. The weld zone does not appear to become severely embrittled due to helium migration.

3.5.7 Future Work

The deflection versus load curves are being analyzed quantitatively to determine the relative effects of fluence, test temperature and deflection rate on strength and ductility. The actual bend angles of the weld bend samples will be taken from post-test photographs. Metallography will also be performed on selected samples in order to determine any microstructural effects.

3.5.8 References

1. Gold, et al, "Materials Technology for Fusion: Current Status and Future Requirements," Nuclear Technology/Fusion, Vol. 1,

TABLE 3.5.1

BEND TEST MATRIX

Sample I.D.	Calculated Fluence* (E >0.1 MeV)($\times 10^{22}$ n/cm^2)	Bend Test Conditions Temp. (°C)	Deflection Rate (mm/sec)
1A5b	7.83 (39 dpa)	400	8.5×10^{-2}
1A5c	7.83 (39 dpa)	620	8.5×10^{-3}
3A5f	4.89 (25 dpa)	400	8.5×10^{-2}
3A5g	4.89 (25 dpa)	620	8.5×10^{-3}
3A6h	4.89 (25 dpa)	620	8.5×10^{-3}
5A5i	3.21 (16 dpa)	400	8.5×10^{-2}
5A5j	3.21 (16 dpa)	400	8.5×10^{-2}
5A6k	3.21 (16 dpa)	620	8.5×10^{-2}
5A6l	3.21 (16 dpa)	510	8.5×10^{-2}
7A5m	1.94 (8 dpa)	400	8.5×10^{-2}
7A5n	1.94 (8 dpa)	400	8.5×10^{-2}
7A6o	1.94 (8 dpa)	620	8.5×10^{-3}
7A6p	1.94 (8 dpa)	400	8.5×10^{-2}
C1	10.65 (53 dpa)	400	8.5×10^{-2}
C2	10.65 (53 dpa)	620	8.5×10^{-2}
c3	10.65 (53 dpa)	620	8.5×10^{-3}
c4	10.65 (53 dpa)	620	8.5×10^{-4}
C5	10.65 (53 dpa)	620	8.5×10^{-1}
C6	10.65 (53 dpa)	400	8.5×10^{-2}
G5	12.59 (63 dpa)	400	8.5×10^{-2}
G6	12.59 (63 dpa)	620	8.5×10^{-3}
H5	12.15 (61 dpa)	400	8.5×10^{-2}
H6	12.15 (61 dpa)	400	8.5×10^{-3}

*All samples were irradiated at approximately 400°C.

April 1981.

2. Long, et al, EBR-II Spectral Parameters - Run 750, HEDL-TME 78-84, March 1979.

4. PATH B ALLOY DEVELOPMENT — HIGHER STRENGTH **Fe-Ni-Cr ALLOYS**

No contributions.

5. PATH C ALLOY DEVELOPMENT — REACTIVE AND REFRACTORY ALLOYS

5.1 MECHANICAL PROPERTY EVALUATIONS OF PATH C VANADIUM SCOPING ALLOYS - R. E. Gold (Westinghouse Electric Corporation)

5.1.1 ADIP Tasks

I.B.11. Stress-Rupture Properties of Reactive/Refractory Metal Alloys (Path C)

I.B.15 Tensile Properties of Reactive/Refractory Metal Alloys (Path C)

5.1.2 Objective

The objective of this program was to develop tensile and creep/stress-rupture data for the unirradiated Path C vanadium Scoping Alloys. In addition, methods have been developed for introducing controlled levels of non-metallic impurities into test specimens in order to examine their effects on mechanical properties.

5.1.3 Summary

Creep/stress-rupture tests were performed on sheet specimens of the three Path C vanadium Scoping Alloys in the temperature range 650 to 800°C. As expected, the V-15Cr-5Ti was strongest in creep, followed by VANSTAR-7 and V-20Ti. These tests represented over 12,000 hours of testing in the ultra-high vacuum creep test stands. In addition to the creep tests, a series of controlled non-metallic contamination exposures were carried out at 800°C. Oxygen was used as the contaminating specie for these tests which demonstrated the capability of an existing UHV microbalance system for introducing controlled levels of contaminants into the vanadium alloys. Fractographic analyses of both creep and tensile tested specimens are also presented.

5.1.4 Progress and Status

The Path C vanadium-base Scoping Alloys which were prepared for the

ETM Research Materials Inventory, sited at the Oak Ridge National Laboratory, are the subject of this evaluation. These include: (compositions in weight percent)

V-20Ti

V-15Cr-5Ti

VANSTAR-7 (V-9Cr-3.3Fe-1.2Zr-0.054C)

This program was initiated to develop the tensile and stress-rupture data base for the unirradiated alloys. Because non-metallic impurities are known to have significant effects on the mechanical behavior of refractory metal alloys, an additional objective of this program was to develop means to introduce controlled levels of impurities such as oxygen and nitrogen into mechanical property specimens.

Specific tasks associated with FY'81 efforts were:

Task 1. Material Procurement
Task 2. Initial Specimen Preparation and Heat Treatments
Task 3. Tensile Evaluations
Task 4. Creep/Stress-Rupture Testing
Task 5. Evaluation of the Effects of Non-Metallic Contamination on Mechanical Properties
Task 6. Microstructural Characterizations

All efforts on the FY'81 experimental program have been completed. The results of Tasks 1 through 3 have been previously reported,[1-2] and are not repeated here. The results of the creep/stress-rupture testing (Task 4) and the preliminary investigation of non-metallic contamination effects (Task 5) are reported here, as are the results of supporting microstructural characterizations (Task 6).

5.1.4.1 Material Identification and Condition

This information, including chemical analyses of the starting materials, pretest heat treatments, and test specimen design were provided in an earlier report.[2]

5.1.4.2 Creep/Stress-Rupture Testing (Task 4)

A series of creep/stress-rupture tests were conducted on the vanadium Scoping Alloys. The purpose of these tests was to provide baseline information on the OFE-ADIP Path C reference heats in order to have this data available for correlation with (1) previous creep data for these and similar vanadium-base alloys, and (2) creep test results to be performed in FY'82 on identical specimens containing intentional additions of oxygen and/or nitrogen.

All tests were conducted on materials in the fully recrystallized condition using ultrahigh vacuum ($<10^{-8}$ torr) test stands. Initial selections of stress were based on estimates of the stress required to produce rupture in approximately 1000 hours in the temperature range 650 to 800°C. These estimates were taken from a recent survey of mechanical property data for vanadium-base alloys.[3]

The results of the creep tests on the Scoping Alloys are summarized in Table 5.1.1. Plots of the strain vs. time data are presented in Figures 5.1.1 through 5.1.3 for V-20Ti, V-15Cr-5Ti, and VANSTAR-7, respectively. In Table 5.1.1, note that for several specimens the stress which was selected was much too low to cause appreciable creep strain in the 500-2000 hour test times which were available for this program in FY'81. Hence, it was necessary to increase the applied stress in order to accelerate the deformation process. The points at which these changes were made are also indicated in Figures 5.1.1 through 5.1.3. In one instance (VANSTAR-7, Specimen 17), because the test stand was of a design which permitted only internal (i.e. in the UHV chamber) loading, the applied stress could not be altered and a decision was made to change the test temperature instead.

Note that, almost without exception, the stresses selected at any given temperature for these tests were low. That is, the present Path C vanadium-base alloys are stronger than the comparable alloys for which data have been reported in the literature. This probably reflects the higher base levels of C, O, and N in the current heats.

TABLE 5.1.1 Summary of Creep/Stress-Rupture Test Data for the Path C Vanadium-Base Scoping Alloys

Alloy	Specimen Number	Temp. (°C)	Applied Stress (MPa)	Applied Stress (ksi)	Time (hrs) (a)	Cumul. Strain. (%)	Final Pressure	
V-20Ti	15	650	148	21.5	1158	(0.02)	1.2×10^{-8}	No rupture
	(Cont'd)	650	218	31.6	2968	50.7	2.0×10^{-9}	
V-20Ti	16	650	276	40	800	34.5	1.2×10^{-9}	
V-20Ti	17	750	172	25	282	(47.7)	1.4×10^{-8}	No Rupture
V-15Cr-5Ti	15	650	414	60	1055	(0.5)	7.4×10^{-9}	No Rupture
V-15Cr-5Ti	16	800	276	40	629	22.5	6.8×10^{-9}	
V-15Cr-5Ti	17	750	368	53.3	115	13.8	2.8×10^{-8}	
V-15Cr-5Ti	18	750	345	50	327	22.4	2.6×10^{-9}	
VANSTAR-7	15	650	276	40	1261	(0.11)	-N.A.-	No Rupture
	(Cont'd)	650	331	48	1671	(0.52)	1.4×10^{-8}	No Rupture
VANSTAR-7	16	750	207	30	2192	(1.02)	2.8×10^{-9}	No Rupture
	(Cont'd)	750	241	35	2428	19.3	2.6×10^{-9}	
VANSTAR-7	17	700	276	40	1200	(0.12)	4.2×10^{-9}	No Rupture
	(Cont'd)	750	276	40	1733	14.8	4.6×10^{-9}	

(a) When a test was continued at a second stress or temperature, the time shown is cumulative.

N.A. - Not Available

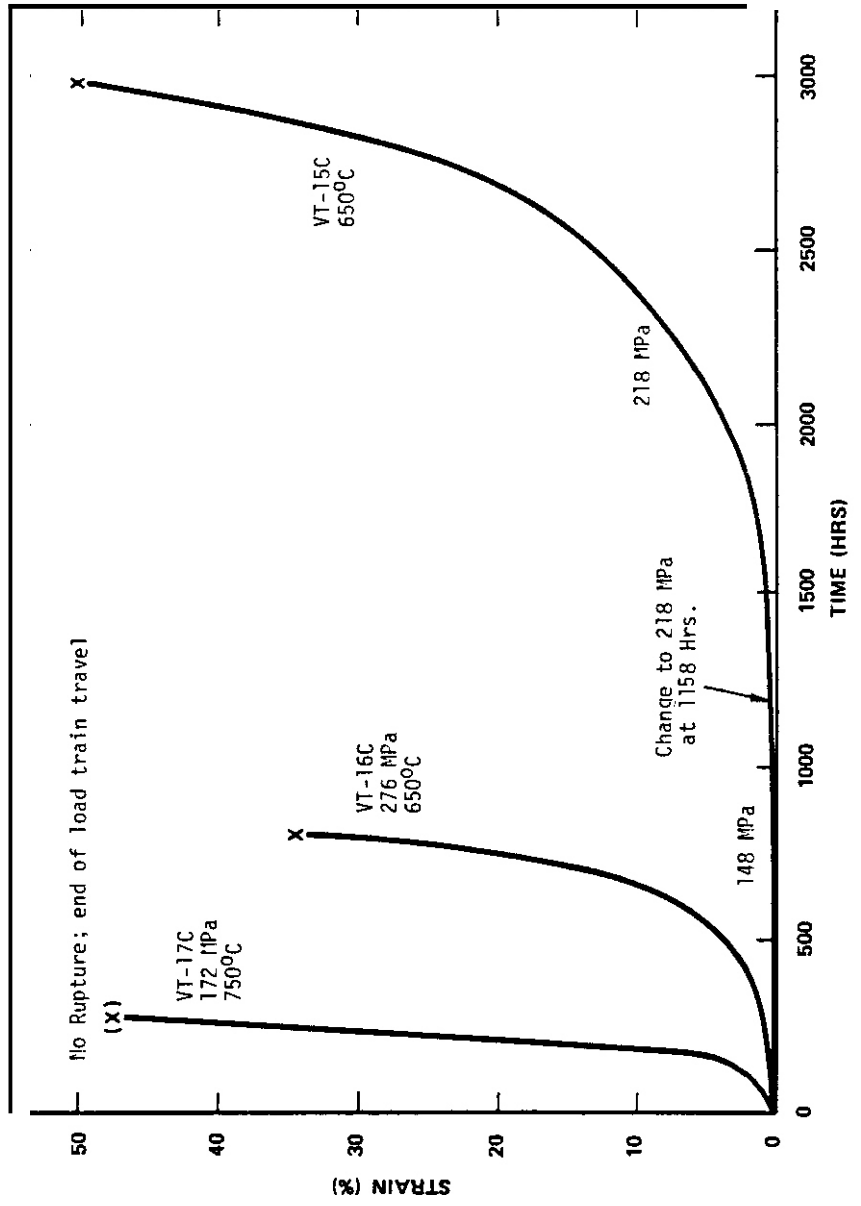
No Rupture; end of load train travel
(X)
VT-17C
172 MPa
750°C
VT-16C
276 MPa
650°C
148 MPa
Change to 218 MPa
at 1158 Hrs.
VT-15C
650°C
218 MPa
STRAIN (%)
TIME (HRS)
0
10
20
30
40
50
500
1000
1500
2000
2500
3000

F 5.1.1 Data V i

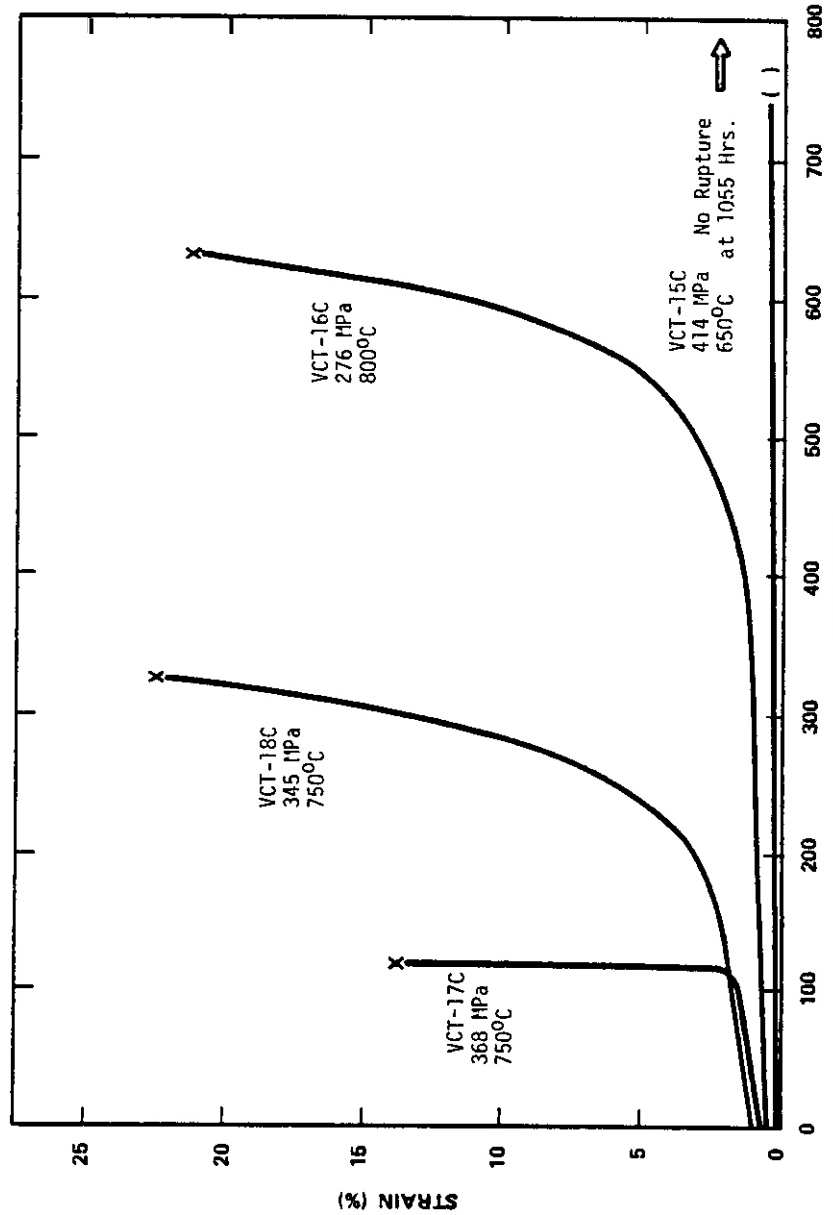

Figure 5.1 2 Test the V-15Cr-5Ti Alloy

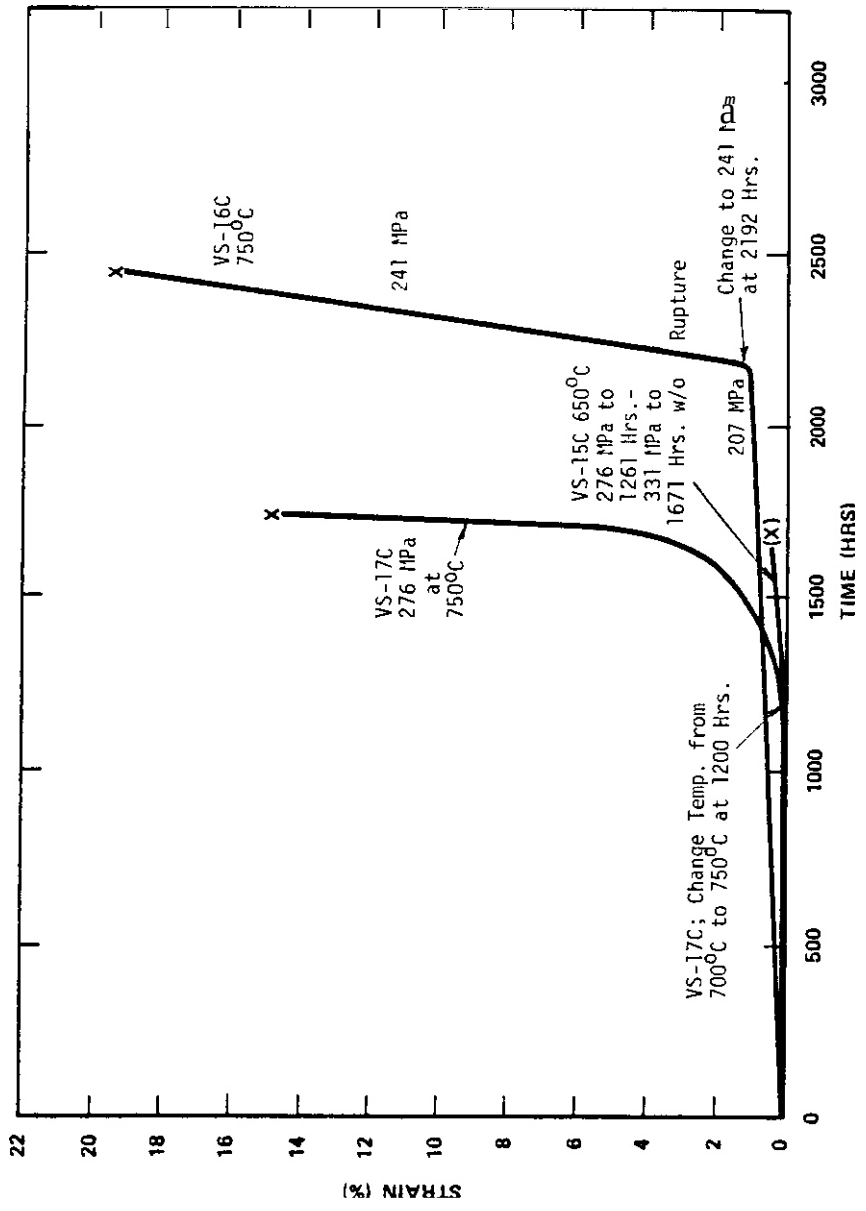

5.1.3 ting for the Al

The complicated time-temperature-stress histories would make it extremely difficult to infer meaningful mechanical property/performance data from these tests. This, however, was not their purpose. These tests have, however, been useful in establishing the approximate time-dependent mechanical strength of the current alloys. This data will be important for selecting test conditions and providing correlation information for mechanical property tests to be conducted in FY'82 on intentionally contaminated specimens of these alloys. Hopefully, it will be possible in the future to conduct more extensive creep/stress-rupture tests to define more completely the time-dependent mechanical response of these alloys.

Selected specimens from these creep-rupture tests were examined in a scanning electron microscope (SEM) in order to characterize the fracture surfaces. These results were part of Task *6* and are reported in Section *5.1.4.4.*

5.1.4.3 Controlled Non-Metallic Contamination Experiments (Task *5)*

An ultrahigh vacuum microbalance system was used to introduce controlled levels of non-metallic impurities into vanadium alloy specimens. This system, depicted schematically in Figure *5.1.4,* is constructed of stainless steel and quartz with copper gasket seals; it is completely bakeable with the exception of the microbalance. The UHV microbalance system was assembled previously for studies of gas-metal reactions between the refractory metals and their alloys and reactive gases such as oxygen and nitrogen.[4] During the FY'81 research period, the system was reassembled and used to perform preliminary "demonstration-of-capability''experiments on the vanadium-base alloys of interest to the present program.

Six (6) contamination experimental runs were carried out; two specimens of each of the three Scoping Alloys were exposed. In view of the fact that these exposures were intended only to establish capability for future evaluations of the effects of non-metallic contaminants on mechanical properties, the number of test variables were minimized by selecting a single reaction temperature (800°C) and using only oxygen as the reacting gas specie.

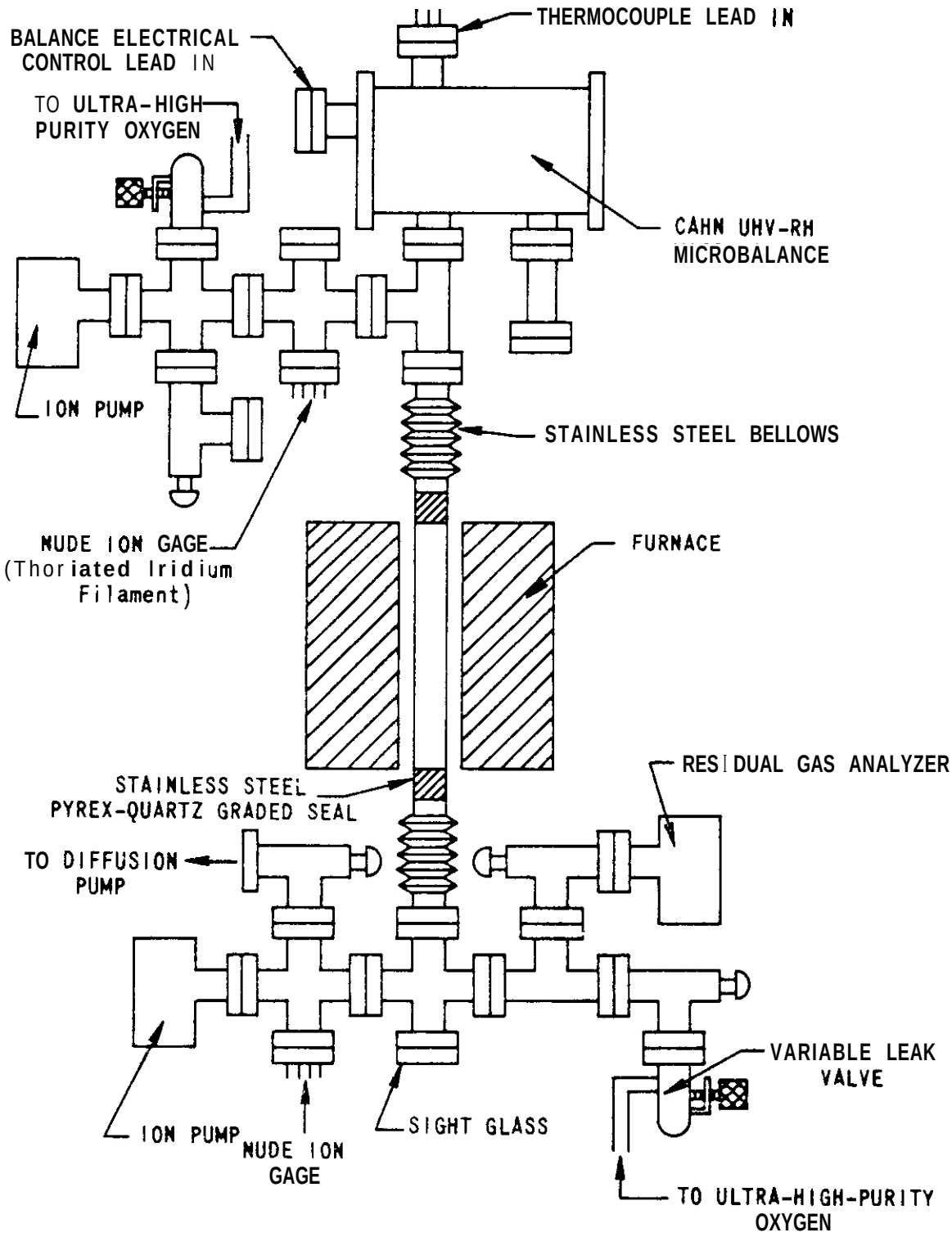

Figure 5.1.4 Ultra High Vacuum Microbalance System for Gas-Metal Reaction Studies

The following is a brief description of the specimen preparations and test procedures:

- Specimens, approximately 20 cm^2 total surface area, were cut from 0.76 mm thick sheet.

- A 0.5 mm diameter hole was drilled near one end.

- Specimens were degreased, etch-cleaned, and given one hour recrystallization heat treatments of:

V-20Ti	1100°C
V-15Cr-5Ti	1200°C
VANSTAR-7	1350°C

- A Pt suspension wire, fitted with a 20 cm long quartz rod at the specimen end, was used to suspend the specimens in the reaction chamber.

- A Type S (Pt-10Rh) thermocouple was suspended at the specimen location in order to measure the reaction temperatures.

- The microbalance was calibrated.

- Evacuation was carried out, using an external turbomolecular pump and, ultimately, an ion pump. A twenty-four hour bakeout at 250°C completed experimental preparations.

- Temperature was increased to 800°C and allowed to stabilize.

- High purity oxygen (Matheson; minimum purity of 99.99%) was admitted to a preselected partial pressure through a calibrated leak valve.

- Reaction continued until a preselected mass gain was noted by the microbalance, which was used to continuously monitor the specimen mass.

- Temperature was decreased; oxygen flow was terminated.

- Specimen was removed and replaced.

The results of the six exposure runs are summarized in Table 5.1.2. Included are the oxygen contamination levels in weight ppm, as determined both by in-situ microbalance measurements during the contamination experiments and by post-exposure chemical analyses. The latter analyses were performed at the Oak Ridge National Laboratory using a neutron activation technique[5]; concentrations are believed to be accurate within approximately ±100 wppm oxygen. Reference to Table 5.1.2 indicates that, with the exception of one of the VANSTAR-7 specimens (Number 2), the agreement between the measured/weighed values and the analyzed values is within this limit of accuracy. There is no obvious explanation for the discrepancy observed in the VANSTAR-7 specimen 2 value. The analyzed values in Table 5.1.2 are for single analyses; repeat analyses are currently underway, as are selected analyses for nitrogen content. The nitrogen analyses should provide some indication of whether uncontrolled or accidental atmospheric (air) contamination occurred during (or after) the oxygen exposures.

These test exposures, while not providing absolute or definitive results, have been sufficient to establish that the UHV microbalance apparatus is capable of being used for the introduction of controlled levels of non-metallic contaminants into vanadium-base alloys.

5.1.4.4 Microstructural Characterizations (Task 6)

Microstructural characterizations of the vanadium alloy specimens tested in FY'81 were limited to fractographic examinations with scanning electron microscopy (SEM). Initially, TEM examinations were also planned;

TABLE 5.1.2 Results of 800°C Oxygen Exposures with Vanadium-Base Scoping Alloys

Alloy	Specimen Number	Mass (g)		Δ Mass (μg)	Exposure Time (hrs)	Oxygen Pickup (wppm)		
		Initial	Final			Target	Meas.(a)	Analyzed(b)
V-20Ti	1	4.7003	4.7034	3100	0.5	600	660	764
	2	4.7310	4.7370	6000	1.3	1000	1267	1147
V-15Cr-5Ti	1	5.2026	5.2059	3300	0.43	600	634	589
	2	5.0650	5.0706	5600	1.6	1000	1104	1024
VANSTAR-7	2	4.9475	4.9519	4400	0.4	600	890	1206
	3	4.8466	4.8515	4900	2.1	1000	1010	1031

(a) Measured via microbalance during oxygen exposures.

(b) Measured by chemical analyses using neutron activation technique. (Ref. 5)

limitations of both time and funding precluded these efforts.

Examination of fracture surfaces of tensile and creep tested specimens revealed no surprises. The surfaces were generally typical of those seen for ductile fractures; this was expected from the tensile elongation values published previously[2], and the rupture strain values presented in Table 5.1.1 of this report. Specific examples of these results are presented below.

V-20Ti. The fracture surface of a specimen tensile tested at 500°C is shown in Figure 5.1.5. The fracture appearance of specimens tested under constant loading conditions (creep) at 650°C is quite similar except for the occasional presence of larger voids or cavities which are typical of specimens tested to failure at high creep strains, Figure 5.1.6.

V-15Cr-5Ti. Under certain test conditions, the fracture surfaces of specimens of this alloy exhibited a mixed mode of fracture. For example, Figure 5.1.7 shows an area of mixed ductile and cleavage fracture in a specimen tested at room temperature. The total elongation of this specimen was 27.7% after 22.4% uniform deformation. At 750°C, there was less evidence of cleavage following tensile testing, Figure 5.1.8. The fracture surface of a creep specimen which ruptured in 327 hours at an applied stress of 345 MPa is shown in Figure 5.1.9. The fracture surface is typical of a ductile failure; the rupture strain was 22.4%.

VANSTAR-7. The fracture surfaces of VANSTAR-7 alloy specimens tensile tested over the range of temperatures from room temperature to 750°C displayed uniformly dimpled rupture over the entire fracture surface. This is shown in Figure 5.1.10 for a specimen tested at 700°C. The two specimens which were creep tested to rupture at 700-750 C showed similarly ductile fracture features.

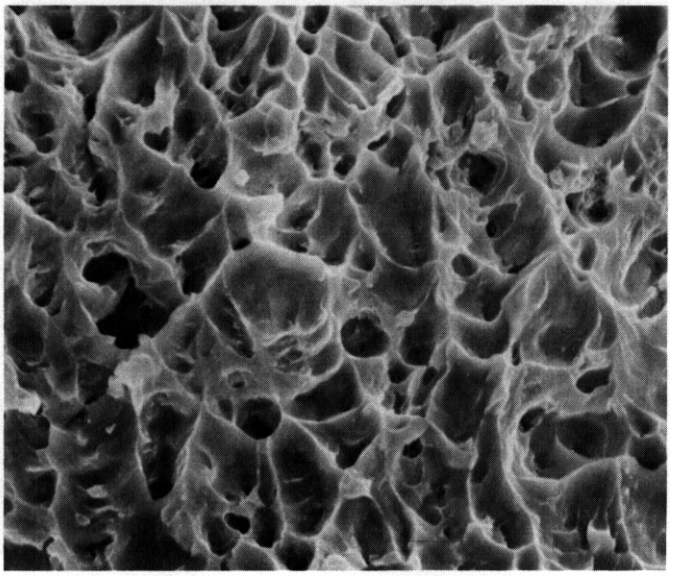

YT-3T 17.4% 1000X

Figure 5.1.5 SEM Micrograph of V-20Ti Tensile Tested at 500°C

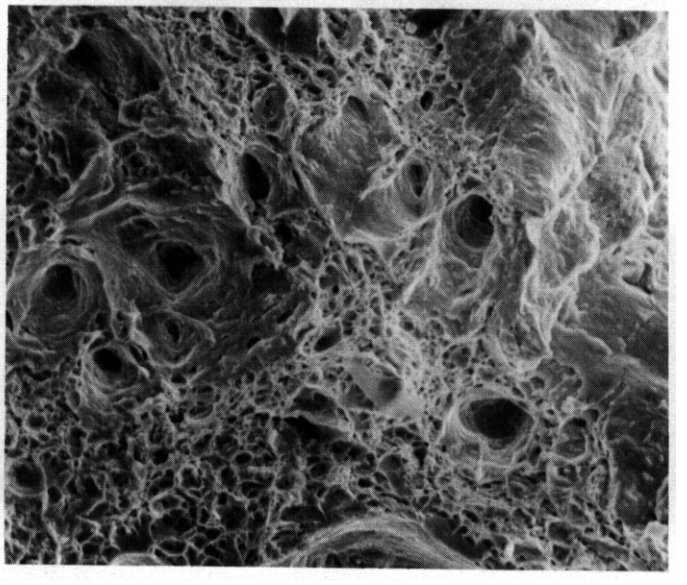

VT-16C 34.5% 300X

Figure 5.1.6 SEM Micrograph of V-20Ti Creep Tested at 650°C at an Applied Stress of 276 MPa

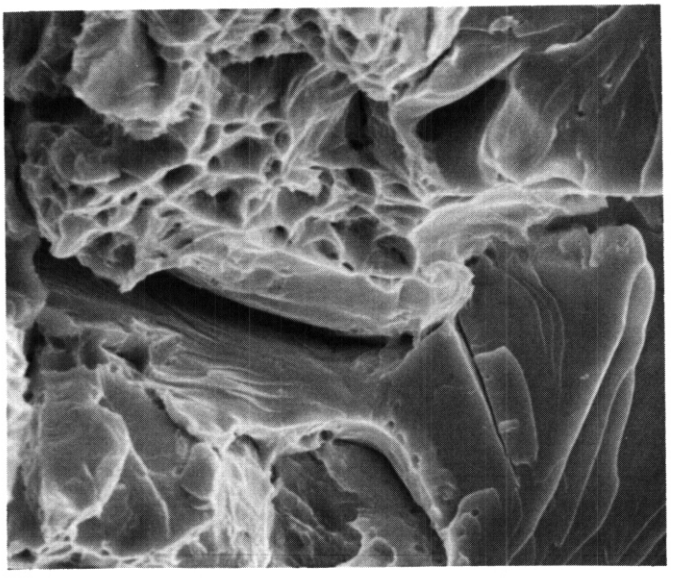

VCT-2T 27.7% 1000X

Figure 5.1.7 SEM Micrograph of V-15Cr-5Ti Tensile Tested at Room Temp.

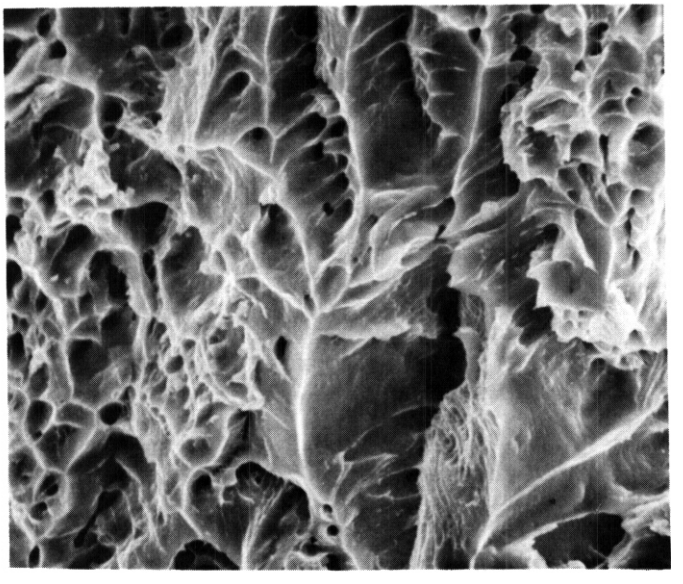

VCT-30T 16.1% 1000X

Figure 5.1.8 SEM Micrograph of V-15Cr-5Ti Tensile Tested at 750°C

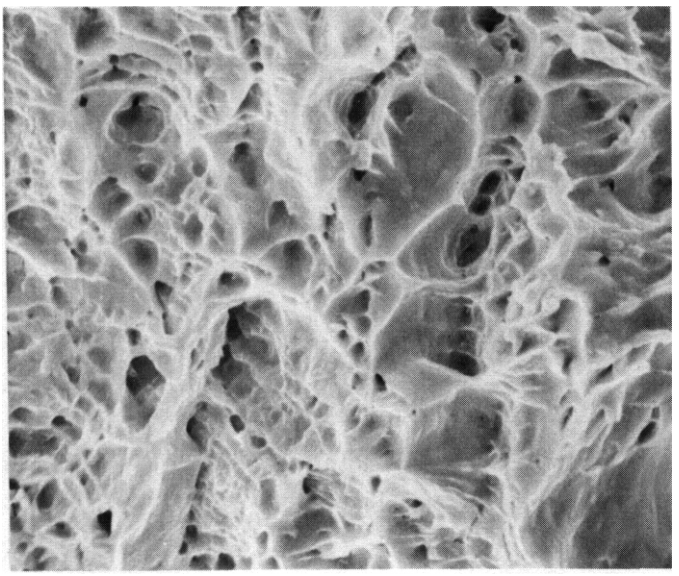

VCT-18C 22.4% 1000X

Figure 5.1.9 SEM Micrograph of V-15Cr-5Ti Creep Tested at 750°C at an Applied Stress of 345 MPa

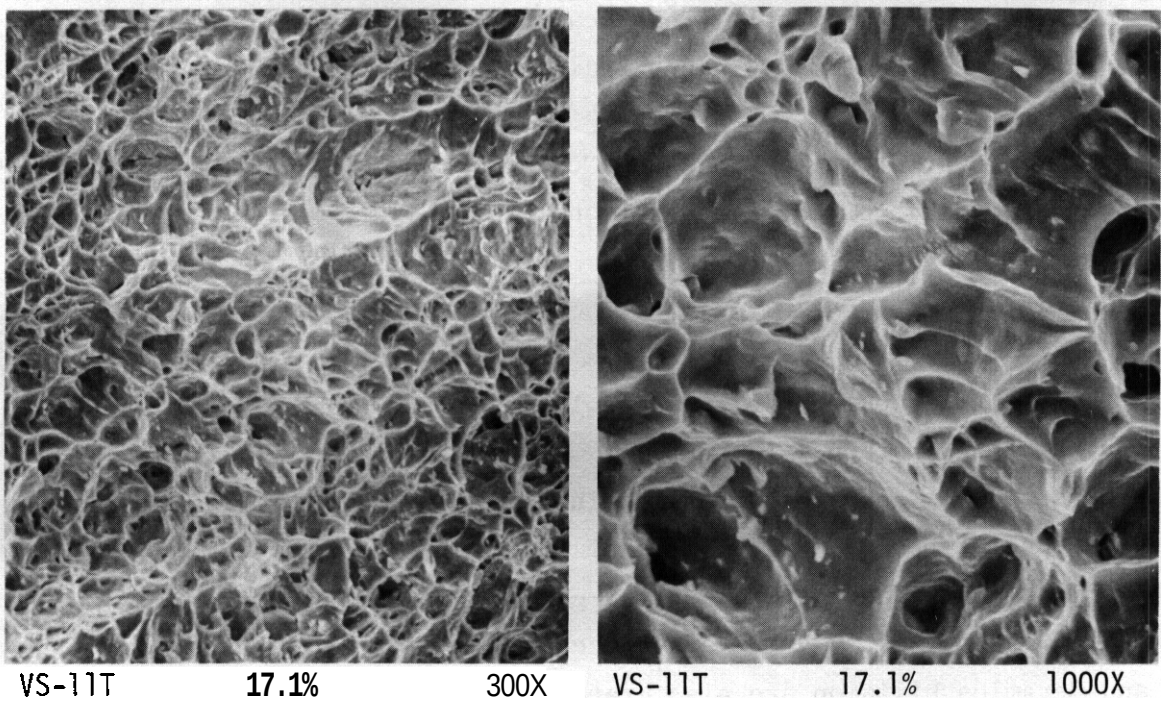

VS-11T 17.1% 300X VS-11T 17.1% 1000X

Figure 5.1.10 SEM Micrograph of VANSTAR-7 Tensile Tested at 700°C

5.1.5 References

1. R. E. Gold and R. L. Ammon, "Mechanical Property Evaluations of Path C Vanadium Scoping Alloys," Alloy Development for Irradiation Performance, Qtrly. Progress Report for Period Ending December 31, 1980, DOE/ER-0045/5, p. 92 (April 1981).

2. R. E. Gold and R. L. Ammon, "Mechanical Property Evaluations of Path C Vanadium Scoping Alloys," Alloy Development for Irradiation Performance, Qtrly. Progress Report for Period Ending March 31, 1981, DOE/ER-0045/6, p. 96 (July 1981).

3. D. L. Harrod and R. E. Gold, "Mechanical Properties of Vanadium and Vanadium-base Alloys," International Metals Reviews, 1980, No. 4, **163-221.**

4. G. A. Whitlow, R. A. Nadler, and R. C. Svedberg, "Vanadium Alloy Cladding Development: Final Report", WARD-3791-47, Westinghouse Advanced Reactors Division, Madison, PA (November 1970).

5. "Oxygen Determination by Fast Neutron Activities," Communication from J. E. Strain of Oak Ridge National Laboratory, November 4, 1981.

Acknowledgements

The author would like to acknowledge the support of J. E. Strain of the Oak Ridge National Laboratory, who performed the neutron activation analyses of oxygen concentrations in the contaminated specimens, and R. Crouse of the Oak Ridge National Laboratory, who performed the SEM examinations. The cooperation and general support of E. E. Bloom, F. W. Wiffen, and J. H. DeVan of the Oak Ridge National Laboratory Metals and Ceramics Division are also gratefully acknowledged.

5.2 FATIGUE BEHAVIOR OF UNIRRADIATED VANADIUM ALLOYS — K. C. Liu (Oak Ridge National Laboratory)

5.2.1. ADIP Task

ADIP Task I.B.3, Fatigue Crack Growth in Reactive and Refractory Alloys.

5.2.2 Objective

The objective of this work is to develop baseline fatigue and crack growth data for unirradiated Path C refractory metal scoping alloys.

5.2.3 Summary

A simple two-term power law was used to fit the strain controlled fatigue data obtained for unirradiated V—15% Cr—5% Ti at room temperature, 550, and 650°C. Comparisons were then made between data generated on this alloy at 550°C and similar data obtained on 20%-cold-worked type 316 stainless steel at the same temperature. This comparison showed the vanadium alloy to have a similar low cycle fatigue life at less than 10,000 cycles but a superior resistance to fatigue damage at higher cyclic lives. The general data trend for this alloy suggested an endurance limit at strain ranges of approximately 0.7 and 0.6% at 550 and 650°C, respectively. Limited testing of VANSTAR-7 indicates fatigue properties slightly inferior to the V—15% Cr—5% Ti alloy.

5.2.4 Progress and Status

5.2.4.1 Fatigue Testing of V—15% Cr—5% Ti

As reported previously,' some problems have been encountered with thermocouple- (spot weld) or thread-induced premature failure of the specimens in regions out of the gage section. A critical realignment of the load columnm was therefore performed using a set of grip alignment jigs specially designed and fabricated for use inside the vacuum chamber. Subsequently, two tests were conducted on V—15% Cr—5% Ti at 550 and 650°C.

The first specimen (AV-521) was cycled at a strain range of 0.8% at 550°C. The test ended in a normal failure at about 600,000 cycles. The

fatigue life fell closely on the 550°C curve established earlier, as shown in Fig. 5.2.1. However, a second test (AV-523) at 650°C ended with a fracture at the specimen shoulder near a thermocouple spot weld. In the latter test, the thermocouple was being used to recalibrate the temperature profile of the test specimen, since a larger induction heating

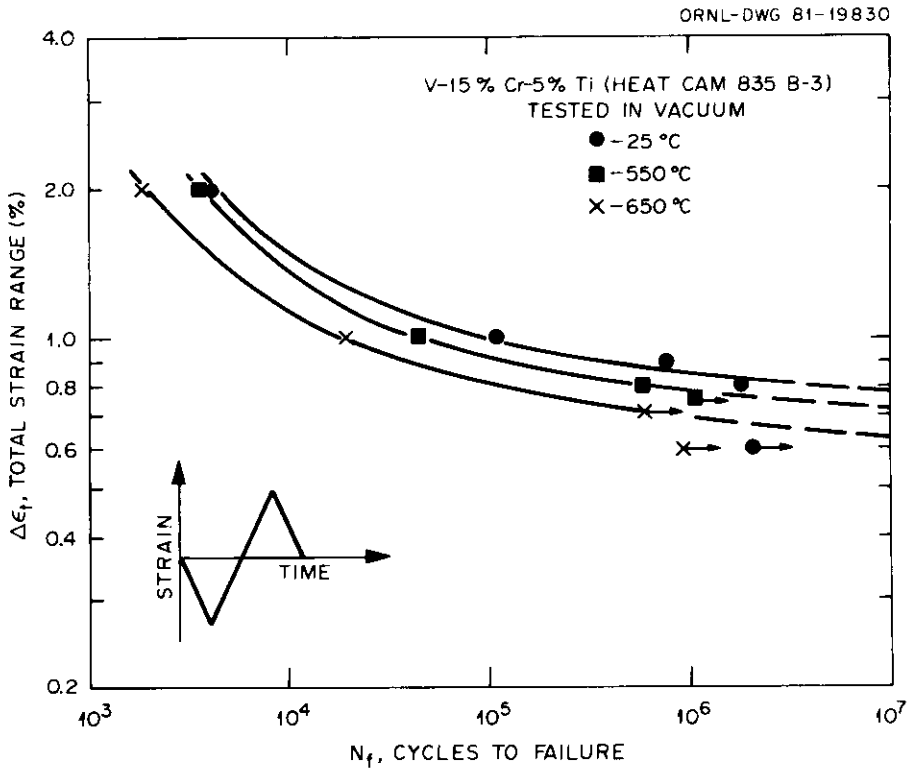

Fig. 5.2.1. Cyclic Fatigue Data for V—15% Cr—5% Ti Tested at 25, 550, and 650°C in Vacuum.

coil was being used. The recurrence of crack initiation at the thermocouple reinforces earlier observation that the alloy is sensitive to stress risers in high-cycle, elevated temperature fatigue. Vacuum fatigue lifetime data on V—15% Cr—5% Ti are summarized in Table 5.2.1 and plotted in Fig. 5.2.1. The plot indicates that a power law relationship between the total strain range and cycles to failure is appropriate. The following equation was used in the analysis of the data:

$$\Delta\varepsilon_t = AN_f^{-\alpha} + BN_f^{-\beta} , \qquad (1)$$

where

$\Delta\varepsilon_t$ = total strain range in %,

N_f = number of cycles to failure, and

A, B, α, and β = material constants.

The values of the material constants that yield the curves fitting the data in Fig. 5.2.1 are tabulated in Table 5.2.2.

Table 5.2.1. Fatigue Lifetime Data for Annealed V–15% Cr–5% Ti Tested in Vacuum

Specimen[a]	Test temperature (°C)	Total strain (%)	Maximum total cyclic stress range, $\Delta\sigma$ (MPa)	Cycles to failure	Mode of test control[b]	Comments
AV–53	27	2.0	1,340	4,345	SC	
AV–51	27	1.0	1,200	109,125	SC	
AV–515	23	0.9	1,074	781,200	SCILC	
AV–520	20	0.8	922	1,860,000	SCILC	
AV–52	27	0.6	830	>2,047,020	SCILC	c
AV–510	550	2.0	1,240	3,783	SC	
AV–58	550	1.0	1,080	43,555	SC	
AV–521	550	0.8	951	<600,000	SC	
AV–511	550	0.75	920	>1,072,410	SCILC	d
AV–54	650	2.0	1,228	1,874	SC	
AV–56	650	1.0	1,080	19,452	SC	
AV–523	650	0.7	786	>572,882	SC	d
AV–57	650	0.6	717	>951,302	SCILC	d

[a] All specimens were annealed 1 h at 1200°C in vacuum.

[b] SC = strain control with strain rate of 4×10^{-3}/s; SC/LC = strain control, transferred to load control with strain rate of 4×10^{-2}/s when the response becomes elastic.

[c] Specimen did not fail; test discontinued.

[d] Specimens ruptured outside the gage section.

The vanadium alloy data are compared in Fig. 5.2.2 to recently obtained 550 and 650°C vacuum fatigue data on 20%–cold–worked type 316 stainless steel. The vanadium alloy data fell within the scatter band of

Table 5.2.2. Materials Constants for Eq. (1) Describing the Fatigue Behavior of Annealed V—15% Cr—5% Ti

Temperature				β
25	1.67	0.048	6208	1.055
550	1.54	0.048	1432	0.887
650	1.66	0.061	1170	0.948

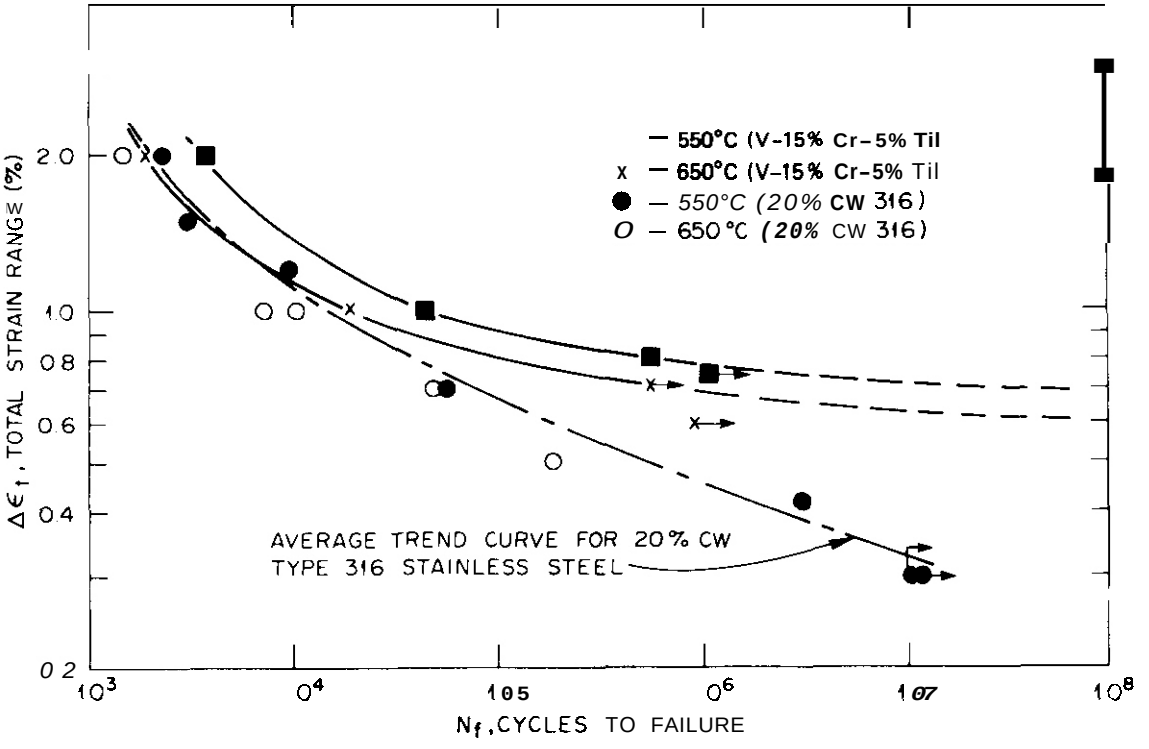

Fig. 5.2.2. Comparison of Fatigue Behavior of 20%-Cold-Worked Type 316 Stainless Steel Tested at 550 and 650°C with V—15% Cr—5% Ti Tested at 550 and 650°C.

stainless steel data in the low cycle range (life below 10^4 cycles). However, at strain ranges below about 0.8% the vanadium alloy exhibited superior fatigue behavior to the stainless steel, which showed an apparent endurance limit at 0.35% strain range.

The additional tests at 550 and 650°C support earlier observation that this alloy has an apparent endurance limit in terms of total strain range of about 0.7 and 0.6% at 550 and 650°C, respectively.

5.2.4.2 Fatigue Testing of VANSTAR-7

Eleven additional tests on VANSTAR-7 bring the total number of completed tests to 16. The fatigue lifetime data are summarized in Table 5.2.3 and plotted in Fig. 5.2.3. To facilitate comparison, the power law equations obtained for V-15% Cr-5% Ti are also plotted in Fig. 5.2.3. All VANSTAR-7 data fell consistently below the curve for V-15% Cr-5% Ti at the corresponding test temperature.

Table 5.2.3. Fatigue Lifetime Data for Annealed VANSTAR-7 Tested in Vacuum

Specimen[a]	Test temperature (°C)	Total strain (%)	Maximum total cyclic stress range, $\Delta\sigma$ (MPa)	Cycles to failure	Mode of test control[b]
VS-713	20	2.0	1,282	3,050	SC
VS-72	20	1.0	1.172	29,344	SC
vs-73	25	0.8	958	<290,000	SC
vs-74	25	0.7	869	2,397,240	SC/LC
VS-712	550	2.0	1,131	1,527	SC
VS-76	550	1.0	958	31,703	SC
vs-77	550	0.8	923	65,412	SC
VS-719	550	0.8	952	49,910	SC
VS-721	550	0.8	924	75,406	SC
VS-715	550	0.7	814	110,656	SC
VS-716	550	0.7	855	112,112	SC
vs-75	650	2.0	1,103	1,703	SC
VS-71	650	1.0	930	8,938	SC
vs-79	650	0.8	923	39,076	SC
VS-710	650	0.7	786	142,037	SC
VS-711	650	0.6	703	174,580	SC/LC

[a] All specimens were annealed 1 h at 1400°C in vacuum.

[b] SC = strain control with strain rate of 4×10^{-3}/s; SC/LC = strain control, transferred to load control with strain rate of 4×10^{-2}/s when the response becomes elastic.

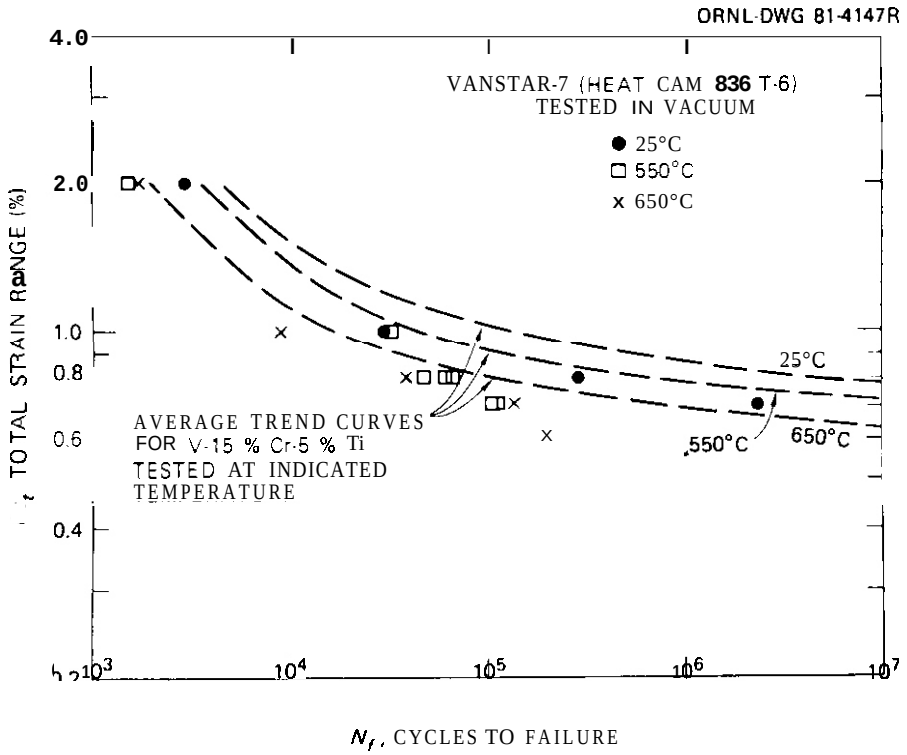

Fig. 5.2.3. Cyclic Fatigue Data for VANSTAR-7 Tested at Room Temperature, 550, and 650°C in Vacuum. Power law equations for V-15% Cr-5% Ti are plotted for comparison.

Unlike the room temperature data, which fell systematically between the 550 and 650°C curves for the V-15% Cr-5% Ti alloy, there are some apparent anomalies in the elevated temperature data for the VANSTAR-7. Since these tests were conducted before the recent realignment of the load column, a final evaluation of these data, in particular those tested in the high-cycle range ($\Delta\varepsilon_t < 0.8\%$) will be deferred until a few more tests at the lower strain range are completed.

A preliminary examination appears to indicate that the cyclic fatigue properties of VANSTAK-7 at 550 and 650°C are about the same. However, VANSTAR-7 shows fatigue resistance inferior to V-15% Cr-5% Ti tested under the same conditions.

5.2.5 Reference

1. K. C. Liu, "Fatigue Behavior of Path C Vanadium Scoping Alloys," *ADIP Quart. Prog. Rep. Dec. 31,* 1980, DOE/ER-0045/5, pp. 98-102.

5.3 THE EFFECT OF 70°C IRRADIATION ON THE TENSILE PROPERTIES OF VANSTAR-7 — F. W. Wiffen (Oak Ridge National Laboratory)

5.3.1 ADIP Task

ADIP Task I.B.15, Tensile Properties of Reactive and Refractory Alloys.

5.3.2 Objective

This experiment was designed to determine the rate of strengthening and ductility change during irradiation of a vanadium alloy at the lowest practical application temperature. Alloy VANSTAR-7 was selected for irradiation at about 70°C in the HFIR reactor. Tensile tests at 25°C and fractography were used to evaluate the effects of irradiation on the properties of interest.

5.3.3 Summary

Irradiation of VANSTAR-7 at about 70°C, followed by tensile tests at 25°C, has shown that plastic instability occurs in this alloy as it does in many other bcc alloys. Plastic instability, which results from dislocation channeling, occurs for displacement damage levels of 0.01 dpa or greater and limits the uniform tensile elongation to about 0.1%. Irradiation strengthening has not yet saturated at a damage level of 1 dpa. Total elongation is still greater than 2% at this damage level, and the fracture mode is fully ductile.

5.3.4 Progress and Status

5.3.4.1 Introduction

The reduction of uniform elongation to near zero by the early onset of plastic instability in irradiated bcc metals and alloys has been observed in a number of systems.[1,2] This behavior is characterized by the shape of a load-elongation curve produced in a tensile test, which indicates that the maximum load-carrying capacity is reached at less than 0.5% plastic elongation. The load drops rapidly with increasing deformation. Materials that deform in this manner exhibit a fully ductile fracture appearance.

Plastic instability has been observed for only relatively low irradiation temperatures, temperatures below which voids form. At these temperatures the dominant microstructural effect of the irradiation is a high concentration of small dislocation loops. These loops are very effective in raising the yield strength of the material, but once deformation is initiated these loops are swept up by glide dislocations. The result is both a "softened" pathway for further deformation and little or no ability of the matrix to work harden.

Radiation hardening and plastic instability in unalloyed vanadium has been reported by Smolik and Chen[3] and Shiraishi et al.[4] No vanadium-base alloys have been examined under conditions that would be expected to produce this deformation mode.

5.3.4.2 Experimental

Sheet tensile samples of VANSTAR-7 were machined from the HSV-309 heat of the alloy produced by the Westinghouse Corporation. The composition of this heat of VANSTAR-7 is

Element	Wt %
V	Balance
Cr	9.4
Fe	3.3
Zr	1.2
C	0.064
O	0.063
N	0.0088

The machined samples were annealed for 1 h in vacuum at 1200°C to produce full recrystallization. The reduced gage section of the samples was 0.76 × 1.52 x 2.0 mm long.

Samples to be irradiated were sealed into aluminum irradiation capsules, two samples per capsule, with extra space filled with aluminum powder and helium at about 0.1 MPa (1 atm). These capsules were irradiated in the HFLR hydraulic tube. The capsules were immersed in the reactor cooling water at about 55°C during irradiation. The specimen temperature during irradiations was estimated to be near 70°C. The total flux at the irradiation position was 3.25 x 10^{19} neutrons/(m^2·s), the fast flux 6.2 × 10^{18} neutrons/(m^2·s).

Postirradiation tests were conducted on an Instron machine. Strain values were calculated from the crosshead motion. All tests were conducted at hot cell ambient temperature, near 25°C.

5.3.4.3 Results

The tensile data generated in this experiment are listed in Table 5.3.1. Typical load–elongation curves are shown in Fig. *5.3.1,* and the strength and ductility properties are given as functions of fluence in Figs. *5.3.2* and *5.3.3.*

The tensile curves (Fig. *5.3.1)* show that both the yield strength and ultimate tensile strength of VANSTAR–7 have increased monotonically with increasing dpa over the fluence range examined. The increase in yield strength is much more rapid than the increase in ultimate strength, with the result that the uniform elongation decreases to zero as the two measures of strength become equal.

There is no indication in this data set that the irradiation hardening has saturated. In fact, comparison with results on a specimen irradiated to *9.3* dpa at *496°C* and then tested at *25°C* shows that VANSTAR–7 can be hardened well beyond the strength level reached by irradiation to 1 dpa at *70°C.* This comparison does not infer that either the hardening mechanism is the same for the two irradiation temperatures or that the maximum achievable strength level should be the same for the two cases. The strength data, given as a function of damage level in Fig. *5.3.2,* shows a simple dependence of the ultimate strength on fluence for the material irradiated at 70°C. However, an approximate extrapolation of this data passes below the strength achieved by the higher temperature irradiation.

Both the uniform and total tensile elongation are reduced by the irradiation (Fig. *5.3.3).* The uniform elongation has decreased rapidly, reaching a near–zero value at a fluence producing 0.01 dpa, at the point where the yield strength has been increased to equal the ultimate tensile strength. The total elongation is not as quickly affected and remains above 2% for all conditions tested. However, this total elongation reflects only the deformation in the neck region of the tested specimen.

Table 5.3.1. The 25°C Tensile Properties of Irradiated VANSTAR-7

Irradiation Parameters			Strain Rate (s^{-1})	Strength, MPa		Elongation, %	
Temperature (°C)	Fluence, >0.1 MeV (neutrons/m^2)	Displacement Level (dpa)		0.2% Yield	Ultimate	Uniform	Total
	0		4.2×10^{-4}	363	534	14.8	21.9
	0		4.2×10^{-4}	341	510	15.2	22.5
	0		4.2×10^{-6}	332	501	13.8	19.0
	0		4.2×10^{-2}	488	571	10.8	18.5
70	1.0×10^{22}	0.00095	4.2×10^{-4}	445	548	11.8	17.6
70	1.0×10^{22}	0.00095	4.2×10^{-4}	433	531	11.6	16.3
70	1.0×10^{23}	0.0095	4.2×10^{-4}	627	627	0.06	8.24
70	1.0×10^{23}	0.0095	4.2×10^{-2}	654	654	0.3	2.3
70	1.0×10^{24}	0.095	4.2×10^{-4}	729	729	0.1	7.6
70	1.0×10^{24}	0.095	4.2×10^{-4}	717	717	0.0	4.3
70	1.0×10^{25}	0.95	4.2×10^{-4}	854	854	0.06	3.5
70	1.0×10^{25}	0.95	4.2×10^{-4}	819	819	0.06	4.5
496	1.5×10^{26}	9.3	3.3×10^{-4}	951	1017	2.5	8.2

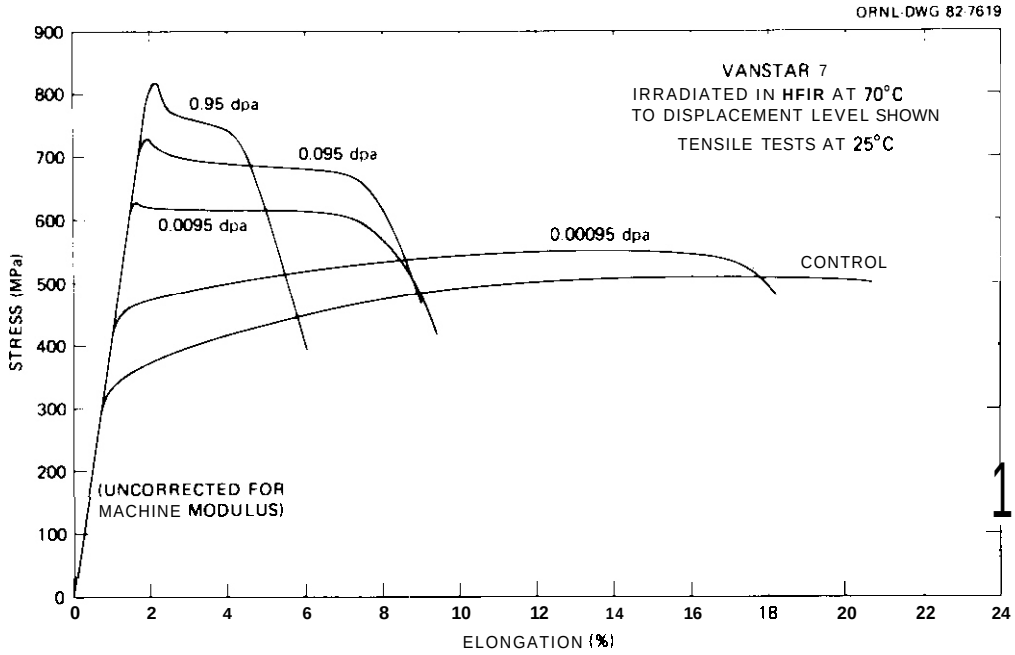

Fig. 5.3.1. Load-Elongation Curves for VANSTAR-7 Irradiated at 70°C to Neutron Fluences up to 1.0×10^{25} neutrons/m^2. Plastic instability is observed for fluences producing 0.0095 dpa or greater.

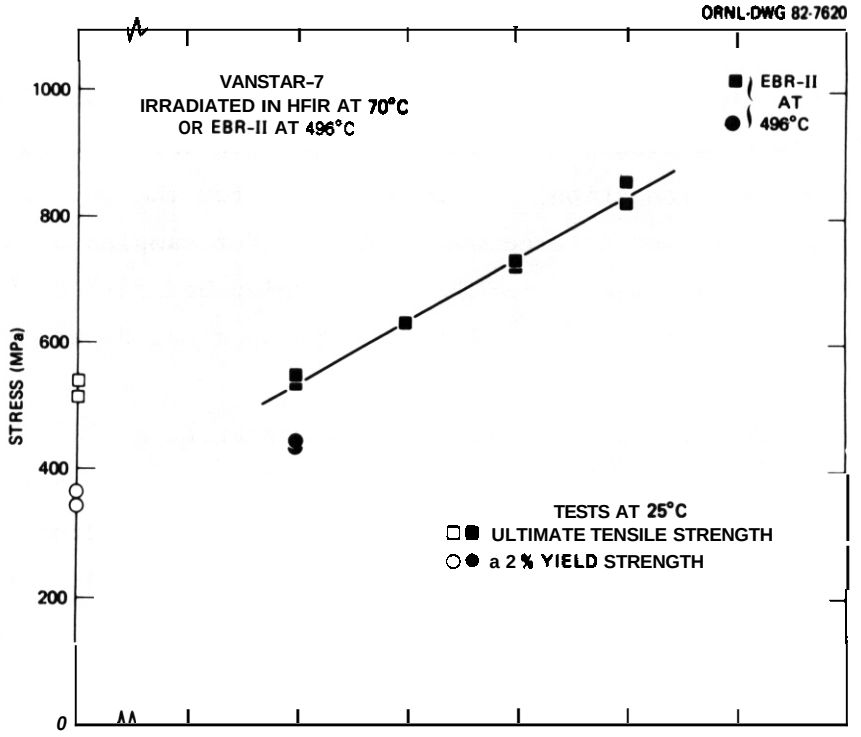

Fig. 5.3.2. Strength Values for Irradiated VANSTAR–7 in Tensile Tests at 25°C.

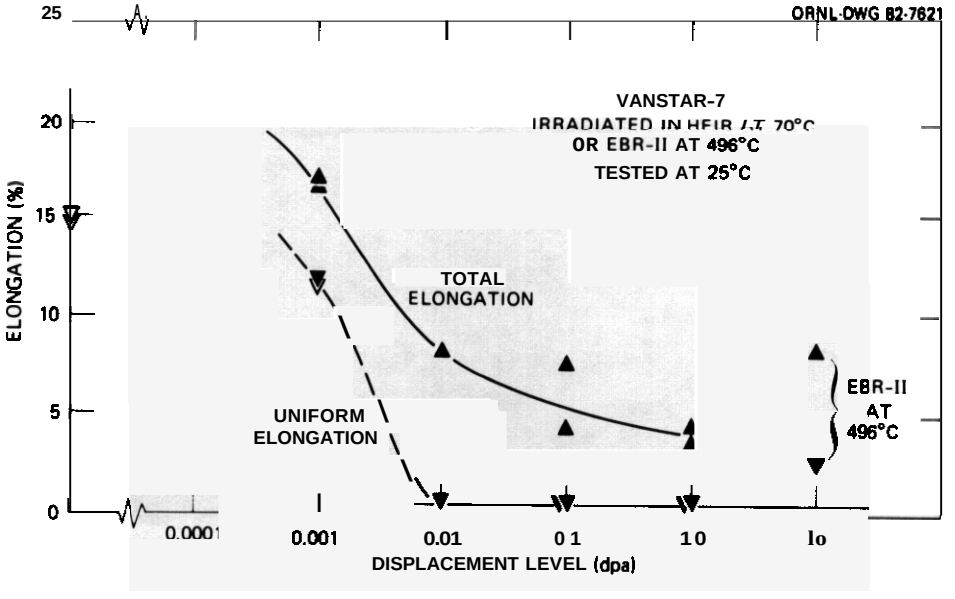

Fig. 5.3.3. Tensile Elongation of Irradiated VANSTAR–7 Measured at 25°C.

In the one sample irradiated at the higher temperature of 496°C the behavior is quite different from that of the material irradiated at 70°C. For the higher irradiation temperature the deformation included some component of work hardening after the yield strength was reached, and both uniform and total elongations are greater than for the low-temperature irradiation. Reduction in area was estimated for samples examined by scanning electron microscopy (SEM). All samples had failed after reduction of area in the range 55 to 75%, with no apparent dependence on the fluence level.

The fracture mode was unaffected by irradiation at 70°C. Scanning electron microscopy examination showed that all samples had failed in a ductile mode, with the characteristic dimples on the fracture surface shown in Fig. 5.3.4. The distribution of dimple sizes was qualitatively similar for all tests. The dimples had originated at precipitates in the sample matrix. There was no indication of any brittle fracture mode, through either cleavage or grain boundary separation. Fractures were nearly perpendicular to the tensile axis in all tests.

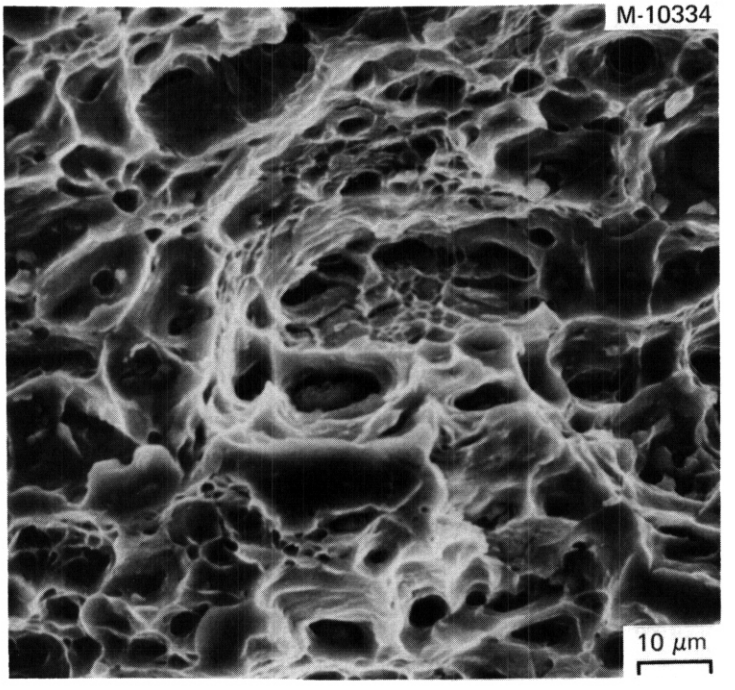

Fig. 5.3.4. Fracture Surface of a VANSTAR-7 Sample Irradiated to 0.95 dpa at 70°C and Then Tensile Tested to Fracture at 25°C.

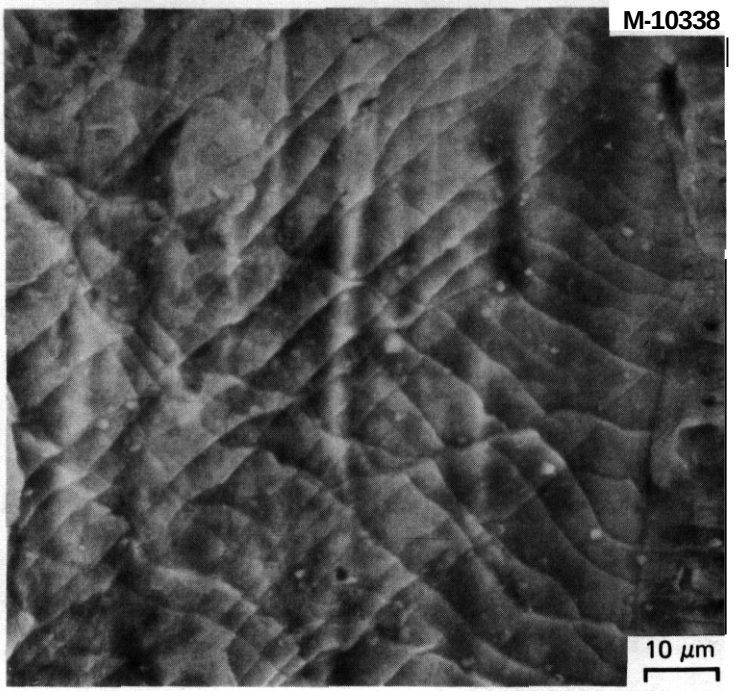

Fig. 5.3.5. Slip Traces on the Flat Gage Section of VANSTAR-7 Irradiated to 0.95 dpa at 70°C and Then Tested in Tension at 25°C.

Slip traces could be seen in some areas of all tested samples in SEM examination of the flat surfaces of the gage section. The trend shown was for the slip traces to be deeper, better defined, and more widely spaced as the fluence increased. An example of these markings in the highest fluence sample irradiated at 70°C is shown in Fig. 5.3.5. These markings show that deformation has been predominantly on two slip systems, with separation between active slip lines on the order of 2 μm. These slip traces could be seen only in areas well away from the fracture, as the extensive deformation in the necked region destroyed any evidence of the early deformation stages.

5.3.5 Discussion and Conclusions

Irradiation of VANSTAR-7 at 70°C, followed by tensile testing at 25°C, has shown effects similar to the behavior reported for unalloyed vanadium[3,4] and numerous other bcc metals and alloys.[1,2] The alloy is rapidly strengthened at low fluences, with nearly equal yield and ultimate tensile strengths resulting for fluences producing 0.01 dpa. Strength increases with increasing fluence, with no evidence of a saturation of strengthening at a displacement damage level of 1 dpa. These irradiation

conditions have significantly reduced the tensile elongation; the uniform elongation is only a few tenths percent for irradiations producing 0.01 dpa or greater, while the total elongation continues to decrease with increasing fluence for the fluence range sampled. The strengthening and ductility loss do not give any indication of a shift in the ductile-to-brittle transition temperature to above room temperature.

The observed hardening and loss of uniform elongation by the onset of plastic instability result from the microstructural damage produced by the irradiation. This damage has been shown for similar materials[2,4] to consist mainly of a high concentration of small dislocation loops. The loops are effective in hardening the material, but once deformation initiates the loops are swept up by deformation dislocation. The result is a channel that is soft for continued deformation. The concentrated deformation results in broad channels free of dislocation loops and coarse slip traces on the free surfaces.[1,4]

While this channeling deformation mode restricts slip and results in a load drop after yielding begins, it does not lead to a brittle fracture mode. Extensive deformation in a necked-down region of the material leads to high local deformation as reflected by large reduction in area at the fracture. In the VANSTAR-7 the fracture occurred by the linking of deformation-produced voids that had nucleated on preexisting precipitates in the alloy matrix.

5.3.6 References

1. F. W. Wiffen, "Plastic Instability in Neutron-Irradiated Niobium Alloys," *ADIP Quart. Prog. Rep. March 31, 1978,* DOE/ET-0058/1, pp. 142–52.
2. F. W. Wiffen, "The Tensile Properties of Fast Reactor Neutron Irradiated BCC Metals and Alloys," pp. 176–97 in *Defects and Defect Clusters in B.C.C. Metals and Their Alloys,* National Bureau of Standards, Gaithersburg, Maryland, 1973.
3. G. R. Smolik and C. W. Chen, "Radiation Hardening in Vanadium," *J. Nucl. Mater.* 35: 94–101 (1970).
4. K. Shiraishi, K. Fukaya, and Y. Katano, "Radiation and Anneal Hardening in Vanadium," *J. Nucl. Mater.* 44: 228–38 (1972).

5.4 FATIGUE CRACK PROPAGATION IN SELECTED TITANIUM ALLOYS -

R. J. Puigh and A. M. Ermi (Hanford Engineering Development Laboratory).

5.4.1 ADIP Task

ADIP Task I.B.3, Fatigue Crack Growth in Reactive/Refractory Alloys (Path C).

5.4.2 Objective

The objective of this study is to quantify the fatigue crack propagation behavior of several candidate titanium alloys.

5.4.3 Summary

Room temperature tests have been performed on selected titanium alloys. At relatively small values for the stress intensity factor, ΔK, the crack growth rates for all titanium alloys investigated are within a factor of three. Each of the titanium alloys has observable crack propagation for stress intensity factors as small as 4.2 MPa $\sqrt{m}$.

5.4.4 Progress and Status

5.4.4.1 Introduction

Titanium alloys have been considered viable candidate alloys for application in fusion power reactors because of their superior strength to weight ratio and better thermal stress properties when compared to stainless steel.[1] The fatigue crack propagation behavior for selected titanium alloys has been measured using the miniature specimen technology.[2,3] These measurements were undertaken to provide baseline FCP data for these alloys. These measurements will be compared with the test results from neutron irradiated miniature CCT specimens when these specimens become available.

5.4.4.2 Experimental Procedure

The gage sections of the miniature CCT specimens were fabricated from 0.076 cm sheet stock for the titanium alloys listed in Table 1. Also shown in Table 1 are the chemical compositions for these alloys.

TABLE 1

TITANIUM ALLOY CHEMICAL COMPOSITIONS †

Alloy (Heat/Ingot #)	C	Fe	N	Al	Si	B	Mo	H	Zr	V	Sn	Mn	O	Cu	Ti
Ti-6Al-4V (891352)	.01	.21	010	6.4	-	-	-	65(PPM)	-	3.9	-	-	12≈	-	BAL.
T-5621S (802881)	.02	.04	.009	4.7	2∃	-	.78	75(PPM)	1.8	-	5.9	<50(PPM)	.09o	-	BAL.
Ti-6242S (N9882)	.018	.06	.005	5.8	0∃0	.001	1.9	.008	4.0	-	1.9	.005	.10	.002	BAL.

†(Weight percent except where noted.)

All gage sections were fabricated with their notch parallel to the rolling direction. The pull tabs were fabricated from commmercially pure titanium to insure weldability of the gage sections to the pull tabs.

The crack length was measured using an electrical potential technique.[2] A direct current of 5 amps is passed through the specimen and the voltage drop across the face of the gage section is measured at two positions. A calibration curve then relates the ratio of the voltages at the two positions to the half crack length. Thin, 0.13 mm diameter commercially pure titanium wire was used for the voltage leads to the gage section to minimize the effects of induced emf's at elevated temperatures. The leads from the specimen to the outside of the test rig are also commercially pure titanium wire.

The cyclic testing of the specimens has been performed using a fatigue machine described in Reference 2. All tests were performed at room temperature (25°C) in air. The Ti-5621S, Ti-6242s and Ti-6Al-4V (beta anneal) tests were performed at a cyclic rate of 6.67 cycles/sec with the ratio of minimum to maximum load, R, equal to 0.05. The mill anneal Ti-6Al-4V was tested at a cyclic rate of *20* cycles/sec and R = 0.10. A sinusoidal loading form was employed in all tests. The stress intensity factor range used for the CCT specimens was[4]:

$$\Delta K = [1-R][\sigma\sqrt{\pi a}][1-0.025(2a/W)^2 + 0.06\ (2a/W)^4][\sec\ (\pi a/W)]^{0.5}$$

where σ is the maximum applied stress, a is the half-crack length and W is the specimen width. The secant method[5] was used to construct the crack growth curves.

5.4.5 Results

Fatigue crack propagation behavior has been measured for the following titanium alloys and thermomechanical treatments: Ti-6Al-4V, both mill anneal (718°C/4hr/AC) and beta anneal (1038°C/30m/AC + 718°C/2hr/AC; Ti-5621S, duplex anneal (974°C/1hr/AC + 593°C/2hr/AC);

and Ti-6242S, duplex anneal (899°C/30m/AC + 788°C/15m/AC). Plots of the crack growth rate, $\frac{da}{dN}$, as a function of the stress intensity factor, AK, are shown for each titanium alloy condition in Figures 1-4. For each titanium alloy condition a minimum of two tests were performed at 25°C. As seen in each of the figures the overlap between the two tests was quite good. In comparing the crack growth rates for these alloys the mill anneal condition of Ti-6A1-4V exhibits the fastest crack growth rate and the beta anneal condition of Ti-6Al-4V exhibits the slowest crack growth rate of the alloys and conditions tested. The dashed curves in Figures 1 and 2 are the results of tests performed on standard sized specimens.(6) The test conditions were: cyclic tension-to-tension loading with a haversine waveform, a frequency of 5 Hz, and a load ratio of R = 0.1. The results of these tests agree with the results from tests using the miniature CCT specimen for both the mill and beta anneal conditions of Ti-6Al-4V.

The fracture surfaces appear to be "typical" for the Ti-6Al-4V (mill anneal), Ti-5621s and Ti-6242s tests.(7) Fractography was performed on the Ti-6Al-4V mill anneal specimen. The fracture surface exhibited a morphology consistent with ductile fracture for low ΔK. At intermediate AK values striation and some cleavage were evident. The fracture surface of the beta anneal Ti-6A1-4V specimens exhibited a much more tortuous path for the crack's path. Earlier investigations of the fatigue crack propagation behavior of beta anneal Ti-6Al-4V have shown that at low crack growth rates the crack path appears to follow prior beta grain boundaries.(7) This may contribute to the relatively superior fatigue crack growth resistance of the beta anneal Ti-6Al-4V. At higher values of AK transgranular crack propagation was evident.

Finally in Figure 5 the FCP results for titanium alloys are compared with the FCP behavior of HT-9 (heat #91353) and 20% CW 316 SS (heat #X-15893) for equivalent test conditions. The titanium alloys are observed to have a crack growth rate which is on average a factor of three greater than the crack growth rate for HT-9 or 20% CW 316 SS. Of more serious concern is the observation that for the titanium alloys crack propagation is observed to occur for relatively low values of

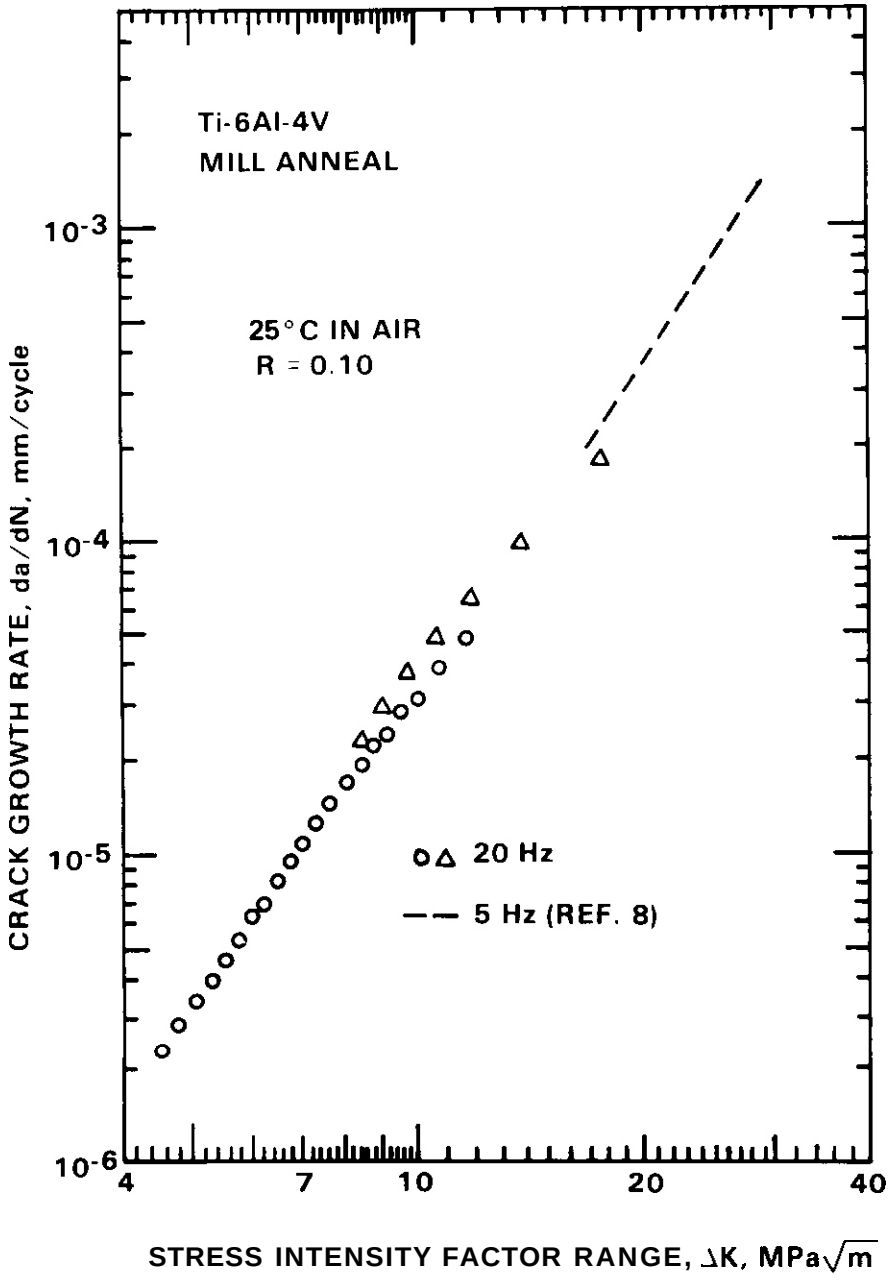

Figure 5.4.1 FCP behavior for mill annealed Ti-6Al-4V.

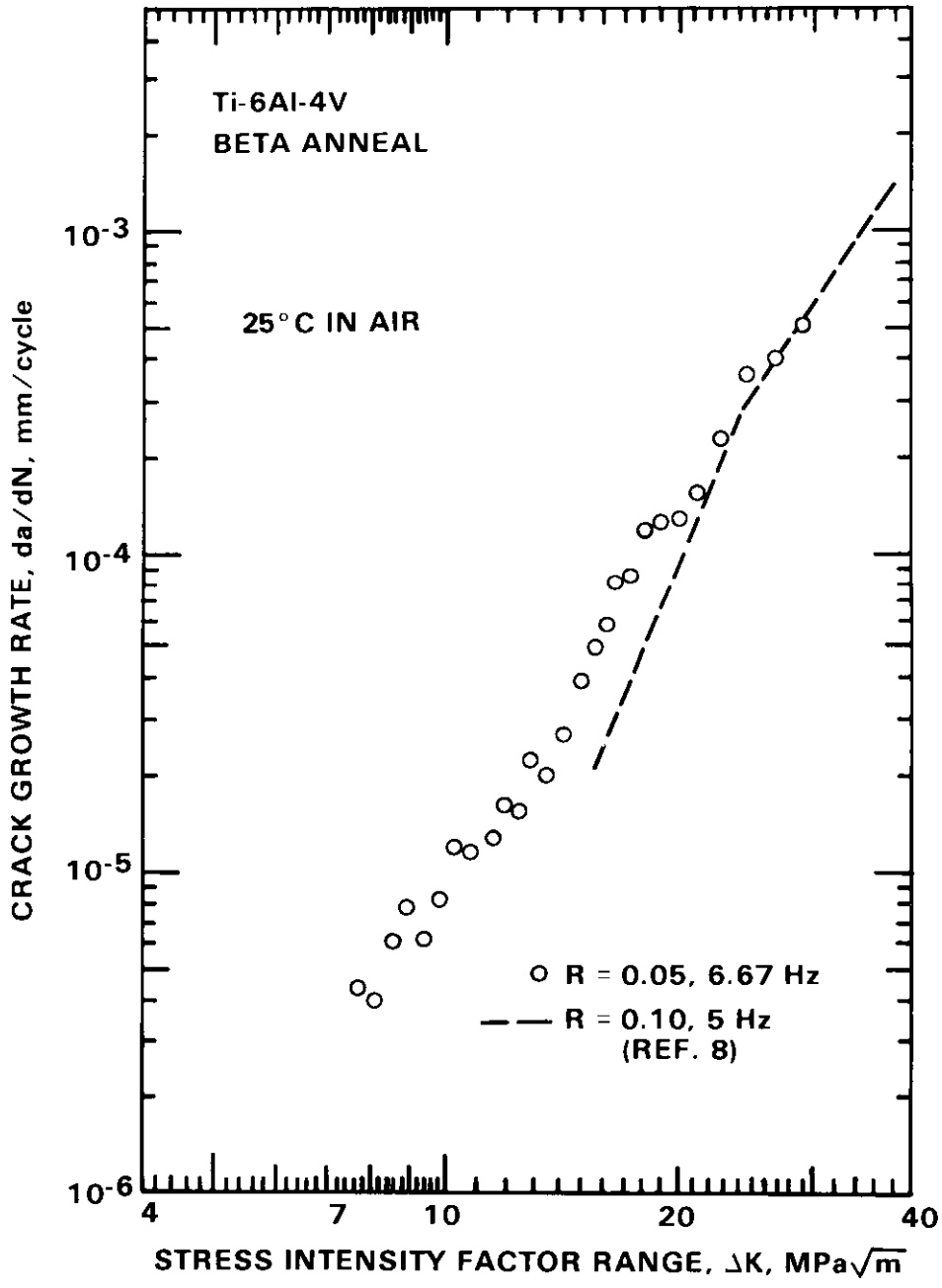

Figure 5.4.2 FCP behavior for beta annealed Ti-6Al-4V.

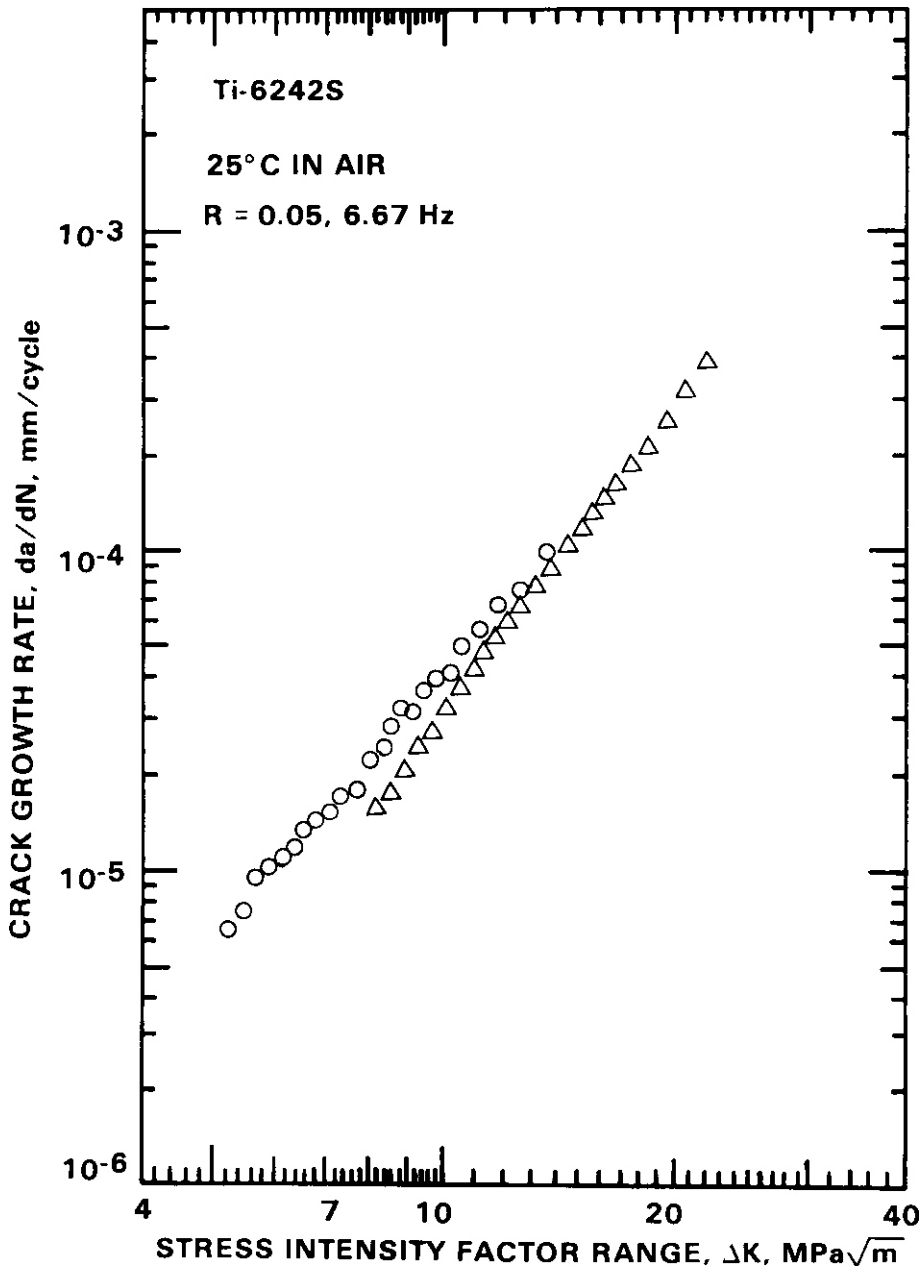

Figure *5.4.3* FCP behavior for Ti–6242s.

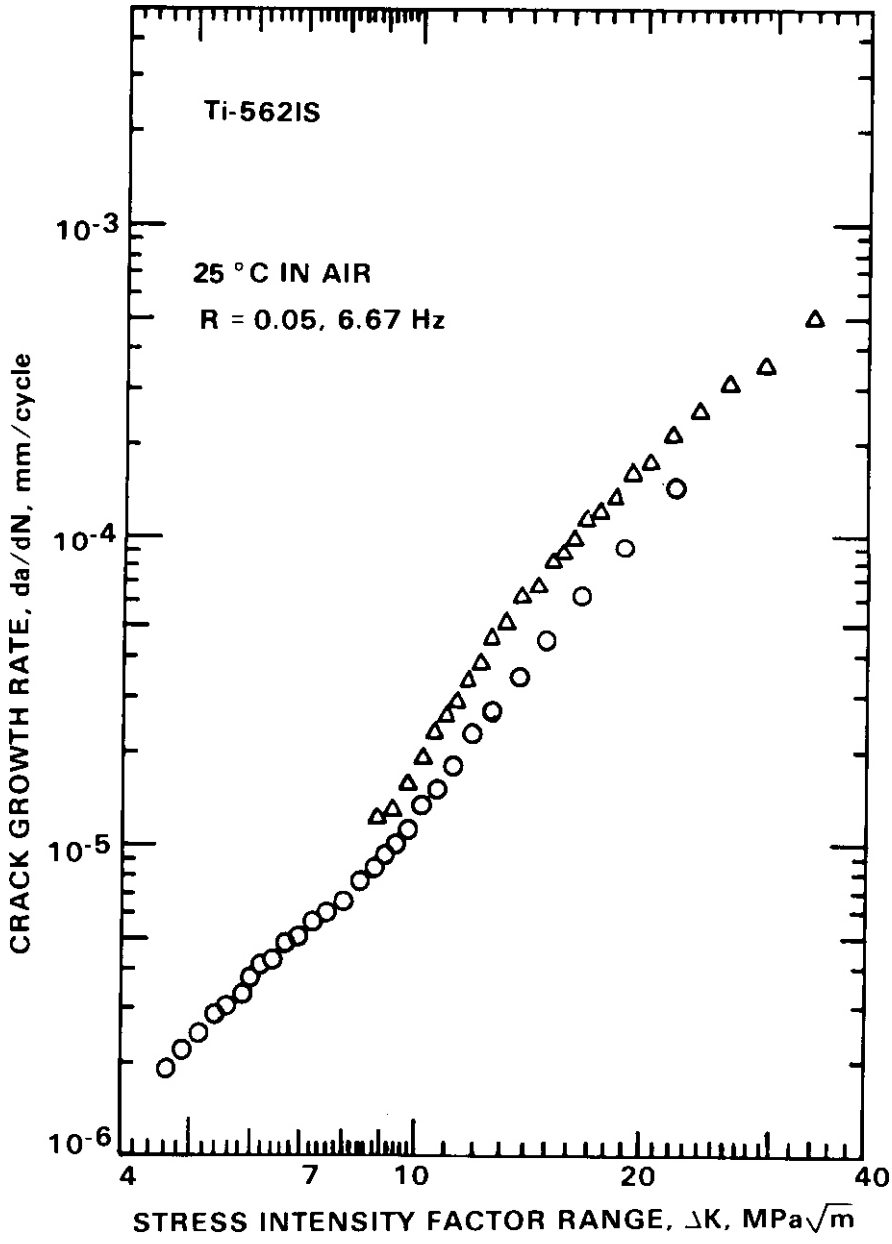

Figure 5.4.4 FCP behavior for Ti–5621s.

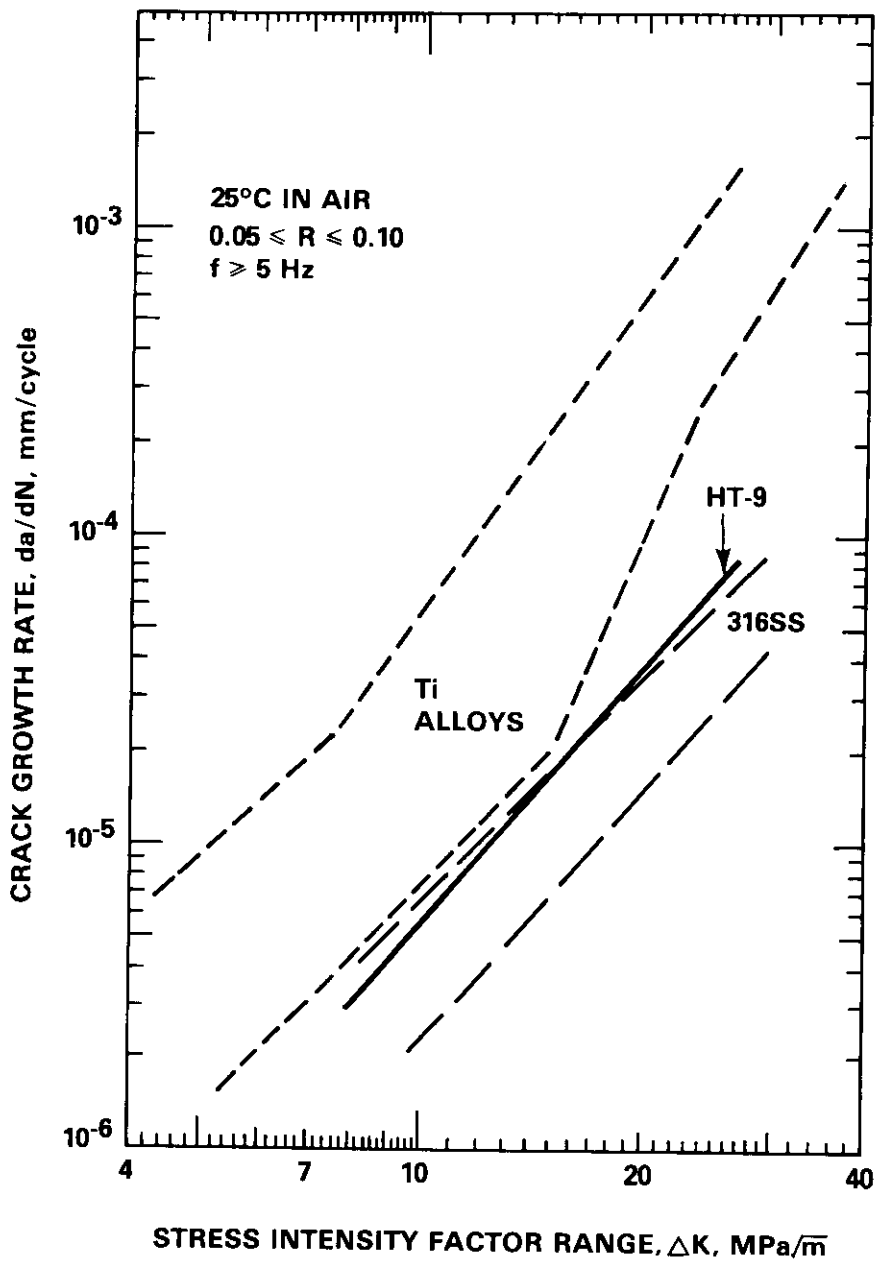

Figure 5.4.5 Comparison of the FCP behaviors of HT-9, 20% CW 316 SS and selected titanium alloys.

$\Delta K \cong 4.2$ MPa $\sqrt{m}$. Limited data on stainless steels tested at a stress ratio of R = -1 suggest that there is no crack growth in stainless steels when the stress intensity factor is less than approximately 6 MPa $\sqrt{m}$.(8)

5.4.6 Future Work

No additional testing is planned in the next reporting period. Eventually elevated temperature baseline testing and the testing of irradiated specimens are envisioned.

5.4.7 References

1. J. W. Davis and G. L. Kulcinski, "Assessment of Titanium for Use in the First Wall/Blanket Structure of Fusion Power Reactors", Electric Power Research Institute, EPRI-836 (Project 472-I), April 1977, 3-9.
2. D. A. Mervyn and A. M. Ermi, "Miniature Specimen Technology for Postirradiation Fatigue Crack Growth Testing", Proceedings of the 8th Symposium on Engineering Problems of Fusion Research, IEEE Pub. No. 79CH1441-5 NPS, Vol. IV (1979),1832-1836.
3. D. A. Mervyn, M. M. Paxton and A. M. Ermi, "Development of the Miniature Fatigue Crack Growth Machine, ADIP *Quarterly Progress Report for Period Ending September 30, 1373,* DOE/ET-0058/7, 29-42.
4. H. Tada, P. C. Paris and G. R. Irwin, The Stress Analysis Handbook, Del Research Corp., St. Louis, MO (1973), 2.2.
5. W. G. Clark and S. J. Hudak, Jr., "Variability in Fatigue Crack Growth Rate Testing", J. Testing and Evaluations, 3 (1975), 454-476.
6. G. R. Yoder, L. A. Cooley and T. W. Crooker, "Observations on Microstructurally Sensitive Fatigue Crack Growth in a Widmanstatten Ti-6Al-4V Alloy", Met. Trans. A, 8A, (1977), 91-101.
7. J. C. Chesnutt, A. W. Thompson and J. C. Williams, "Influence of Metallurgical Factors on the Fatigue Crack Growth Rate in Alpha-Beta Titanium Alloys", Technical Report AFML-TR-78-68, Air Force Material's Laboratory, (1977), 91-101.

8. S. Stanzl and E. Tschegg, "Fatigue Crack Growth and Threshold Measured at Very High Frequencies", Metal Science, April 1980, 137–143.

6. INNOVATIVE MATERIAL CONCEPTS

No **contributions.**

7. PATH E ALLOY DEVELOPMENT — FERRITIC STEELS

7.1 EVIDENCE OF SEGREGATION TO MARTENSITE LATH BOUNDARIES IN TEMPER-EMBRITTLED 12Cr-1Mo-.3V STEEL (HT-9) - T. A. Lechtenberg (General Atomic Company)

7.1.1 ADIP Task

The Department of Energy (DOE)/Office of Fusion Energy (OFE) has stated the need to investigate ferritic steel alloys under the ADIP program task. Ferritic Steels Development (Path E).

7.1.2 Objective

This section reports and discusses the results of Auger electron spectroscopy on HT-9 specimens fractured in-situ at 10^{-9} torr. The work was performed at Sandia Laboratory in Livermore by Dr. Bernie Mills. Also, the relationship of these results and those previously generated describing the microstructure are discussed.

7.1.3 Summary

Fracture properties and a detailed microstructural examination of 12Cr-1Mo-.3V Steel (HT-9) have been reported previously (1,2). It has been shown that HT-9 is susceptible to a degree of temper embrittlement (TE). In these studies material was austenitized at 1000°C and tempered at 650°C, both for an hour followed by an air cool. Half of the Charpy V-notch specimens were subsequently aged at 550°C for 100 hrs, and transition temperature curves were generated for both conditions. The data showed that there was an increase in the ductile to brittle transition temperature (DBTT) of 80°C due to thermal aging (this is shown in Fig. 1). This was expected because TE is classically associated with slow cooling through or aging in the temperature regime of 600-450°C. The specific temperatures are dependent upon alloy composition. Other investigators (3-5) have shown the decrease in toughness (increase in DBTT) to be the result of segregation of tramp impurity elements such as Sn, P, S, and Sb, to the prior austenite grain boundaries. These are thought to 'pull' electrons from the nearest metallic bonds leaving them weak. and an easy path for crack propagation (3,6).

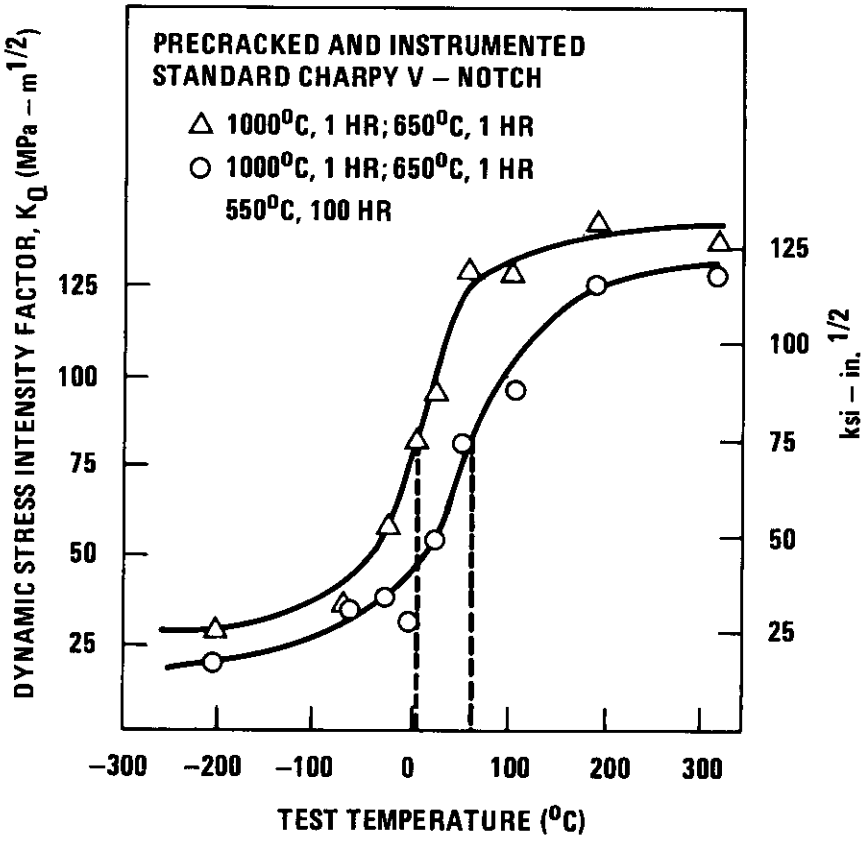

Fig. 1. Dynamic stress intensities (K_{Id}) of 12Cr-1Mo-.3V steel after austenitizing at 1000C for an hour and tempering at 650C for an hour, both followed by air-cooling showing the effect of ageing at 550C for 100 hr.

However, the fracture surfaces of the precracked Charpy specimens used in this investigation did not exhibit a change in fracture mode as a result of aging. The fracture mode at all temperatures tested (except the highest in the unaged case) was interlath (between martensite lath boundaries) with some ductile tearing. The cleavage facets are the size and approximate morphology of the martensite laths in the structure. and so were presumed to be so. The surfaces are shown in Fig. 2. This anamoly with classical behavior prompted further investigation to determine why the propagating crack followed the lath boundaries. A careful transmission electron microscopic (TEM) examination showed that $M_{23}C_6$ carbides were decorating the martensite lath boundaries. It also showed these carbides precipitated from thin films of austenite retained at the lath boundaries during cooling from austenitization. These films were also shown to be supersaturated in carbon which promoted their stabilization. Subsequent tempering resulted in the precipitation of the carbides leaving a semicontinuous network surrounding the martensite laths. A TEM analysis showed that there was little or no change in the morphology or amount of the $M_{23}C_6$ carbides at the boundaries after aging at 550°C for 100 hr. The laths had recovered by some subgrain formation. but the microstructures appeared very similar.

This quarterly reports Auger electron spectroscopy performed at Sandia Laboratory on specimens fractured in-situ and produced from the Charpy specimens from which all other data had been generated. In order to understand the causes of embrittlement and possible cures, Auger analysis was done to identify segregating specie. Ramification of the work may lead to a choice of better melting practice. It was found that the quenched. tempered. and aged condition had martensite lath surfaces considerably enriched in S as compared to the unaged material. The increase in the DBTT as a result of aging is associated with an increase in the concentrations of S at lath boundaries. These results are discussed and possible solutions are suggested. Also. tempering prior to aging causes an increase in P and Si levels at the lath boundaries. This may be associated with expulsion of these elements as $M_{23}C_6$ carbides precipitate.

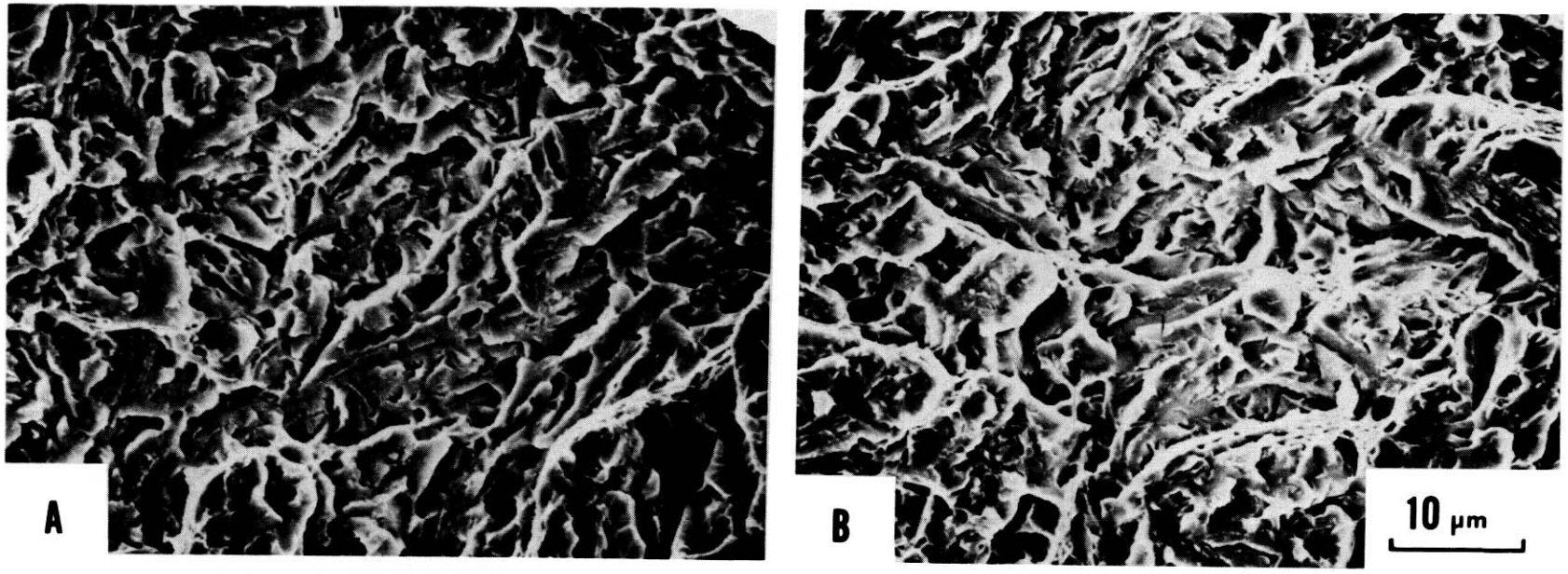

Fig. 2. Scanning electron micrographs of the 12Cr-1Mo-.3V steel after fracture. (A) Quenched and tempered condition, (B) Q+T and aged at 550C for 100 hr. The fracture morphology is typical of martensite lath cleavage. Note that the fracture mode was identical for both conditions.

7.1.4 Experimental Procedure

The material used in this investigation was obtained from the National Breeder Material Stockpile (heat No. 91354) at HEDL in the form of 1-5/16 in. diameter rod. The chemistry is given in Table 7.1.1. The as-received material had been heated to 1100°C for at least an hour. hot worked with reheats to 1150°C between each pass. slow cooled. and tempered at 750°C for 1 hour followed by an air cool.

Table 7.1.1 Chemistry of 12Cr-1Mo-0.3V Alloy (HT-9) (wt. %)

C	Cr	Mo	V	W	Ni	Mn	Si	P	S	Fe
0.21	12.09	1.02	0.33	0.54	0.58	0.50	0.21	0.008	0.003	Bal.

Specimen blanks for standard Charpy V-notch tests were cut from this plate. They were heated to 1000°C for an hour. and air-cooled. then tempered for an hour at 650°C. Half were then aged at 550°C for 100 hr to promote temper embrittlement. These specimens were tested with and without a precrack on a Dynatup drop weight impact tester with an ETI300 microprocessor. The technique is completely described in Ref. 7. Auger specimens were machined from the broken specimens. These specimens were broken in-situ at 10^{-9} torr to reduce contamination. They were cooled for half an hour to near liquid nitrogen temperature by holding against a LN_2-cooled block. The specimens are notched and fracture was performed by striking them with a tup in the machine.

Because of the poor resolution of the Auger spectrometer in the scanning mode the surfaces were examined on a scanning electron microscope at General Atomic to ensure that he fractures appeared similar to those seen on the surfaces of the impact specimens.

7.1.5 Results and Discussion

The conditions of 12Cr-1Mo-0.3V (HT-9) fractured in the Auger spectrometer were: (1) 1000°C austenitization and 650°C tempering both

for an hour and followed by an air cool (Q and T condition). and (2) the same treatment but followed by thermal aging at 550°C for 100 hrs (aged condition). The latter was *to* promote temper embrittlement which is known *to* happen at that temperature.

The experiment was designed to first fracture and analyze the aged condition. The Auger spectrometer in the scanning mode does not have sufficient resolution to ensure that one lath facet would be observed. However. it is important to ensure that data be collected from the lath cleavage facets because these were the overwhelmingly dominant feature observed previously on the SEM and. therefore. considered the 'weakest' link. However. reducing the scanning area increases the time for data collection and the uncertainty that the chemical results are representative of all lath facets.

Although scanning individual lath boundaries in sufficient quantity to be meaningful is ideal. this was deemed *too* time consuming. So, one lath facet was scanned and those results were compared to a scan that incorporated many laths (~25). There was little difference observed when corrected for oxygen and carbon contamination. Thus. all other scans were performed on regions which contained approximately 5 lath cleavage facets. The results are listed in Table 7.1.2. This table shows the chemical analysis in atomic percent for the bulk and the two conditions studied. The bulk chemistry is calculated from weight percent values listed in Table 7.1.1.

Segregation in Unaged Material: The effects of processing and the heat treatments listed above are seen by comparing the bulk analysis to that of the material quenched and tempered at 1000° and 650°C.

The carbon concentrations of the lath boundaries were increased from the bulk from 1.1 at % to 3.6 at %. This is probably due to $M_{23}C_6$ carbide precipitation at lath interfaces because the carbon was bonded as a carbide. This could be determined because the peak slope is dependent upon the type of bonding in the atom and was compared *to* known standard peaks. The Cr remained close to the bulk value although slightly higher due *to* the Cr-rich carbides. There was little difference in the Ni concentrations, whereas some Mo desegregation occurred

Table 7.1.2
SURFACE ANALYSIS BY AUGER ELECTRON SPECTROSCOPY (ATOMIC PERCENT)

	Fe	C	Cr	Mo	W	V	Ni	Mn	Ti	Si	Al	P	S	Cu	N
Bulk(≡)	81	1.1	14.6	0.7	0.17	0.45	0.6	0.6	0.003	0.5	0.06	0.013	0.005	0.035	0.023
1000°C 1hr air-cool		3.6	17	0.4	(c)	(d)	0.6	(d)	0.6	1.4	(c)	(c)	0.1	(c)	(c)
650°C 1hr air-cool															
1000°C 1hr air-cool		z z	∃	(b)	(c)	(ϑ)	0.8	(d	0.8	z.5	(c)	(c)	0.3	(c)	(c)
650°C 1hr air-cool															
550°C 100hr air-cool															

(a) Calculated from bulk composition.
(b) Looked for the 220 eV Mo M_5 $M_{4,5}$ $M_{4,5}$ peak rather than the 190 eV M_4 $M_{2,3}$ $M_{4,5}$ and saw no signal.
(c) Not detected; a detection limit of 0.5 atomic percent might be expected for phosphores.
(d) Interferences by major constituents preclude unequivocal determination.

and no W was observed at all. This may be due to limited solubility of W and Mo in $M_{23}C_6$ in this alloy. The V peak could not be observed due to interference by Fe. The elements with largest percent increases over bulk concentration were Si. P, and S. Phosphorous and sulfur are known to segregate when this class of steels is cooled slowly through the 600°-450°C range and both were concentrated one to two orders of magnitude higher at the lath boundary (8). The material received an air cooling after tempering at 650°C, so the increase in S and P is probably due to that. It would not be due to processing history or austenitization because one important feature of temper embrittlement is its reversibility by heating to any temperature higher than the embrittling range followed by a faster cooling (3). This redistributes the S and P, then the faster quench prevents it from resegregating.

The increase in Si is more difficult to rationalize. It is known that Si increases the activity of carbon in low-alloy steels. and inhibits carbide coalescense and growth (9). Owen theorized that in a Si-bearing steel. Si is expelled when carbides nucleate and grow. However. it has a lower diffusion rate than C, so may effectively form a 'halo' around the carbide. inhibiting further diffusion of carbon into the carbide and. therefore. further growth. The Si observed was covalently bonded, again determined by comparing to standard peaks.

Segregation Due to Aging: The effect of aging 100 hrs at 550°C can be seen by comparing it to the quenched and tempered condition. The concentration of carbon has increased little. This verifies an earlier conclusion that tempering at 650°C produces a stable carbide (2). The Cr content is much smaller than could be expected. Although more work would be required to determine the reason, it may be due to a surface-to-volume effect. Auger analyzes the first few atomic layers with little contribution from subsequent ones. Their was a noticeable. albeit small. coalescense of $M_{23}C_6$ lath carbides after aging at 550°C observed in the TEM. The surface-volume ratio would be changed such that much more Cr could be 'hidden' from the Auger spectrometer in larger carbides. The lower Cr content. then. may not be due to desegregation but an experimental effect. Again. W was not detected and the

V peaks were masked. After aging. the Si content remained nearly constant indicating it is not a segregant at this temperature. So silicon may be a segregant although it is difficult to rationalize since little increase was observed after aging, and there is sufficiently more of the specie in the alloy available to pollute the boundaries. Also. this tends to support the Owen expulsion theory because little more carbide precipitated as measured by X-ray extraction and as observed in the TEM, and the silicon concentration at the boundaries mirrored this. The phosphorous concentration increased somewhat but not significantly. An estimate places it at the same order as in the quenched and tempered condition, perhaps slightly higher. This may be due to the inherent behavior of phosphorous that mimics silicon (9). The sulphur content on the boundary increased three-fold after aging. This is certainly due to the aging time and temperature. and is consistent with thermodynamic predictions and other observations.

7.1.6 *Conclusions*

The results of this study indicate that the degree of temper martensite embrittlement reported earlier may be caused by three factors. These are: the precipitation of a second phase at the martensite lath boundaries. the segregation of impurities at the same, or the expulsion of silicon and phosphorous. Although embrittlement may occur there is still significant energy needed to cause fracture. and the upper-shelf energy decreases very little. Also, it has been shown that martensite lath boundaries are also subject to 'micropollution' as are prior austenite grain boundaries. It was thought that high-angle boundaries were more subject to brittle fracture due to more severe stress concentrations at nodes (10). It now seems apparent that the lath packets' boundaries are also of high enough angle to cause a fracture brittle. Also. because the smaller laths have much more surface area than on austenite boundaries. segregant embrittlement may be significantly reduced in these alloys. Fracture occurs along martensite lath boundaries and is made easier by the presence of segregants. This is temper embrittlement. Recent evidence on a 9Cr-1Mo alloy shows that tempered

martensite embrittlement is exacerbated by higher silicon concentrations (11) which agrees with these conclusions. but is unrelated to the loss in toughness due to temper embrittlement.

7.1.7 References

1. Lechtenberg. T. A. and S. Helfrich, 'The Fracture Properties of a Temper Embrittled 12Cr-1Mo-0.3V Steel.' Alloy Development for Irradiation Performance Quarterly Progress Report for the Period Ending June 30, 1980. DOE/ER-0045/3, pp. 201-215.
2. Lechtenberg. T., 'Microstructural Evaluation of a Temper Embrittled 12Cr-1Mo Alloy (HT-9),' an ADIP Quarterly for the Period Ending September 30, 1980. DOE/ER-0045/5.
3. McMahon, C., **Mat. Sci. and Eng.**, **42** (1980) 215.
4. Woodford. D. and R. Stepien, **Met. Trans. A**, **11A** (1980) 1951.
5. Edwards, B. and E. Little. **Ferritic Steels for Fast Reactor Steam Generators.** B.N.E.S.. London (1978) 145.
6. Losch. W.. **Scripta Met.**, 13 (1979) 661.
7. Ireland, D., 'Proposed Standard Method of Test for Impact Testing of Precracked Charpy Specimens of Metallic Materials.' Effects Technology Inc.. Goleta. Ca, 93111.
8. Druce, S. and B. Edwards. U.K. Atomic Energy Authority. Harwell, Report No. AERE-R9904, September, 1980. Oxfordshire. U.K.
9. Owens. W., Trans. ASM, **46** (1954) 812.
10. Otahni, and C. McMahon. **Acta. . .23** (1975) 373.
11. Sikka, V., presented at ASM International Conference on Production. Fabrication. Properties and Applications of Ferritic Steels for High Temperature Service. Warren. PA. 5-10 October 1981.

7.2 AN AUGER ANALYSIS OF A SUPERHEATER TUBE OF HT-9 IN-SERVICE FOR 80.000 HRS AT 600C - T. A. Lechtenberg (General Atomic Company)

7.2.1 ADIP Task

The Department of Energy DOE/Office of Fusion Energy (OFE) has stated the need to investigate Ferritic/Martensitic alloys under the ADIP program task. Ferritic Steels Development (Path E).

7.2.2 Objective

The objective of this contribution is to report an Auger analysis on an in-situ fractured surface of a superheater tube of HT-9 that was in-service for 80,000 hr at 600C. This is intended to supplement a concurrent contribution which discusses short-term processing effects on this same alloy.

7.2.3 Summary

It has been shown in the previous Contribution (Sec. 7.1) that the microstructure of HT-9 to be placed in-service or in irradiation experiments is critically affected by prior processing and heat treating steps taken prior to that. This paper presents data suggesting that long-term thermal ageing effects on the mechanical properties are not as dependent on the metalloid or nonmetallic impurities such as silicon or sulphur, but are controlled by larger. more slowly diffusing species such as copper.

7.2.4 Experimental

Material for this study was obtained from Sulzer Brothers. The tube was obtained from a coal-fired plant in Ruetlingen. West Germany and had been in service at 600C for 80,000 hr. Archive material from the same tube was also obtained to compare post-exposure properties. Mechanical property data has been reported elsewhere (Ref. 1). Auger analysis specimens were machined from broken half Charpy V-notch

specimens used in the evaluation of mechanical properties of Ref. 1. These were fractured in-situ in a Physical Electronic Model 590 Scanning Auger spectrometer after cooling for half an hour in contact with a copper block at -195C. For more details. the reader is referred to the paper above. The vendor chemistry of the material is given in Table I.

7.2.5 Results and Discussion

The results of fracture tests on half-size Charpy-V notch specimens are reproduced from Ref. 1 in Table II. A full transition curve could not be obtained due to unavailability of aged material. However. the tests did show that a transition did occur probably between room temperature and -45C. For the archive (unaged) material the energy absorbed during fracture was 53 Joules at 22C and 18J at -45C. As a result of ageing. the fracture energies dropped considerably. The 80,000 hr aged specimens absorbed 18J at 22C and 7J at -45C. So ageing at 600C reduced the upper shelf energy from 535 to 18J, and the lower shelf decreased from 19J to 7J. Although the ageing clearly reduced the fracture enegies, the fracture modes did not change. This behavior has been reported by others also (Ref. 2), that is, the 9-12%Cr class of steels may suffer a reduced impact toughness when aged in the range of 450-600C but the fracture mode may not change immediately. Temper embrittlement is associated with segregation of impurities to high angle boundaries, and in low-alloy steels such as AISI 4340 (Ref. 3) or 2-1/4Cr-1Mo (Ref. 4) invariably results in a low-energy fracture which occurs at prior-austenite grain boundaries. However. the higher alloy contents of the 9-12% Cr class appear to inhibit this change in fracture mode to intergranular.

Previously the change in fracture energy was attributed to precipitation at martensite lath boundaries (Ref. 1). However. a careful examination failed to justify the degree of embrittlement seen (Table II). This could be due to minor microstructural changes observed in the TEM. The microstructure appeared fully recrystallized. Typical micrographs are shown in Fig. 1. The aged material has completed recrystal-

Table I.
Chemical Composition of HT-9 Superheater Tubes (wt. %)

Fe	C	Cr	Mo	W	V	Ti	Si	Mn	Ni	N	P	S	Cu
bal.	.205	11.7	1.02	0.49	0.35	0.003	0.22	0.50	0.57	0.005	0.006	0.003	0.035

Table II.
Energy of Fracture of Half-Sized Charpy V-Notch Specimens of Archive and 80,000 hr Aged HT-9

Condition*	Temperature (°C)	Half-Size Specimens Impact Energy (J)**
1050C 1/2 hr, 780 C 1/2 hr	-45	19
	22	53
1050C 1/2 hr, 780C 2-1/2 hr	-45	7
600C 80,000 hr	22	18

*All followed by air cooling.
**Average of three specimens.

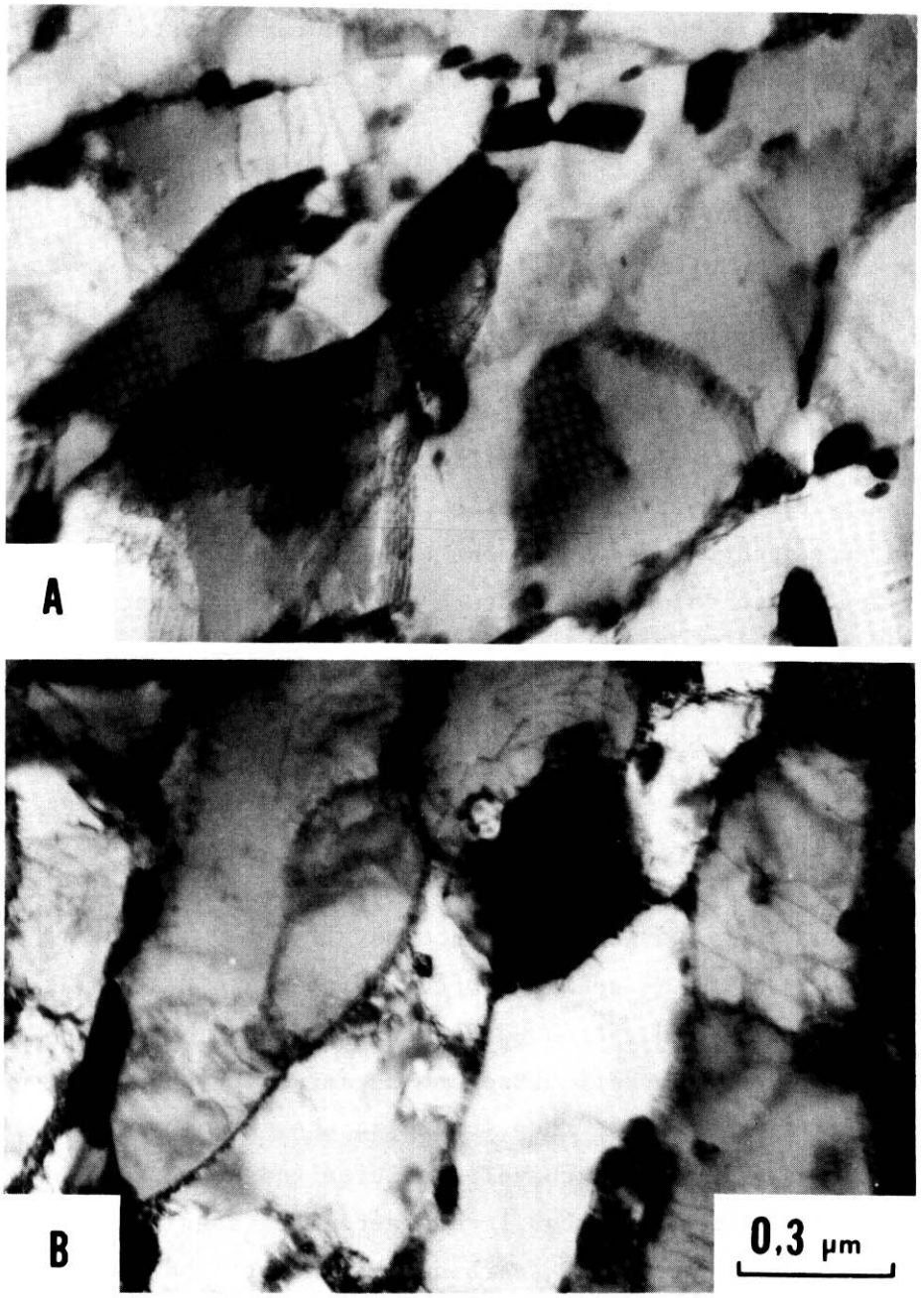

Fig. 1. Transmission electron micrographs of HT-9. Photograph A shows the condition of the archive material (1050C, 1/2 hr; 780C, 2.5 hr). Martensite laths are still evident being surrounded by $M_{23}C_6$ carbides. Part B shows the material aged in-service for 80,000 hr at 600C. Note that recovery is complete, but the microstructures of both conditions appear very similar.

lization, although the martensite lath structure is still apparent. Stable $M_{23}C_6$ carbides have effectively pinned the boundaries ensuring a particularly stable microstructure. Were it not for these carbides remaining at the martensite lath boundaries. this alloy would have approached the stable morphologies of large spherical carbides in a soft ferrite matrix resulting in a loss in strength and creep properties When comparing the archivel microstructure with that of the aged material it is seen that some coalescence of $M_{23}C_6$ carbides has occurred. This. however. tends to reduce the effectiveness of the argument that these carbides are the culprit in embrittlement because no other phase was seen in the TEM in either condition.

In this study. Auger specimens cut from the same Charpy V notch specimens used to determine fracture energies were fractured in-sutu at 10^{-9} torr to reduce surface contamination. They were cooled sufficiently to ensure a brittle type fracture. although subsequent SEM examination showed both exhibited a cleavage fracture along martensite lath boundaries. Nowhere was intergranular fracture clearly observed. SEM analyses of both surfaces (as well as lower magnification photographs of the entire fracture surfaces) confirm very similar fracture modes without any intergranular fracture.

The Auger chemical analyses of both interlath fracture surfaces are given in Table III. Compared to the bulk composition there were increases in silicon. nickel. nitrogen, titanium. phosphorous. sulfur. and copper. There was little or no change in the chromium or molybdenum concentrations. For the archivel condition (quenched and fully tempered) the chromium and carbon levels were increased due to precipitation of chromium-rich $M_{23}C_6$ carbides at the lath boundaries as seen in the TEM analysis. There was a slight increase in both specie upon ageing, probably resulting from a more increased precipitation as the microstructure evolved toward equilibrium. Silicon increased from 0.51 to 1.7 atomic percent (at%) during tempering. and then to 2.5 at%after ageing. Nickel remained at 0.6 at% levels after tempering. but. due to ageing. the Auger analysis showed levels at 0.9 at%. This may be a true segregation effect and has been reported in aged Ni-base alloys (Ref.8).

Table III.
Auger Electron Spectroscopic Analysis
for Archive, and Exposed Material (Atomic Percent)

	Fe	Cr	[illegible]	[illegible]	V	[illegible]i	Mn	Ni	N	[illegible]	[illegible]i	C	P	S	[illegible]	Fe
Bulk Chemistry[a]	[illegible]1.0	[illegible]4.6	[illegible]	0.17	[illegible]	0.51	0.59	0.63	0.023	[illegible]	0.003	1.10[illegible]	0.013	0.005	0.03 *	[d]
Quenched and Tempered Archive	76.7	16.6	0.50	(b)	[illegible]b)	1.7	—	0.6	0.7	[illegible]b)	.8	3.1	0.80	0.20	—	
Aged 80,000 hrs at 600°C	72[illegible]	19[illegible]	0.50	[illegible]b)	(b)	2.3	—	0.9	1.3	[illegible](b)	[illegible]	4.7	1.50	[illegible]0	0.70	

(a) Calculated from weight percent.
(b) Not detected.
(c) Not applicable.

Nitrogen has increased significantly during tempering and ageing. It increased from a bulk concentration of 0.023 at% to 0.7 at% after tempering and 1.3 at% after aging. This was not seen on the fracture surfaces of the 550C short-term aged material reported previously (Sec. 7.1). Other segregants were phosphorous and sulfur. Both increased significantly. the phosphorous up to 1.5 at% and sulfur to 0.3 at%. Copper also increased from 0.035 at% to 0.70 at% after ageing. although no signal was detected in the archive material.

When these results are compared to those reported for the short-term 550C aged material several differences become apparent. First. long-term ageing appears to have a different (or more complete) set of chemical 'actors' in embrittlement. Large. more slowly diffusing species such as copper and nickel now are segregating in significant quantities. The phosphorous concentration also increases significantly. This may be due to a change in the way molybdenum is associated in the matrix and to coalesced carbides because it is known that Mo inhibits temper embrittlement (Ref. 9). Nitrogen segregates when this alloy is exposed at 600C but does not at 550C as seen in the shorter term aged material reported in this same quarterly.

7.2.6 Summary

The microstructure of HT-9 is remarkably stable when aged at temperatures up to 600C. Although the lath-like structure is retained due to the pinning action of very stable $M_{23}C_6$ carbides. recrystallization has occurred within the laths to produce low-dislocation density ferrite subgrains. These ferrite grains 'locked' into a lath-like structure probably account for the superior higher temperature creep and strength properties of HT-9 and the similiar ORNL modified 9Cr-1Mo alloy.

Long term aging at 600C causes some loss in toughness of HT-9 although upper shelf energies remain significant. Types of segregating species are altered considerably due to the 600C and long-term ageing compared to the short-term 550C ageing. Copper, nickel, silicon.

nitrogen. and phosphorous segregate under these conditions. In the long term. larger atoms (Cu) segregate when compared to short-term ageing. The copper and phosphorous are segregants after long-term exposures. Because at shorter times mainly sulphur and silicon segregate, long-term exposure causes further embrittlement. and this may be controlled by the copper and phosphorous impurity levels. These results have ramifications on the maximum allowable chemical specifications of HT9.

References

1. Chafey. J. and Thompson, L., 'Proceedings. Material-Environment Interactions in Structural and Pressure Containment Service Symposium.' ASME, New York. New 2.Druce, S. and Edwards. B., U.K. AEA Hartwell Report No. AERE-R9904, September 1980, Oxfordshire. U.K.
3. Bhat. M., 'The Effect of Al and Si Additions on the Microstructure and Mechanical Properties of AISI 4340.' Ph.D. Thesis. University of California. Berkeley. Calif.. 1977.
4. Qu, Z. and Kuo. K., 'Embrittlement of 2-1/4 CrMoV Steel Bolts After Long Exposure at 540°C,' Met. Trans. A, 12A (7) 1981. 1333.
5. Edwards. B., and Little. E.. Proceedings. 'Ferritic Steels for Fast Reactor Steam Generators.' BNES, London, 145, 1978.

7.3 THE EFFECT OF HYDROGEN CHARGING ON THE TENSILE PROPERTIES OF HT-9 BASE METAL

J. M. Hyzak and W. M. Garrison (Sandia National Laboratories, Livermore, CA)

7.3.1 ADIP Task

The Department of Energy (DOE) Office of Fusion Energy (OFE) has cited the need for these data under the ADIP Program Task, Ferritic Alloy Development (Path E).

7.3.2 Objective

The goal of this study is to evaluate the hydrogen compatibility of 12Cr-1Mo ferritic/martensitic steel for use in first wall and blanket structures. This report summarizes data on the effect of internal hydrogen on the room temperature tensile properties of HT-9 base metal.

7.3.3 Summary

This report summarizes results on the effect of hydrogen, introduced by cathodic charging, on the tensile properties of HT-9 from the National Fusion heat supplied by General Atomic. Three microstructures were tested; as-quenched (Q), quenched-and-tempered (Q/T), and quenched-and tempered and cold worked (Q/T/CW). These data will serve as the baseline for the continuing study of hydrogen effects on the tensile and toughness properties of HT-9 base metal and weld microstructures.

Tensile specimens were cathodically charged at 0.003 A/cm^2 and 0.006 A/cm^2 for up to 1500 minutes, immediately copper plated, and tested at room temperature. Previous testing has shown that the tensile properties of quenched-and-tempered HT-9 from a different heat were not degraded by hydrogen even at charging levels of 0.006 A/cm^2 for 150 minutes[1,2]. However, hydrogen exposure significantly affected the Q/T specimens from the National Fusion heat. Charging at 0.003 A/cm^2 for only 90 minutes reduced the tensile ductility by *63%* and changed the fracture mode from that of dimpled rupture to a combination of intergranular cracking and martensite interlath fracture. Unexpectedly, the quenched-and-tempered specimens which were cold worked (Q/T/CW) were

not as sensitive to hydrogen charging. Charging at 0.006 A/cm^2 for 150 minutes neither lowered the tensile ductility nor changed the fracture mode. This is surprising since, in general, higher strength microstructures are more severely degraded by hydrogen. Current efforts are aimed at understanding these results, and assessing their impact on the applicability of HT-9 as a first wall material.

7.3.4 Progress and Status

7.3.4.1 Experimental Procedure

Tensile tests were performed on base metal samples from the National Fusion heat of HT-9 cathodically charged with hydrogen, and copper-plated to retard outgassing. The charging solution was 4 percent sulfuric acid containing 5mg of sodium arsenate. The current densities employed were 0.003 A/cm^2 (0.02 A/in^2) and 0.006 A/cm^2 (0.04 A/in^2) for times up to 1500 minutes (Table I). Specimens were copper-plated in an acid copper bath immediately after charging, and aged at room temperature for 24 hours before testing in order to evenly distribute the hydrogen.

The National Fusion heat of HT-9 was tested with quenched-and-tempered and as-quenched (Q) microstructures. All material was austenitized at 1040°C/30 min. and air cooled; the tempering treatment was 750°/1 hr. with an air cool. In addition, the Q/T microstructure, which is of primary interest in this study, was evaluated at both the tempered (Q/T) and tempered plus cold worked (Q/T/CW) strength levels. The non cold worked specimens (Q/T, Q) were taken from plate 1-6-1 (3/8" thick) of the National Fusion heat of HT-9 supplied by General Atomic in the stress relieved condition. The cold worked specimens (Q/T/CW) were machined from material taken from plate 1-3-4 (5/8" thick) of the National Fusion heat that was cold swaged 50% after heat treating.

Tensile bars had a nominal 0.287 cm (0.113 in.) gage diameter and a 2.54 cm (1.00 in.) gage length. The tensile axis of each specimen was perpendicular to the rolling direction of the plate. All tests were run at 0.051 cm/min. (0.02 in./min.) extension rate. Following

completion of the tests, the fracture surfaces were examined by optical microscopy and SEM.

7.3.4.2 Tensile Test Results - Base Metal

The results of the tensile tests are presented in Table I. All three microstructures exhibited some degradation in properties due to cathodic charging. For the Q/T microstructure, there was a 63% reduction in ductility when the charging time was increased from 15 to 90 minutes at a current density of 0.003 A/cm^2 (this corresponds to an average hydrogen concentration of approximately 15 wt. ppm). This ductility loss represents a significant degradation in hydrogen compatibility compared to preliminary testing on Q/T specimens from a different heat of HT-9[1,2]. Earlier results had shown no loss in ductility when Q/T specimens were cathodically charged at 0.006 A/cm^2 for up to 150 minutes.

The fracture surfaces of the uncharged and moderately charged (0.003 A/cm^2 - 15 min.) Q/T specimens exhibited cup-cone centerline cracking (Fig. 1a) with a dimpled rupture fracture mode that is particularly evident at high magnification (Fig. 1b). This corresponds to the fracture mode observed for the Q/T material in the earlier study[1,2]. The loss in ductility for those specimens more severely charged was associated with an abrupt change in fracture mode. Failure resulted from a combination of classical intergranular cracking and martensite interlath fracture (Fig. 2a) At lower magnification (Fig. 2b), areas of surface connected fracture and the presence of large secondary cracks are evident. Neither of these fracture morphologies was previously observed[1,2].

The as-quenched microstructure was tested as a means of assessing in a preliminary way the hydrogen compatibility of a hardened microstructure[1,2]. First wall structures will be subject to irradiation hardening which may significantly affect the mechanical properties in the presence of injected and transmutant hydrogen. As shown in Table I, large losses in ductility, up to 76%, resulted after charging at 0.003 A/cm^2 for 15 minutes ($\sim$3.5 wt. ppm H_2). As with the Q/T results, there was significant scatter in the ductility losses even at a single charging condition.

Table I

Tensile Properties of HT-9 National Fusion Heat Subject to Cathodic Charging

Spec #*	Charging Cond.**	Yield Strength MPa (ksi)	Ultimate Strength MPa (ksi)	Reduction in Area (%)
Q/T 1	Uncharged	727 (105.5)	927 (134.4)	54.8
Q/T 4	Uncharged	694 (100.6)	909 (131.8)	56.9
Q/T 2	0.003 A/cm^2-15 min.	707 (102.5)	943 (136.7)	51.8
Q/T 6	0.003 A/cm^2-15 min.	767 (111.3)	911 (132.1)	54.4
Q/T 7	0.003 A/cm^2-90 min.	733 (106.3)	907 (131.5)	21.6
Q/T 5	0.003 A/cm^2-150 min.	735 (106.6)	920 (133.5)	33.0
Q/T 8	0.003 A/cm^2-150 min.	729 (105.8)	893 (129.5)	25.9
Q/T 3	0.006 A/cm^2-150 min.	712 (103.3)	907 (131.5)	27.6
Q 1	Uncharged	1210 (175.5)	1609 (233.3)	39.2
Q 11	Uncharged	1249 (181.2)	1613 (233.9)	41.6
Q 7	0.003 A/cm^2-15 min.	1404 (203.6)	1555 (225.6)***	9.7
Q 8	0.003 A/cm^2-15 min.	1362 (197.6)	1633 (236.8)	24.9
Q 10	0.003 A/cm^2-15 min.	1324 (192.0)	1595 (231.4)	13.6
Q 6	0.003 A/cm^2-150 min.		1056 (153.1)***	4.0
Q 9	0.003 A/cm^2-150 min.		1062 (154.0)***	3.1
Q/T /CW 1	Uncharged	1226 (177.8)	1229 (178.3)	44.0
Q/T /CW 2	0.003 A/cm^2-15 min.	1165 (168.9)	1207 (175.1)	41.4
Q/T /CW 3	0.003 A/cm^2-150 min.	1229 (178.2)	1187 (172.1)	45.7
Q/T /CW 4	0.006 A/cm^2-150 min.	1216 (176.3)	1253 (181.7)	40.1
Q/T /CW 5	0.006 A/cm^2-1500 min.	1184 (171.7)	1223 (177.4)	19.3

*Q/T Quenched-and-Tempered
Q/T/CW Quenched-and-Tempered, Cold Worked
Q As-Quenched

**Current Density (amps/cm^2) and Charging Time (minutes)

***Fracture Stress

(a)

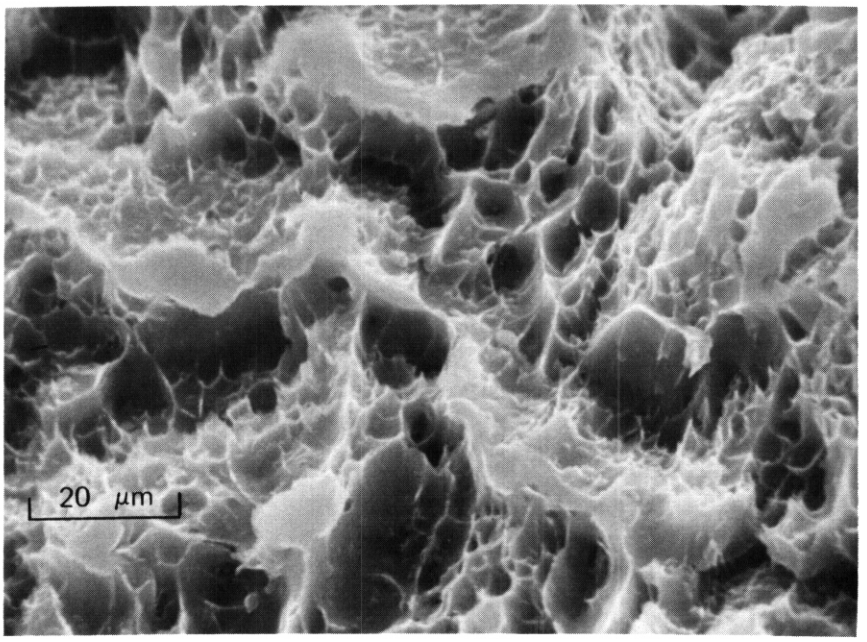

(b)

Figure 1. SEM fractographs of HT-9 quenched-and-tempered (Q/T) tensile specimen, uncharged: (a) low magnification of cup-cone fracture; (h) high magnification showing dimpled rupture fracture mode.

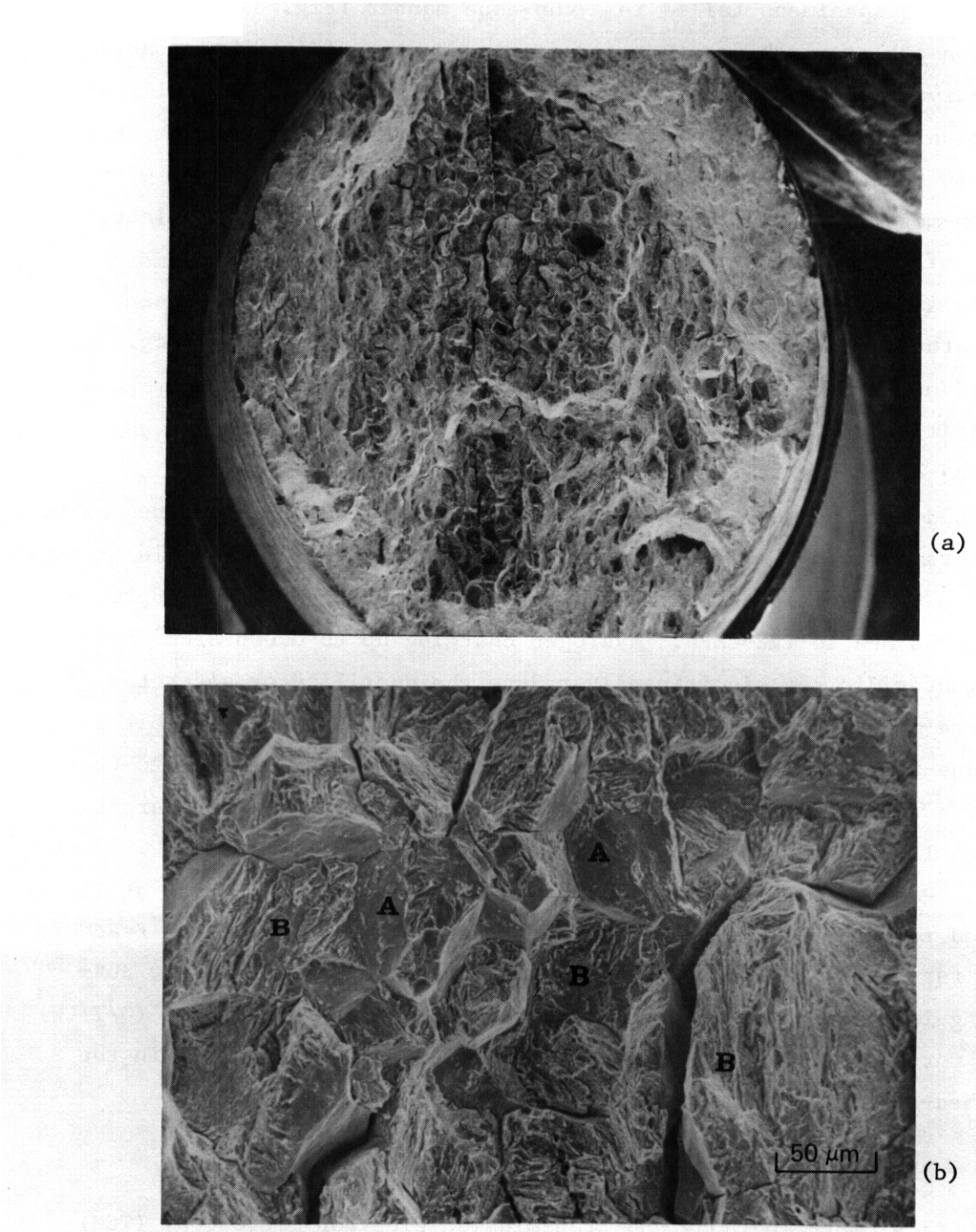

Figure 2. SEM micrographs of HT-9 Q/T tensile specimen from National Fusion heat, hydrogen charged at 0.003A/cm^2 for 90 minutes: (a) low magnification of brittle fracture surface revealing parallel secondary cracks; (b) higher magnification showing regions of intergranular cracking (A) and martensite interlath fracture (B).

The fracture morphology was again a function of hydrogen content. Uncharged Q specimens failed in a cup-cone manner (Fig. 3a) by a combination of interlath fracture and dimpled rupture (Fig. 3b). Large secondary cracks were also present which run parallel to the rolling direction of the plate. Although the cause of these large cracks has not been positively identified, they are most likely associated with the non-metallic inclusions and solute banding in the rolling plane. After cathodic charging, the as-quenched specimens failed in a more brittle manner. The fracture mode changed from dimpled rupture and interlath fracture to entirely martensite interlath cracking (Fig. 4a). Instead of the cup-cone fracture mode. there were large areas of surface initiated fracture (pig 4b) which may be indicative of a hydrogen assisted crack growth type of failure sequence.

Cold working was also used as a means of producing a hardened microstructure for compatibility testing. Swaging increased the yield strength of the Q/T material 78%, to 1226 MPa, and raised the UTS from approximately 918 MPa to 1229 MPa. Hydrogen charging up to 0.006 A/cm^2 for 150 minutes did not significantly reduce the ductility or alter the fracture mode for the Q/T/CW specimens. Fracture surfaces exhibited cup-cone fracture with a dimpled rupture fracture mode similar to that reported for the Q/T unembrittled specimens. Increasing the charging time to 1500 minutes at 0.006 A/cm^2 resulted in a dramatic loss in ductility. However, even with only 19.3% R_A, the fracture mode was still dimpled rupture (Fig. 5) and not the intergranular or interlath fracture noted for the Q/T hydrogen charged specimens. These results are surprising in that one would expect the higher strength conditions (Q/T/CW) to be more susceptible to hydrogen embrittlement than material in the quenched-and-tempered state.

7.3.4.3 Alloy Characterization - Base Metal

Optical metallography and transmission electron microscopy (TEM) have been initiated to characterize the three microstructures (Q/T, Q/T/CW, Q). TEM studies to date have shown that the as-quenched material consists of lath martensite with retained austenite between the laths

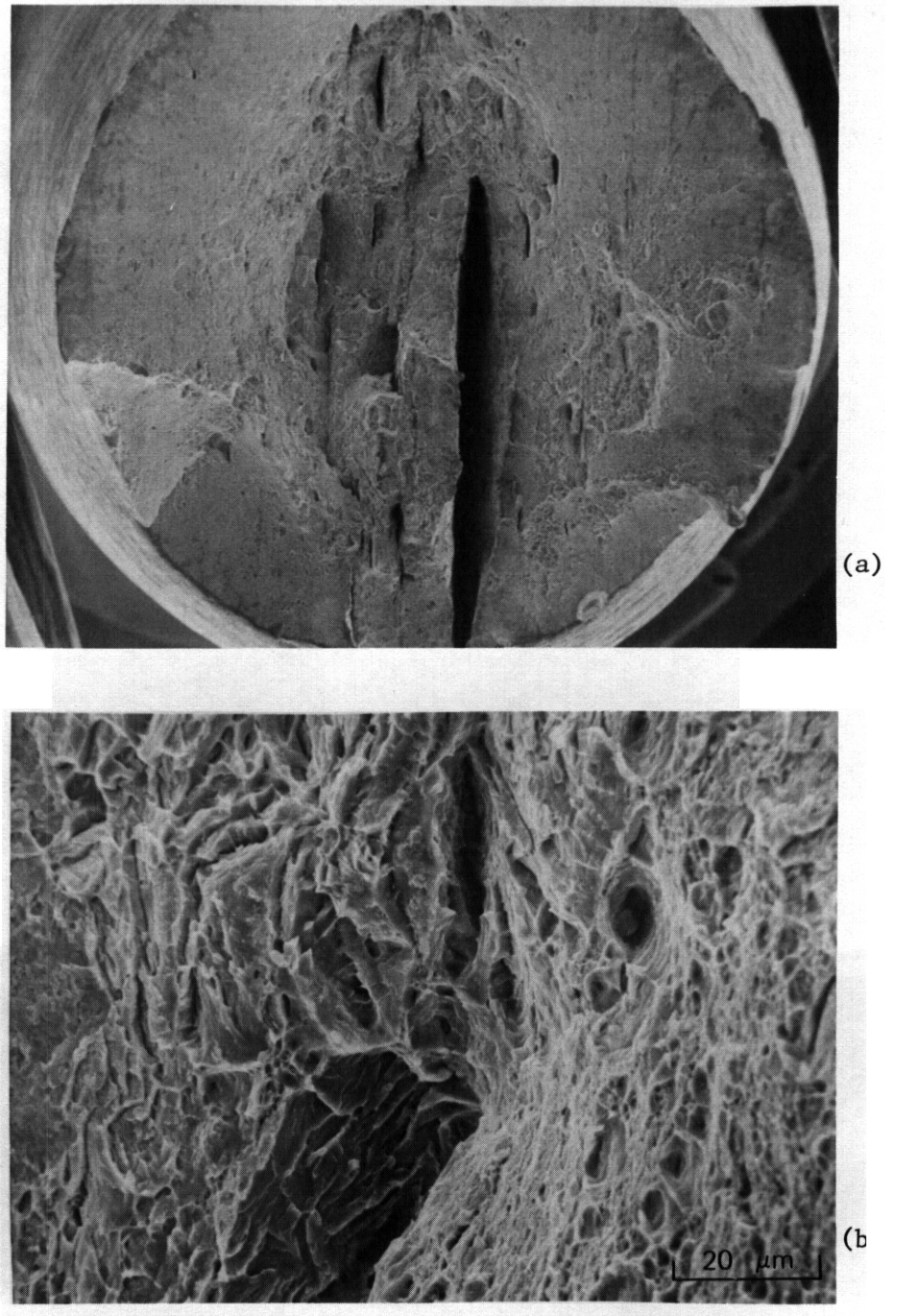

Figure 3. SEM fractographs of HT-9 as-quenched (Q) tensile specimen, uncharged: (a) low magnification *of* cup-cone fracture and large secondary cracks; (b) higher magnification showing fracture mode of dimpled rupture and martensite interlath cracking.

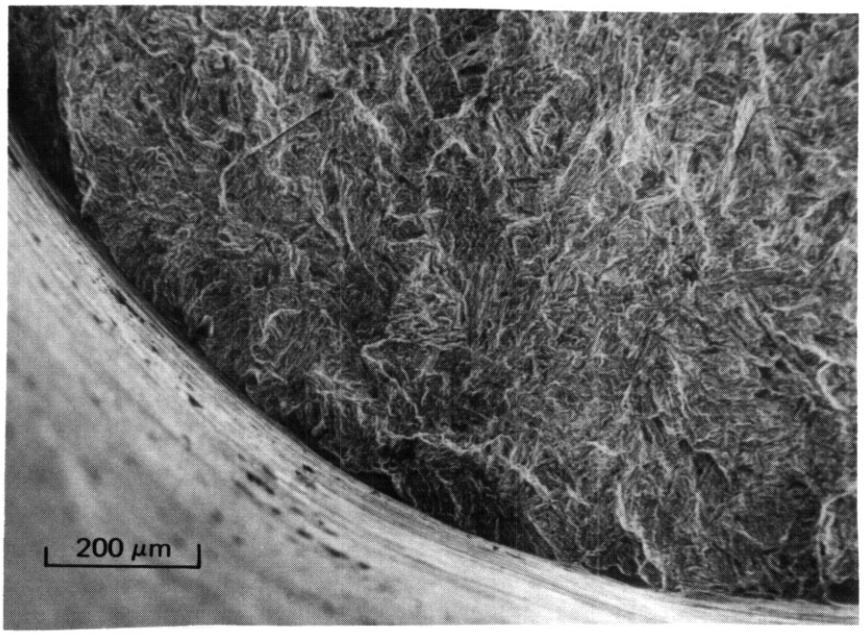

(a)

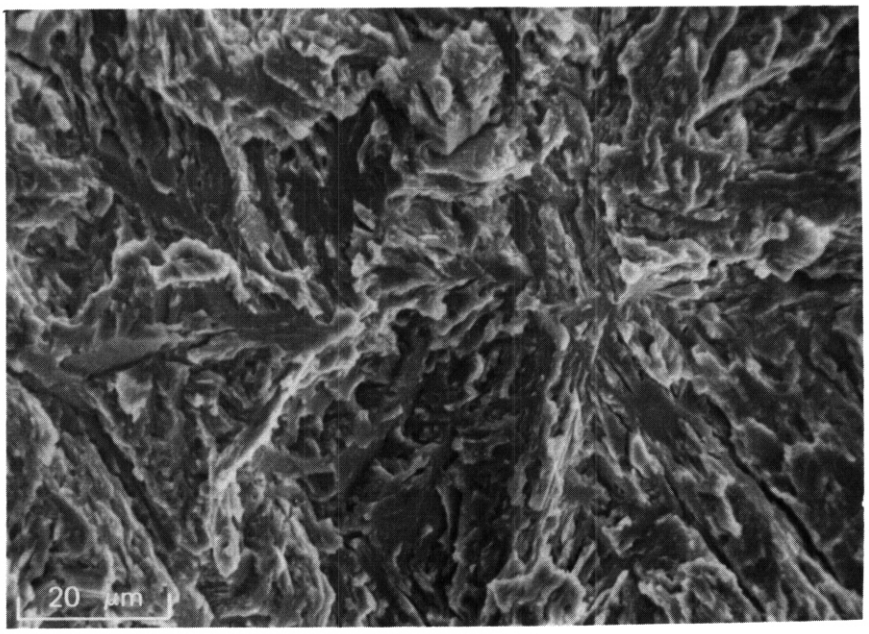

(b)

Figure 4. SEM fractographs of HT-9 as-quenched (Q) tensile specimen; charged at 0.003A/cm^2 for 15 minutes: (a) low magnification showing surface connected brittle fracture; (b) higher magnification revealing martensite interlath fracture mode.

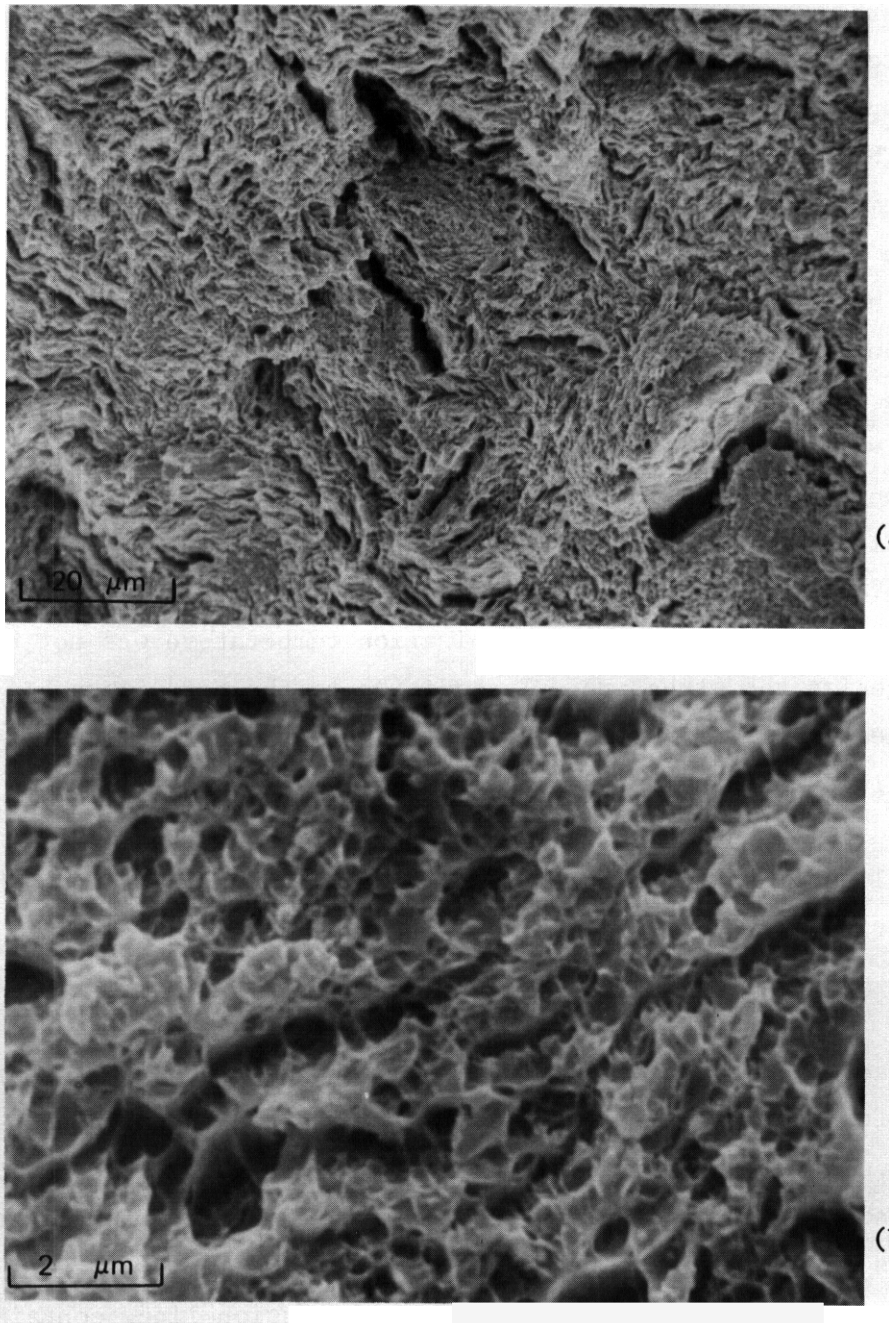

Figure 5. SEM fractographs of HT-9 quenched-and-tempered and cold worked (Q/T/CW) tensile specimen, charged at 0.006A/cm^2 for 1500 minutes: (a) "woody" type of fracture appearance; (b) higher magnification revealing dimpled rupture fracture mode.

(Fig. 6). Precipitation of intra-lath carbides was also observed in this material (Fig. 7). Upon tempering, the as-quenched martensite decomposes to a duplex structure of ferrite and large alloy carbides. These carbides precipitate early-on at the martensite lath boundaries. As the tempering time increases, these carbides coarsen, and the martensite transforms to ferrite of low dislocation density and low carbon content. The former martensite lath boundaries are, however, still evident after tempering, as they are decorated by large alloy carbides (Fig. 8).

The surprising behavior of the Q/T microstructure when hydrogen charged has focused particular attention on characterization of the inclusion content, chemical segregation and banding. Preliminary results indicate that there are numerous non-metallic and ferrite stingers in plates 1-6-1 and 1-3-4 of the National Fusion heat. In the as-quenched condition, specimens from plate 1-6-1 showed a large amount of ferrite banding indicating significant chemical segregation (Fig. 9a). Banding was also observed in the quenched-and-tempered microstructure (Fig. 9b) perhaps indicating that the austenization temperature was not high enough to homogenize the structure. In addition to the metallographic examination, electron microprobe analysis will be performed to identify the segregating elements in the bands. Several specimens will also be fractured in the scanning Auger microprobe in order to identify the elemental species at the grain boundaries which may be responsible for the intergranular failures observed after hydrogen charging.

7.3.4.4 Tensile Testing - Weld Metal

In addition to testing of base metal properties, the research program for the near term includes evaluating the hydrogen compatibility of particular HT-9 weld microstructures. Lippold [3,4] has previously identified four distinct microstructures in the heat affected zones of GTA welds in HT-9. These regions are:

1. A two phase region adjacent to the fusion line, containing martensite and a small proportion of ferrite;

2. A fully martensitic region exhibiting a relatively coarse prior austenite grain size;

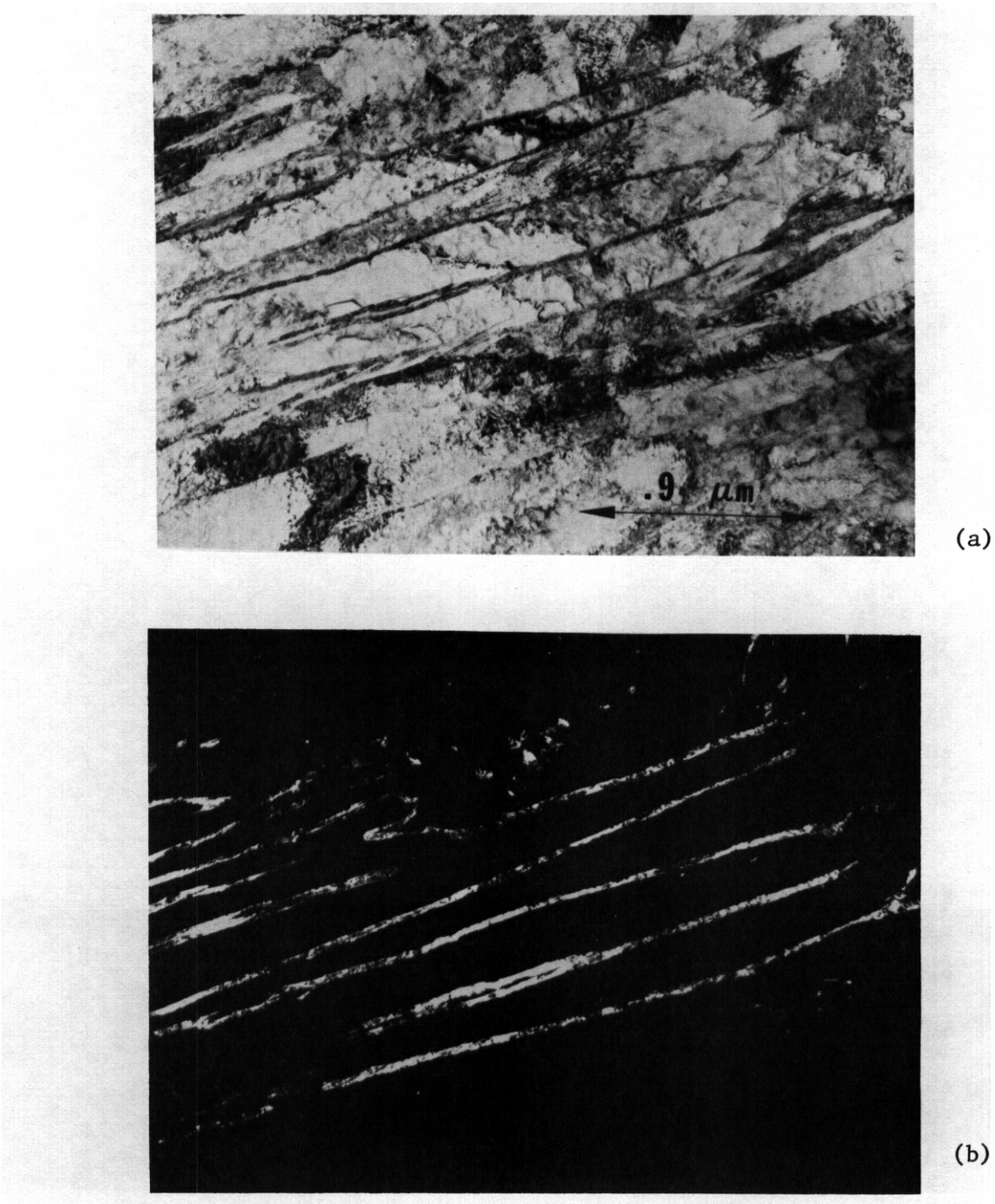

Figure 6. TEM micrographs of HT-9 in the as-quenched condition: (a) a bright-field image of the martensite laths; (b) a dark-field image of the inter-lath retained austenite.

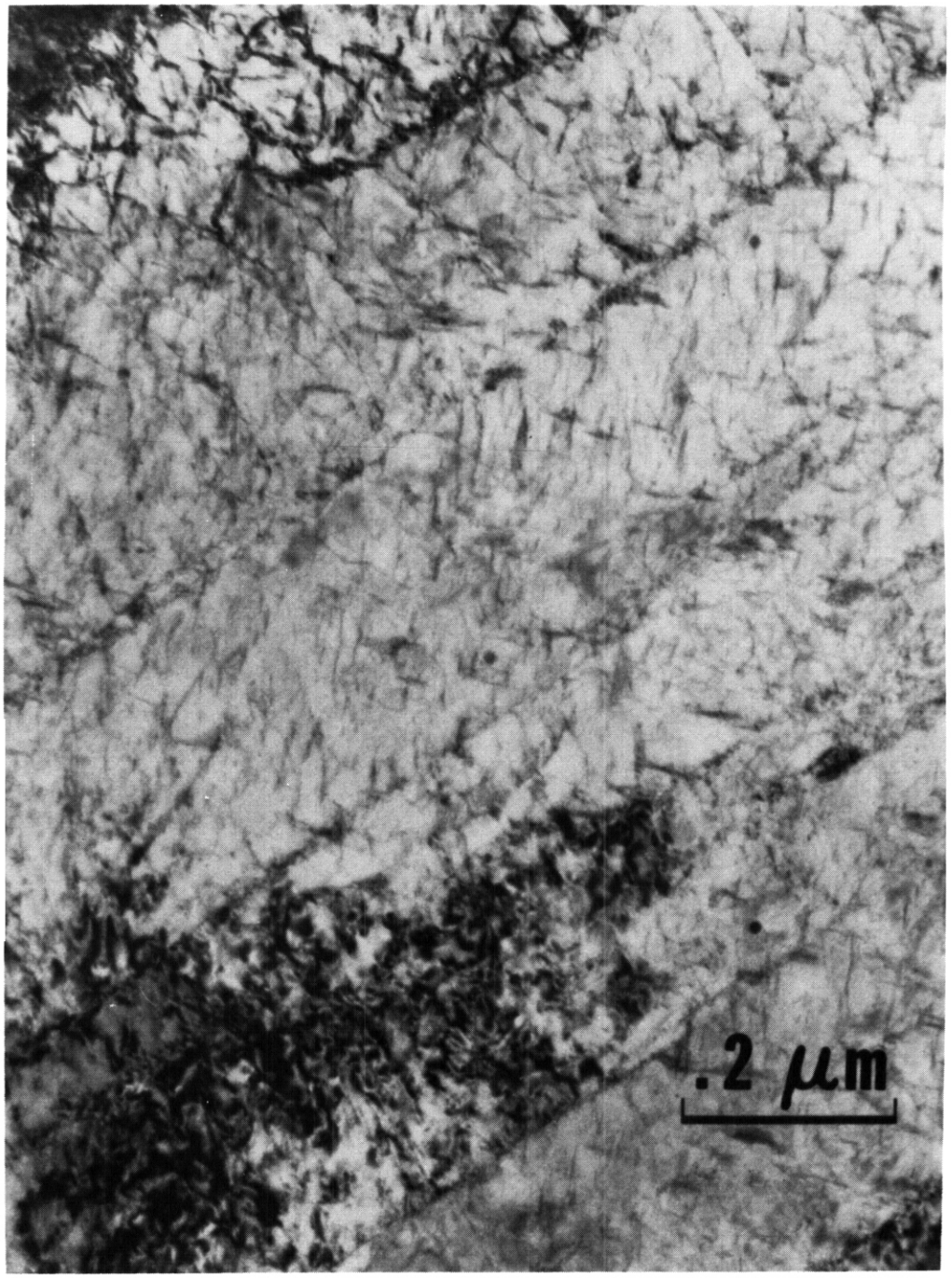

Figure 7. TEM micrograph of *ET-9* in the as-quenched condition. Fine carbides have precipitated within the martensite laths.

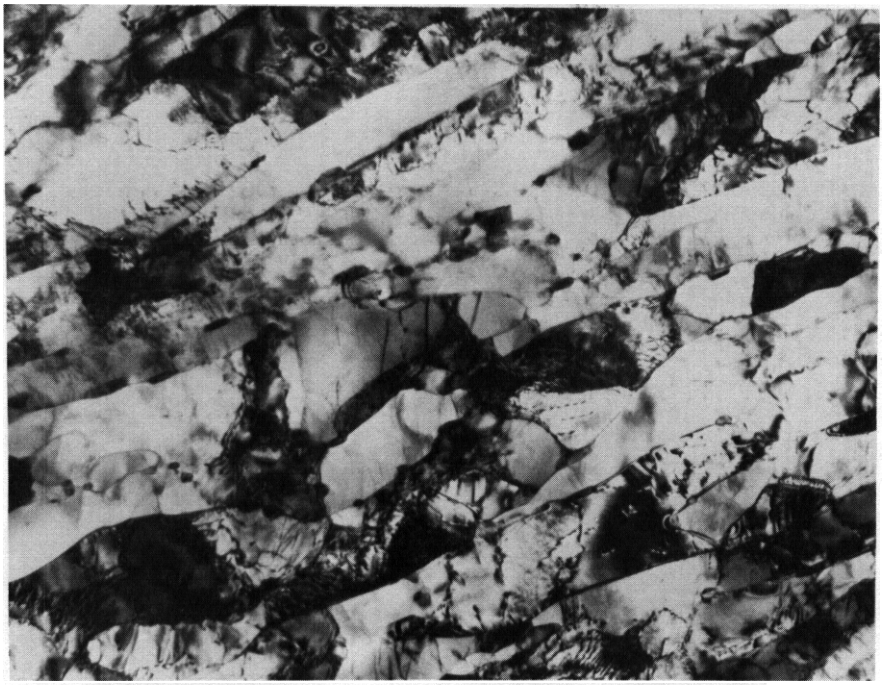

(a)

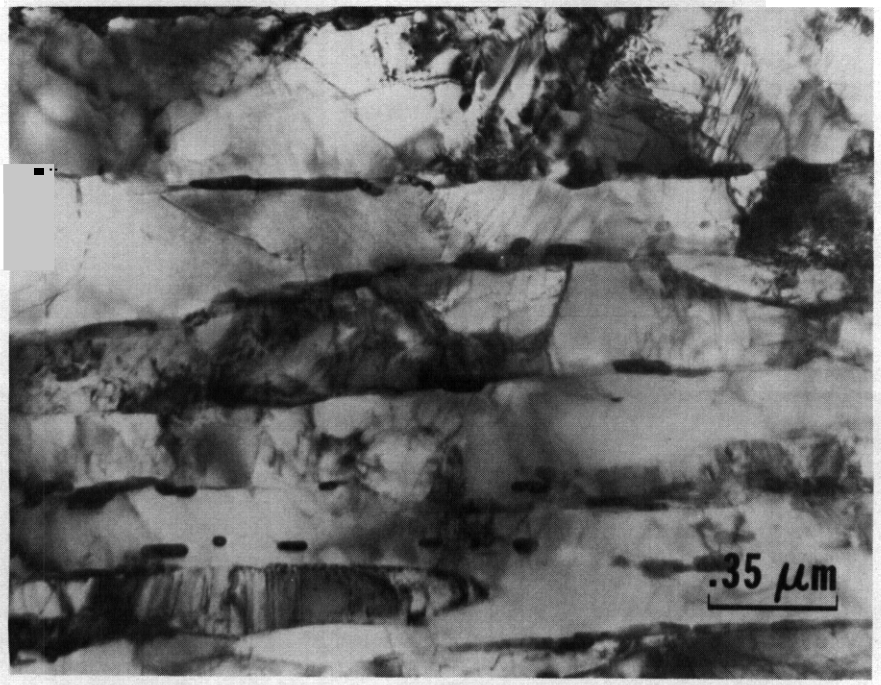

(b)

Figure 8. TEM bright-field micrographs of HT-9 in the quenched-and-tempered condition. Micrographs illustrate the fine grain size of the ferritic matrix; (b) large alloy carbides are shown delineating the prior martensite lath boundaries.

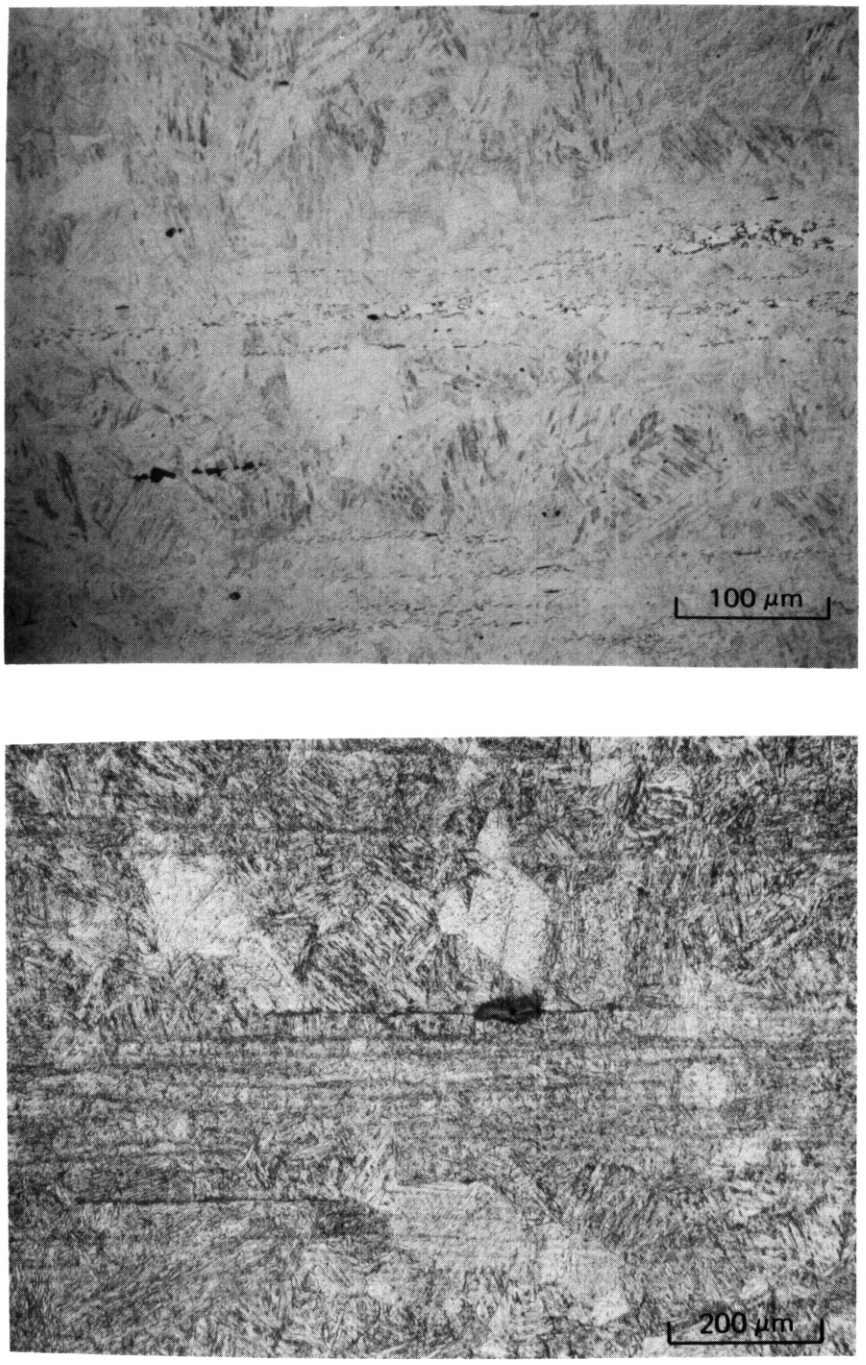

Figure 9. Optical micrographs of banding in HT-9 plate 1-6-1 of National Fusion heat: (a) ferrite banding in as-quenched specimens; (b) banding in quenched-and-tempered microstructure.

3. A martensitic region exhibiting a finer prior austenite grain size and undissolved carbides;

4, An overtempered base metal microstructure containing martensite and carbides.

Tensile specimens have been heat treated using the Gleeble programmable thermo-mechanical generator to simulate microstructures #1 and #2. These were chosen to be tested first since they include a two phase microstructure and the microstructure with the highest hardness, respectively. Cathodic charging and testing of these specimens will begin shortly.

7.3.4.5 Discussion

The tensile results of the cathodically charged base metal specimens from the National Fusion heat of HT-9 present some reason for concern. In a preliminary study of HT-9 material from another source, hydrogen did not significantly affect the tensile ductility of the quenched-and-tempered microstructure at charging levels up to 0.006 A/cm^2 for 150 minutes[1,2]. From these data it was concluded that the hydrogen compatibility of HT-9 base metal should not be a problem for first wall applications. Results on the National Fusion heat of material are dramatically different, however. Hydrogen effects including a 63%loss in ductility and a change in fracture mode to intergranular fracture were observed for the Q/T specimens at charging levels as low as 0.003 A/cm^2 for 90 minutes. It was also unexpected that the quenched-and-tempered material which had been cold worked to 1226 MPa yield strength was considerably more hydrogen tolerant than the Q/T material tempered to 727 MPa. Research is now focusing on how to explain these observations. Present concerns include understanding the influence of banding and non-metallic inclusions on the failure process. The effect of retained austenite on hydrogen compatibility may also be of importance. Plans also include the testing of specimens that have undergone a homogenization heat treatment to reduce elemental segregation.

The results of the cold worked Q/T specimens are encouraging, however. They indicate that a hardened microstructure with a yield strength of 1226 MPa can still be relatively hydrogen compatible. Embrittlement

was not observed until hydrogen levels well above 15 wt. ppm were attained. These levels are considerably greater than those anticipated in a first wall application[5]. It should be noted that even at these hydrogen concentrations, the Q/T/CW specimens failed by dimpled rupture and not by intergranular fracture. This indicates that hydrogen did not cause any substantial reduction in fracture strength of the grain or martensite lath boundaries.

The as-quenched specimens were as susceptible to hydrogen attack as had been reported previously[2,6]. Low level cathodic charging (0.003 A/cm^2-15 min.) resulted in a large decrease in ductility and a change in fracture mode. It has been proposed that retained austenite at the lath boundaries may be responsible for the pronounced hydrogen susceptibility[2,6]. The austenite phase is mechanically unstable, and it most likely transforms to a twinned martensite structure during tensile straining. The resulting high carbon martensite is particularly brittle and may lead to interlath fracture. Transmission electron microscopy of the as-quenched material has confirmed the presence of retained austenite at the lath boundaries.

7.3.5 Conclusions

Tensile testing of hydrogen charged specimens from the National Fusion heat of HT-9 indicates:

1. Quenched-and-tempered material can be susceptible to embrittlement at hydrogen levels above 'L5 wt. ppm. However, this finding is contray to earlier results on a different heat of HT-9. Microstructural reasons for the difference in behavior are being sought.

2. Quenched-and-tempered HT-9 that had been cold swaged to increase the strength level was particularly tolerant of hydrogen; charging to levels of 'L15 wt. ppm did not significantly affect the ductility or fracture mode.

3. The as-quenched microstructure is very susceptible to hydrogen embrittlement. Cathodic charging to ~3.6 wt. ppm hydrogen reduced the ductility to less than 10%RA.

4. Metallographic examination showed extensive banding in the National Fusion heat material. Ferrite stingers were particularly evident

indicating local chemical inhomogeniety. SEM analysis of the fracture surfaces of various specimens also indicated severe secondary cracking in similar orientation to the banding and stingers. Electron microprobe and scanning Auger analysis are continuing to determine the segregants and their relationship to the fracture process.

7.3.6 References

1. J. M. Hyzak and R. E. Stoltz, "The Effect of Internal Hydrogen on the Mechanical Properties of HT-9: Room Temperature", ADIP Quarterly Progress Report, March 31, 1981, DOE/ER-0045/6, pp. 180-190.

2. J. M. Hyzak and R. E. Stoltz, "Hydrogen Compatibility of HT-9 Martensitic Stainless Steel", Proceedings Second International Conference on Fusion Reactor Materials, American Nuclear Society/American Society for Metals, Seattle, May, 1981 (to be published).

3. J. C. Lippold, "Weldability of HT-9: The Autogeneous GTA Process", ADIP Quarterly Report, March 31, 1980, DOE/ER-0045/2, pp. 98-108.

4. J. C. Lippold, "Microstructural Characterization of Autogeneous GTA Welds in a 12Cr-1Mo-0.3V Steel", SAND80-8236, Sandia National Laboratories, Livermore, CA, 1980.

5. R. E. Stoltz, M. I. Baskes, and G. W. Look, "Calculations of Hydrogen Isotope Loading in HT-9 First Wall Structures", ADIP Quarterly Report, September 30, 1980, DOE/ER-0045, pp. 151-159.

6. R. M. Horn and R. O. Ritchie, Met. Trans., 9A, 1978, pp. 1039-1053.

7.4 INTERPRETIVE REPORT ON THE WELDABILITY OF 12Cr-1Mo-.3V-.5W (HT-9) MARTENSITIC STEEL FOR USE IN FIRST WALL/BLANKET STRUCTURES IN FUSION REACTORS - PART 1, A REVIEW OF CURRENT TECHNOLOGY -

J. C. Lippold (Sandia National Laboratories) and
T. A. Lechtenberg (General Atomic Company)

7.4.1 ADIP Task

The Department of Energy (DOE)/Office of Fusion Energy (OFE) has stated the need for this investigation under the ADIP program task, Ferritic Steels Development (Path E).

7.4.2 Objective

Considerable effort within the ADIP Path E Development Group has been focused on the weldability and fabrication issues associated with the candidate alloy HT-9. Initial programs at both General Atomic and Sandia have addressed the issues of welding processes. welding variables. preheat and post-weld heat treatment. and the accompanying microstructural and mechanical property changes in the heat affected zone (HAZ) and fusion zone. The purpose of this report is to review the work which has been completed within the ADIP Path E program in an effort to establish guidelines for the welding of HT-9 and to identify areas of future research which will be critical for the successful fabrication of complex structures for fusion machines.

7.4.3 Summary

A review of the current literature. industrial experience in both the U.S. and Europe. and the results of research performed under the ADIP Path E program has resulted in a number of observations and recommendations regarding the weldability and long term integrity of HT-9. In the opinion of the authors. the weldability characteristics of HT-9 does not preclude this alloy from consideration as a first wall/blanket material for fusion machines. Indeed. weldability observations on this alloy. to date. are encouraging. However. although the transformation and tempering response of the fusion zone and heat-affected zone (HAZ)

has been well characterized. optimization of the welding process and process parameters will be necessary in order to successfully fabricate the first wall modules. In particular. there are several factors which may affect weld joint integrity and must be studied to further define the weldability of HT-9. These include evaluation of the effects of hard triaxial restraint. discontinuities and defects. delay time prior to post-weld heat treatment and horizontal and vertical weld positions. In addition, the weldability and weld integrity of product forms pertinent to first wall/blanket structures must be studied. Evaluation of these aspects is the next logical step in determining whether reliable weld joints of HT-9 can be fabricated in the shop or field. Both the gas tungsten-arc (GTA) and laser welding processes have been demonstrated as suitable techniques for joining HT-9. although the choice of laser welding as a primary or secondary joining process will require considerable process control to ensure reliable welded joints. Finally. in order to optimize both the welding process and the postweld heat treatment (PWHT) which will be required it is necessary to determine the minimum mechanical properties necessary to ensure the fabrication and safe operation of fusion reactor devices.

The second part of this report to be published in a future ADIP quarterly will focus on areas of future research which will be necessary to qualify HT9 weldments for use in irradiation and hydrogen environments.

7.4.4 Progress and Status

This report presents a review and evaluation of the available literature concerned with the welding and metallurgy of the 12Cr-1Mo-.3V-.5W (HT-9) martensitic stainless steels. Commercial experience has demonstrated that these materials are readily weldable if proper precautions are taken regarding preheat and post-weld heat treatment (PWHT). However, the heat treatments necessary to ensure good welding behavior and extended service reliability are stringent when compared to alloys such as austenitic stainless steels. Therefore, it is necessary to assess the sensitivity of the martentsitic steels such as HT-9

to weld process control and the implications of the required controls with respect to field or shop fabrication of typical fusion device first wall structures. As a result. the initial Path E tasks have focused on the optimization of the welding processes and/or variables to minimize the need for preheat and PWHT. The following section reviews producer-recommended (Sandvik) experience and recent **ADIP** sponsored research which are germane to the subject of weldability and joint integrity of HT-9.

7.4.4.1 Producer's Recommendations

Sandvik alloy HT-9 is a commercially available 12Cr-1Mo-.3V-.5W steels with 0.20C. **It** is fully martensitic and air-hardenable. **It** was originally developed for use in mildly corrosive environments at temperatures up to 650C (1200F) (Ref. 2). The material may be welded using shielded metal arc (SMA), gas tungsten arc (GTA), or gas metal arc (GMA) welding processes. Sandvik recommends that the weld joint be preheated to 200-400C (390-750F). The pre-welding thermal treatment is used to slow the weld cooling rate. reduce the thermal shock to the weld region. and to drive off any moisture and hydrocarbons absorbed on the plate surface. In the case of multipass welds an interpass temperature of 250C (480F) is sometimes specified to prevent the transformation to untempered martensite which occurs upon cooling to **room** temperature. Finally, a martensite post-weld heat treatment (PWHT) in the temperature range of 740-780C (1365-1470F) for 1/2-2 hours is required immediately following welding. Parts must be handled carefully between the welding and tempering operation since the regions of hard. untempered martensite are present in the fusion zone and a portion of the HAZ.

7.4.4.2 Commercial Experience

Heat treatable. high strength. creep resistant steels containing 12%Cr have seen extensive use throughout the world since the early 1950s. A wide variety of such steels are available and they have been utilized in a diversity of applications.

In the U.S. the major applications of steels of this type have been in steam turbines, jet engines. gas turbines. etc. Alloys such as AISI types 410. 420. 422 and various modifications (e.g., Greek Ascoloy. Lapelloy. Chromodur) have been used in components of such systems in applications where moderate corrosion resistance and good retention of strength at elevated temperature are required.

In Europe the alloys have seen similar usage. In addition. the Europeans have made very widespread use of certain alloys of this type in elevated temperature, pressure containment applications including steam piping and steam generator reheater and superheater tubing.

Two of the larger users of 9-12%Cr steels in steam generators for fossil fired plants in Europe have been Sulzer Brothers (Switzerland) and the United Kingdom Central Electricity Generating Board (CEGB). Of particular interest is the relatively few weld failures. Only two failures have been reported which related directly to welding.

Another major European application of, specifically. X20CrMoV(W) 121 (a German steel of HT-9 type) has been in steam piping. A tabulation of some of the typical service history data for such piping is shown in Table 7.4.1. As indicated, the steel has been used in these applications for 20 years and has been used in large diameter heavy walled piping.

The latter is particularly important since all the piping is welded and welding is recognized as one of the more difficult aspects of the martensitic/ferritic steels. The Europeans have developed welding procedures suitable for the fabrication of pipe up to 30 in. diameter with walls up to 2 in. thick.

The strength of welds in alloys of this class is another subject that has received attention in European studies and available data suggests that welds exhibit both short and long time properties that adequately match the base metal. Likewise. European concern about retention of adequate toughness properties after long time elevated temperature service has resulted in the generation of 50.000 hrs. laboratory aging data showing that alloys similar to HT-9 indeed retain good toughness. These laboratory aging data have been confirmed by

Table 7.4.1.

Typical Service Data for X20CrMoV(W)121 Steam Piping

Plant Data			Main Steam			Reheat Steam					
Name	Location	Size (MW)	Press (atm)	Temp (°C)	Pipe o.d.(ins.)	Pipe ll(ins.)	Press (atm)	Temp (°C)	Pipe o.d.(ins.)	Pipe wall (ins.)	Start Up Year
Arzberg	FRG	300	220	540	11	1.4	55	540	17	0.5	1974
Neurath A,B,C,	FRG	300	200	535	14	1.3	--	---	--	---	1972
Neurath D,E	FRG	600	195	535	20	1.8	--	---	--	---	1975
Weisweiler G,H,	FRG	600	195	535	20	1.8	--	---	--	---	1974
Frimmersdorf Q	FRG	300	200	535	14	1.3	--	---	--	---	1970
Robert Frank IV	FRG	450	286	540	8.5	1.4	--	---	--	---	1973
Lausward	FRG	300	215	540	12	1.5	55	540	29	1.4	1976
Asnaesvaerket	Denmark	255	210	545	9	1.0	--	---	--	---	1968
Stigsnaevaerket	Denmark	250	210	560	9	1.3	--	---	--	---	1969
Skaerbackvaerket	Denmark	250	190	545	11	1.3	--	---	--	---	1969
IS Vestkraft	Denmark	250	193	545	12	1.2	--	---	--	---	1969
Studstrupvaerket	Denmark	250	174	545	13	1.4	--	---	--	---	1972
Fynsvaerket	Denmark	256	185	535	8	0.9	--	---	--	---	1974
NEFO Kraftwerk	Denmark	300	199	535	13	1.6	--	---	--	---	1976
Hanasaari	Finland	150	160	535	9	1.1	--	---	--	---	1973
KW Amer-Centrale	Holland	175	195	575	6	1.3	--	---	--	---	1960
Centrale-Velsen	Holland	460	181	535	18	2.0	--	---	--	---	1974
KW Maasvlalete	Holland	550	199	540	17	1.9	--	---	--	---	1974
KW Rovinari	Rumania	330	196	540	10	1.2	--	---	--	---	1974
KW Wolfersheim	FRG	65	210	550	7.5	0.9	--	---	--	---	1962
KW Standinger	FRG	250	260	545	9	1.3	--	---	--	---	1964
Robert Frank III	FRG	300	260	545	10	1.4	--	---	--	---	1967
KW Westfalen	FRG	320	226	550	12	2.0	--	---	--	---	1968
GKW Weser Veltheim	FRG	300	198	535	13	1.4	--	---	--	---	1969
KW Offleben C	FRG	325	181	525	10	1	--	---	--	---	1972
KW Gertsheinwerk	FRG	?	181	530	13	1.4	--	---	--	---	1972
KW Franken I	FRG	300	225	540	14	1.8	--	---	--	---	1972
KW Neideraubein	FRG	600	175	530	18	1.5	--	---	--	---	1973
KW Lunen	FRG	?	136	525	10	0.7	--	---	--	---	1971

Table 7.4.1. (Cont'd.)

Typical Service Data for X20CrMoV(W)121 Steam Piping (Continued)

Name	Location	Size (MW)	Main Steam Press (atm)	Main Steam Temp (°C)	Main Steam Pipe o.d. (ins.)	Main Steam Pipe wall (ins.)	Reheat Steam Press (atm)	Reheat Steam Temp (°C)	Reheat Steam Pipe o.d. (ins.)	Reheat Steam Pipe wall (ins.)	Start Up Year
KW Moorberg	FRG	515	215	540	16	2	--	---	--	---	1973
KW Scholven	FRG	714	210	535	19	2.2	--	---	--	---	1974
KW Emsland	FRG	365	181	530	13	1.4	--	---	--	---	1974
KW Frauken	FRG	300	225	540	14	1.8	--	---	--	---	1975
KW Veltheim	FRG	450	235	540	12	1.8	--	---	--	---	1975
KW Huckingen	FRG	300	176	530	13	1.3	--	---	--	---	1975
HKW Niehler Hafen	FRG	300	178	540	13	1.6	--	---	--	---	1975

independent tests performed at General Atomic on a section of X20CrMoV(W)121 boiler tube that had been exposed for 80,000 hrs. at 600°C (1112°F) in a German boiler superheater (Ref. 3). Comparison of the properties of the tube after service with that of archive material showed that the exposed material retained remarkably good residual toughness. These experimental data corroborate the good long time service experience with high temperature, pressure-containing welded structures in these materials.

7.4.4.3 Weld Process/Parametric Optimization

Industrially recommended weld practices for HT-9 include a preheat. interpass temperature control. cool-down control following welding, and a post-weld heat treatment. Recommended preheats range from 200-400C for thicknesses greater than 1.0 cm. although, generally, there is no industrially recognized bounds placed on this requirement. Only two fabricators (Sulzer and Brown- Boveri) stipulate interpass temperature control, the ranges suggested are 430-500C or 120-150C. Some manufacturers/fabricators require the weld be allowed to cool no lower than 120-150°C following welding and prior to the PWHT. Post-weld heat treatment is required by all producers and fabricators. and generally ranges from 720-780C for 1.5-2.0 hr. These recommendations indicate that there is some latitude in welding HT-9 and that the required process controls area function of specific components' configurations or weld methods. For this reason. the weld parameter study was initiated with the objective of defining precisely which conditions are required and what latitude exists for welding HT-9. Restrained welds were made to ensure that the as-welded joint resisted fracture under stress because this would be the minimum case for any realistic component condition.

In the weld parameter study. welds have been made using the GTA process on thicknesses from .35-1.3 cm with preheats from 100-300C, interpass temperatures from 100-300C, and post-weld heat treatments of760C for 2-1/2 hr (Ref. 4). All material had been heat treated to the industrially standard condition prior to welding (1050C, 1/2 hr; 760C, 2-1/2 hr; both followed by air-cooling). In the study to date.

preheating has had two effects, (1) higher preheat temperatures will increase the upper-shelf energy slightly. and (2) higher preheats tend to reduce weldment quality in the thicker section welds. The first effect had been reported earlier and was attributed to a tempering effect from the higher thermal input (Ref. 4). The second effect is seen in that the weld puddle tends to be less easily controlled at higher preheat temperatures.

There has been no cracking observed in any weld process studied thus far which required the rejection of the weldment according to ASME Code Section IX acceptance standards for dye penetrant and radiographic examination. More severe restraint. such as in thicker welds and components. may exacerbate cracking.

Preliminary conclusions from this study indicate that there is some latitude in welding plates in a laboratory full-restraint condition. although strict adherence to technique will be required. There are indications that preheat temperature can be minimized. which will facilitate welding of components, although this will require further study. This will be greatly dependent upon the design used for any component. and it must be emphasized that the configuration of a first wall module may require further optimization of weld techniques. Interpass temperature control has had no significant effect in this laboratory study. Still. a massive structure may have to sit idle in the as-welded condition prior to PWHT and may require some type of intermediate stress relief. The high strength of the as-welded joint in a stressed condition (i.e., a structure) may be prone to delayed cracking. It is proposed that some welded joints be exposed to moisture while still restrained to determine the proclivity of slow crack growth.

An investigation was initiated at Sandia in conjunction with the Naval Research Laboratory (NRL) to evaluate the effect of laser welding parameters on the quality of bead-on-plate weldments (Ref. 5). A 15kW continuous wave CO_2 laser located at NRL was utilized in this investigation. Welds were made in unrestrained 6.35mm HT-9 plate using a variety of travel speed/focal length combinations at a constant laser

power level of 6kW. Welds performed at sharp focus (at the plate surface) with weld travel speeds from 1.27 to 4.23 mm/sec exhibited scattered porosity and occasional centerline cracking. Defocusing the laser beam either above or below the plate surface produced welds which exhibited severe porosity and centerline cracking, as shown in Fig. 7.4.4.1.

It should be pointed our. however. that this study was not designed to optimize the laser welding process but, rather, to determine the sensitivity of the alloy to a wide range of welding parameters. Numerous welds were produced at sharp focus which were free of both porosity and cracking. Use of the laser welding process as a fabrication tool will require more extensive optimization based upon these initial results.

7.4.4.4 Transformation and Tempering Behavior of the GTA and Laser Welds

During the welding of the 12Cr-1Mo-0.3V martensitic stainless steels the fusion zone and portions of the HAZ near the fusion line are transformed to untempered martensite. The presence of this constituent in the microstructure severely reduces the fracture toughness of the weld region and, consequently. necessitates a stringent postweld heat treatment to restore acceptable mechanical properties. In order to determine how the welding process and selection of welding parameters may affect both the transformation and tempering response of the fusion zone and HAZ the microstructural evolution during the welding and subsequent tempering of laser at GTA welds was evaluated (Refs. 6,7,8).

The as-welded microstructure in the HAZ of a GTA weld in HT9 was related to the behavior predicted by the Fe-Cr-C equilibrium phase diagram, as illustrated in Fig. 7.4.4.2. The microstructure exhibited four distinct regions:

1. A two-phase region at the fusion line consisting of untempered martensite and ferrite. the ferrite being distributed along prior austenite grain boundaries;

EFFECT OF FOCAL DISTANCE

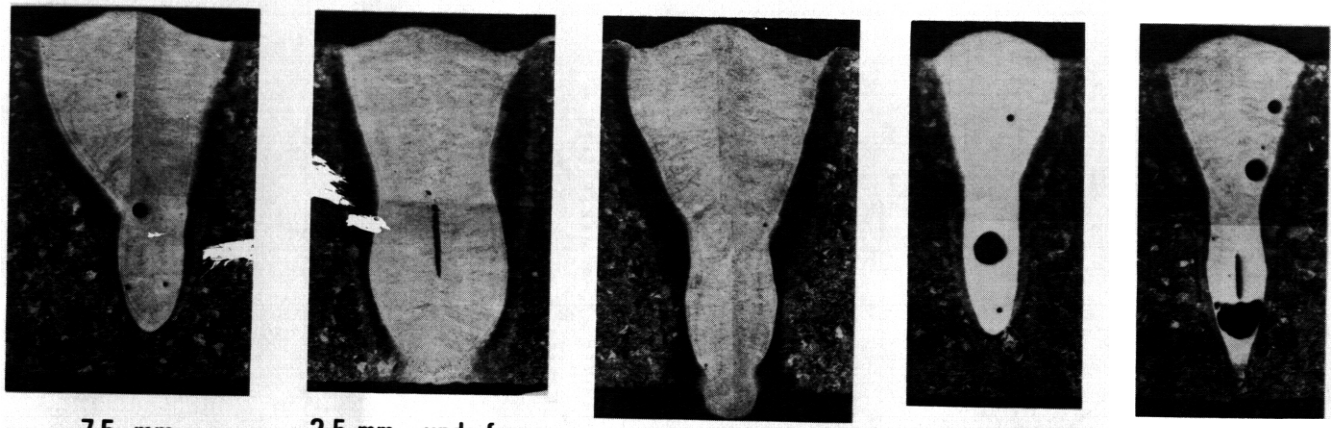

7.4.4.1 The Effect of Focal Distance Relative to the Plate on the Weld Integrity of HT9 Laser Welds

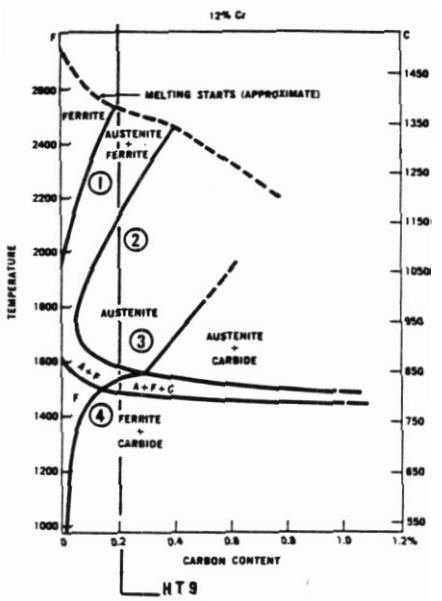

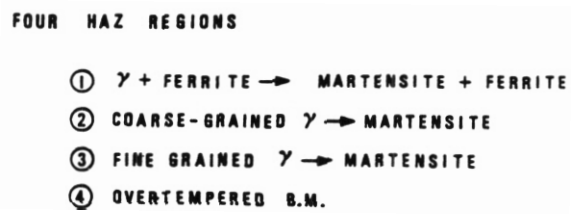

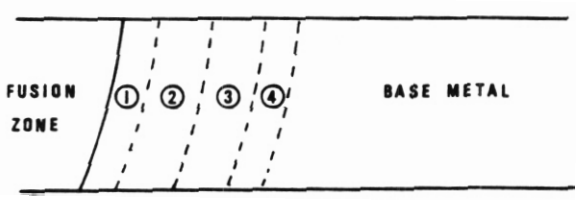

7.4.4.2 **The Relationship Between the As-Welded Microstructure of an HT9 GTA Weld and the Phase Regions of the Fe-Cr-C Pseudo-Binary Diagram.**

2. A region of untempered martensite exhibiting a coarse prior austenite grain size;

3. A region containing untempered martensite and undissolved alloy carbides; and

4. An overtempered base metal microstructure containing tempered martensite and alloy carbides.

Within the HAZ of the laser welds only Regions 2 and 4 were observed. presumably due to the rapid heating and cooling rates which tend to inhibit the formation of Regions 1 and 4.

The microhardness traverse shown in Fig. 7.4.4.3 illustrates the change in hardness which corresponds to the individual microstructures. Regions of highest hardness are found in the fusion zone and that portion of the HAZ near the fusion line (Region 2). These two regions are separated by a softer region at the fusion line corresponding to the two-phase mixture of martensite and ferrite. The tempering response of this microstructure for tempering temperatures of 400. 600. and 800°C (752. 1112. and 1472°F) is shown in Fig. 7.4.4.4. Note that the 400°C temper reduces the as-welded hardness only slightly and that tempering at 800°C is necessary to reduce the hardness to the level of the base metal.

Although the as-welded hardness of the laser welds is actually higher than that of the GTA welds the tempering response at the same tempering temperatures is similar. as illustrated in Fig. 7.4.4.5. Again, note that an 800°C temper is required to restore the weld region to the condition of the quenched and tempered base metal. The tempering response of both the GTA and laser welds is summarized in Fig. 7.4.4.6. These results indicate that from. a metallurgical standpoint. the laser welding process offers no advantage over higher heat input processes such as GTA welding. The formation of brittle. untempered martensite in the weld region can be minimized but not completely eliminated using low heat input processes. Furthermore. the tempering

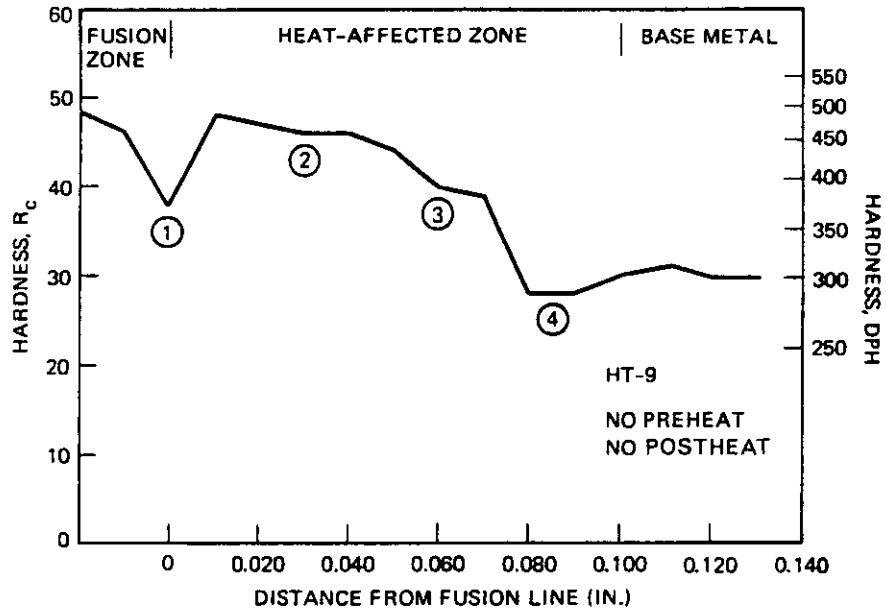

7.4.4.3 Microhardness Traverse Across the Heat-Affected Zone of an HT9 GTA Weld in the As-Welded Condition.

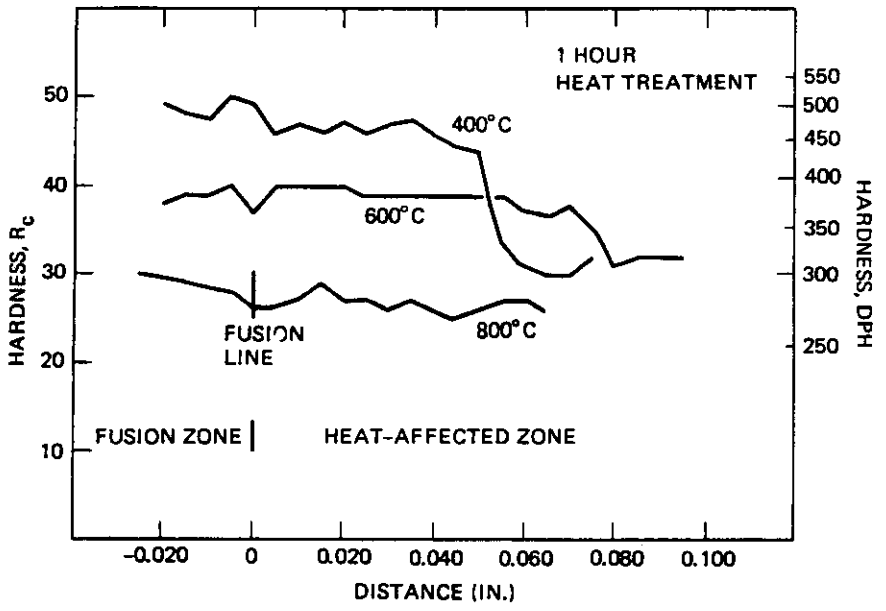

7.4.4.4 Effect of Postweld Heat Treatment on the Heat-Affected Zone Hardness of a GTA Weld in HT-9.

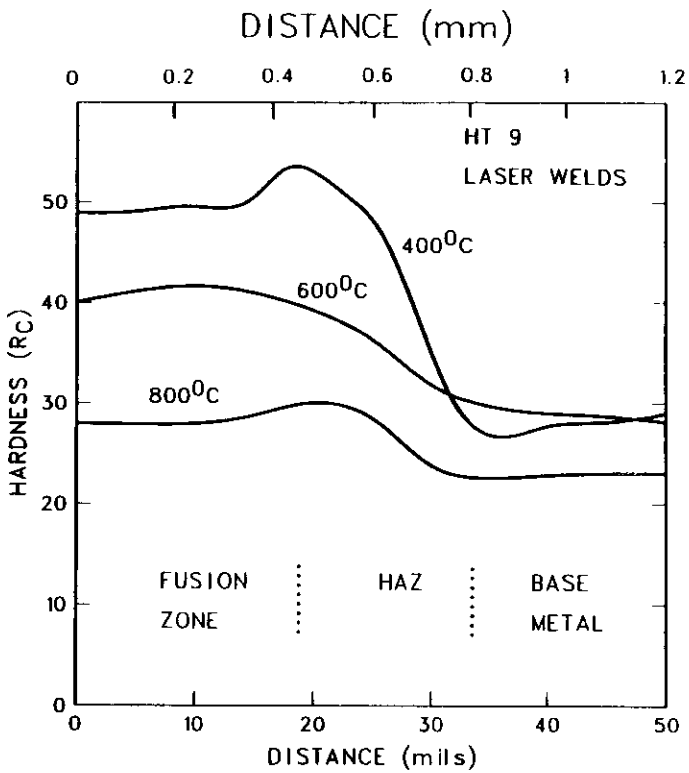

7.4.4.5 Tempering Response of the Weld Region of an HT-9 Laser Weld.

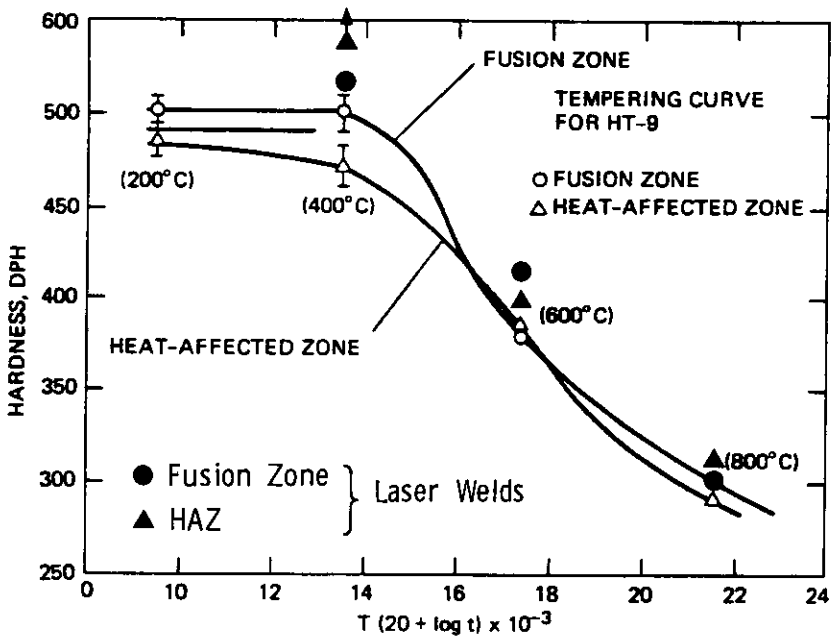

7.4.4.6 Tempering Curve for the Heat-Affected Zone and Fusion Zone of HT-9 GTA and Laser Welds.

response of the untempered martensite which forms in either situation is nearly identical.

7.4.5 Observations and Recommendations

The following comments are based upon information which is available in the literature and the results of investigations performed under the support of the ADIP Path E program.

1. There appears to be no metallurgical advantage favoring the use of low heat input (such as laser) versus high heat input (GTA, GMA, SMA, etc.) welding process on the as-welded joint. In either case regions of hard, untempered martensite are produced in the fusion zone and portions of the HAZ.

2. Regardless of the choice of welding processes and/or parameters a postweld heat treatment will be necessary to restore adequate toughness to the weld region.

3. Preheat temperatures are not critical in the laboratory and might be minimized for component welding. In the laboratory, preheat temperatures are not deleterious up to ~300C. Higher preheats may effect weld quality in that weld puddles are less easily controlled. Therefore, weld position is an important parameter to investigate. Some preheat will probably be necessary in welding a completely constrained tube bank or corrugated sheet to a massive structure. Specific requirements for thicker weldments and more prototypic configuration are yet to be evaluated.

4. Welds have been made satisfactorily using both the GTA and laser welding process. Use of either of these processes for fabrication of fusion devices will require further optimization.

5. It should be recognized it will be necessary to optimize the weld processes. parameters and heat treatments to produce property combinations with the result that weldments are consistent with design requirements.

7.4.6 References

1. Metals Handbook, Vol. 6. 'Welding and Brazing.' American Society for Metals (1971), p. 210.
2. Sandvik Handbook, 'Stainless Tubular Products for the Process Industries - High Temperature Tube and Pipe.' April 1974. p. 28.
3. Chafey. J. and Thompson. L., 'Post Service Evaluation of a Superheater Tube in Service at 600C for 80.000 hr,' Proceedings. Material Environment Interactions in Structural and Pressure Containment Service Symposium. ASMF. New York. N.Y.. (1980) 53.
4. Rosenwasser. S. N., Thompson. L. D., Stevenson. R. D., Lechtenberg. T. A., Thurgood. B. E.. and Holko. K. H., 'Welding and Fabrication of Candidate Ferritic Steel.' ADIP Progress Report for Period Ending December 31, 1979. pp. 82–99.
5. Lippold. J. C., 'Analysis of Laser Welds in HT9,' ADIP Quarterly Progress Report for Period Ending September 30, 1980 pp. 126–139.
6. Lippold. J. C., 'Weldability of HT9: The Autogenous GTA Process.' ADIP Progress Report for Period Ending March 31, 1980. pp. 98–108.
7. Lippold. J. C., 'Tempering and Transformation Behavior of HT9 Weldments.' ADIP Progress Report for Period Ending June 30. 1980. pp. 216-225.
8. Lippold. J. C., 'Tempering Behavior of Laser Welds in €IT–9.' ADIP Progress Report for Period Ending March 31, 1981, pp. 191–207.

7.5 FRACTURE TOUGHNESS MEASUREMENTS FOR UNIRRADIATED 9CR-1MO USING ELECTROPOTENTIAL TECHNIQUES - F. H. Huang and G. L. Wire (Hanford Engineering Development Laboratory)

7.5.1 ADIP Task - ADIP Fusion

7.5.2 Objective

The upper shelf toughness of 9Cr-1Mo was measured using electropotential techniques with the single specimen method. The goal is to characterize the fracture behavior of potential fusion first wall ferritic materials.

7.5.3 Summary

The electropotential technique has been applied to determine J_{1c} on single specimens of HT9. The technique was extended to 9Cr-1Mo in this work. Fracture toughness tests were performed on unirradiated 9Cr-1Mo specimens at 25, 232 and 427°C, and on HT9 specimens at 25 and 232°C for comparison. Continuous crack extension measurements and J versus Δa curves were obtained through the use of a semi-empirical expression in terms of V/V_o and a/a_o. The analysis of test results shows that for HT9, the single specimen method agrees well with the multi-specimen method in determining J_{IC}, however, there is noticeably larger (order 15%) uncertainty for 9Cr-1Mo tested at 427°C. Alloy 9Cr-1Mo shows less variation in the temperature dependence of J_{1c} and a higher resistance to crack propagation than HT9.

7.5.4 Progress and Status

7.5.4.1 Introduction

A single specimen method using an electropotential technique for fracture toughness measurements has been developed.[1] The use of this method can reduce the volume required for irradiation testing of fracture toughness specimens by a factor of 4. In addition, the technique has been applied to the precracking of the specimens to replace the optical method which is tedious and time consuming when used in the hot-cell.[2]

Test specimens were fabricated from alloys 9Cr-1Mo and HT9. These ferritic alloys are being evaluated for first wall applications in fusion reactors. The test results of HT9 were reported in Reference 1. For comparison purposes, both 9Cr-1Mo and HT9 specimens were precracked and subsequently tested using a hydraulic testing system. The electropotential was monitored without interruption during precracking and testing. The test results were compared with those obtained from the multi-specimen method.

7.5.4.2 Experimental Procedure

The 2.54 mm thick circular compact tension specimens were fabricated from modified 9Cr-1Mo (heat number XA3364) developed by Combustion Engineering and ORNL. They were given the final heat treatment of 1038°C/5 min/AC + 760°C/1 hr/AC. Test specimens of the same dimensions were also machined from HT9 bar stock received in the mill annealed condition, which consists of hot work at 1149°C for 1 hour, and tempering at 740-760°C for 1 hour and air cooling. The test specimen assembly was electrically insulated by ceramic parts contained in the couplings of the pull rods. All specimens were fatigue precracked with a servo-hydraulic system to a crack length of 1.3 mm at a stress intensity factor of 36 MPa $\sqrt{m}$ for 9Cr-1Mo specimens and 28 MPa $\sqrt{m}$ for HT9 specimens. The precrack lengths were measured by a travelling microscope during the precracking. Following the precracking fracture toughness tests were performed at 25, 232 and 427°C using a split furnace. After the test was completed, each cracked specimen was heat tinted at 500°C for 1 hour to reveal the crack extension (Fig. 7.5.1).

The values of J were calculated from load versus load-line displacement curves in the form:[3]

$$J = \frac{1 + a}{1 + \alpha^2} \frac{2A}{Bb} \qquad (1)$$

where A is the area under load versus load-line displacement curve, B is the specimen thickness, b is unbroken ligament size, $\alpha = 2[(a/b)^2 + (a/b) + 1/2]^{1/2} - (2a/b + 1)$.

Fig. *7.5.1.* Crack extension as revealed by hint tinting for (a) HT9 and (b) 9Cr-1Mo.

7.5.4.3 Results and Discussions

J versus Aa for HT9 tested at room temperature and *232°C* using a MTS testing machine are shown in Fig. 7.5.2. Also shown in the figure are the test results obtained using an Instron testing machine. They are in good agreement. The potential changes and their corresponding crack lengths were measured simultaneously and are shown in Fig. *7.5.3* and Fig. *7.5.4.* In these figures, V_o is the initial potential drop across the crack of length a_o prior to precracking. The final crack extensions revealed by heat tinting for each test were plotted in these figures as filled points. As can be seen from the figures, the slope of V/V_o versus a/a_o curve for precracking is larger potential change resulting from a larger crack area advancement for fatigue precracked specimens which have nearly straight crack fronts. Based on this experimental observation, an empirical expression for the calibration curve in terms of V/V_o and a/a_o where a_o is the initial crack length prior to testing, was formulated' as

$$V/V_o = (X_o - 1)\ \mathrm{Tanh}\ [\frac{o}{\Delta a^*}\ (\frac{a}{a_o} - 1)] + \beta(\frac{a}{a_o} - 1) + 1 \qquad (2)$$

where X_o, β are the intercept and slope of the straight line portion of the V/V_o versus a/a_o curve at larger crack extensions. Here Aa* is the blunting at crack initiation, which can be estimated from a widely accepted blunting curve description $\Delta a = J/2\sigma_f$, where $\sigma_f = (\sigma_{ys} + \sigma_{uts})/2$.

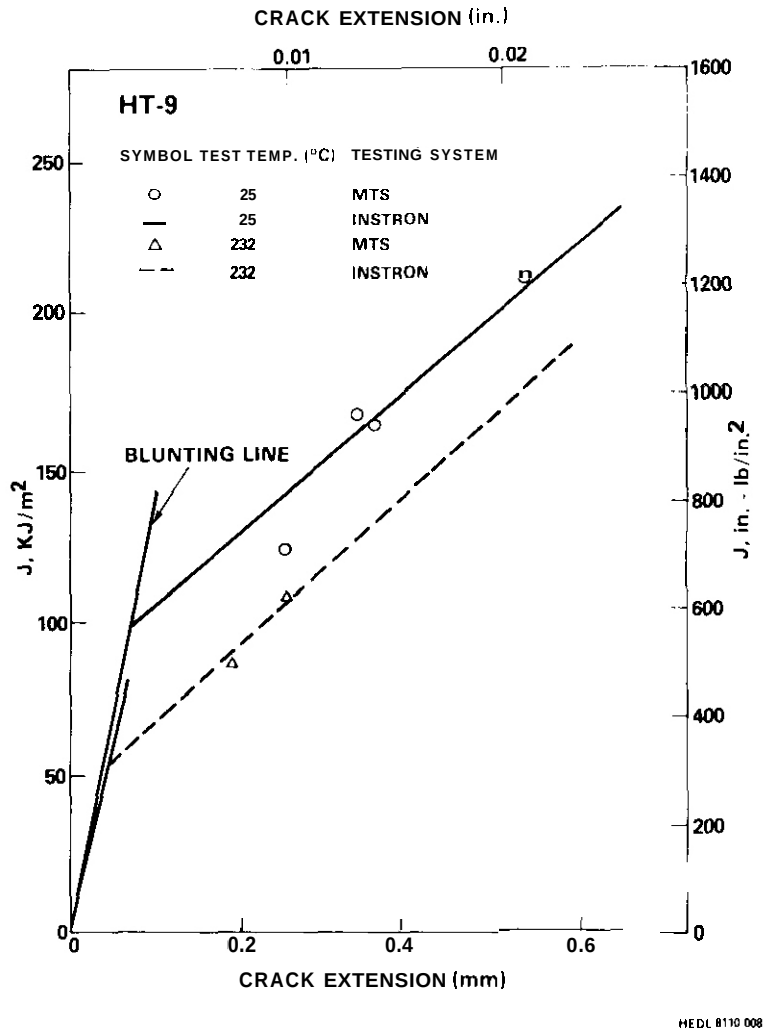

Fig. 7.5.2. J versus Aa for HT9 tested at 25°C and 232°C.

In Fig. 7.5.4 the calibration curve (solid line) was derived from experimental data in the form of equation (2) for HT9. Using this calibration curve, J versus Aa curves can be obtained from each single specimen test. They are shown in Fig. 7.5.5 for HT9. Overall, the values of J_{1c} estimated from the single specimen method agree with that estimated from the multi-specimen method for HT9.

The V/V_o versus a/a_o data for the precracking and interrupted testing of 9Cr-1Mo are shown in Fig. 7.5.6 and Fig. 7.5.7. The solid line in Fig. 7.5.7 represents the electropotential calibration curve in the form of equation (2) with a slope of 1. This curve was used to calculate the continuous crack extensions for constructing J versus Aa curves which are plotted in Fig. 7.5.8 and Fig. 7.5.9 for 9Cr-1Mo tested at 232°C and 427°C, respectively.

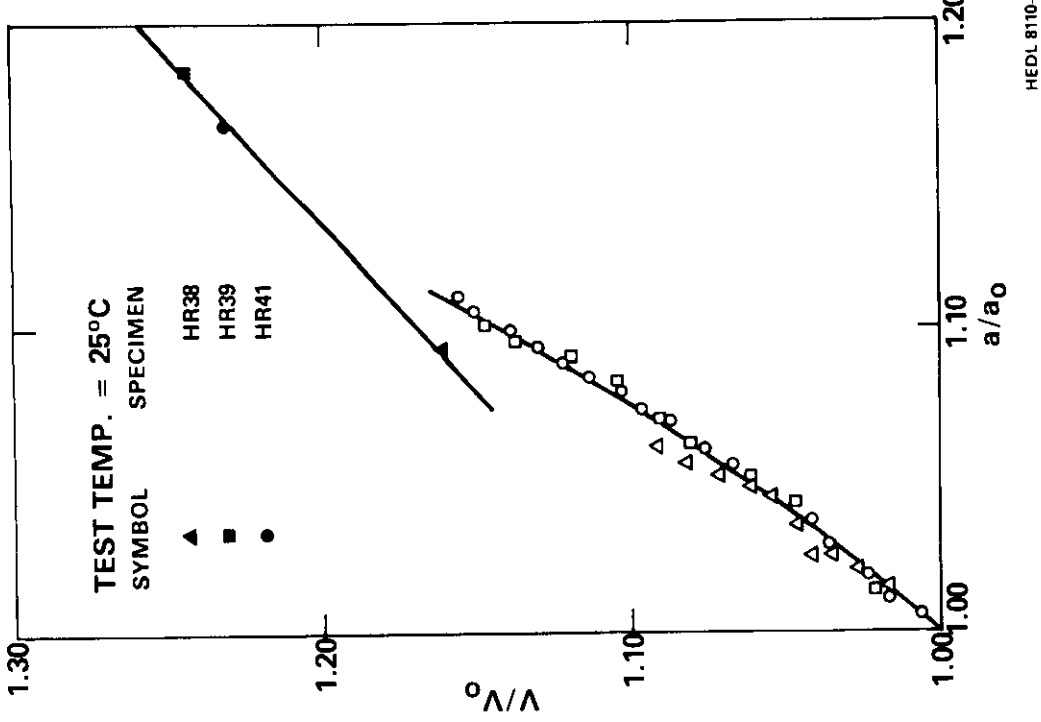

Fig. 7.5.3. V/V_o versus a/a_o for the precracking and interrupted testing of HT9 specimens.

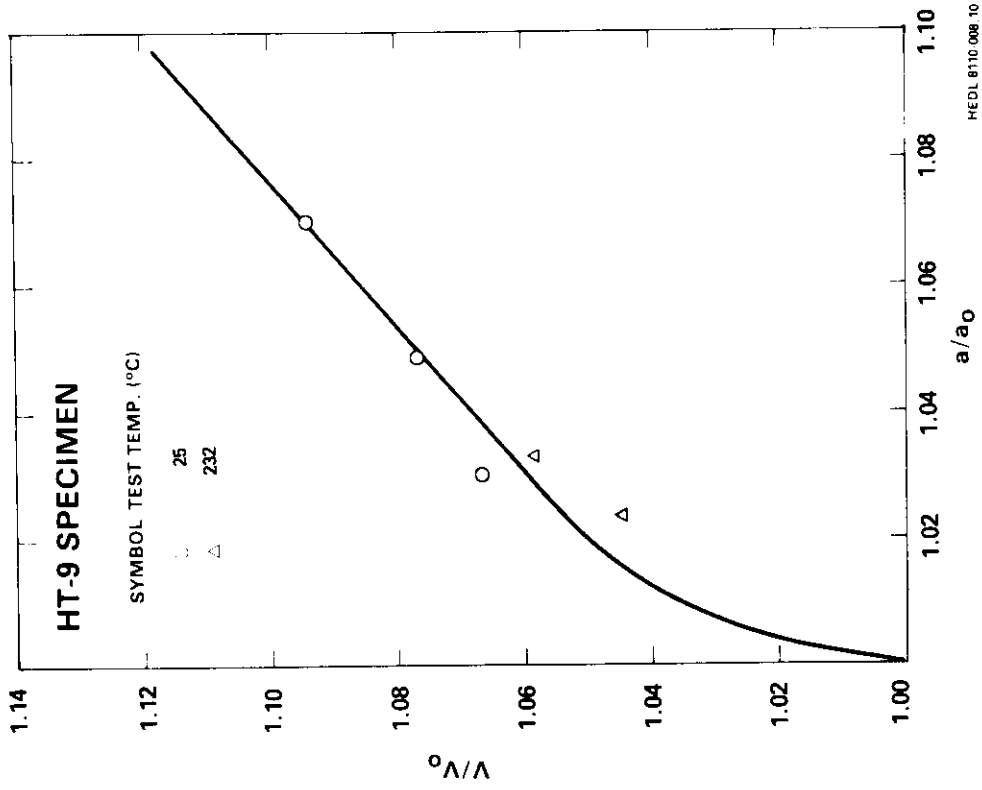

Fig. 7.5.4. Electropotential calibration curve for HT9.

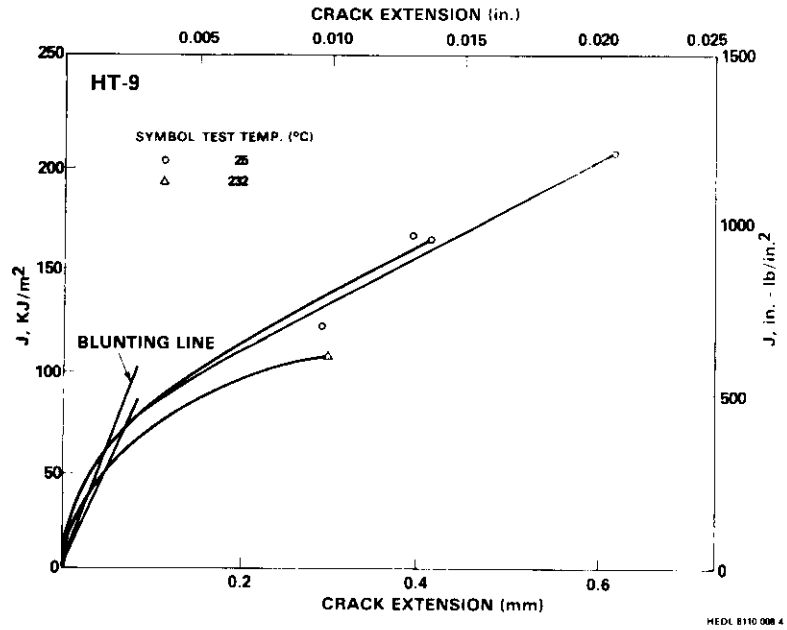

Fig. 7.5.5. J versus Δa curves obtained via an electropotential calibration curve for HT9.

The test results of unirradiated 9Cr-1Mo tested at elevated temperatures are compiled in Table 7.5.1 and the temperature dependence of J_{1c} is shown in Fig. 7.5.11. The values of J_{1c} determined from both multi-specimen (Fig. 7.5.10) and single specimen methods for 9Cr-1Mo tested at elevated temperatures were compared. The values of J_{1c} at 25 and 232°C obtained from the two methods are in very good agreement, however, there is a 15% difference for J_{1c} at 427°C. This is within expected scatter for the J_{1c} assessment. Also plotted in Fig. 7.5.11 are J_{1c} values as a function of test temperature for HT9. As shown in the figure, the variation in the temperature dependence of J_{1c} in 9Cr-1Mo is smaller than that for HT9. Furthermore, the tearing modulus of 9Cr-1Mo is larger than that of HT9 indicating that 9Cr-1Mo is more resistant to crack propagation than HT9. The fracture surface of 9Cr-1Mo exhibits different features than those of HT9. Delta ferritic stringers which are evident on the fracture surfaces of HT9 do not exist in 9Cr-1Mo.

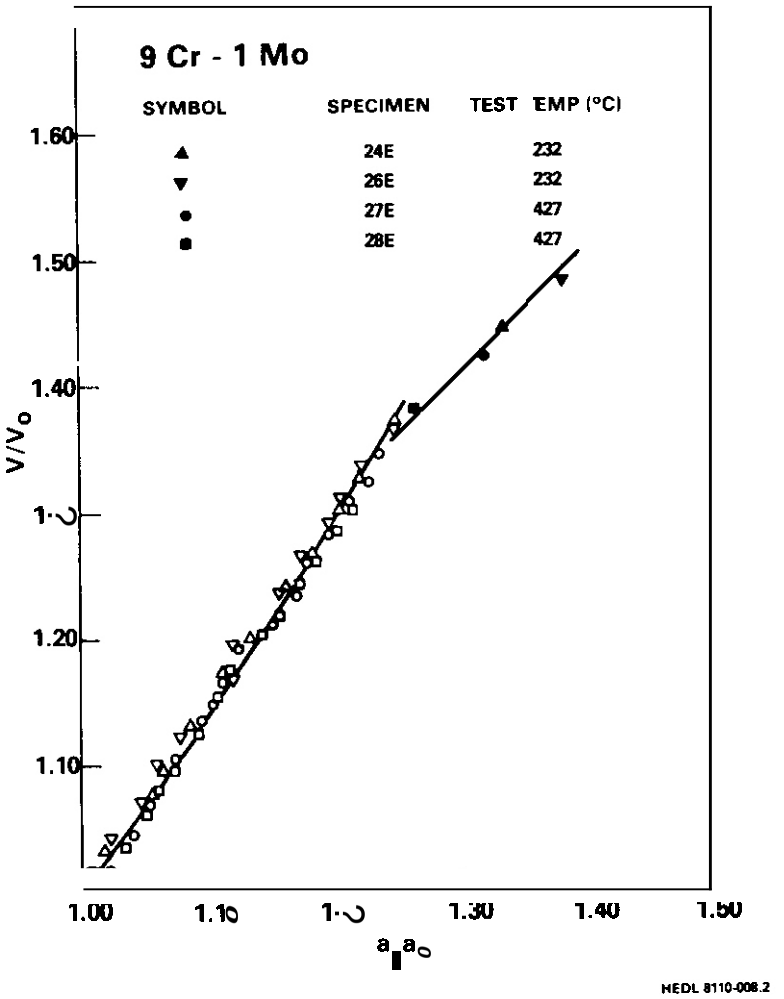

Fig. 7.5.6. V/V_o versus a/a_o for the precracking and interrupted testing of 9Cr-1Mo specimens.

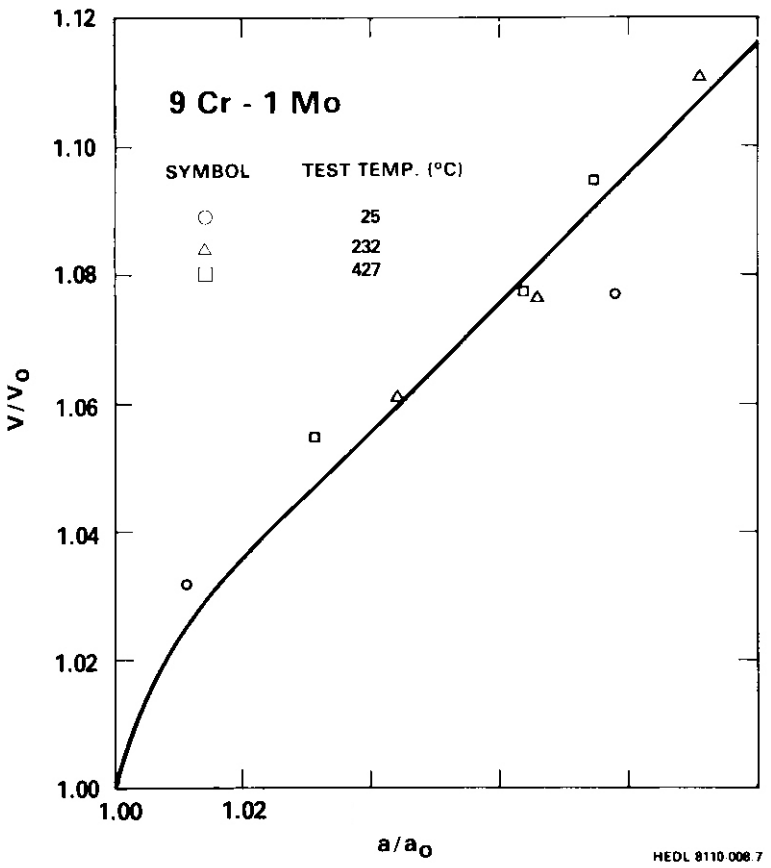

Fig. 7.5.7. Electropotential calibration curve for 9Cr-1Mo.

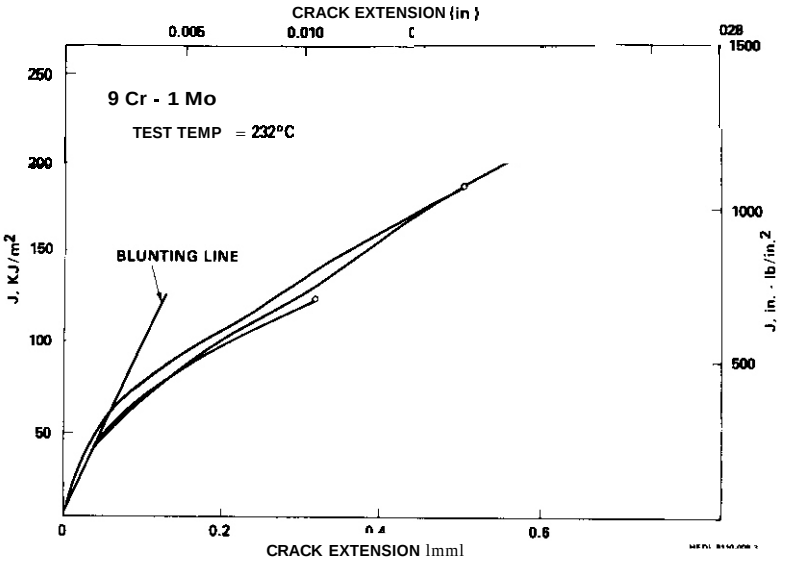

Fig. 7.5.8. J versus Aa curves obtained via an electropotential calibration curve for 9Cr-1Mo tested at 232°C.

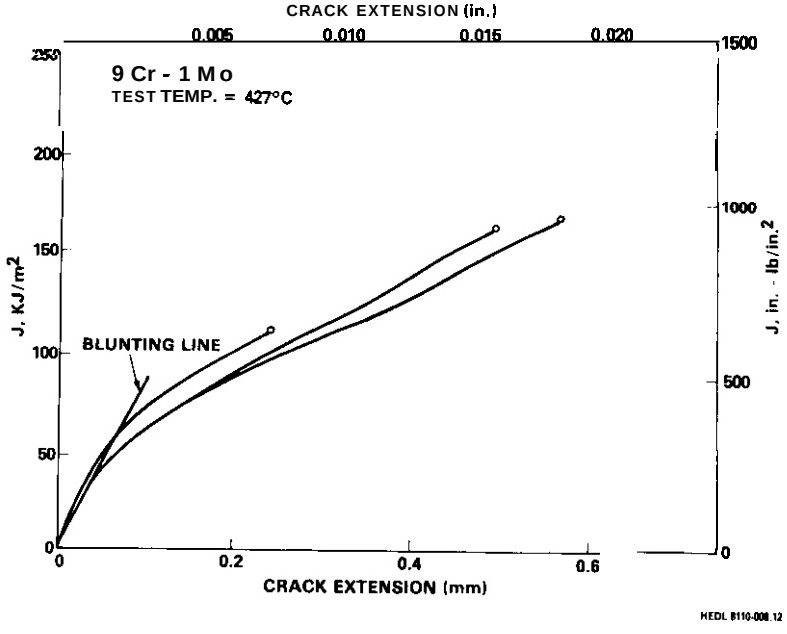

Fig. 7.5.9. J versus Aa curves obtained via an electropotential calibration curve for 9Cr-1Mo tested at 427°C.

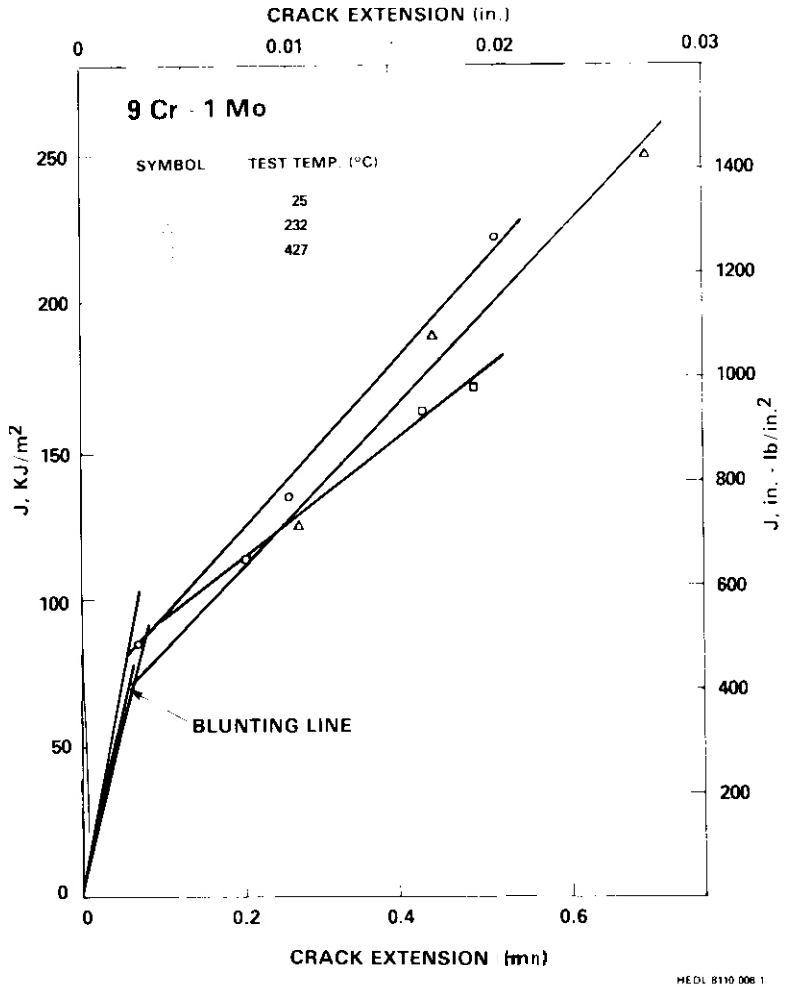

Fig. 7.5.10 J versus Δa tested at elevated temperatures for 9Cr-1Mo.

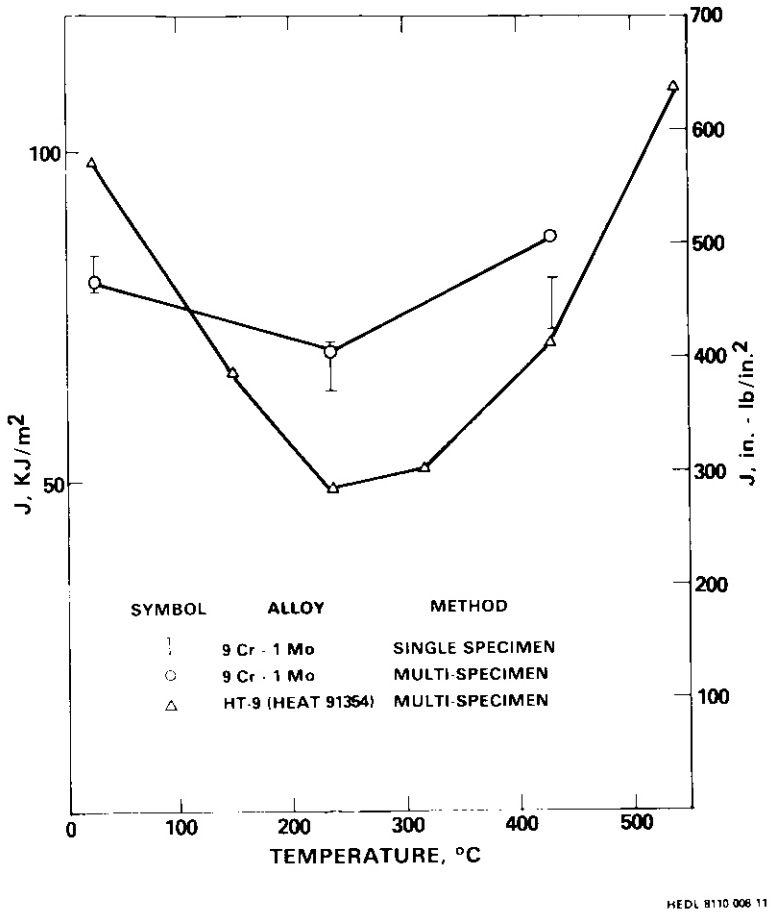

Fig. 7.5.11. Temperature dependence of fracture toughness for 9Cr-1Mo and HT9.

Table 7.5.1. Fracture Toughness Test Results and Mechanical Properties of 9Cr-1Mo

Test Temp. ("C)	a_{ys} (KSI	MPa)	a_{ys} (KSI	MPa)	J_{1c} (in-lb/in^2	kj/m^2)	T*
25	83	572.2	100	689.4	470.6	82.4	160
232	73	503.3	90	620.5	411.8	72.1	177
427	70	482.6	78	537.7	513.1	89.8	147

T* = Tearing Modulus

7.5.5 References

1. F. H. Huang and G. L. Wire, "*Analysis of Single Specimen Tests on HT9 for J_{1c} Determination*," ADIP Quarterly Progress Report, April-June 1980.
2. F. H. Huang and G. L. Wire, "*Measurements of the Fatigue Precracked Length of Fracture Toughness Specimen Using an Electropotential Technique*," ADIP Quarterly Progress Report, July-September 1980.
3. G. A. Clarke and J. D. Landes, "Evaluation of the J-Integral for the Compact Specimen," *Journal of Testing and Evaluation, Vol* 7, p. 264, 1979.

7.6 TEM SPECIMEN PREPARATION FOR THE HFIR-MFE-RB1 EXPERIMENT – D. T. Peterson (Hanford Engineering Development Laboratory)

7.6.1 ADIP Task

The Department of Energy, Office of Fusion Energy has cited the need for these data under the ADIP Program Task, Ferritic Materials Development (Path E).

7.6.2 Objective

The objective of this work is to study the microstructural response of ferritic alloys to low temperature irradiation.

7.6.3 Summary

TEM specimens of the ferritic alloys HT-9, 9Cr-1Mo and 2¼Cr-1Mo have been prepared for inclusion in the HFIR-MFE-RBI irradiation. The specimen matrix encompasses all the conditions being irradiated in the EBR-II AD-2 test. Additionally, the matrix includes specimens of HT-9 weld fusion zones and simulated heat-affected zones to study the microstructural response of weldments.

7.6.4 Progress and Status

1.6.4.1 Introduction

The AD-2 experiment was the first concerted investigation of ferritic alloys by the ADIP Program. This test is being irradiated in EBR-II to exposures of about 15 and 30 dpa at irradiation temperatures of 390, 450, 500 and 550°C.[1] As the coolant inlet temperature of EBR-II is 370°C, irradiations cannot be performed in that reactor below about 390°C. However, the irradiation response of materials at temperatures below 400°C is of considerable interest. With a coolant temperature of only 50°C HFIR offers the capability of performing irradiations below 400°C.

The present HFIR test, designated MFE-RBI, is designed to operate at the coolant temperature of 50°C with goal exposures of 10 and 20 dpa.[2] Reference 2 describes the preliminary specimen matrix for this test. In addition to HT-9, 9Cr-1Mo and 2¼Cr-1Mo, nickel doped variants of HT-9 and

9Cr-1Mo will be irradiated in this test. These nickel doped alloys were developed by ORNL to enhance the production of helium during irradiation in mixed spectrum reactors such as HFIR.[3] This report describes the TEM specimen matrix for the standard heats of HT-9, 9Cr-1Mo and 2¼Cr-1Mo. Specimens of the nickel doped alloys are being fabricated by ORNL.

7.6.4.2 Specimen Matrix

The TEM specimen matrix is listed in Table 7.6.1. Due to the difficulties involved in preparing TEM specimens from mechanical properties specimens the matrix encompasses conditions that are representative of all the mechanical properties specimens. Also included in the matrix are alternate treatments intended to provide backup information in case the properties of the standard treatments are not adequate. A brief discussion of each of the conditions follows. Conditions HA through K5 and HK are the only conditions not currently being irradiated in the AD-2 test.' However, these conditions are being included in the reconstitution of the test.

7.6.4.3 HT-9

Conditions HI and H2 correspond to the standard treatments used for the mechanical properties specimens in the AD-2 test.' Only a treatment corresponding to condition H1 is being used for the mechanical properties specimens in the RB1 test.[5] These two conditions are intended to investigate the effects of prior austenite grain size and tempering time on post-irradiation mechanical properties.

Condition H3 uses a lower tempering temperature which is closer to the nose of the carbide precipitation curve. This treatment is intended to decrease dislocation recovery while enhancing carbide precipitation.

Conditions H4 and HA correspond to the two treatments used for the fracture toughness and miniature Charpy specimens in the AD-2 test.[6]

Conditions H5 and H7 are intended to assess the effect of cold working on microstructural development. These combined with the other treatments provide a comparison of the effects of different dislocation structures: treatments HI, H2, H4 and HA produce highly recovered dislocation structures, treatment H3 is intended to produce a less recovered dislocation structure, and treatments H5 and H7 produce cold worked dislocation structures.

Table 7.6.1. TEM Specimen Matrix for the HFIR-MFE-RB1 Test

Alloy*	Code	TMT
HT-9	HI	40% CW + 1038°C/5 min/AC + 760°C/0.5 hr/AC
HT-9	H2	40% CW + 1038°C/0.5 hr/AC + 760°C/2.5 hr/AC
HT-9	H3	40% CW + 1038°C/5 min/AC + 675°C/2.5 hr/AC
HT-9	H4	40% CW + 1050°C/0.5 hr/AC + 780°C/2.5 hr/AC
HT-9	H5	1038°C/5 min/AC + 760°C/0.5 hr/AC + 20% CW
HT-9	H7	1038°C/5 min/AC + 760°C/0.5 hr/AC + 30% CW
HT-9	HA	Mill annealed round bar.
HT-9	HT	Weld fusion zone + 760°C/2 hr/AC
HT-9	HU, HV	HAZ #1 + 760°C/2 hr/AC
HT-9	HX, K1	HAZ #2 + 760°C/2 hr/AC
HT-9	K2, K3	HAZ #3 + 760°C/2 hr/AC
HT-9	K4, K5	HAZ #4 + 760°C/2 hr/AC
9Cr-1Mo	HB	40% CW + 1038°C/1 hr/AC + 760°C/1 hr/AC
9Cr-1Mo	HK	40% CW + 1038°C/0.5 hr/AC + 760°C/0.5 hr/AC
9Cr-1Mo	HE	40% CW + 1038°C/5 min/AC + 760°C/1 hr/AC
9Cr-1Mo	HF	40% CW + 1038°C/5 min/AC + 675°C/2.5 hr/AC
9Cr-1Mo	HH	1038°C/1 hr/AC + 760°C/1 hr/AC + 20% CW
9Cr-1Mo	HJ	1038°C/1 hr/AC + 760°C/1 hr/AC + 30% CW
2¼Cr-1Mo	HL	900°C/0.5 hr/AC + 700°C/1 hr/AC
2¼Cr-1Mo	HN	900°C/0.5 hr/AC + 650°C/1 hr/AC
2¼Cr-1Mo	HP	920°C/10 min/WQ + 720°C/1 hr/AC
2¼Cr-1Mo	HR	40% CW + 750°C/1 hr/AC

*HT-9 - Ht. 91353
9Cr-1Mo - Ht. 30176
2¼Cr-1Mo - Ht. 56447

Specimens HT through K5 were produced by a joint effort between HEDL and Sandia National Laboratories, Livermore. These specimens provide a straightforward means of determining the effects of irradiation on weldments. The weld fusion zone specimens (condition HT) were taken from autogeneous GTA welds performed on 0.31 mm thick sheet.' The four simulated heat-affected zones were produced by resistance heating

cylindrical specimens on a Gleeble.[7] Subsequently, specimens were sliced off from around the center of the specimen. The exact thermal history of each Gleeble specimen is known only for a 6 mm region about the center of the specimen. For traceability, every disk cut from each specimen was given a distinct code.

The four simulated heat-affected zones are intended to simulate the four distinct microstructural regions of the heat-affected zone.[3] Zone 1 simulates the region of the heat-affected zone that is adjacent to the fusion zone. It consists of martensite and delta ferrite. Zone 2 is martensitic with coarse prior austenite grains. Zone 3 is martensitic with fine prior austenite grains and incomplete dissolution of carbides. Zone 4 consists of overtempered base metal.

7.6.4.4 9Cr-1Mo

Condition HB corresponds to the standard treatment used for the mechanical properties specimens in the AD-2 test' while condition HK corresponds to the standard treatment used for the mechanical properties specimens in the RB1 test.[5] Condition HE has a shorter austenization time which is consistent with the small section size of the TEM specimens.

Conditions HF, HH and HJ are the same as the corresponding conditions of HT-9 (H3, H5 and H7).

7.6.4.5 2¼Cr-1Mo

The series of treatments used for 2¼Cr-1Mo are intended to provide an assessment of the effect of matrix structure on the overaging response of the carbides; treatment HL produces a fine-grained bainitic structure, treatment HP uses a water quench from the normalizing treatment to produce a martensitic structure, and treatment HR uses a subcritical anneal to produce a ferritic structure. Condition HL is the standard treatment used for both the AD-2 and this test.'" Treatment HN uses a lower tempering temperature than the standard treatment to produce a higher pre-irradiation tensile strength.

7.6.5 Future Work

Microstructural examinations will be performed on selected specimens after the first discharge at 10 dpa.

7.6.6 References

1. R. J. Puigh and B. A. Chin, "Test Plan for the Investigation of Irradiation Effects Upon Mechanical Properties of Ferritic Alloys," ADIP Quarterly Progress Report, October-December, 1979, DOE/ER-0045/1, 105.
2. J. M. Vitek, R. L. Kuceh, M. L. Grossbeck and J. W. Woods, "HFIR-MFE-T1, -T2, and -RB1: Experiments to Evaluate the Effects of Low-Temperature Irradiation on Ferritic Alloys," ADIP Quarterly Progress Report, July-September, 1980, DOE/ER-0045/4, 26.
3. R. L. Klueh and J. M. Vitek, "Characterization of Ferritic Steels for HFIR Irradiation," ADIP Quarterly Progress Report, April-June, 1980, DOE/ER-0045/3, 294.
4. R. J. Puigh and N. F. Panayotou, "Specimen Preparation and Loading for the AD-2 Ferritics Experiment," ADIP Quarterly Progress Report, April-June, 1980, DOE/ER-0045/3, 260.
5. R. J. Puigh and R. D. Stevenson, "Fabrication of Materials for the RB-1 Experiment in HFIR," ADIP Quarterly Progress Report, October-December, 1980, DOE/ER-0045/5, 170.
6. D. T. Peterson, "Microstructural Examination of HT-9 Archive Material From the AD-2 Test," ADIP Quarterly Progress Report, October-December, 1980, DOE/ER-0045/5, 212.
7. J. C. Lippold, Private Communication.
8. J. C. Lippold, "Weldability of HT-9: The Autogeneous GTA Process," ADIP Quarterly Progress Report, January-March, 1980, DOE/ER-0045/2, 98.

7.7 MINIATURE CHARPY SPECIMEN TEST DEVICE DEVELOPMENT AND IMPACT TEST RESULTS FOR THE FERRITIC ALLOY HT9 - W. L. Hu and N. F. Panayotou (Hanford Engineering Development Laboratory).

7.7.1 ADIP Task

The Office of Fusion Energy, DOE, has established the need to determine the fracture toughness of candidate fusion program ferritic alloys (Path E).

7.7.2 Objective

The objective of this work is to develop an instrumented impact testing capability which will permit the determination of the ductile to brittle transition temperature and the dynamic fracture toughness of irradiated ferritic alloys.

7.7.3 Summary

A miniature charpy v-notch (CVN) type impact specimen geometry has been selected and two instrumented drop towers have been purchased from Effects Technology, Incorporated (ETI) and received at HEDL. Impact testing of unirradiated HT9 miniature CVN specimens has been performed at temperatures of -100°C to +100°C. The ductile to brittle transition temperature obtained is in excellent agreement with data obtained using full size HT9 CVN specimens. Dynamic fracture toughness data can also be obtained. However, improved instrumentation will be required to obtain dynamic fracture toughness data outside the lower shelf region.

7.7.4 Progress and Status

7.7.4.1 Introduction

Ferritic alloys such as HT9 are susceptible to brittle failure under certain service conditions. Furthermore, it is well known that the temperature at which ferritic alloys undergo a transition in fracture mode from ductile to brittle shifts toward higher temperatures with increasing neutron exposure. Accordingly the change in the ductile to brittle

transition temperature (DBTT) with fluence can be an important factor in the selection of alloys for fusion reactor applications.

A standard method of determining the DBTT of ferritic alloys involves the use of a Type A CVN specimens 10 mm square and 55 mm long with a 45°, 2 mm deep notch.[1] The test method involves the heating or cooling of the test specimen to a specific temperature, its rapid transfer to the test position and the impact loading of the specimen in three point bending by a moving mass of known kinetic energy which is great enough to break the specimen. The energy required to break a specimen is determined over a range of temperatures. This data can then be used to specify the minimum temperature at which a component, with a thickness identical to that of the charpy specimen, will exhibit ductile behavior.

A miniature CVN specimen geometry was chosen for this study of the effect of irradiation on the dynamic fracture toughness of candidate ferritic alloys. HEDL's miniature specimen is compared in Fig. 7.7.1 with a standard CVN specimen. The miniature specimen is approximately

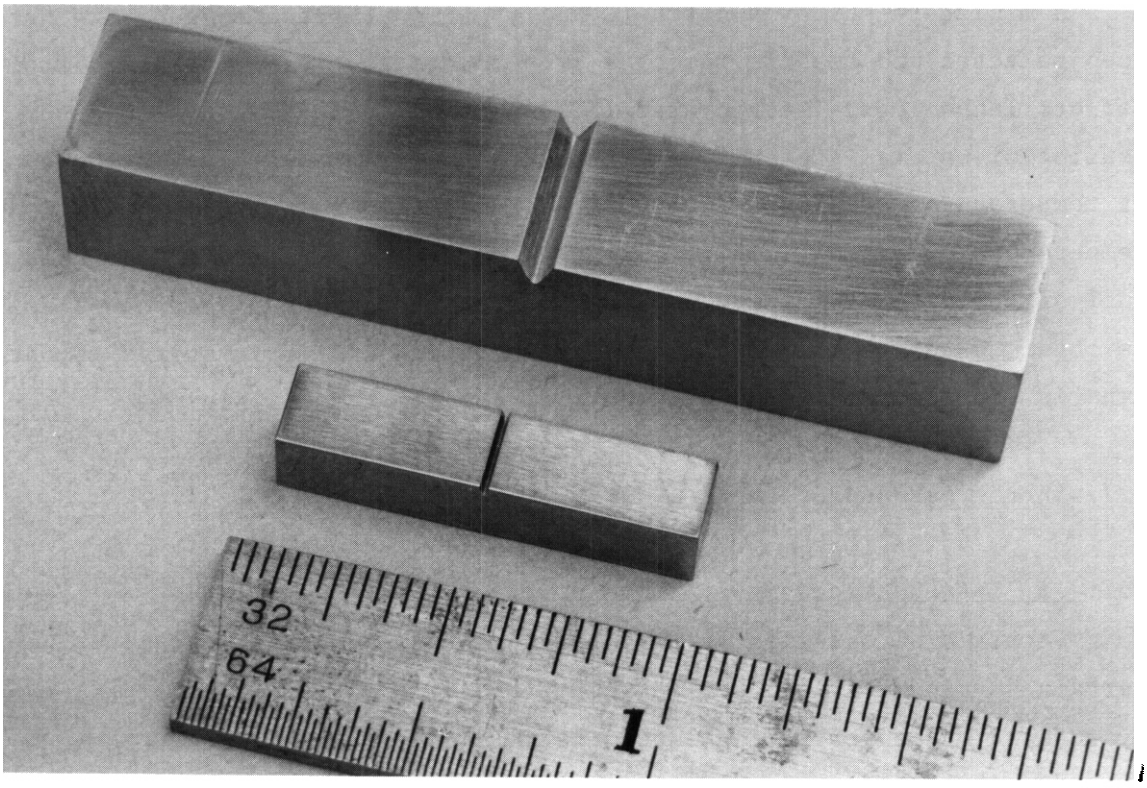

Fig. 7.7.1. Comparison of full size and HEDL half size charpy v-notch specimens.

a one-half size CVN specimen. The use of this miniature specimen geometry permits eight specimens to be irradiated in the volume occupied by one standard CVN specimen. Eight specimens are usually sufficient to define the entire DBTT curve. The results obtained with miniature CVN specimens are valid for components of equal thickness. When compared to full size CVN specimens, however, it is noted that miniature CVN specimens will indicate better behavior, that is the DBTT is shifted to a lower test temperatures. This is usually attributed to the fact that sufficient constraint cannot be developed at the root of the notch of a sub-size specimen. However the shift in DBTT following irradiation has been found to be independent of specimen size, so that miniature CVN specimens can be used to determine the relative effect of irradiation on fracture behavior.[2]

A drop tower was chosen as the impact test device instead of the more conventional pendulum device. The drop tower is a more flexible test bed since it can be easily adapted to various specimen geometries whereas a pendulum device is usually designed for a particular geometry. In addition the drop tower requires less floor space, an important consideration for hot cell testing applications. One method of determining the energy required to break the specimen, when a drop tower is employed, involves instrumenting the striker or tup with strain gages *so* that a load versus time signal of the test can be obtained. This signal can be integrated electronically *so* that the energy absorbed during fracture can be obtained. This signal can be integrated electronically so that the energy absorbed during fracture can be determined. If fatigue precracked specimens are employed the load-time signal which is obtained can also be used to extract dynamic fracture toughness data. This type of instrumented charpy testing is rapidly gaining acceptance and a standard on the instrumented testing of precracked specimens is currently under review by an ASTM working group.

To date both notched and precracked miniature charpy specimens of unirradiated HT9 have been tested. A specially designed temperature conditioning chamber and specimen transfer mechanism, which will permit remote testing of miniature CVN specimens, have been designed and are currently being integrated with the drop tower. The installation of the

122 J drop tower in the hot cell facility and the first testing of irradiated HT9 and 9Cr-1Mo miniature CVN specimens, irradiated in the AD-2 experiment to a fluence of 14 dpa, will be performed during the next reporting period. The larger capacity drop tower, 285 J, will be used for control testing. The capacity of both drop towers can be increased by substituting tungsten for the lead weights currently in use.

7.7.4.2 Experimental Procedure

The dimensions of the full size and miniature CVN specimens used in this study are shown in Fig. *7.7.2.* In cross section the miniature specimen is essentially a one-half size charpy specimen. However the length of the HEDL half size CVN specimen could not be scaled to that of a one-half size charpy due to irradiation vehicle constraints.[3] Furthermore, the notch dimensions were reduced from the standard dimensions in order to obtain greater constraint at the notch tip.

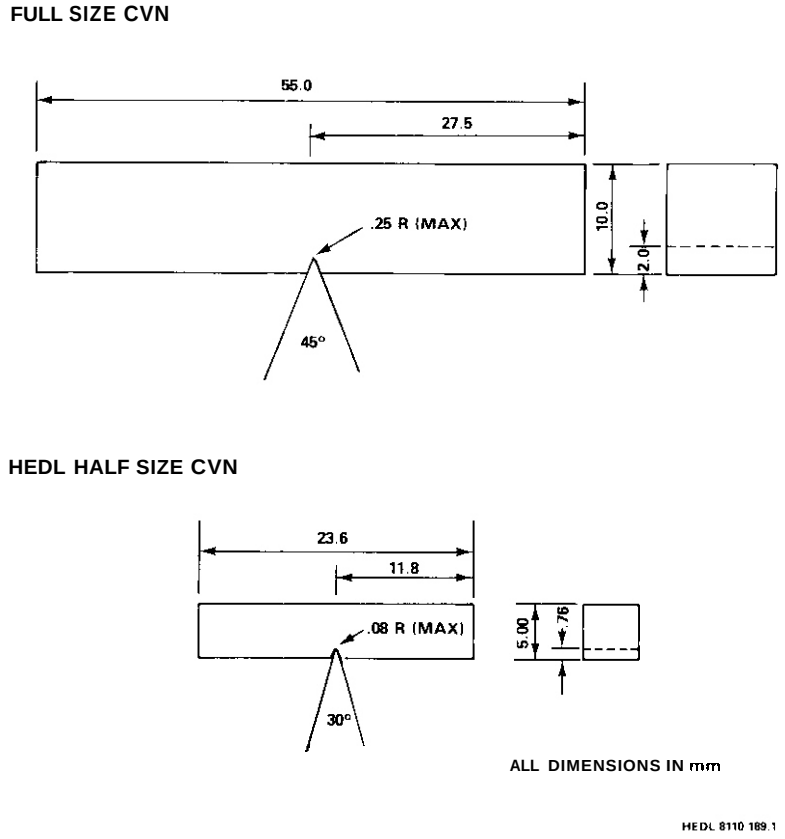

Fig. *7.7.2.* Full size and HEDL half size charpy v-notch specimen dimensions.

The full size CVN specimens were machined directly from 33.3 mm diameter bar stock of HT9 heat number 91354. The details of the specimen prior history were reported elsewhere.[4] These specimens were the control specimens for a Naval Research Laboratory (NRL) assembled EBR-II experiment described in Reference 4. It should be noted that the heat treatment specified in Reference 4 for these full size CVN specimens and referred to as the "as received" condition is incorrect. The only heat treatment applied to the stock material was performed by the vendor and consisted of hot working, after soaking for a minimum of one-half hour at 1140°C, followed by air cooling to room temperature, followed by tempering at 750°C for one hour and then finally, air cooling to room temperature. A tempered martensite microstructure resulted from this heat treatment. The specimens machined from this stock were not subsequently heat treated.

The HEDL half size CVN specimens were machined from hot rolled 6.4 mm thick plate stock supplied to HEDL by General Atomic Company. The stock material was heat treated by General Atomic Company for ten minutes at 1038°C, air cooled to room temperature and was then reheated to 760°C and maintained at temperature for thirty minutes and then air cooled. The HEDL half size precracked CVN specimens have the same prior history as the full size specimens except for the orientation of the specimen with respect to the bar stock. The prior history of the full size and the half size and precracked half size CVN specimens is summarized in Table 7.7.1. Despite differences in the prior history of the specimens the resulting prior austenite grain size and Vickers microhardenss of the tempered martensite microstructure is quite comparable. The orientation of the specimens with respect to the stock material is illustrated in Fig. 7.7.3. The full size CVN specimens were machined so that the specimen would be loaded in the longitudinal direction and the crack would propagate along a chord of the cross section of the bar. The HEDL half size specimens were machined so that the specimen would be loaded in the transverse direction and the crack would propagate along the longitudinal direction of the plate. The HEDL precracked half size specimens were machined so that the specimen would be loaded in a radial direction and the crack would propagate in an orthogonal radial direction of the cross

Table 7.7.1. HT9 CVN Specimen Prior History

	NRL	HEDL	
	Full Size	Half Size	Precracked Half Size
Heat Number	91354	91354	91354
Processing	Hot Forming	Hot Rolling	Hot Forming
Stock Form	33.3mm dia. bar	6.4mm thick plate	33.3mm dia. bar
Stock Heat	750°C/30min/AC	1038°C/10min/AC 760°C/30min/AC	750°C/30min/AC
Specimen Heat Treatment	None	None	None
ASTM Prior Austenite Grain Size	8	8	8-9
Microhardness DPH, 500 g load	270	265	265

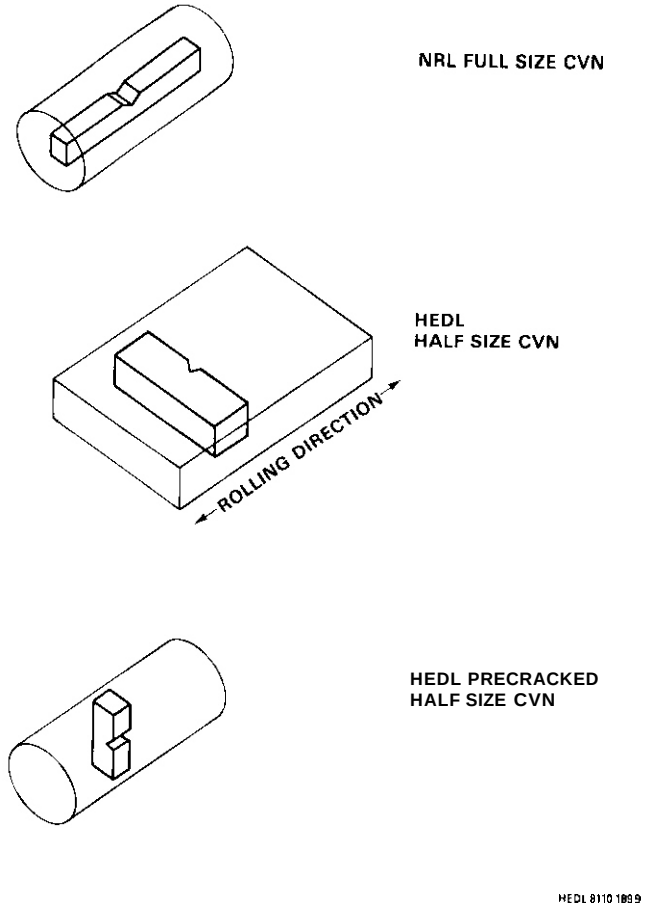

Fig. 7.7.3. Orientation of CVN specimens with respect to the stock material.

section of the bar. Full size and miniature CVN specimens having the identical orientation were not available for this work.

The vendor specified composition and an independent overcheck of the composition of this bar stock is given in Table 7.7.2.

Table 7.7.2. Chemical Composition of HT9 Heat Number 91354

Element	Weight Percent	
	Vendor	Overcheck
C	0.21	0.20
Mn	0.50	0.39
P	0.008	
S	0.003	
Si	0.21	0.14
Ni	0.58	0.49
Cr	12.11	12.39
Mo	1.03	0.99
V	0.33	0.45
Ti	0.002	
Co	0.01	
Cu	0.04	0.07
Al	0.034	
B	0.0007	
As	<0.005	
N	0.004	
Ta	<0.01	
W	0.53	
Fe	Balance	Balance

A total of six HEDL half size CVN specimens and eleven HEDL precracked half size specimens were tested. The precracked specimens were fatigue precracked in accordance with ASTM specification E-399.[5] The details of the procedure were reported in a previous ADIP quarterly progress report.[3]

The experimental setup used to test the HEDL half size CVN specimens is shown in Fig. 7.7.4. The drop tower consists of a weighted crosshead which is allowed to fall freely along smooth guide columns, an instrumented

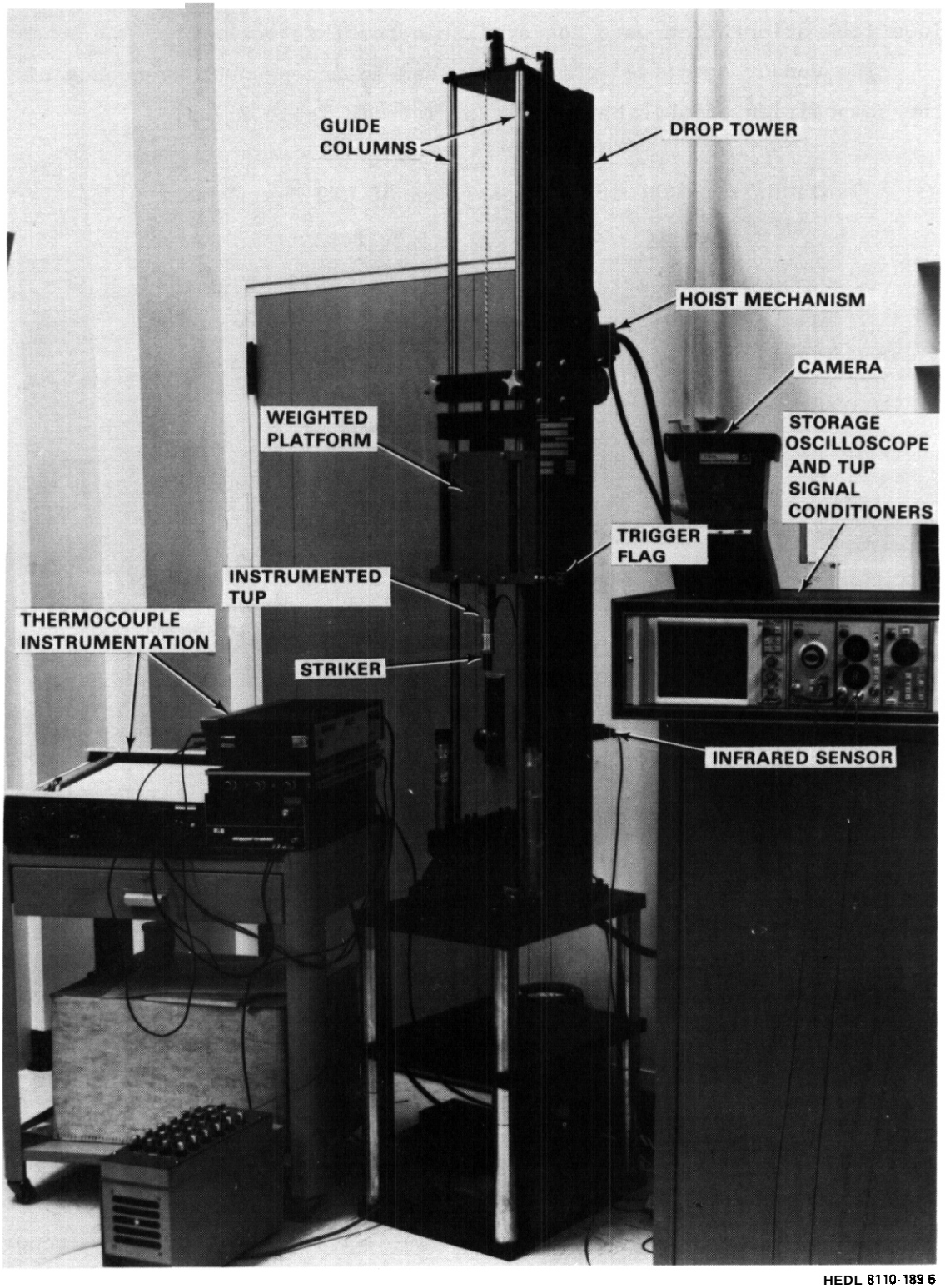

Fig. *7.7.4.* **Experimental set up used to test HEDL half size CVN specimens.**

tup assembly and a hoist mechanism which allows for remote raising and releasing of the weighted crosshead. The specimen to be tested is placed on a set of anvils and the crosshead travel is limited by a set of stops positioned outside the guide columns. The separation between the support anvils was set so that a span equal to 4w, where W is the width of the specimen (5.0 mm) would be obtained. The span was taken as the distance between the points of contact of the specimen with the anvils. The signal from the instrumented tup is fed to a storage oscilloscope. The oscilloscope is triggered when a flag on the crosshead passes in front of an infrared sensor which is fixed to the drop tower support frame. Each specimen to be tested was instrumented with a thermocouple. The thermocouple wires were spot welded separately on either side of the notch so that the temperature of the specimen at the time of failure could be determined. Specimen temperature conditioning was accomplished with the specimen in place on the anvils using either a heated air stream or liquid nitrogen vapor. The velocity of the crosshead just prior to specimen contact was *2.4* m/sec for each test performed.

7.7.4.3 Experimental Results

The initial calibration of the instrumented tup required the adjustment of the load signal gain control *so* that the maximum load obtained during dynamic testing was identical to the maximum load determined during the slow bend testing of a strain rate insensitive alloy. The specimen used for calibration was a one-half size Type A CVN specimen of 6061 aluminum in the T651 heat-treated condition, supplied to HEDL by ETI. The radius of the striker was scaled to one-half the radius specified for full size CVN testing' mainly so that available finite element analyses of charpy test specimens can be unambiguously applied to our specimen geometry. The time rate of change of the specimen temperature was also examined over the range of temperatures studied for this work. The time rate of change of the specimen temperature ranged from about +2°C/sec at -100°C to about -1°C/sec at +100°C for specimens tested in a room whose ambient temperature was about 22°C. Based on these results and given that the fracture event occurs on a millisecond time scale, the specimen temperature was assumed to be constant during the test.

A comparison between the ductile to brittle transition temperature curve obtained using full size and HEDL half size CVN specimens is shown in Fig. 7.7.5. The data has been normalized on an area basis. The area used is the specimen width multiplied by the length of the unbroken ligament. The trend line represents the results obtained by NRL using full size CVN specimens. An indication of the scatter in the NRL data is also shown. The data points shown are the values obtained using the HEDL half size CVN specimens. The results obtained using HEDL half size CVN specimens are listed in Table 7.7.3. In all cases the fracture energy could be resolved to a precision of ±.14 J (±0.1 ft-lb).

Table 7.7.3. HEDL Half Size CVN Test Data

Specimen Number	Test Temperature (°C)	Total Fracture Energy (J)	Normalized Total Fracture Energy (J/cm^2)
62-10	-100	2.4	11.5
62-6	-47	5.2	24.4
62-7	-12	13.3	63.0
62-8	0	17.6	83.0
62-5	22	20.6	96.7
62-9	100	31.6	149.2

The results obtained using precracked HEDL half size CVN specimens are shown in Fig. 7.7.6 through Fig. 7.7.8. The fracture energy versus test temperature results are shown in Fig. 7.7.6 and listed in Table 7.7.4. The fracture energy ranges from less than .14 J at -181°C to a maximum of 5 J at +73°C. The DBTT determined using precracked HEDL half size CVN specimens is in good agreement with that determined using full size specimens and HEDL half size CVN specimens. Graphical reproductions of the photographs of the load-time traces and scanning electron microscope views of the fracture surface of a specimen tested at -20°C and at +100°C are shown in Fig. 7.7.7 and Fig. 7.7.8 respectively. In both cases the oscilloscope was set to display both the load versus time signal and the integrated load versus time or fracture energy versus time signal. The brittle behavior exhibited by unirradiated HT9 at -20°C is typical of the behavior of specimens on the lower shelf and is evidenced by the failure of the

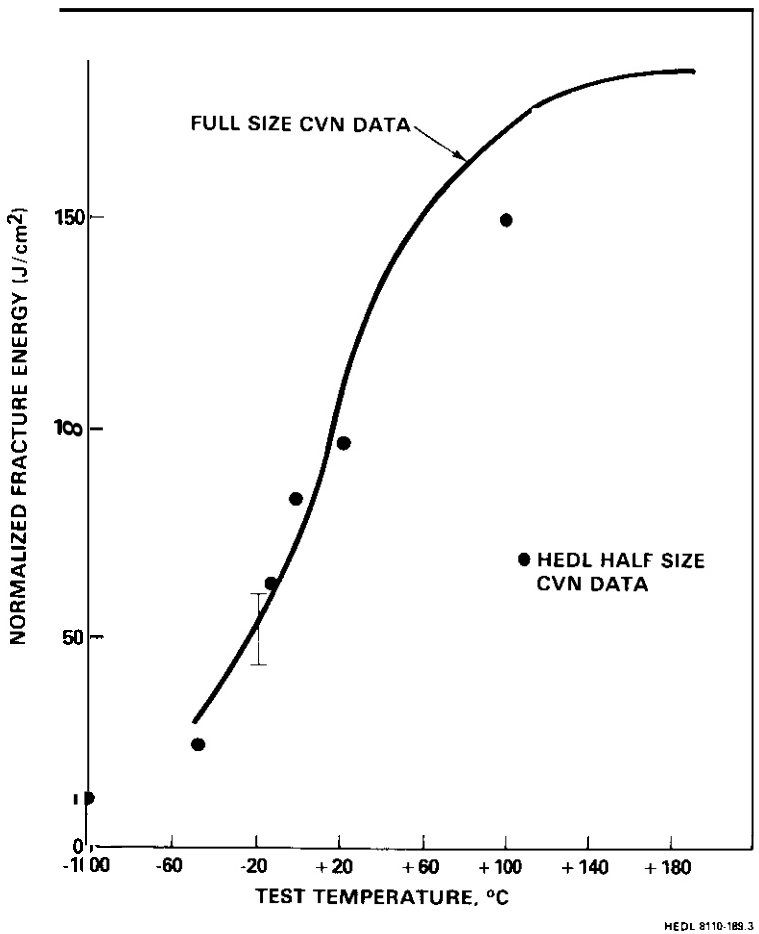

Fig. 7.7.5. Comparison of full size and HEDL half size CVN HT9 specimen data normalized on an area basis.

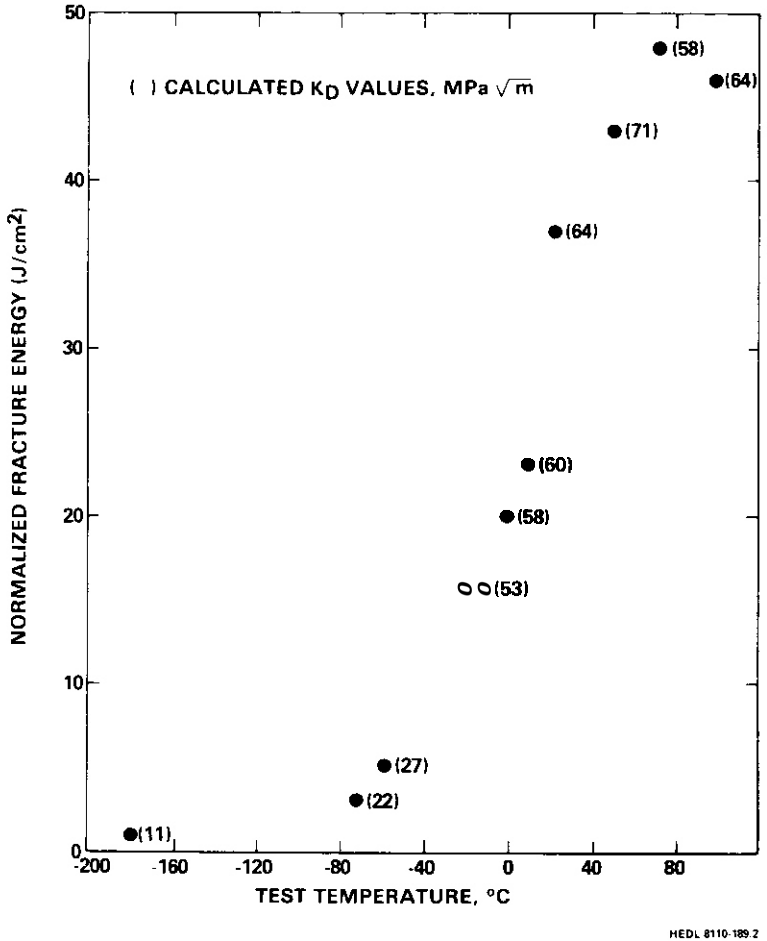

Fig. 7.7.6. Total fracture energy versus test temperature data for precracked HEDL half size CVN HT9 specimens. Parenthetical numbers are calculated dynamic fracture toughness values.

Table 7.7.4. HEDL Precracked Half Size CVN Specimen Test Data

Specimen Number	Test Temperature (°C)	Crack Length (cm)	Area (cm^2)	Total Fracture Energy (J)	Normalized Total Fracture Energy (J/cm^2)
TT52	-181	0.295	0.1032	<0.14	<1
TT24	-73	0.307	0.0968	0.3	3
TTlO	-58	0.305	0.0981	0.5	5
TT36	-20	0.310	0.0955	1.5	16
TT34	-10	0.310	0.0955	1.5	16
TT31	0	0.310	0.0955	1.9	20
TT53	10	0.302	0.0994	2.3	23
TT50	22	0.300	0.1006	3.7	36
TT40	50	0.295	0.1032	4.5	44
TT03	73	0.290	0.1058	5.0	47
TT39	100	0.318	0.0916	4.2	46

specimen during the linear elastic portion of the load-time trace, the relatively small total fracture energy, 1.5 J, as well as by the fractographic examination. The specimen suffered little macroscopic deformation and a closer examination of the crack extension region of the fracture surface indicated little evidence of ductile tearing. The specimen tested at 100°C, on the other hand, suffered a large amount of plastic deformation prior to failure, as indicated by the non-linear load versus time trace and the total fracture energy of 4.2 J. The specimen suffered a large amount of macroscopic plastic deformation and a closer examination of the crack extension region of the fracture surface indicates that the predominant fracture mode was ductile tearing.

7.7.4.4 Discussion

The agreement between the DBTT determined using full size and HEDL half size specimens is surprising. The half size specimens were expected to exhibit a transition in their fracture behavior at a lower temperature than the full size specimens since the half size specimens should offer less constraint. One explanation of this finding is that the increased

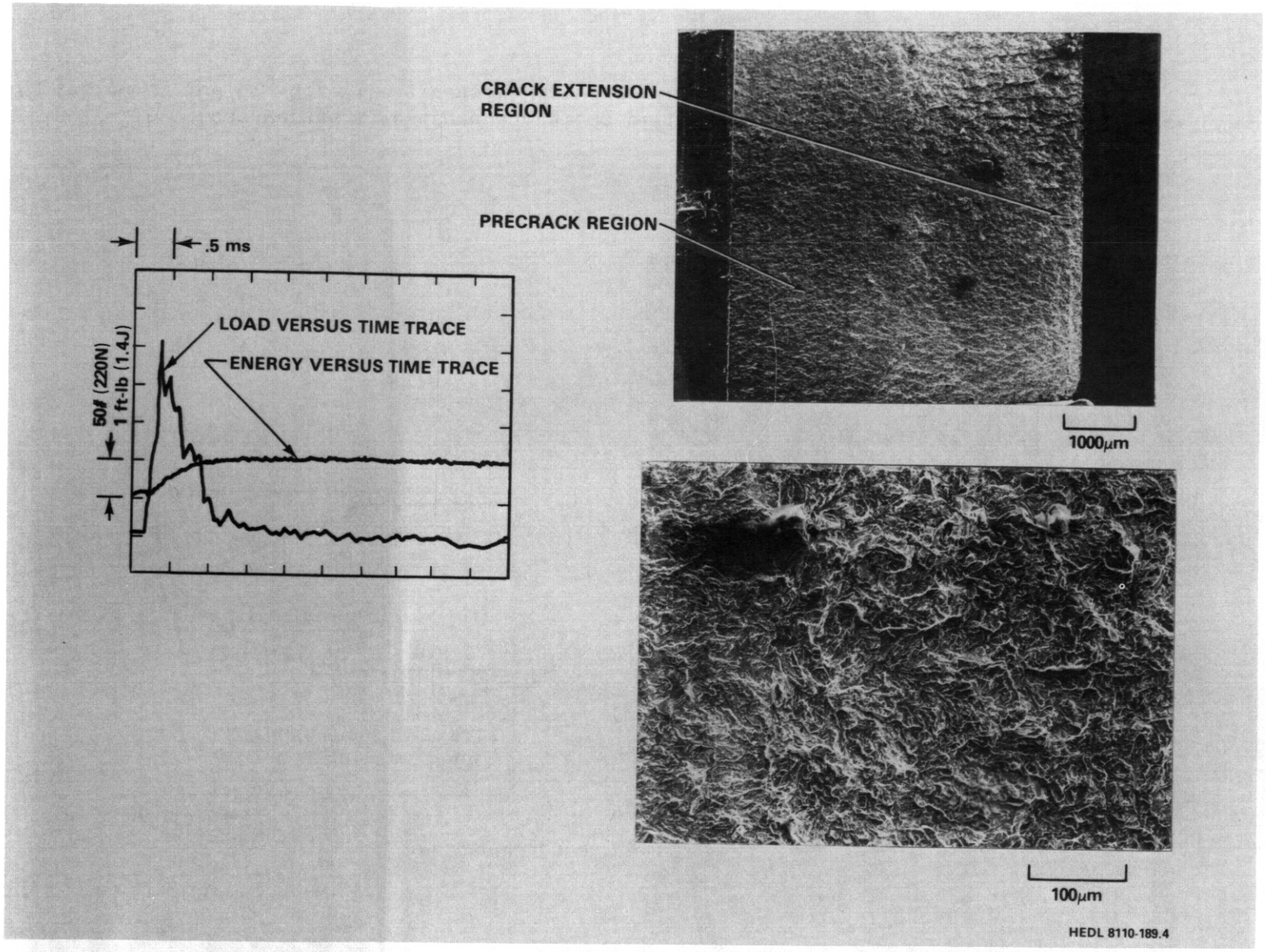

Fig. 7.7.7. Load time trace and views of the fracture surface of a HEDL half size CVN specimen of HT9 tested at -20°C. Note that the failure occurred in the linear elastic portion of the load time history and the lack of any macroscopic specimen deformation.

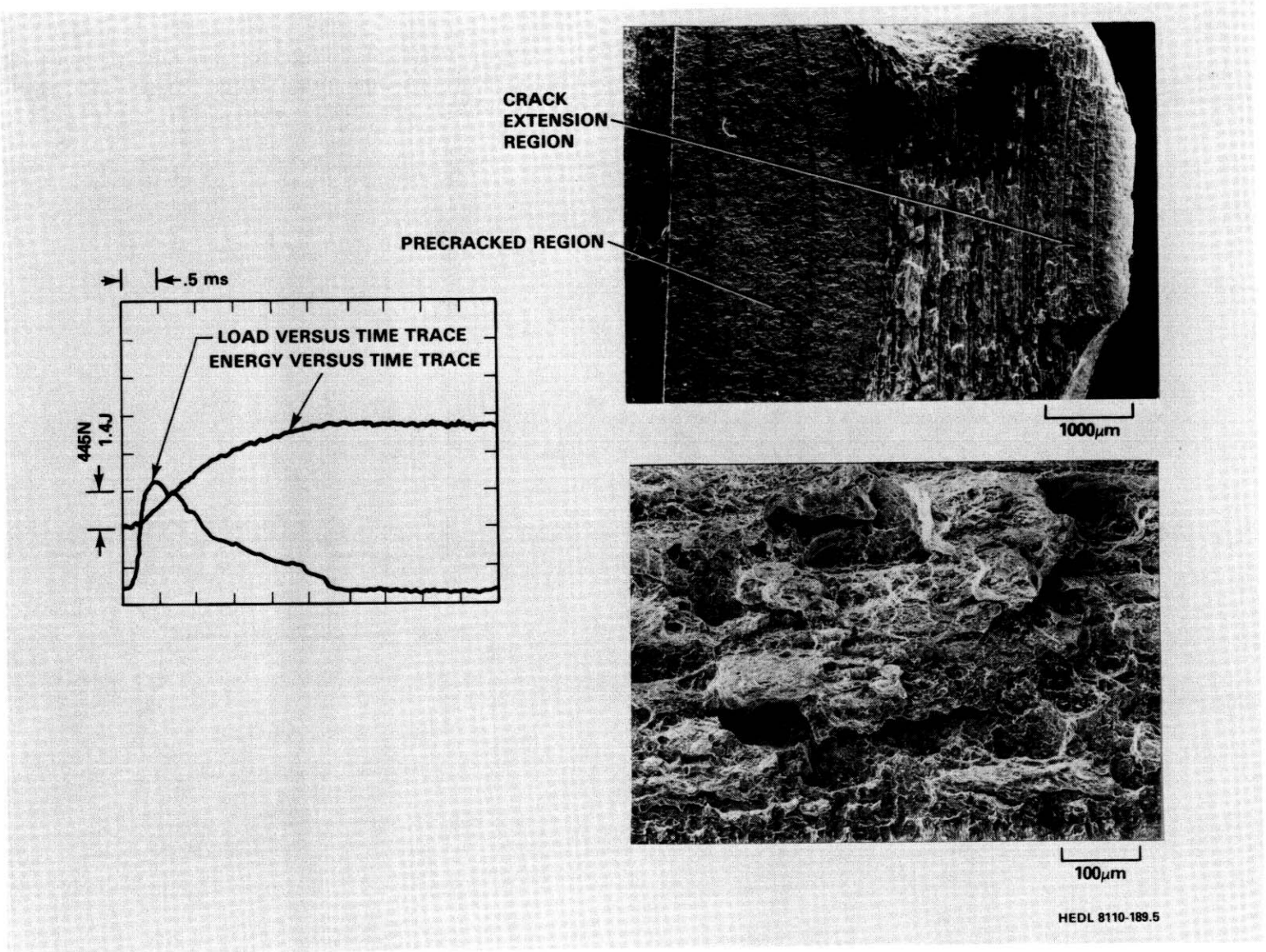

Fig. 7.7.8. Load versus time trace and views of the fracture surface of a HEDL half size CVN specimen of HT9 tested at 100°C. Note the extensive macroscopic specimen deformation.

constraint due to either the reduced notch dimensions or the fatigue precrack may have offset the reduced constraint due to the reduced thickness of the HEDL half size specimens. However a recent report comparing one-third size CVN specimens of A302B in which the notch tip radius was comparable to the radius of the HEDL half size specimens found a shift in the DBTT determined by the one-third size specimens with respect to the DBTT from full size specimens.[6] The shift was either *40* or *80°C* depending on if the data was normalized on an area or volume basis. Therefore the agreement obtained in this study may be fortuitous especially given the differences in specimen prior history and orientation.

The data obtained from precracked HEDL half size CVN specimens can be used to obtain the dynamic fracture toughness. For three point bending[5] the fracture toughness K can be expressed as

$$K = \frac{PS}{Bw^{3/2}} f\left(\frac{a}{w}\right)$$

where P is the load, S is the span, B is the specimen width, w is the specimen thickness, a is the crack length and $f\left(\frac{a}{w}\right)$ is given by

$$f\left(\frac{a}{w}\right) = \frac{3\left(\frac{a}{w}\right)^{1/2}\left[1.99 - \left(\frac{a}{w}\right)(1 - \frac{a}{w})(2.15 - 3.93\frac{a}{w} + 2.7\frac{a^2}{w^2})\right]}{2(1 + 2\frac{a}{w})(1 - \frac{a}{w})^{3/2}}$$

For this work $S = 4w$ and $w = B = 5$ mm. If we allow $P = P_{max}$ and if the load time behavior is linear elastic then $K = K_D$, the dynamic linear elastic fracture toughness. K_D values were calculated for all the precracked specimens which were tested and the values are shown in Fig. 7.7.6. For specimens on the lower shelf, where the load versus time behavior is linear elastic, this procedure is valid. For specimens in the transition and upper shelf regions, where the load versus time behavior is not linear elastic, the load, or energy, at the transition between linear and nonlinear behavior is usually used to calculate an elastic-plastic fracture toughness. The resolution of the present instrumentation is not sufficient to permit this to be done. The use of a digitized data acquisition unit is being considered to improve the resolution of the initial portion of the load versus time signal.

At a test temperature of 22°C, the calculated value of K_D is about 64 MPa $\sqrt{m}$. This value can be compared to the room temperature fracture toughness of HT9 determined under static testing conditions. Using

one-half inch thick compact tension specimens a K_Q of 119 MPa $\sqrt{m}$ was determined for HT9. Using one-tenth inch thick specimens of HT9 a J_{Ic} value of 99.8 KJ/m^2 was determined.* This can be converted to the elastic fracture toughness K_J by the standard formulation

$$K_J = \left(\frac{JE}{1 - \nu^2}\right)^{\frac{1}{2}}$$

where E and v are Young's Modulus and Poisson's ratio respectively.[9] The K_J calculated in this manner is *146* MPa $\sqrt{m}$. The K_D determined under dynamic loading conditions would be expected to be less than either K_Q or K_J since the fracture toughness of HT9 is known to be strain rate sensitive. Therefore the K_D determined from precracked HEDL half size CVN specimens is qualitatively consistent with the fracture toughness values obtained under static test conditions.

7.7.5 Conclusions and Future Work

A miniature CVN specimen has been designed and found to be a valid test article. Two instrumented impact test frames have been procured and instrumented testing of HEDL half size CVN specimens of HT9 has been performed. The results correlate unexpectedly well with data obtained independently from full size CVN specimens. The agreement obtained may be fortuitous due to differences in the prior history and orientation of the HEDL half size and the full size CVN specimens. Work is continuing on the development of a conditioning chamber and transfer device which will permit the remote testing of the HEDL half size specimens. The use of a computer to store and analyze the data obtained from the instrumented testing is being considered in order to improve the determination of K_D. In cell installation of the 122 J drop tower and testing of HEDL half size specimens of HT9 and 9Cr-1Mo, irradiated to 14 dpa in the AD-2 experiment, will be completed during the next reporting period.

7.7.6 References

1. *Annual Book of ASTM Standards, Part 10,* "Standard Methods for Notched Bar Impact Testing of Metallic Materials," pp. 235-251.
2. M. Grounes, "Review of Swedish Work on Irradiation Effects in Pressure Vessel Steels and on Significance of Data Obtained," *Effects of Radiation on Structural Metals, ASTM STP 426,* Am. Soc. Testing Mats., pp. 224-259, 1967.

3. R. J. Puigh and N. F. Panayotou, *"Specimen Preparation and Loading for the AD-2 Ferritics Experiment,"* ADIP Quarterly Progress Report, DOE/ER-0045/3, pp. 261-293, April-June 1980.
4. F. A. Smidt, Jr., J. R. Hawthorne and V. Provenzano, "Fracture Resistance of HT9 After Irradiation at Elevated Temperature," *Effects of Radiation on Materials: Tenth Conference, ASTM STP 725,* D. Kramer, H. R. Brager and J. S. Perrin, Eds. *Am.* Soc. Testing Mats., pp. 269-284, 1981.
5. *Annual Book* of *ASTM Standards, Part 10,* "Standard Methods for Plane-Strain Fracture Toughness of Metallic Materials," pp. 512-533.
6. G. E. Lucas, G. R. Odette, W. Schekhard, C. Pendleton, F. Haggag, M. Dooley, W. Server and P. McConnel, *"Small Specimen Test Development,"* DAFS Quarterly Progress Report, DOE/ER-0046/4, pp. 46-64, February 1981.
7. F. F. Huang, HEDL, Private Communication.
8. F. F. Huang and G. L. Wire, *"Analysis of Single Specimen Tests on HT9 for J_{Ic} Determination,"* ADIP Quarterly Progress Report, DOE/ER-0045/3, pp. 236-254, April-June 1980.
9. D. Landes and J. A. Begley, "Test Results from J-Integral Studies; An Attempt to Establish a J_{Ic} Testing Procedure," *Fracture Analysis ASTM STP 560,* *Am.* Soc. Testing Mats., pp. 170-186, 1974.

7.8 EFFECTS OF A WATER QUENCH ON HT-9 - J. M. McCarthy and D. S. Gelles (Hanford Engineering Development Laboratory)

7.8.1 ADIP Task

The Department of Energy (DOE)/Office of Fusion Energy (OFE) has cited the need to investigate ferritic alloys under the ADIP program task, Ferritic Steels Development (Path E). The tasks involved are akin to task number 1.B.13, Tensile Properties of Austenitic Alloys, task number 1.C.2, Microstructures and Swelling in Austenitic Alloys and task number 1.C.1, Microstructural Stability.

7.8.2 Objective

The objective of the experiment was to determine the effect of the post-austenitization quenching on the toughness of tempered HT-9.

7.8.3 Summary

Charpy specimens of HT-9 were given a heat treatment 5 minutes at 1038°C followed by a water quench, then 1 hour at 760°C followed by air cooling. Surface cracks were found in all three specimens following heat treatment. Charpy tests were performed on these HT-9 specimens to determine the effect of water quenching relative to air cooling. A Charpy test at 23°C (upper shelf behavior) showed the water-quenched HT-9 to be 1.70 times as tough as the HT-9 air cooled. The tests performed at -59°C (lower shelf behavior) showed a similar increase in toughness (up to 1.71 times). The consequence of a water quench is therefore found to be a large increase in upper shelf energy which results in an effective DBTT shift of ~40°C but only a small change in the lower shelf behavior.

7.8.4 Progress and Status

7.8.4.1 Introduction

Lichtenberg' has noted retained austenite at martensite lath boundaries in air cooled HT-9. He ascribes this observation to carbon segregation ahead of the expanding martensite plates, creating austenite enriched in carbon and therefore stabilized against transformation to

martensite. Tempering treatments result in precipitation of $M_{23}C_6$ at these carbon rich regions. Furthermore, a faster quenching rate produced by a warm water quench reduces the retained austenite film.

It is anticipated (and subsequently shown but not reported by Lichtenberg) that a reduction in the amount of retained austenite will alter carbide precipitation and result in a finer dispersion of carbide particles with reduced development at martensite lath boundaries. Such a change in microstructure can be expected to alter toughness properties. It was the purpose of this experiment to determine if a change in carbide distribution, which can be expected from a rapid quench, will significantly improve toughness behavior.

7.8.4.2 Experimental Procedure

HT-9 half-sized Charpy specimens were quartz encapsulated in an argon atmosphere and austenitized at 1038°C for 5 minutes. Quenching was performed by breaking the ampule under water to give a maximum quenching rate. Specimen TT63 was fatigue precracked prior to the quench treatment, whereas specimens Q1 and Q2 were fatigue precracked after the water quench treatment. The fatigue crack growth rates were consistent in both cases, indicating that the cracks formed by the heat treatment did not effect the precracking process. The specimens were then tempered in air at 760°C for 65 minutes and allowed to air cool. The Charpy test was then performed. A detailed description of these tests, equipment development, procedure and variables measured can be found in Reference 2.

7.8.4.3 Results and Discussion

Cracks were visible on the surfaces of all three specimens following the water quench as shown by Figures 7.8.1 through 7.8.5. (One had been fatigue cracked prior to heat treatment.) The fatigue crack growth rate was uniform throughout the entire process of pre-cracking indicating that the cracks formed by the heat treatment did not affect this process. Most of the cracks were surface cracks as confirmed by examining the cross section of one specimen, Q1, in the Scanning Electron Microscope (SEM). Micrographs of the deepest surface cracks found in this examination are shown in Figures 7.8.6 and 7.8.7. The most severe crack was about *40*

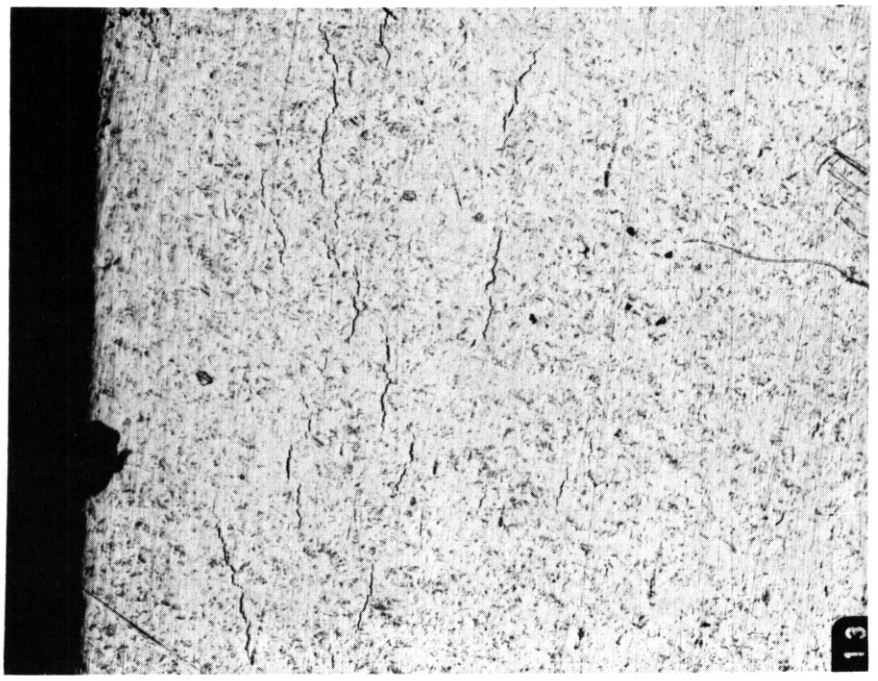

Fig. 7.8.1. **Specimen** Q1 **Surface Following Water Quench** (50x). **This Specimen Shows a Network of Shallow Surface Cracks (See Figures 7.0.6 and** 7.8.7).

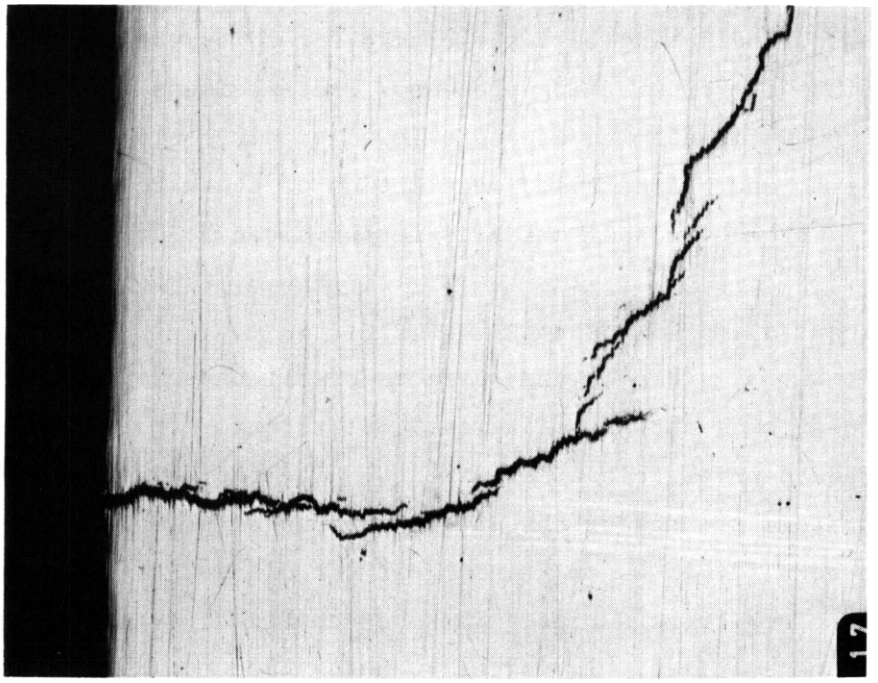

Fig. 7.8.2. **Specimen** Q2 **Surface Following Water Quench** (50x). **The Cracks in this Specimen were** of **Greater Length and Depth than** Q1.

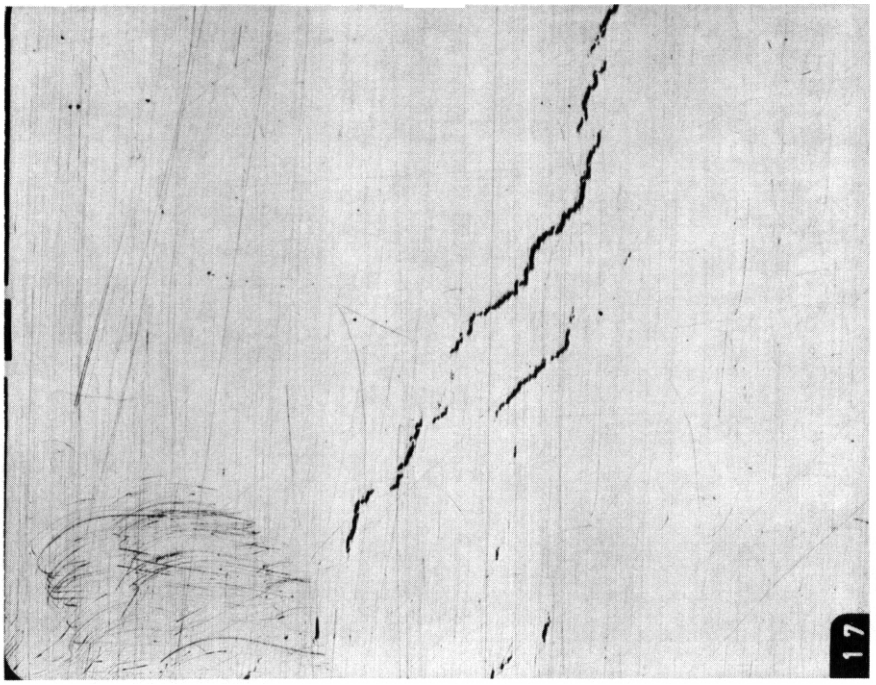

Fig. 7.8.3. Specimen Surface Following Water Quench (50x).

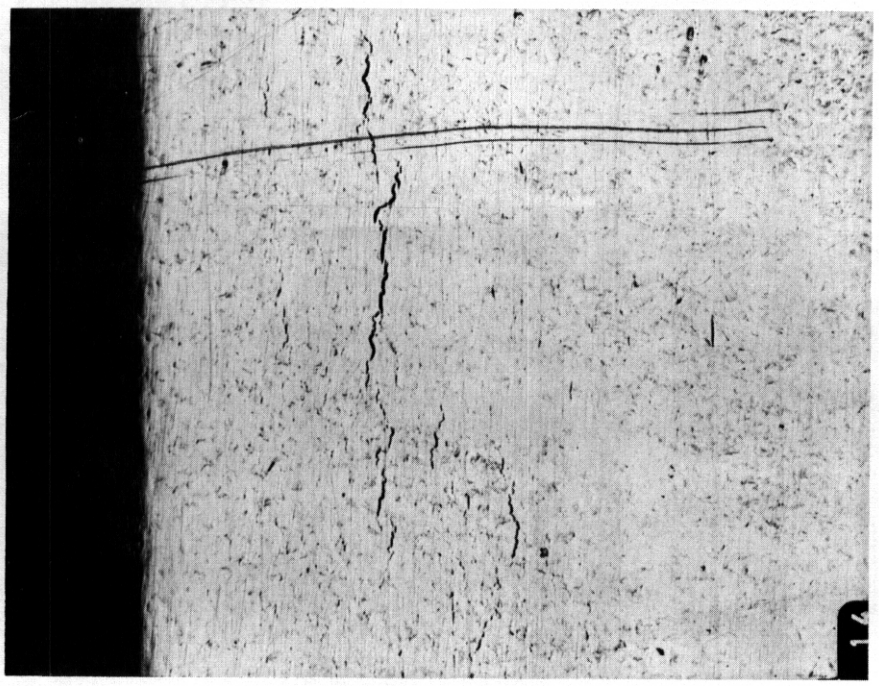

Figure 7.8.4. Specimen Q1 Surface Following Water Quench (50x).

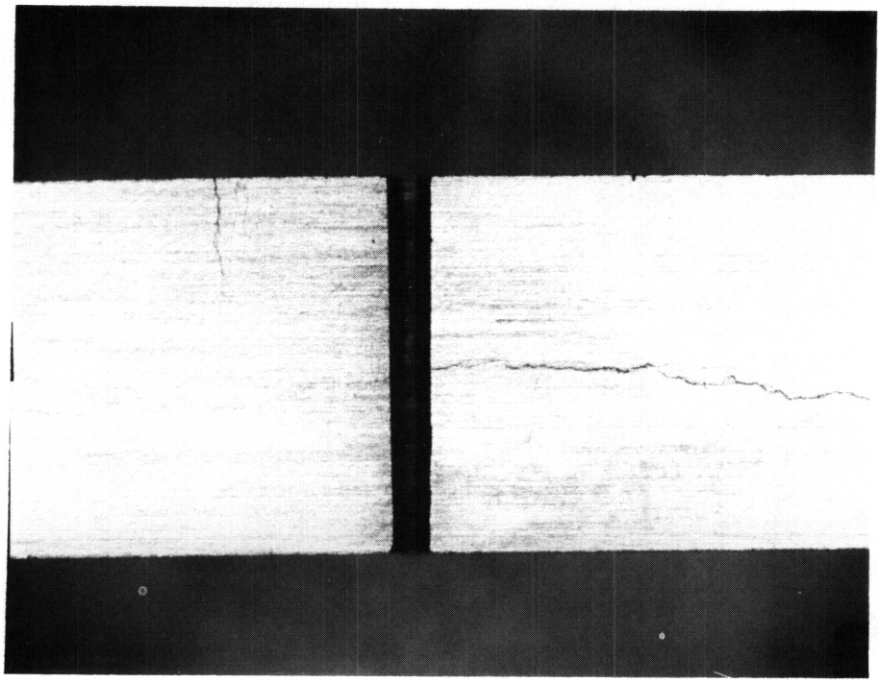

Fig. 7.8.5. Charpy Specimen Q2 Surface Following Heat Treatment (10x). The Longitudinal Crack had a Depth of .25 cm Following Charpy Test.

Fig. **7.8.6.** Cross Section of Charpy Specimen Q1 Showing Crack with a Depth of ∿40 μ.

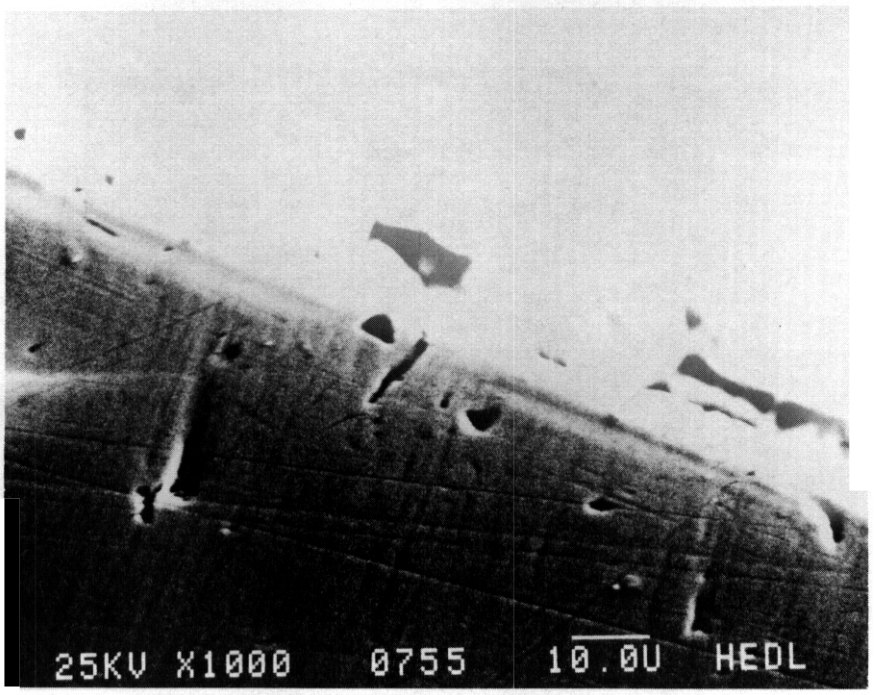

Fig. 7.8.7. Cross Section of Charpy Specimen Q1 Showing Crack with a Depth of ∿10 μ.

microns deep. However, in a second specimen, Q2, a longitudinal crack reached a depth of .2 cm. Thus, all the cracks formed by the water quench were not just surface cracks. Also, Q2 had much longer continuous cracks on its surfaces than the other two specimens given a water quench.

Figures 7.8.8, 7.8.9, and 7.8.10 show the results of the Charpy tests on the water-quenched HT-9. Figures 7.8.11 and 7.8.12 are Charpy tests performed on HT-9 without a water quench.[2] In each Figure, the lower curve represents the loading of the specimen; the upper curve represents the energy C_v necessary to start and move the crack through the specimen. Table 7.8.1 shows the C_v for each specimen.

Figure 7.8.13 shows the temperature dependence of energy-absorbed (C_v) for heat treated HT-9 without a water quench,[2] compared with a water-quenched HT-9 curve. The C_v values for the water-quenched HT-9 specimens are also shown for comparison. Specimen TT63 is shown by Table 7.8.1 to have a C_v less than specimen Q1, although it is the same material and the Charpy test was performed at nearly the same temperature.

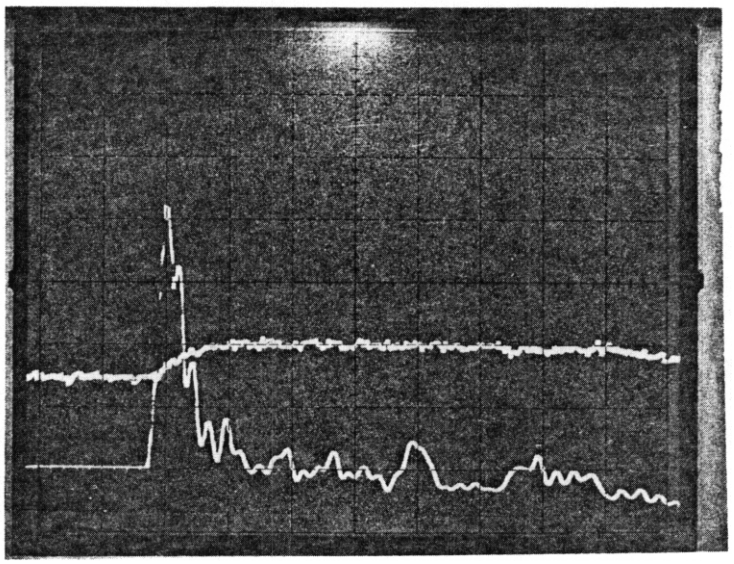

Fig. 7.8.8. Charpy Test Specimen Q1. T = -59.3°C, C_v = .53 ft.-lb.

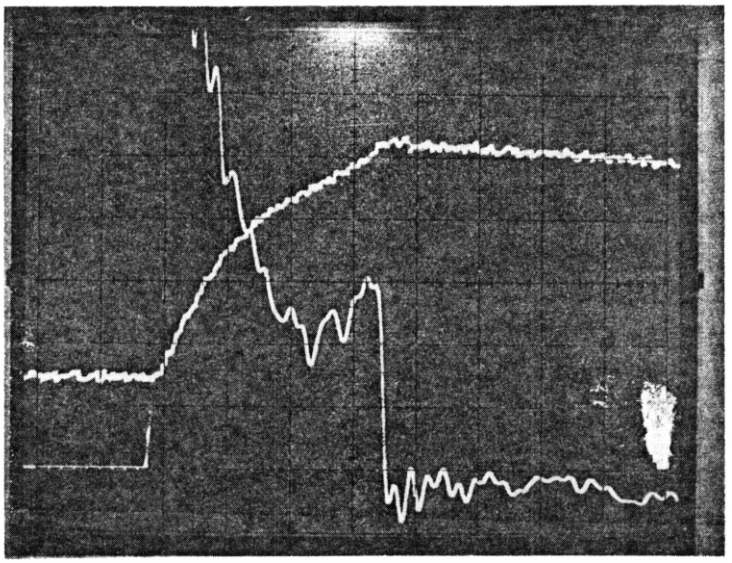

Fig. 7.8.9. Charpy Test Specimen Q2. T = 25°C, C_v = 3.9 ft.-lb.

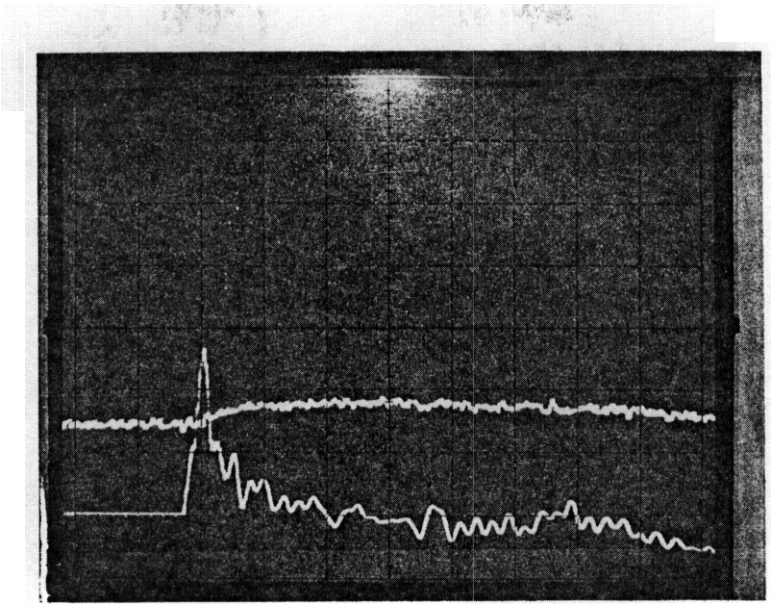

Fig. 7.8.10. Charpy Test Specimen TT63. T = -59°C, C_v = .30 ft.-lb.

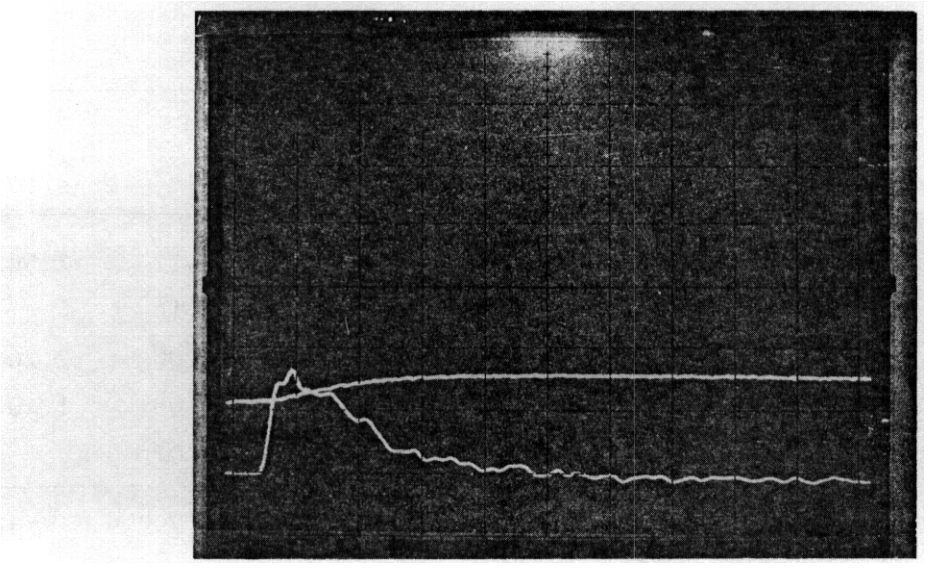

Fig. 7.8.11. Charpy Test Specimen TT50. T = 23°C, C_v = 2.3 ft.-lb.

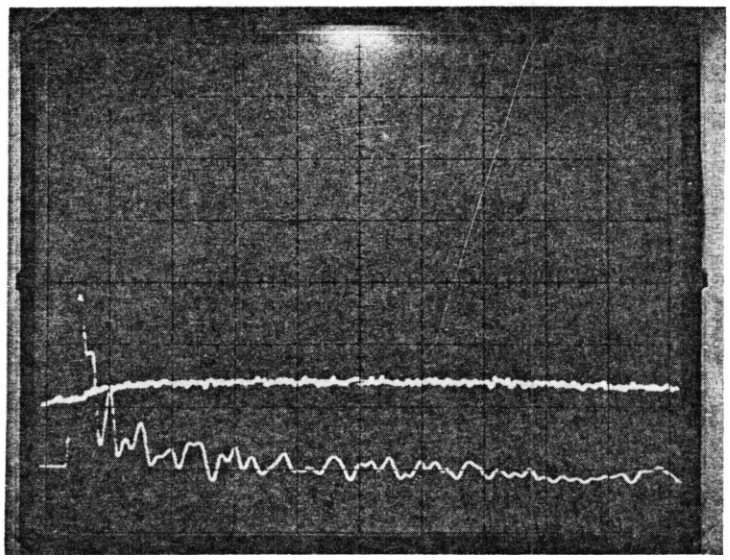

Fig. 7.8.12. Charpy Test Specimen TT10. T = -58.4°C, C_v = .31 ft.-lb.

Table 7.8.1

Specimen	Water Quench Heat Treatment	T (°C)	Pre-Crack Depth a (cm)	Fracture Energy C_v ergs/10^7	C_v* (1) ergs/10^7-cm
Q1	Yes	-59.3 ± .1	.22 ± .01	.718 ± .12	2.56
Q2	Yes	23	.25	5.28 ± .14	
TT63	Yes	-59	.32	.407 ± .00	2.26
TT10	NO	-58.4	.20	.42 ± .09	1.40
TT50	NO	23	.20	3.12 ± .07	

*The width of the specimens w = .5 cm. The fracture distance d = w-a; $C_a = \frac{C_v}{a}$ for brittle behavior.

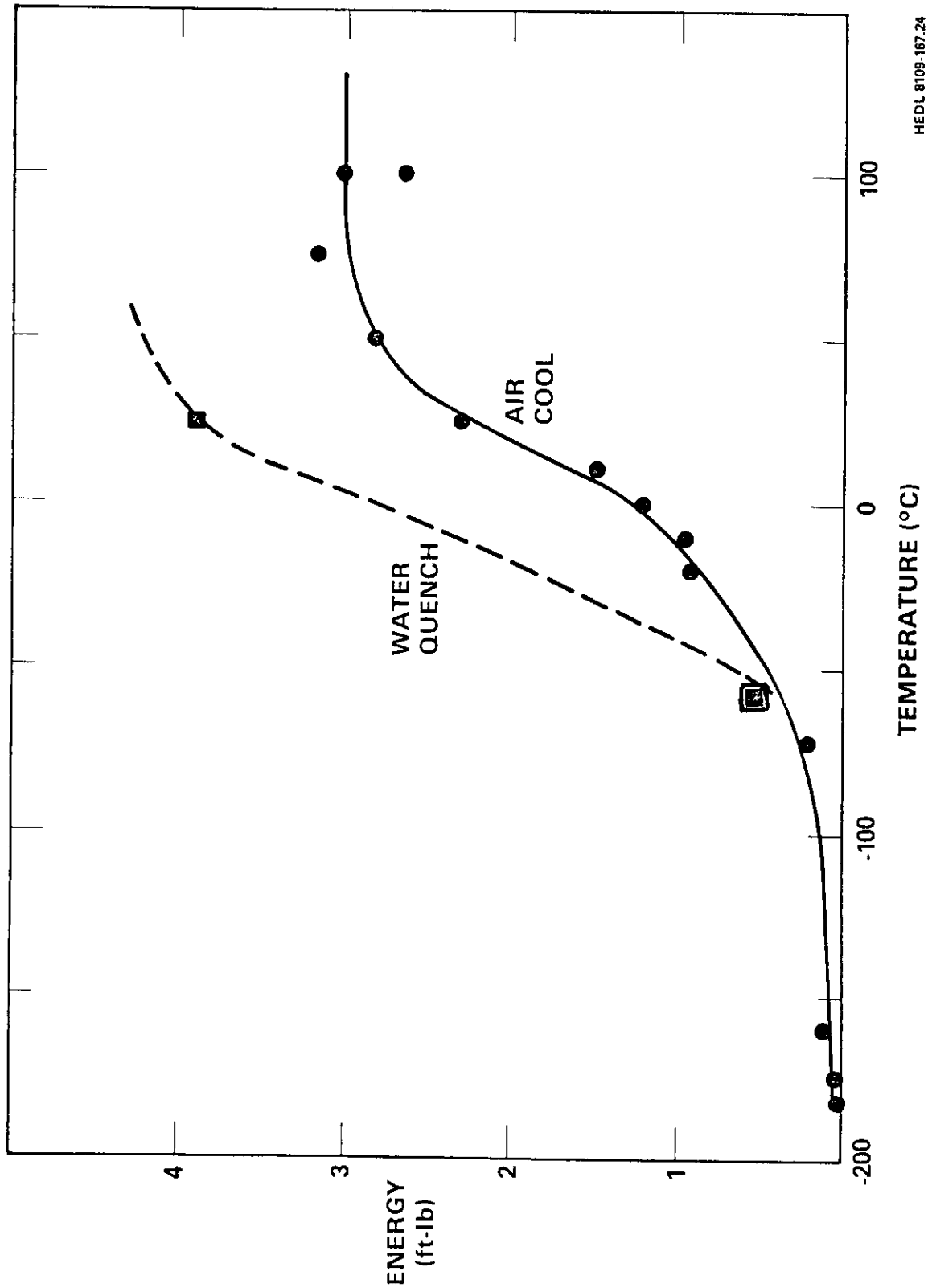

Fig. 7.8.13. The Effect of Quench Rate on DBTT in HT-9 Miniature Charpy Specimens.

This can be attributed to the difference in d, the distance through which the fracture surface propagates during the Charpy test. The parameter "d" is much less for TT63 than for Q1 and consequently C_V is proportionately less for TT63. The value of C_V for TT63 in Table 7.8.1 is normalized by "d". In this instance, lower shelf behavior, C_V has a linear dependence on "d". The energy necessary to start the crack is small compared to the energy of propagation (brittle behavior). The toughness at both high and low temperatures is found to have increased by water-quenching. However, the absolute changes to the lower shelf response are small. If the DBTT is defined as occurring at 2 ft.-lb., water-quenching appears to have decreased the DBTT by about 40°C.

7.8.5 Conclusions

The effect of a water quench heat treatment for HT-9 was found to significantly increase toughness at high temperatures. However, it does not significantly alter low temperature behavior. The DBTT was shifted down by ~40°C. Although a water quench procedure appears to be a means of significantly reducing the DBTT of HT-9, the presence of sizable cracks in one specimen may present a serious problem when using this heat treatment.

7.8.6 References

1. T. A. Lichtenberg, "The Microstructural Evaluation of Embrittled 12Cr-1Mo-0.3V Steel," DOE/ER-0045/5, (10-12, 1980), 143.
2. N. F. Panayotou and W. L. Hu, "Miniature Charpy Test Device Development and Preliminary Results for Ferritic Alloy HT-9," this document.

7.9 EFFECT OF HEAT TREATMENT VARIATIONS ON 9 Cr-1 MoVNb AND 12 Cr-1 MoVW FERRITIC STEELS — J. M. Vitek and R. L. Klueh (Oak Ridge National Laboratory)

7.9.1 ADIP Tasks

ADIP tasks are not defined for Path E, ferritic steels, in the 1978 program plan.

7.9.2 Objective

The objective of this study is to evaluate the effect of variations in heat treatment conditions on the structure of Path E ferritic steels. This will allow for a more complete understanding of the unirradiated and irradiated behavior of these alloys.

7.9.3 Summary

The effect of variations in the heat treatment of 9 Cr-1 MoVNb and 12 Cr-1 MoVW have been evaluated. Dissolution of carbides during austenitization was found to be somewhat faster in 9 Cr-1 MoVNb than in 12 Cr-1 MoVW. The effect of cooling rate after austenitization was strongly dependent on the austenitization time and temperature. The 9 Cr-1 MoVNb alloy structure was found to be more sensitive to cooling rate than the structure of 12 Cr-1 MoVW. Under some circumstances, furnace cooling of 9 Cr-1 MoVNb after austenitizing resulted in a ferrite plus carbide structure rather than a martensite lath structure, and in addition the carbide was not the same as that formed during tempering. The precipitation reactions in both alloys are essentially complete after tempering 1 h at 650°C. In 12 Cr-1 MoVW the principal carbides are chromium-iron rich $M_{23}C_6$ and vanadium rich MC, whereas those in 9 Cr-1 MoVNb were chromium-iron rich $M_{23}C_6$ and niobium-vanadium rich MC.

7.9.4 Progress and Status

7.9.4.1 Introduction

At the start of the ferritic research effort within the **ADIP** program, the heat treatments used for normalizing and tempering were limited in

number. However, as the ferritic program has expanded, the number of heat treatments used, especially for materials included in irradiation experiments, has also increased in number. This has occurred without a complete investigation into the effects of heat treatment variations on the structures in these materials. This investigation was started to examine certain aspects of this question. In particular, the precipitation-dissolution processes were studied as a function of heat treatment.

7.9.4.2 Experimental Procedure

The alloys used in this investigation were those being investigated in the Path E, ferritic steels, portion of the ADIP program. They were 9 Cr-1 No modified with vanadium and niobium additions and 12 Cr-1 No (similar to Sandvik HT9) with vanadium and tungsten additions. The materials, from the series produced by Combustion Engineering, are being used to evaluate helium effects on postirradiation properties.[1] Only the two standard alloys have been examined, and their compositions are presented in Table 7.9.1.

Table 7.9.1. Compositions of Alloys Investigated

Element	Contents,[a] wt %	
	9 Cr-1 MoVNb Heat M-3590	12 Cr-1 MoVW Heat MA-3587
Chromium	8.62	11.99
Molybdenum	0.98	0.93
Carbon	0.09	0.21
Nitrogen	0.05	0.02
Nickel	0.11	0.43
Manganese	0.36	0.50
Tungsten	0.01	0.54
Vanadium	0.21	0.27
Niobium	0.06	0.02

[a]Balance iron.

The precipitation-dissolution response of both alloys has been followed primarily by chemical extraction methods. Samples made from 0.76 mm-sheet (0.030 in.) were heat treated and extractions made using a 10% HCl-90% methanol solution at 1.5 V. In addition to determining the weight percent of precipitate extracted, electron microscopy was used on thinned foil specimens and extraction replicas to follow the structures and determine the precipitate compositions. Hardness measurements (diamond pyramid or Rockwell F scale) were also made as a function of the heat treatment.

Four different austenitizing conditions were investigated with temperature and hold times of 1000°C for 1 h, 1040°C for 5 min, 1040°C for 1 h, and 1100°C for 1 h. Following the austenitizing treatment, the specimens were either cooled in a flowing helium gas or furnace cooled* (typically 12 h to get below 200°C). The short time austenitizing treatment was specifically included to represent the treatment used by HEDL to maintain a fine austenite grain size. Tempering conditions varied from 1 h at 650°C to 2.5 h at 780°C, with a standard 0.5 h at 1050°C normalization treatment used in these studies.

7.9.4.3 Results

The extraction results on 9 Cr-1 MoVNb and 12 Cr-1 MoVW as a function of tempering treatment are given in Fig. 7.9.1. After a 1-h tempering treatment, the amount of precipitate in 12 Cr-1 MoVW is 3.5 wt %, independent of the tempering temperatures examined. Increasing the tempering time to 2.5 h at 650 and 780°C did not result in any additional precipitation. The results on 9 Cr-1 MoVNb show 1.4% precipitate after tempering, again independent of tempering temperature or time except for the case of 1 h at 650°C, where only 1.0% precipitate was extracted. The smaller amount of precipitate in the fully tempered condition can be directly attributed to the lower carbon content in the 9 Cr-1 MoVNb material.

---

* In steel-making terminology, air cooling from the austenite temperature range is referred to as a normalizing treatment. When furnace cooled, a steel is said to be "annealed" or "fully annealed." In the present discussion, the steel rapidly cooled in flowing helium is referred to as normalized.

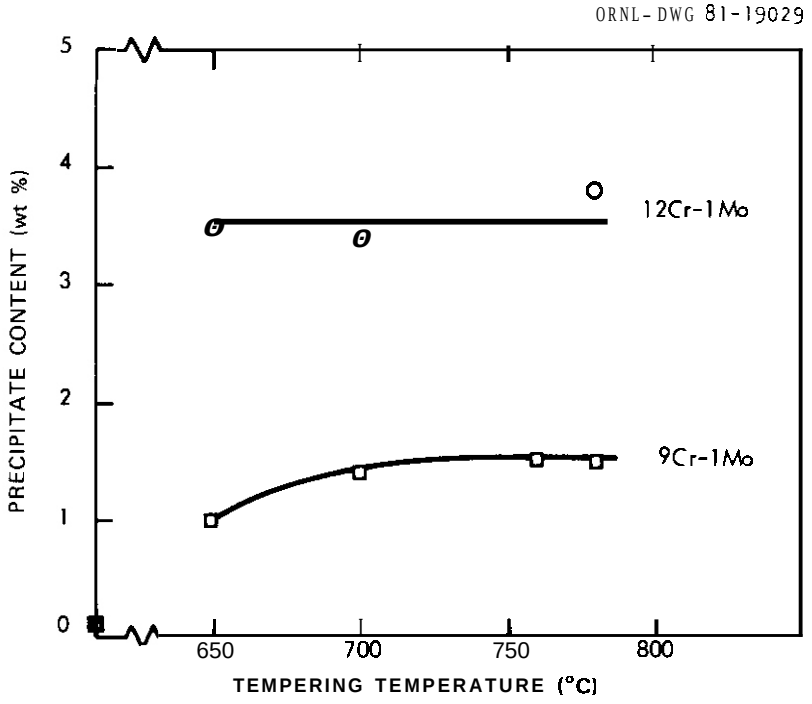

Fig. 7.9.1. Quantity of Extracted Precipitate as a Function of Tempering Temperature. Tempering time was kept constant at 1 h.

Analytical electron microscopy of extraction replicas indicated the types of carbides found in both 9 Cr-1 MoVNb and 12 Cr-1 MoVW after tempering are similar. Most carbides, including all of the larger ones, in 9 Cr-1 MoVNb were of the $M_{23}C_6$ type, rich in chromium and iron as shown by a typical spectrum in Fig. 7.9.2(a). In addition, many niobium or vanadium rich MC carbides were also found. A typical spectrum of these precipitates is given in Fig. 7.9.2(b). The ratio of niobium to vanadium varied over nearly the entire range of 0 to 1. As in 9 Cr-1 MoVNb, the most common precipitate found in 12 Cr-1 MoVW was the $M_{23}C_6$ carbide. An MC carbide was also found, but these were vanadium rich, with niobium only a minor constituent. This is due to the much lower niobium content in the 12 Cr-1 MoVW alloy.

Hardness results as a function of tempering temperature are presented in Fig. 7.9.3. In contrast to the extraction results, the hardness decreases continuously with increasing tempering temperature. This effect cannot be attributed to additional precipitation, but rather is due to coarsening of precipitates and cell rearrangement within the lath network. Typical micrographs of 12 Cr-1 MoVW after normalization and

ORNL-Photo 610881

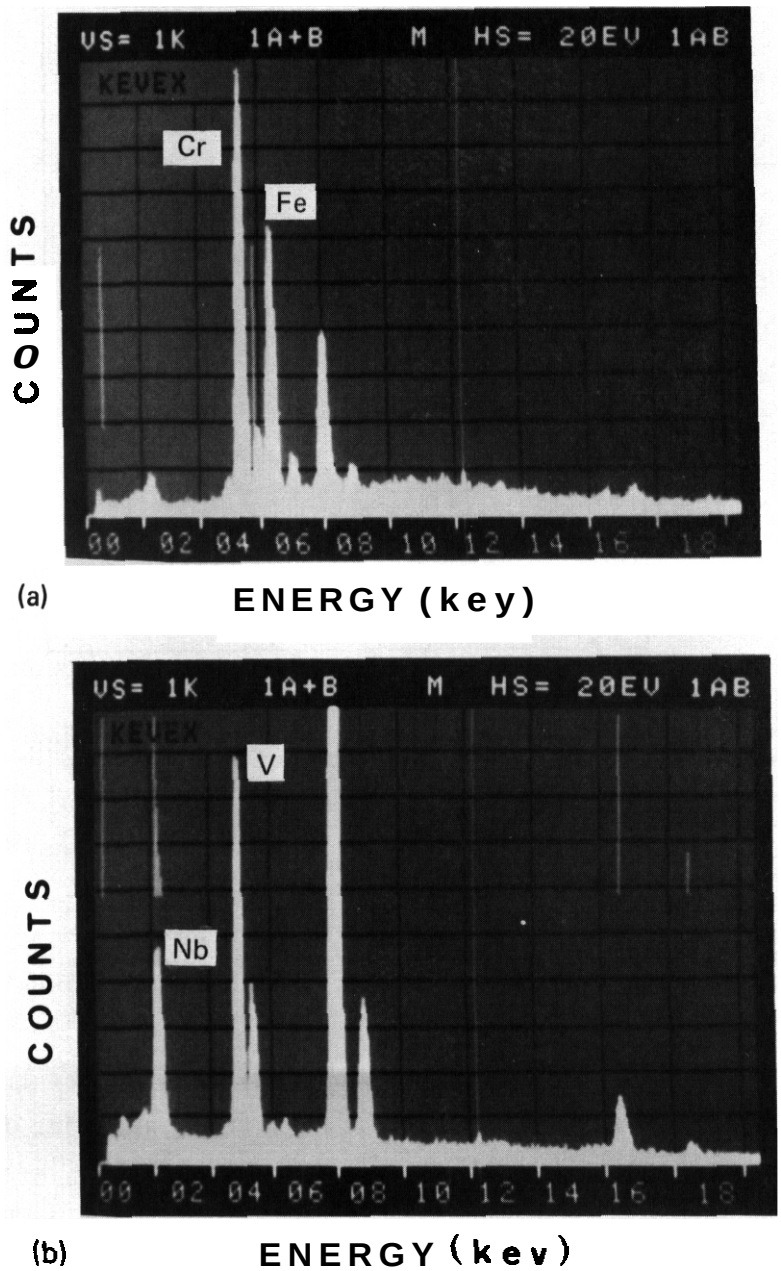

Fig. 7.9.2. Typical Energy Spectra of Precipitates Found after Tempering 9 Cr-1 MoVNb. (a) $M_{23}C_6$ carbide and (b) MC carbide. The peaks at 8 and 8.9 keV are from the copper grid supporting the extraction replicas.

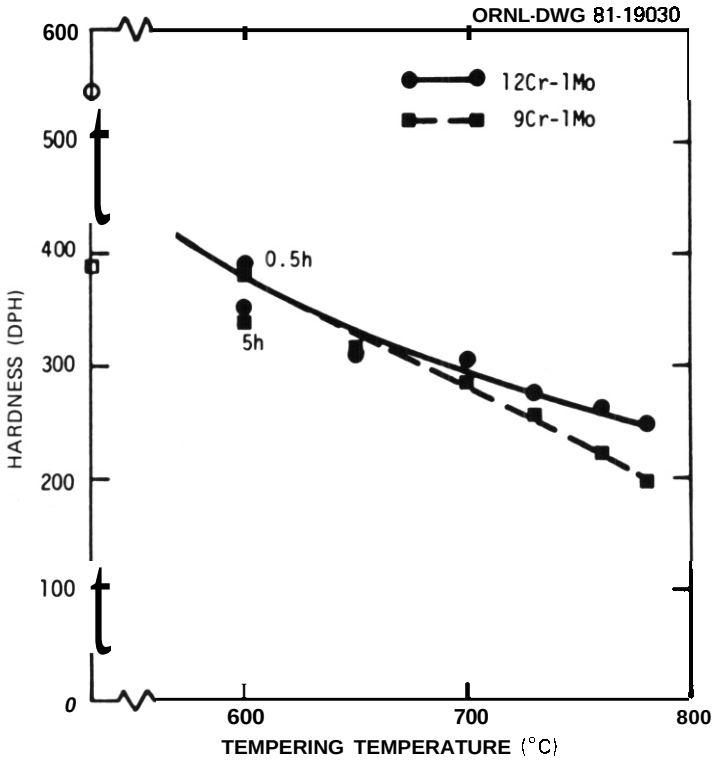

Fig. 7.9.3. Diamond Pyramid Hardness as a Function of Tempering Temperature for Normalized Steels. Tempering times are 1 h except as noted.

after normalizing and tempering are shown in Fig. 7.9.4. In this figure, the common lath structure is evident after normalizing. After tempering, the carbide precipitation is evident as well as the well-defined cell structure of ferrite.

The hardness and extraction results as a function of heat treatment for 9 Cr-1 MoVNb are given in Table 7.9.2. It is apparent from the results on air cooled material that complete dissolution of carbides (within the accuracy of the extraction method) occuks under all of the time-temperature conditions investigated. As can be expected, during furnace cooling extensive precipitation occurs. However, the amount of precipitation decreases as the austenitization time or temperature increases, with the result that no precipitation occurs during furnace cooling after austenitization at 1100°C. The hardness results parallel the extraction findings, in that hardness of furnace cooled material increases to a fully normalized value of about 18 R_F as the austenitizing time and temperature increase.

ORNL-Photo 6105-81

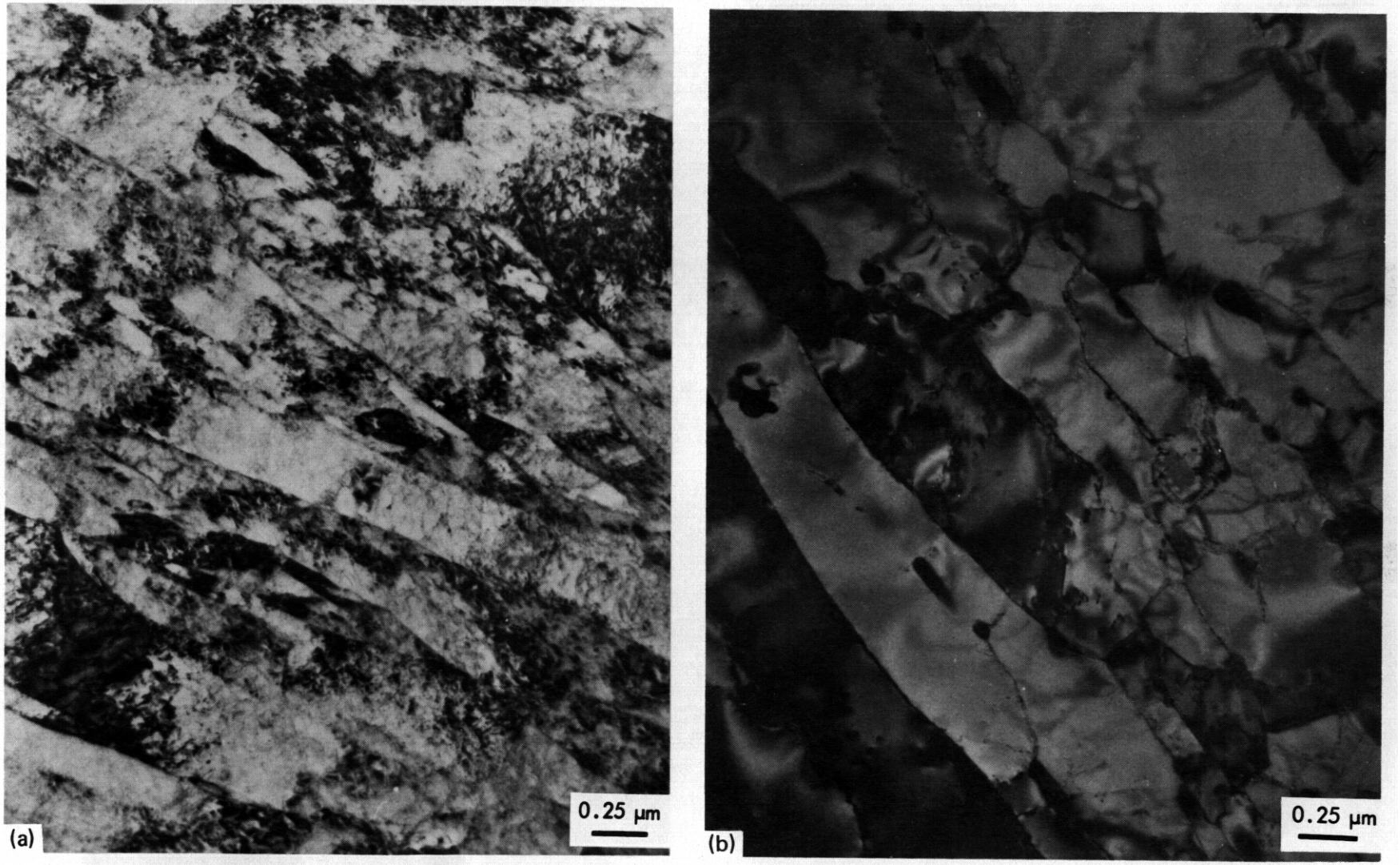

Fig. 7.9.4. Typical Microstructures of 12 Cr-1 MoVW. (a) Normalized: 1 h at 1000°C and air cooled. (b) Normalized and tempered: 0.5 h at 1050°C, air cooled, 2.5 h at 780°C.

ORNL-Photo 6110-81

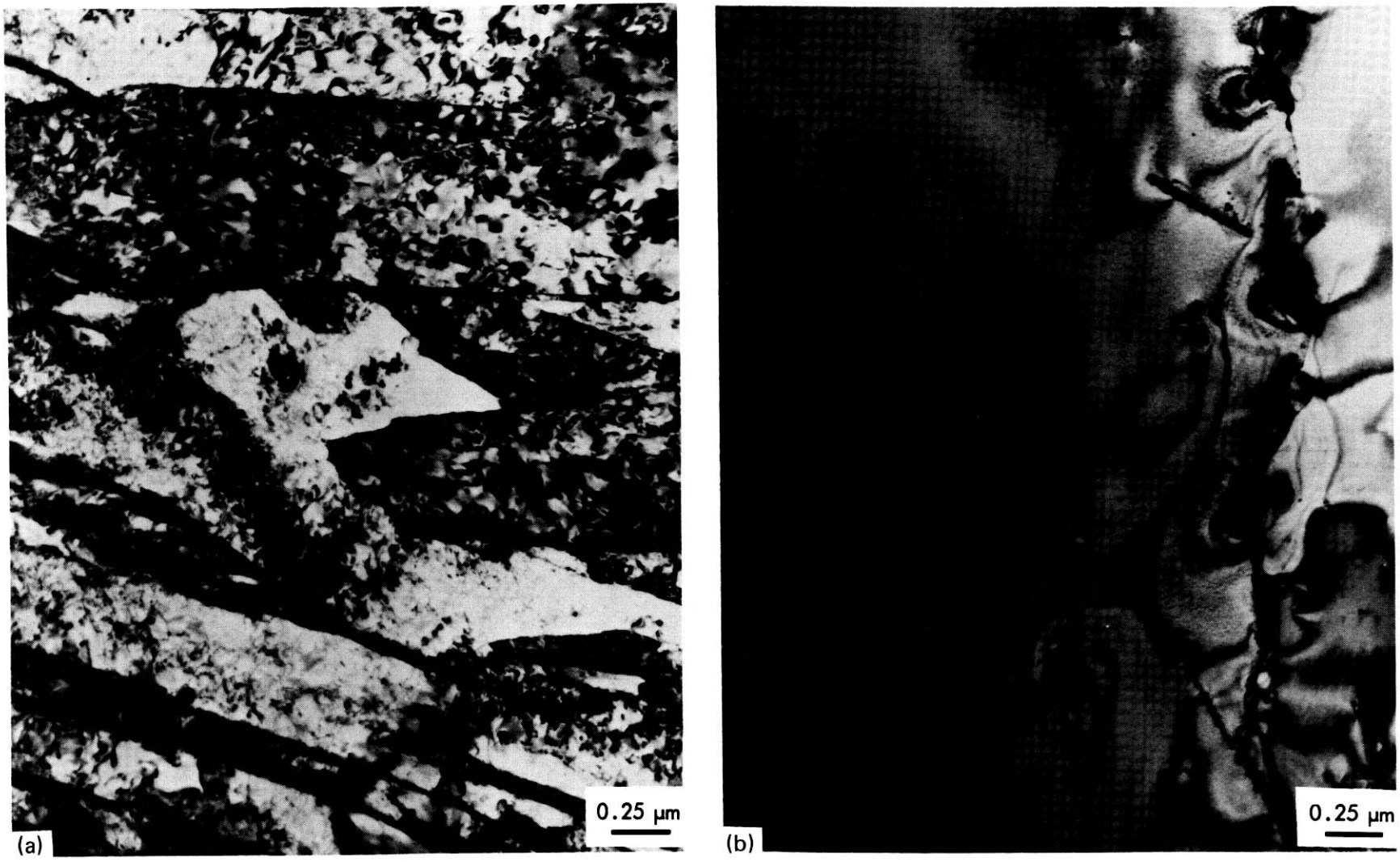

Fig. 7.9.5. Microstructure of 9 Cr-1 MoVNb as a Function of Cooling Rate after Austenitizing at 1000°C for 1 h. (a) Air cooled and (b) furnace cooled.

Table 7.9.2. Hardness and Extraction Results on 9 Cr-1 MoVNb as a Function of Heat Treatment

Austentization		Furnace cool		Air cool	
Temperature (°C)	Time	Hardness (R_F)	Precipitate (%)	Hardness (R_F)	Precipitate (%)
As cold worked		13.2	1.5	13.2	1.5
1000	1 h	8.3	1.0	18.2	0.0
1040	5 min	a	1.0	17.9	0.0
1040	1 h	16.3	0.3	17.9	0.0
1100	1 h	18.3	0.0	17.5	0.0

[a]Too low to measure.

Electron microscopy revealed that the structure after furnace cooling 9 Cr-1 MoVNb from the lower temperatures was dramatically different from that found after air cooling. As shown in Fig. 7.9.5, rather than a martensitic lath structure, a relatively dislocation free ferrite and carbide structure was found after furnace cooling. As the austenitization time or temperature increased, the structure became more heavily dislocated; and after 1 h at 1100°C and furnace cooling, the structure consisted entirely of martensitic laths. Electron microscopy revealed the extensive degree of precipitation after austenitizing for 1 h at 1000°C and furnace cooling (Fig. 7.9.6). Furthermore, the type of precipitate was different from that found in the tempered condition, being rich in chromium [Fig. 7.9.6(b)]. The precipitates have not yet been identified.

Hardness and extraction results on 12 Cr-1 MoVW as a function of heat treatment are given in Table 7.9.3. Air cooling results indicate solutioning of this alloy requires either longer times or higher temperatures than 9 Cr-1 MoVNb. Furnace cooling of 12 Cr-1 MoVW from all temperatures results in precipitation, but the greatest amount of precipitation occurs after austenitizing at the lowest temperature. However, in contrast to the results for 9 Cr-1 MoVNb, furnace cooling does not significantly affect the microstructure. The types of carbide found are similar to those found in the tempered condition, and the matrix structure consists of martensitic laths as shown in Fig. 7.9.7.

ORNL-Photo 6109-81

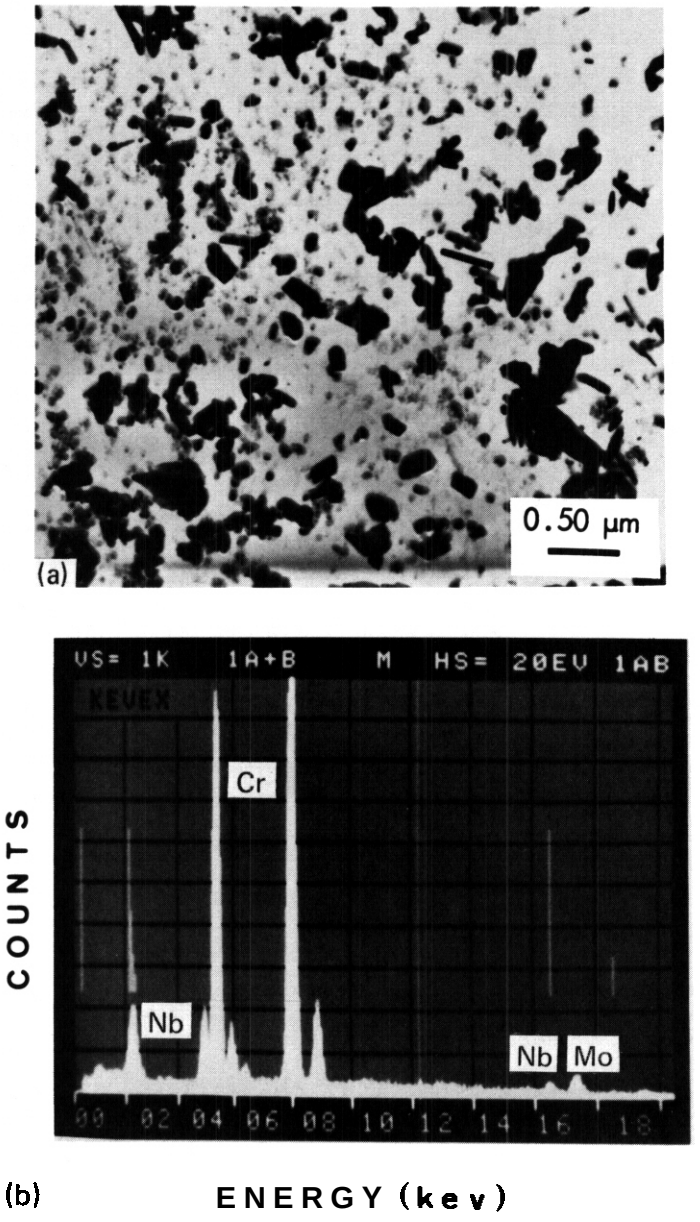

Fig. 7.9.6. (a) Extraction Replica Revealing Extensive Precipitation in 9 Cr-1 MoVNb after Austenitizing at 1000°C for 1 h and Furnace Cooling. (b) Typical energy spectrum of chromium rich precipitate found after furnace cooling. Peaks at 8 and 8.9 keV are due to copper grid.

ORNL-Ptioto 6103-81

Fig. 7.9.7. Microstructure of 12 Cr-1 MoVW after Austenitizing at 1000°C for 1 h and Furnace Cooling.

Table 7.9.3. Hardness and Extraction Results on 12 Cr-1 MoVW as a Function of Heat Treatment

Austentization		Furnace cool		Air cool	
Temperature (°C)	Time	Hardness (R_F)	Precipitate (%)	Hardness (R_F)	Precipitate (%)
As cold worked		17.2	3.7	17.2	3.7
1000	1 h	19.4	1.1	21.9	0.3
1040	5 min	20.4	0.3	22.2	0.1
1040	1 h	20.1	0.2	22.5	0.0
1100	1 h	19.6	0.3	22.2	0.0

7.9.5 Conclusions and Future Work

The present results point out that the heat treatment conditions may result in substantial structural variations in the ferritic steels 9 Cr-1 MoVNb and 12 Cr-1 MoVW. These results provide a basis for interpreting both unirradiated and irradiated properties and structures. Similar work to evaluate the effect of nickel in the nickel-doped heats of these steels should be carried out in the future.

7.9.6 Reference

1. R. L. Klueh and J. M. Vitek, "Characterization of Ferritic Steels for HFIR Irradiation," ADIP *Quart. Prog. Rep. June* 30, 1980, DOE/ER-0045/3, pp. 294-308.

7.10 TENSILE PROPERTIES OF FERRITIC STEELS AFTER LOW-TEMPERATURE HFIR IRRADIATION — R. L. Klueh and J. M. Vitek (Oak Ridge National Laboratory)

7.10.1 ADIP Task

ADIP Tasks are not defined for Path E, ferritic steels, in the 1978 program plan.

7.10.2 Objective

The goal of this project is to evaluate the properties of irradiated ferritic steels. Irradiation in the High Flux Isotope Reactor (HFIR) is used to produce both displacement damage and transmutation helium at levels relevant to fusion reactor service.

7.10.3 Summary

Tensile specimens from small heats of ferritic (martensitic) steels based on 12 Cr-1 MoVW, 9 Cr-1 MoVNb, and the low-alloy ferritic 2 1/4 Cr-1 Mo steel have been irradiated in HFIR to displacement damage levels of up to 9.3 dpa and helium contents of 10 to 82 at. ppm. The 12 Cr-1 MoVW- and 9 Cr-1 MoVNb-base compositions were irradiated along with similar alloys to which nickel had been added for helium production.

During the present reporting period, irradiated specimens of 2 1/4 Cr-1 Mo steel in the normalized-and-tempered and isothermally annealed conditions were tensile tested at room temperature and 300°C. The yield strength and ultimate tensile strength of the irradiated samples displayed considerable hardening over the unirradiated condition. The increased strength was accompanied by decreased ductility. The strength and ductility values of the normalized-and-tempered 2 1/4 Cr-1 Mo steel compared favorably with the results on the 12 Cr-1 MoVW and 9 Cr-1 MoVNb steels. In the isothermally annealed condition, 2 1/4 Cr-1 Mo steel is considerably weaker than the normalized-and-tempered steel. However, after irradiation the isothermally annealed steel retains considerably more ductility than the other alloys did for tests at 300°C.

7.10.4 Progress and Status

The HFIR-CTR-33 irradiation experiment was primarily designed to determine the effect of transmutation helium on the tensile properties of

12 Cr-1 MoVW and 9 Cr-1 MoVNb ferritic (martensitic) steels. Nickel was added to the base compositions to produce helium during HFIK irradiation through the reaction sequence $^{58}Ni(n,\gamma)^{59}Ni$: $^{59}Ni(n,\alpha)^{56}Fe$. In addition to these steels, 2 1/4 Cr-1 Mo steel specimens without any nickel additions were also irradiated. In previous quarters we reported on the tensile behavior of the 12 Cr-1 MoVW and 9 Cr-1 MoVNb alloys after irradiation.[1,2] In this report we will present the irradiated properties of 2 1/4 Cr-1 Mo steel and compare them with the high-chromium alloys.

7.10.4.1 Alloys Irradiated

Details on the chemical composition of the 12 Cr-1 MoVW and 9 Cr-1 MoVNb steels were previously given.[3,4] The chemical composition in weight percent of the 2 1/4 Cr-1 Mo steel (heat 72768) is

2.2 Cr	0.003 Co
0.8 Mo	0.01 Ti
0.48 Mn	0.12 C
0.07 Ni	0.016 N
0.31 Si	0.007 O
0.1 cu	

To obtain the sheet from which the test specimens were taken, a piece of 38-mm-diam tube with a 9-mm-wall thickness was split, flattened, and cold rolled to a thickness of 0.76 mm. Specimens were irradiated and tested in the normalized-and-tempered and isothermally anealed conditions. The steel was normalized by heating to 900°C in a helium atmosphere for 0.5 h and then rapidly cooling in flowing helium; the specimens were tempered 1 h at 700°C. The isothermal anneal was also carried out in a helium atmosphere. This heat treatment consisted of heating for 0.5 h at 900°C, furnace cooling to 700°C where it was held 2 h, and then cooling in flowing helium.

The microstructure after the normalize-and-temper heat treatment is bainitic (Fig. 7.10.1), while the isothermally annealed microstructure is primarily proeutectoid ferrite (75-80%) with the balance bainite (Fig. 7.10.2).

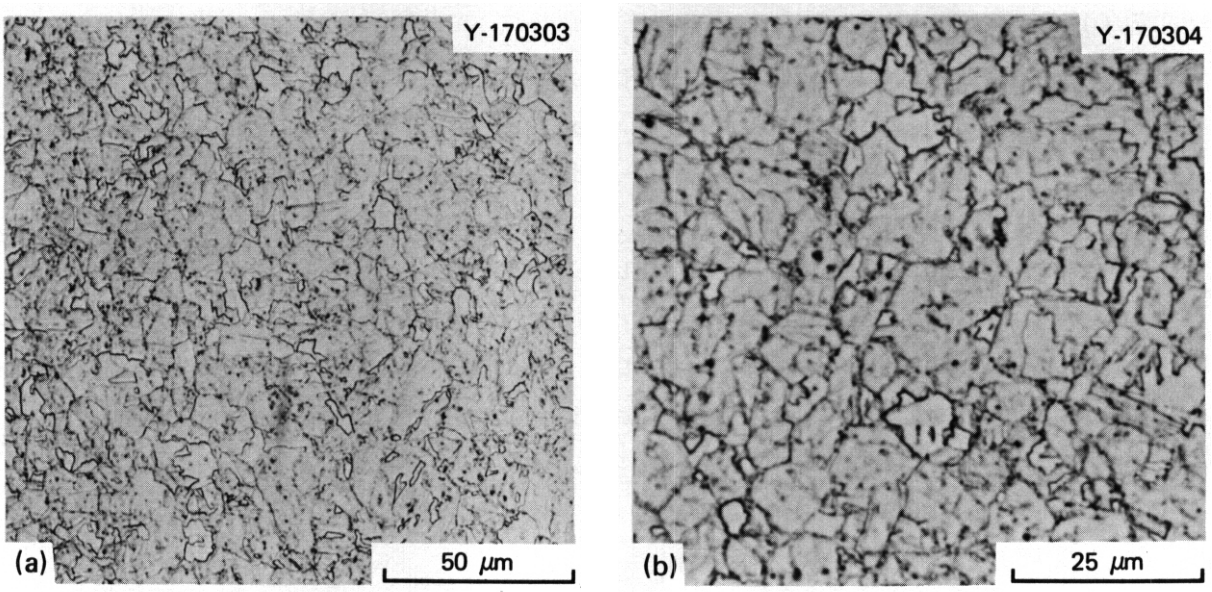

Fig. 7.10.1. Microstructure of Normalized-and-Tempered 2 1/4 Cr-1 Mo Steel.

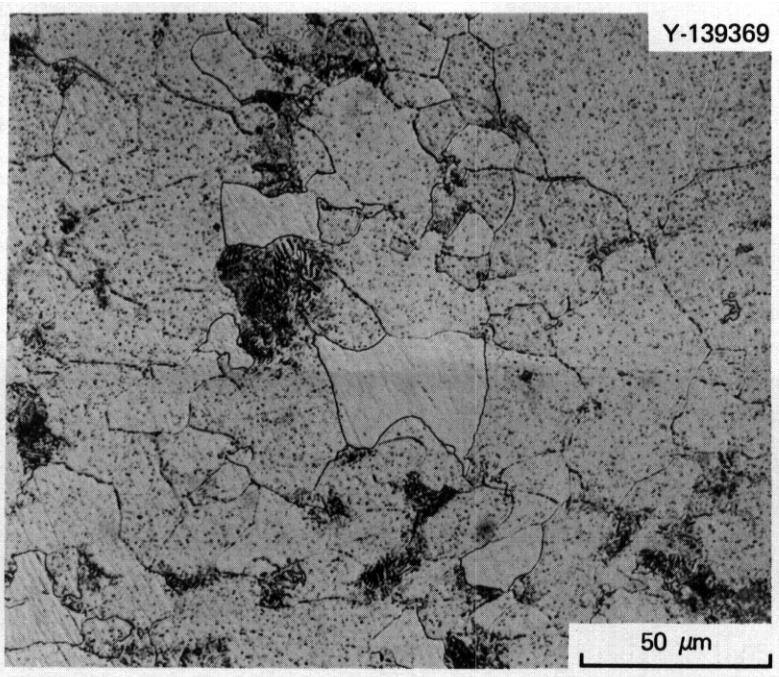

Fig. 7.10.2. Microstructure of Isothermally Annealed 2 1/4 Cr-1 Mo Steel.

7.10.4.2 Experimental Procedure

Sheet tensile specimens in this experiment were of an SS-1 type, with a reduced gage section 20 mm long by 1.52 mm wide by 0.76 mm thick (Fig. 7.10.3). Three normalized-and-tempered and three isothermally annealed specimens of 2 1/4 Cr-1 Mo steel were irradiated at about 50°C. The maximum total fluence for HFIR-CTR-33 was 5.0 x 10^{26} neutrons/m^2 and the maximum fast fluence 1.3 x 10^{26} neutrons/m^2 (>0.1 MeV).[1,4] After immersion density measurements, the specimens were tensile tested at room temperature and 300°C. Tests were conducted in a vacuum chamber on a 44-kN capacity Instron universal testing machine at a strain rate of 4.2 x 10^{-5}/s.

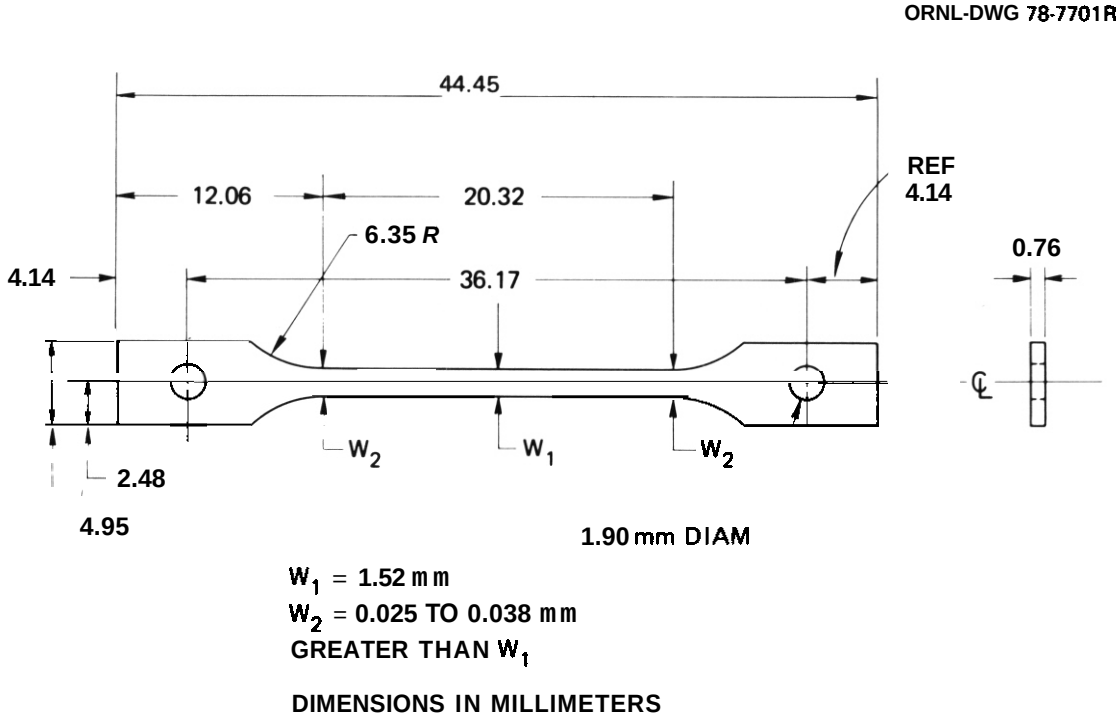

Fig. 7.10.3. The SS-1 Type Tensile Specimen.

7.10.4.3 Results

As reported previously,[1] there was no detectable change in the density of the specimens caused by irradiation.

Room temperature and 300°C tensile tests were made on irradiated and unirradiated (control) specimens from the 2 1/4 Cr-1 Mo steel in the two

heat-treated conditions. The irradiation parameters, test conditions, and measured tensile properties for each specimen tested are given in Table 7.10.1.

Table 7.10.1. Tensile Properties of Unirradiated and Irradiated[a] 2 1/4 Cr-1 Mo Steel

Fluence, >0.1 MeV (neutrons/m^2)	Displacement level (dpa)	Helium concentration[b] (at. ppm)	Test temperature (°C)	Strength, MPa		Elongation, %	
				Yield	Ultimate	Uniform	Total
Normalized and tempered[c]							
0			25	581	*663*	8.4	12.8
0.89 x 10^{26}	6.4	8	25	1027	1027	0.1	1.7
0			300	5kl	632	6.3	9.4
1.2 x 10^{26}	8.6	9	300	807	809	0.4	3.8
Isothermally annealed							
0			25	372	504	*14.6*	19.0
1.2 x 10^{26}	8.6	9	25	729	729	0.1	3.0
0			300	*343*	528	8.8	13.1
1.2 x 10^{26}	8.6	9	300	552	*574*	6.7	10.1

[a] Irradiation was in HFIR at about 50°C.

[b] Calculated level of helium from ^{58}Ni and ^{10}B; the alloy was assumed to contain 0.0007 wt % B (total).

[c] Specimens were normalized by heating 0.5 h at 900°C, then rapidly cooled in flowing helium. They were tempered I h at 700°C.

[d] Specimens were isothermally annealed by heating 0.5 h at 900°C, furnace cooling to 700°C, holding for 2 h, then cooling in flowing helium.

The normalized-and-tempered steel is considerably stronger than the isothermally annealed steel, both before and after irradiation. The unirradiated strength difference is a reflection of the different microstructures: tempered bainite is considerably stronger than the highly ductile proeutectoid ferrite.

The low-temperature irradiation hardened the steel in both heat treated conditions and resulted in a substantial decrease in ductility. After irradiation there was little difference in the ductility for the two microstructures tested at 25°C. The extremely low uniform elongation in the room temperature tests is similar to the observations on the 12 Cr-1 MoW and 9 Cr-1 MoVNb steels.[1,2] At the 300°C test temperature, however, the isothermally annealed steel retains much more ductility than does the normalized-and-tempered steel.

These results were compared with the results for the 12 Cr-1 MoVW and 9 Cr-1 MoVNb alloys[1,2] without any nickel additions (Figs. 7.10.4 to 7.10.6). The unirradiated 0.2% yield strength (Fig. 7.10.4) and the ultimate tensile strength (Fig. 7.10.5) of the normalized-and-tempered 2 1/4 Cr-1 Mo steel were comparable to the value for the high-chromium steels in a similar condition. In fact, the yield strength for the normalized-and-tempered 2 1/4 Cr-1 Mo steel is slightly greater than that of the other two steels. The room-temperature ultimate tensile strength of the normalized-and-tempered 2 1/4 Cr-1 Mo steel is similar to that of

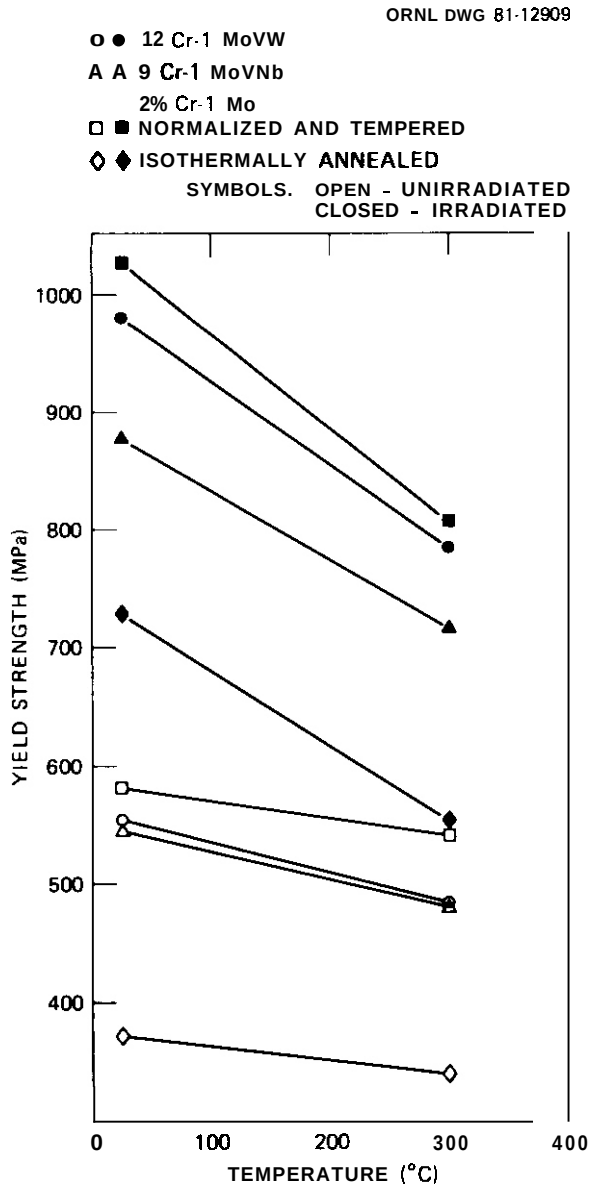

Fig. 7.10.4. The 0.2% Yield Strength of 2 1/4 Cr-1 Mo, 9 Cr-1 MoVNb, and 12 Cr-1 MoVW Steels Unirradiated and After HFIR Irradiation.

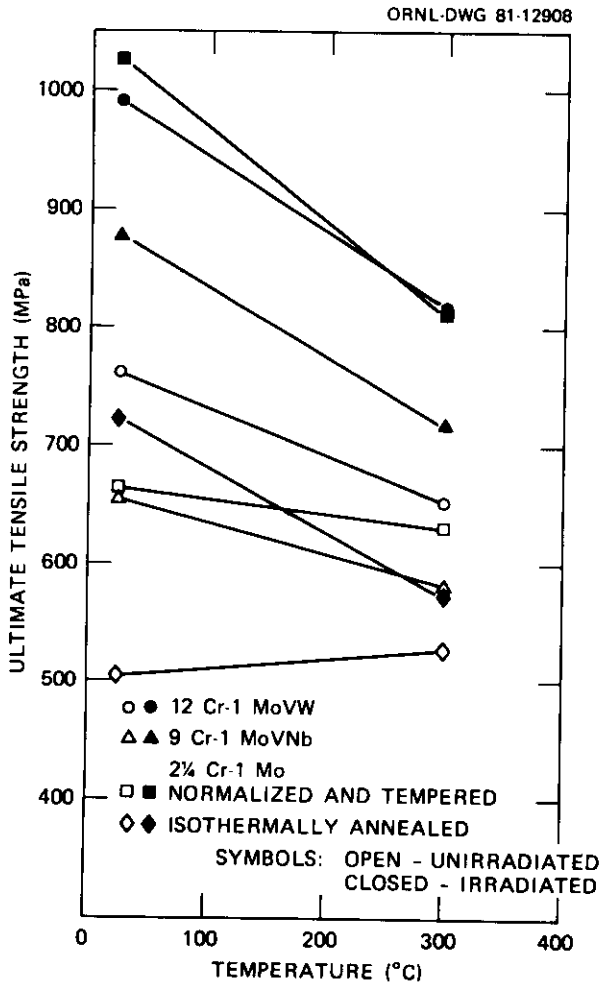

Fig. 7.10.5. The Ultimate Tensile Strengths of 2 1/4 Cr-1 Mo, 9 Cr-1 MoVNb, and 12 Cr-1 MoVW Steels Unirradiated and After HFIR Irradiation.

the 9 Cr-1 MoVNb steel and below that of the 12 Cr-1 MoVW steel; at 300°C it is above that for the 9 Cr-1 MoVNb steel and similar to that of the 12 Cr-1 MoVW steel.

The strength of the 2 1/4 Cr-1 Mo steel in the isothermally annealed condition is considerably less than that of the other steels. The increase in the ultimate tensile strength of the unirradiated, isothermally annealed 2 1/4 Cr-1 Mo steel between room temperature and 300°C is a reflection of the dynamic strain aging that occurs in this steel.[5] The relatively smaller rate of decrease in ultimate tensile strength between room temperature and 300°C for the normalized-and-tempered 2 1/4 Cr-1 Mo steel than for the two high-chromium alloys is similarly a reflection of dynamic strain aging. The relative effect of dynamic strain aging is more pronounced in the isothermally annealed condition than when normalized and tempered, as has been noted previously.[5]

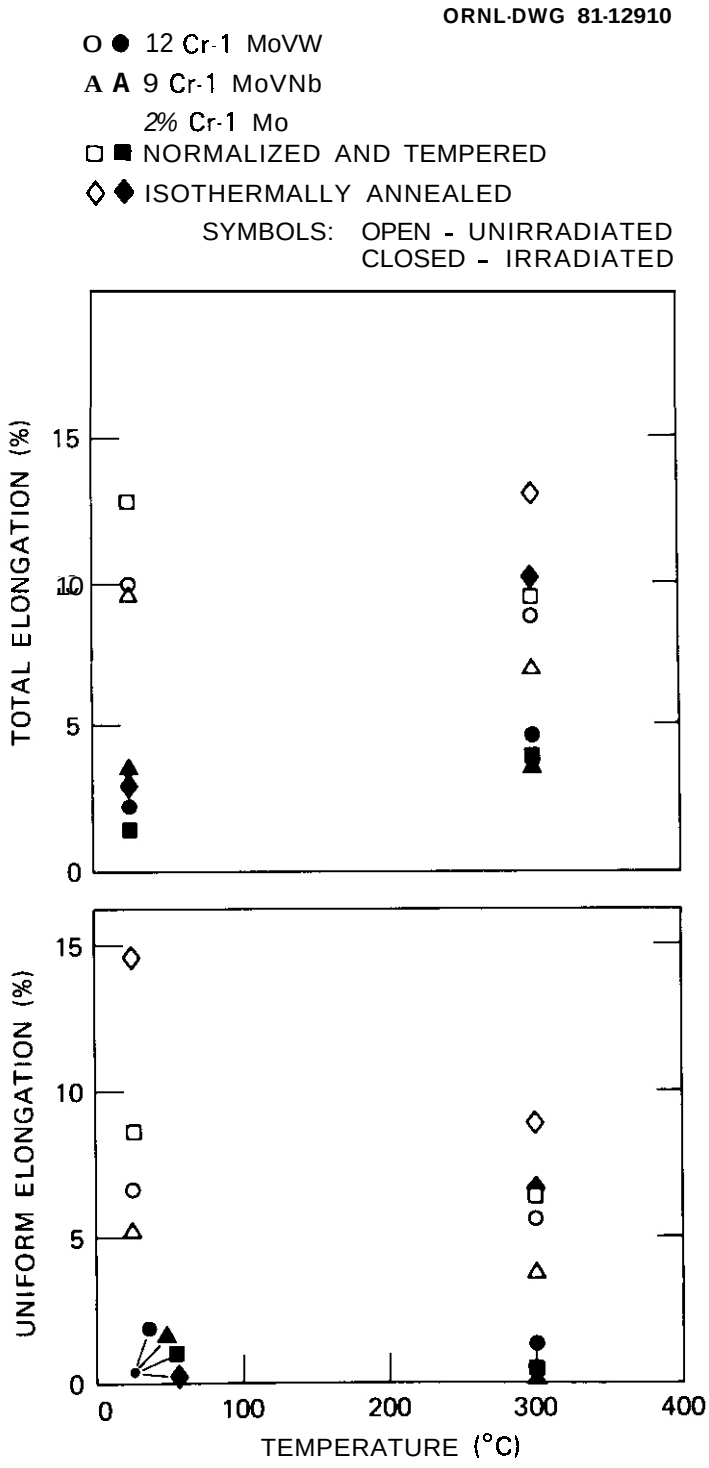

Fig. 7.10.6. The Uniform and Total Elongation of 2 1/4 Cr-1 Mo, 9 Cr-1 MoVNb, and 12 Cr-1 MoVW Steels Unirradiated and After HFIK Irradiation.

All of the steels displayed large increases in strength after irradiation, with the greatest strength achieved in the normalized-and-tempered 2 1/4 Cr-1 Mo steel. Under most test conditions, the ductility changes were comparable (Fig. 7.10.6). At room temperature all steels showed a large decrease in uniform and total elongation. At 300°C, all but the isothermally annealed 2 114 Cr-1 Mo steel displayed comparable changes in ductility. Both the uniform and total elongations of the isothermally annealed steel was substantially greater than that for the high-chromium steels and the normalized-and-tempered 2 1/4 Cr-1 Mo steel.

7.10.5 Future Work

The primary objective of this study is to determine the effect of helium on mechanical properties. No effect could be detected for the nickel-doped steels irradiated at 50°C and tested at room temperature and 300°C.[1,2] For most alloys, small amounts of helium cause a loss of ductility at temperatures above approximately one half the absolute melting temperature. To determine if this also occurs in the ferritic steels, we will test the remaining 9 Cr and 12 Cr alloys with and without nickel at 700°C.

7.10.6 References

1. R. L. Klueh and J. M. Vitek, "Tensile Properties of Ferritic Steels After Low-Temperature HFIR Irradiation," *ADIP Quart. Prog. Rep. Dea. 31, 1980,* DOE/ER-0045/5, pp. 218–25.
2. R. L. Klueh and J. M. Vitek, "Tensile Properties of Ferritic Steels After Low-Temperature HFIR Irradiation," *ADIP Quart. Prog. Rep. Mar. 31, 1981,* DOE/ER-0045/6, pp. 139–47.
3. M. L. Grossbeck, V. K. Sikka, T. K. Roche, and R. L. Klueh, "Preparation of Nickel-Doped Ferritic Alloys for HFIR Irradiation to Produce Helium," *ADIP Quart. Prog. Rep. Dec. 31, 1979,* DOE/ER-0045/1, pp. 100-04.
4. M. L. Grossbeck and J. W. Woods, "An Irradiation Experiment to Scope the Tensile Properties of Ferritic Alloys – HFIR-CTR-33," ADIP *Quart. Prog. Rep. June 30, 1980,* DOE/ER-0045/3, pp. 30–34.
5. R. L. Klueh, "Heat Treatment Effects on the Tensile Properties of Annealed 2 1/4 Cr-1 Mo Steel," *J. Nucl. Mater. 68:* 294–307 (1977).

8. STATUS OF IRRADIATION EXPERIMENTS AND MATERIALS INVENTORY

8.1 IRRADIATION EXPERIMENT STATUS AND SCHEDULE (Oak Qidge National Laboratory)

There are a large number of planned, in-progress, or completed reactor irradiation experiments that support the ADIP program. Table 8.1.1 presents a summary of the parameters that describe experiments that have been completed. Experiments that have been removed from the reactor only recently, are currently undergoing irradiation, or are planned €or future irradiation are included in the schedule bar charts of Table 8.1.2.

Experiments are now under way in the Oak Ridge Research Reactor (ORR) and the High Flux Isotope Reactor (HFIR), which are mixed spectrum reactors and in the Experimental Breeder Reactor (EBR-II), which is a Fast reactor.

During the reporting period experiments HFIR-MFE-T3 was installed in the target region of HFIR. This experiment is the first to contain Charpy specimens of ferritic steels. The second disk irradiation experiment, HFIR-CTK-31, and HFIR-CTR-29, a tensile property experiment, have completed scheduled irradiation and been removed from the reactor.

Table 8.1.1. Descriptive Parameters for Completed ADIP Program Fission Reactor Irradiation Experiments

Experiment	Major Objective	Alloy	Reactor	Temperature (°C)	Displacement Damage (dpa)	Helium (at. ppm)	Duration (month)	Date Completed
ORR-MFE-1	Scope the effects of composition and microstructure on tensile, fatigue, and irradiation creep	Paths A, B, C	ORR	250–600	2	≤10	4	6/78
ORR-MFE-2	Scope the effects of composition and microstructure on tensile, fatigue, and irradiation creep	Paths A, B, C	ORR	300–600	6	≤60	15	4/80
Subassembly X-264	Effect of preinjected helium on microstructure, tensile properties, and irradiation creep	316, PE-16, V–20% Ti, V–15% Cr–5% Ti, Nb–1% Zr	EBR-II	500–825	8	2–200	4	1/77
AA-X Subassembly X-287	Effect of preinjected helium on microstructure, tensile properties, and irradiation creep	316, PE-16, V–20% Ti, V–15% Cr–5% Ti, Nb–1% Zr	EBR-II	400–700	20	2–200	23	12/78
Subassembly X-217D	Stress relaxation	Titanium alloys	EBR-II	450	2		1	1/78
Pins B285, B286, and B284	Swelling, fatigue, crack growth, and tensile properties	Titanium alloys	EBR-II	370–550	25		14	9/79
HFIR-CTR-3	Swelling and tensile properties	PE-16, Inconel 600	HFIR	300–700	4.3–9	30–1800	3	2/75
HFIR-CTR-4	Swelling and tensile properties	PE-16	HFIR	300–700	2.2–4.5	100–350	2	3/77
HFIR-CTR-5	Swelling and tensile properties	PE-16, Inconel 600	HFIR	300–700	4.3–9	30–1800	3	4/75

Table B 1 1 (Continued)

Experiment	Major Objective	Alloy	Reactor	Temperature (°C)	Displacement Damage (dpa)	Helium (at. ppm)		ate pleted
HFIR-CTR-6	Swelling and tensile properties	PE-16, Inconel 600	FIR	300–700	4.3–9	350–1800	3	/75
HFIR-CTR-7	Swelling and tensile properties	PE-16	FIR	300–700	9–18	1250–3000	7	/77
HFIR-CTR-8	Swelling and tensile properties	PE-16	FIR	300–700	9–18	1250–3000	7	/77
HFIR-CTR-9	Swelling and tensile properties	316, 316 + Ti	FIR	280–680	10–16	400–1000	6	/77
HFIR-CTR-10	Swelling and tensile properties	316, 316 + Ti	FIR	280–680	10–16	400–1000	6	/77
HFIR-CTR-11	Swelling and tensile properties	316, 316 + Ti	FIR	280–680	10–16	400–1000	6	/77
HFIR-CTR-12	Swelling and tensile properties	316, 316 + Ti	FIR	280–680	7–10	200–500	4	/77
HFIR-CTR-13	Swelling and tensile properties	316, 316 + Ti	FIR	280–680	7–10	200–500	4	/77
HFIR-CTR-14	Fatigue	316	FIR	430	9–15	400–1000	7	2/77
HFIR-CTR-15	Fatigue	316	FIR	550	6–9	200–400	4	0/78
HFIR-CTR-16	Weld characterization, swelling and tensile properties	316 PE-16 Inconel 600	FIR	55	6–9	150–2700	4	/77
HFIR-CTR-17	Weld characterization	316	HFIR	280–620	7–13	180–460	5	1 7
HFIR-CTR-18	Swelling and tensile properties	316 PE-16	HFIR	280–700	17–27	1600–5600	2	6 8
HFIR-CTR-19	Weld characterization	316	HFIR	280–620	7–10	200–500	4	1 7
HFIR-CTR-20	Fatigue	316	HFIR	430	6–9	200–400	4	1 8
HFIR-CTR-21	Fatigue	316	HFIR	550	9–15	400–1000	7	7 8
HFIR-CTR-22	Fatigue	316	HFIR	430	6–9	200–400	4	3 8
HFIR-CTR-23	Fatigue	PE-16	HFIR	430	6–9	370–1000	3	2 9
HFIR-CTR-24	Temperature calibration, and tensile properties	316	HFIR	300–620	2.2	30	1	1 7

Table 8.1.2. Objectives and Schedule for Current and Planned ADIP Program Reactor Irradiation Experiments

Experiment Designation	Major Objective
A. Oak Ridge Research Reactor	
ORR-MFE-3	[1] Effect of irradiation on postirradiation fatigue crack growth in representative path A, B, and C alloys.
ORR-MFE-4	[2] Effect of irradiation on tensile, fatigue, and irradiation creep of path A PCA (Prime Candidate Alloy) and path B base research alloys. Spectral tailoring to maintain correct He/dpa ratio. Irradiation on continuing basis. 330–600°C
ORR-MFE-5	In-reactor fatigue crack growth experiment. 325–460°C
ORR-MFE-CG6	In-reactor fatigue crack growth experiment 325–460°C

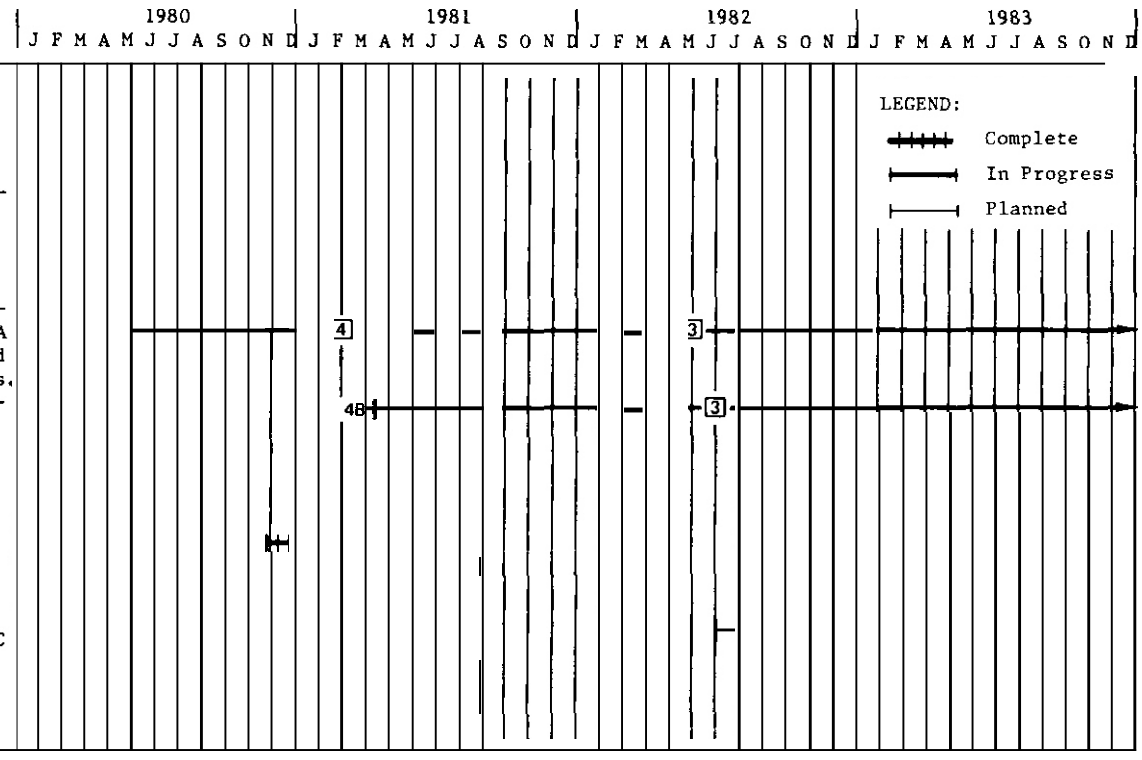

[1] Experiment cancelled.

[2] MFE-4A operates at 330 and 400°C. MFE-4B will operate at 500 and 600°C.

[3] Approximate schedule for specimen charge out.

[4] Removed from reactor for thermocouple repairs.

Table 8.1.2. (Continued)

Experiment Designation	Major Objective	1980 J F M A M J J A S O N D	1981 J F M A M J J A S O N D	1982 J F M A M J J A S O N D	1983 J F M A M J J A S O N D
B. Experimental Breeder Reactor (EBR-II)					
Experiment plan depends on alloy availability. EBR-II space not yet identified.	Effect of irradiation on swelling, tensile, fatigue, and crack growth properties of V and Nb scoping alloys. 370, 450, 550, and 650°C. Position in reactor not finalized, therefore no fluence estimate. [1]				
AD-2 (6 pins in separate subassemblies of row 4)	To supplement present EBR-II data on ferritic alloys with data on crack growth, fatigue, and fracture toughness. Temperature 390, 450, 500, and 550°C. 19 and 38 dpa.	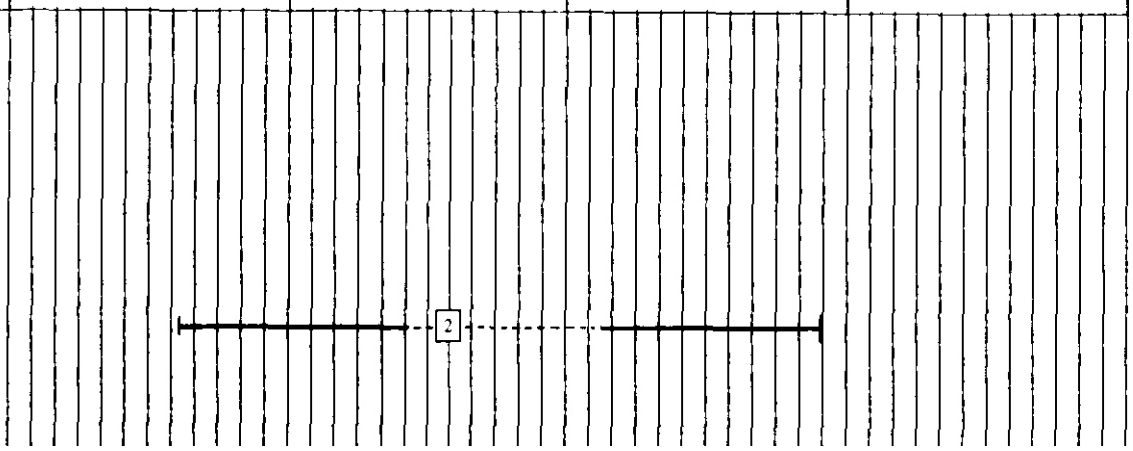			

[1] Delayed for undetermined period.

[2] Interim examination. Experiment out of reactor.

Table 8 W 2 (Cooo<inued)

Experiment Designation	Major Objective	1979 J F M A M J J A S O N D	1980 J F M A M J J A S O N D	1981 J F M A M J J A S O N D
C High Flux Isotope Reactor (HFIR)				
HFIR CTR 25	Temperature calibration, tensile properties of MFE ref. 316, 2.25 dpa, 30 at. ppm He [1]			
HFIR-CTR 26	Swelling and tensile properties of MFE ref. 316, 32 dpa, 1900 at. ppm He	———		
HFIR-CTR-27	Swelling and tensile properties of MFE ref. 316, 56 dpa, 3450 at. ppm He	———	———	
HFIR CTR 8	Swelling and tensile properties of MFE ref. 316, 32 dpa, 1900 at. ppm He		———	
HFIR-CTR-29	Swelling and tensile properties of MFE ref. 316, 56 dpa, 3450 at. ppm He		———	———
HFIR-CTR-30	Swelling and tensile properties, Paths A, B, and D microstructural variations, 40 dpa, 2500 at. ppm He (Path A)		———	———
HFIR-CTR-31	Swelling and tensile properties, Paths A, B and D microstructural variations, 20 dpa, 1200 ppm He (Path A)		———	———
HFIR CTR-32	Swelling and tensile properties, Paths A, B and D microstructural variations, 10 dpa, 500 ppm He (Path A)		———	
HFIR-CTR-33	Swelling and tensile properties, Path E alloys, 10 dpa, 50°C		———	

[1] Delayed for undetermined period.

Table 3.1.2 (Continued)

Experiment Designation	Major Objective	1981 J F M A M J J A S O N D	1982 J F M A M J J A S O N D	1983 J F M A M J J A S O N D	1984 J F M A M J J A S O N D
HFIR-MFE-T1	Swelling, tensile properties, and fatigue of path E alloys. 10 dpa, up to 75 ppm He depending upon alloy, 55°C.				
HFIR-MFE-T2	Swelling, tensile properties, and fatigue of path E alloys. 30 dpa, up to 250 ppm He depending upon alloy, 55°C.				
HFIR-MFE-T3	Impact properties of path E alloys. 10 dpa, up to 75 ppm He depending upon alloy, 55°C.				
HFIR-MFE-RB1	Swelling, microstructure, crack growth, fracture toughness, impact, tensile, and fatigue properties of path E alloys, 55°C.				
HFIR-MFE-RB2	Similar to HFIR-MFE-RB1.				

8.2 ETM RESEARCH MATERIALS INVENTORY — F. W. Wiffen, T. K. Roche (Oak Ridge National Laboratory) and J. W. Davis (McDonnell Douglas)

8.2.1 ADIP Tasks

ADIP Task I.D.1, Materials Stockpile for MFE Programs.

8.2.2 Objective

Oak Ridge National Laboratory maintains a central inventory of research materials to provide a common supply of materials for the Fusion Reactor Materials Program. This will minimize unintended materials variables and provide for economy in procurement and for centralized recordkeeping. Initially this inventory is to focus on materials related to first-wall and structural applications and related research, but various special purpose materials may be added in the future.

The use of materials from this inventory for research that is coordinated with or otherwise related technically to the Fusion Reactor Materials Program of DOE is encouraged.

8.2.3 Materials Requests and Release

Materials requests shall be directed to ETM Research Materials Inventory at ORNL (Attention: F. W. Wiffen). Materials will be released directly if:

(a) The material is to be used for programs funded by the Office of Fusion Energy, with goals consistent with the approved Materials Program Plans of the Materials and Radiation Effects Branch.

(b) The requested amount of material is available, without compromising other intended uses.

Materials requests that do not satisfy both (a) and (b) will be discussed with the staff of the Materials and Radiation Effects Branch, Office of Fusion Energy, for agreement on action.

8.2.4 Records

Chemistry and materials preparation records are maintained for all inventory material. All materials supplied to program users will be accompanied by summary characterization information.

8.2.5 Summary of Current Inventory and Material Movement During Period April 1 to September 30, 1981

A condensed, qualitative description of the content of materials in the ETM Research Materials Inventory is given in Table 8.2.1. This table indicates the nominal diameter of rod or thickness of sheet for product forms of each alloy and also indicates by weight the amount of each alloy in larger sizes available for fabrication to produce other product forms as needed by the program. Table 8.2.2 lists materials received into the inventory during this reporting period. Table 8.2.3 gives the materials distributed from the inventory.

Alloy compositions and more detail on the alloys and their procurement and/or fabrication are given in earlier ADIP quarterly progress reports.

Table 8.2.1 Summary Status of Material Availability in the ETM Research Materials Inventory

Alloy	Product form			
	Ingot or bar,[a] weight (kg)	Rod,[b] diameter (mm)	Sheet,[b] thickness (mm)	Thin-wall tubing, wall thickness (mm)
		Path A Alloys		
Type 316 SS	900	16 and 7.2	13 and 7.9	0.25
Path A PCA[d]	490	12	13	0.25
USSR — Cr–Mn Steel[e]	0	10.5	2.6	0
NONMAGNE 30f	0	18.5	10	0
		Path E Alloys		
PE–16	140	16 and 7.1	13 and 1.6	0.25
B–1	180	0	0	0
B–2	180	0	0	0
B–3	180	0	0	0
B–4	180	0	0	0
B–6	180	0	0	0
		Path C Alloys		
Ti–64	0	0	2.5 and 0.76	0
Ti–6242s	0	63	6.3, 3.2, and 0.76	0
Ti–5621s	0	0	2.5 and 0.76	0
Ti–38644	0	0	0.76 and 0.25	0
Nb–1% Zr	0	6.3	2.5, 1.5, and 0.76	0
Nb–5% Mo–1% Zr	0	6.3	2.5, 1.5, and 0.76	0
V–20% Ti	0	6.3	2.5, 1.5, and 0.76	0
V–15% Cr–5% Ti	0	6.3	2.5, 1.5, and 0.76	0
VANSTAR–7	0	6.3	2.5, 1.5, and 0.76	0

Table 8.2.1. (Continued)

Alloy	Product form: Ingot or bar,[a] weight (kg)	Rod,[b] diameter (mm)	Sheet,[c] thickness (mm)	Thin-wall tubing, wall thickness (mm)
Path D Alloys — No Material in Inventory				
Path E Alloys				
HT9	0	0	4.5 and 18	0
HT9 + 1%Ni	0	0	4.5 and 18	0
HT9 + 2% Ni	0	0	4.5 and 18	0
HT9 + 2% Ni + Cr adjusted	0	0	4.5 and 18	0
T-9 modified	0	0	4.5 and 18	0
T-9 modified + 2% Ni	0	0	4.5 and 18	0
T-9 modified + 2% Ni + Cr adjusted	0	0	4.5 and 18	0
2 1/4 Cr-1 Mo	0	0	[g]	0

[a] Greater than 25 mm, minimum dimension.

[b] Less than 25 mm in diameter. Some Path A and Path B alloys are available in two different diameters.

[c] Less than 15 mm thick. Some Path A, Path B, and Path C alloys are available in two or three different thicknesses.

[d] Prime Candidate Alloy.

[e] Rod and sheet of a USSR stainless steel supplied under the U.S.-USSR Fusion Reactor Materials Exchange Program.

[f] NONMAGNE 30 is an austenitic steel with base composition Fe-14% Mn-2% Ni-2% Cr. It was supplied to the inventory by the Japanese Atomic Energy Research Institute.

[g] Material is thick-wall pipe, rerolled as necessary to produce sheet or rod.

Table 8.2.2. ETM Research Materials Inventory, Fusion Reactor Program, Receipts 4-1-81 to 9-30-81

Alloy	Product form	Dimensions (mm)	Quantity (m)	Quantity (m^2)	Quantity (pieces)	Source
Path A Alloys — Austenitic Stainless Steels						
NONMAGNE *30*	Rod	18.5 diam	1.05 long		5	JAERI
	Plate	10 thick		0.1 each	6	

Table 8.2.3. EIM Research Materials Inventory, Fusion Reactor Program, Disbursements 4–1–81 to 9–30–81

Alloy	Heat	Product form	Dimensions[a] (mm)	quantity (m)	quantity (m^2)	Sent to
Path A Alloys - Austenitic Stainless Steels						
Type 316 stainless steel–reference heat	X–I5893	Rod	6.5 diam	6.6		Radiation Effects Group, ORNL
		Sheet	0.25 thick 20% cold worked		0.06	Solid State Division, ORNL
		Sheet	0.25 thick annealed		0.10	Solid State Division, ORNL
		Sheet	0.25 thick 20% cold worked		0.05	University of Wisconsin, Madison, WI
		Sheet	0.51 thick 20% cold worked		0.03	university of Wisconsin, Madison, WI
		Sheet	0.51 thick annealed		0.04	university of Wisconsin, Madison, WI
Path C Alloys – Reactive and Refractory Alloys						
V–20 Ti	832	Sheet	0.76 thick		0.01	Argonne National Laboratory
	832	Rod	6.35 diam	1.04		Argonne National Laboratory
V–15 Cr–5 Ti	834	Sheet	0.76 thick		0.01	Argonne National Laboratory
	835B	Rod	6.35 diam	1.2		Argonne National Laboratory
Ti–6 Al-4 V	MI–896596–02	Sheet	2.8 thick mill annealed		0.03	University of Missouri, Columbia, MO
	RMI–891352	Sheet	0.76 thick mill annealed		0.02	university of Wisconsin, Madison, WI
		Sheet	0.76 thick duplex annealed		0.005	University of Wisconsin, Madison, WI
Ti–624%	MI–803701–06	Sheet	0.76 thick duplex annealed		0.05	University of Wisconsin, Madison, WI
	RMI–803701–05	Sheet	32 thick duplex annealed		0.03	university of Missouri. Columbia. MO

[a] Characteristic dimension – thickness for plate and sheet, diameter far rod and tubing.

9. MATERIALS COMPATIBILITY AND HYDROGEN PERMEATION STUDIES

9.1 COMPATIBILITY OF AUSTENITIC AND FEKKITIC STEELS WITH Pb–17 at. % Li –

P. F. Tortorelli and J. H. DeVan (Oak Ridge National Laboratory)

9.1.1 ADIP Task

ADIP TAsk I.A.3, Perform Chemical and Metallurgical Compatibility Analyses.

9.1.2 Objective

The purpose of this program is to determine the chemical compatibility of fusion reactor candidate materials with possible coolants and tritium breeding materials. Specimens are exposed to static lithium and lithium–lead melts to identify the kinetics and mechanisms that govern corrosion. Other program objectives include (1) to determine the effects of N, C, H, and O on apparent solubilities of metals in lithium and lithium–lead; (2) to determine the carbon and nitrogen partitioning coefficients between alloys and these melts; (3) to determine the effects of soluble (Ca, Al) and solid (Y, Zr, Ti) active metal additions on corrosion by lithium; and (4) to determine the tendencies for mass transfer between dissimilar metals.

9.1.3 Summary

Type 316 stainless steel and HT9 suffered significant weight losses when exposed to static Pb–17 at. % Li, particularly at 500°C. This was in contrast to the negligible weight changes of these alloys when they were exposed to pure lithium under similar conditions. However, the magnitude of the weight losses in Pb–17 at. % Li were apparently not sufficient to change the tensile properties of these alloys or to cause sufficient attack of the specimens exposed at 300 and 400°C. It appears that, for ferrous alloys, the application of Pb–17 at. % Li as a semistagnant breeding fluid in a fusion reactor may be limited to temperatures of 400°C or less. Containment alloys of low nickel and chromium activities would be preferable.

9.1.4 Progress and Status

Lead–lithium molten alloys provide one possible alternative to molten lithium for tritium–breeding in fusion reactors.[1] We have therefore

initiated a study of the compatibility of candidate structural alloys with molten lead–lithium by exposing tensile specimens of type 316 stainless steel and Sandvik HT9 to the low melting point (235°C) eutectic composition of Pb–17 at. % Li. The experimental conditions were similar to those used for pure lithium static tests.[2] Type 316 stainless steel and HT9 specimens were sealed with appropriate amounts of lead and lithium under argon in capsules of similar composition. The specimens (two in each capsule) were anchored so as to prevent them from floating to the Pb-Li/Ar interface (see Fig. 9.1.1). The capsules were placed (upside down with respect to Fig. 9.1.1) in tube furnaces at 300 to 900°C (±10°C) for various exposure times. Since the melting point of pure lead (327°C) was above that of our lowest exposure temperature, the temperature of the 300°C capsules was first raised to 400°C for 1 h to form the liquid Pb–17 at. % Li alloy (with a melting point of 235°C) and then was lowered to 300°C. At the completion of a test, the specimens exposed to the Pb–Li

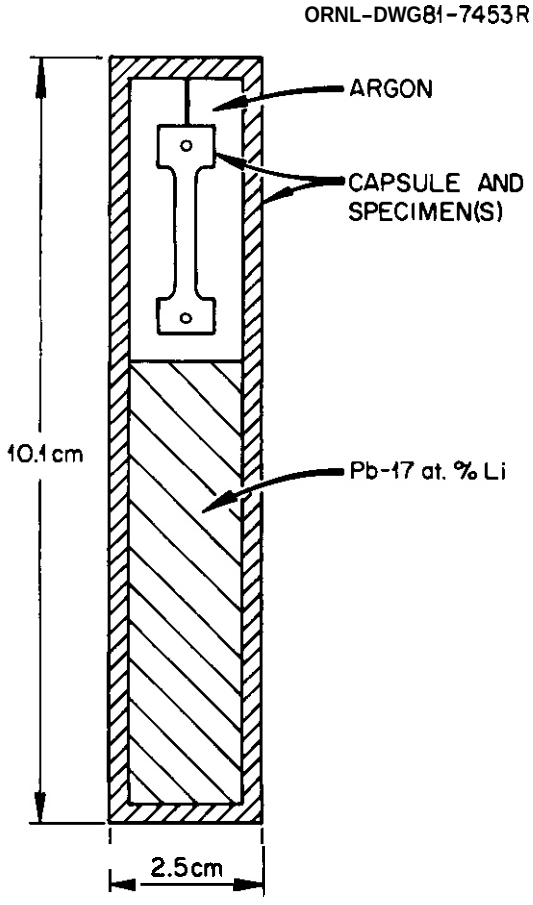

Fig. 9.1.1. Capsule and Specimen Configuration Used in This Study. Capsule was inverted during exposure.

were cleaned by immersion in liquid mercury and/or pure lithium followed by a water rinse. Use of lithium for this purpose was found to be more efficient and did not affect the specimens at temperatures near the melting point of lithium. The cleaning procedure was repeated until specimen weights became constant, which then indicated that most of the residual lead had been removed. The lead used in the present experiments was as-received high purity (99.99%) metal while the lithium was previously purified by cold trapping and gettering.

Specimen weight changes for type 316 stainless steel and HT9 exposed to static Pb-17 at. % Li are listed in Tables 9.1.1 and 9.1.2. In general, the total specimen weight loss increased with increasing exposure time and temperature. Despite the large weight losses of certain specimens, there did not appear to be any measurable effect on the bulk properties of the steels since no significant changes in tensile properties (relative to the argon exposures) were observed. The differences between the tensile data for the specimens exposed to Pb-17 at. % Li and that €or the argon-exposed specimens were minimal and, in most cases,

Table 9.1.1. Weight Changes of Type 316 Stainless Steel Exposed to Static Argon and Pb-17 at. % Li

Exposure temperature (°C)	Exposure time (h)	Weight change,[a] g/m^2	
		Pb-17 at. % Li	Argon
300	1000	-0.4	-0.1
	3000	-0.4	0.0
	5000	-1.0	0.0
400	1000	-0.9	-0.1
	3000	-1.2	0.0
	5000	-3.2	0.0
500	1000	-7.6	+0.1
	3000	-14.6	0.0
	5000	-12.2	+0.1
900	20	-11.9[b]	+0.1

[a]Average of measurements from two specimens unless otherwise noted.

[b]Average of measurements from six specimens.

Table 9.1.2. Weight Changes of HT9[a] Exposed to Static Pb-17 at. % Li

Exposure temperature (°C)	Exposure time (h)	Weight change,[b] (g/m^2)
300	1000	-2.3
	3000	-6,6
400	1000	-3,2
	3000	-5,6
500	1000	-6.5
	3000	-7.6

[a]Normalized and tempered.

[b]Average of measurements from two specimens.

fell within the scatter due to experimental uncertainty. Metallographic examination of polished cross sections revealed very little attack of type 316 stainless steel by Pb-17 at. % Li below 500°C, and only moderate attack after 3000 and 5000 h at 500°C (see Figs. 9.1.2-9.1.5). Reference to Figs. 9.1.2 through 9.1.5 shows also that there was no perceptible difference in the metallographic appearance of stressed (gage length) and unstressed (shoulder sections) surfaces after exposure to the Pb-Li alloy. No grain boundary penetration was observed. Energy dispersive x-ray analysis indicated negligible changes in the surface compositions of specimens exposed to Pb-17 at. % Li and argon relative to unexposed material (see Table 9.1.3). This is in contrast to the behavior of type 316 stainless steel in flowing lithium in which nickel and, to a lesser extent, chromium are preferentially dissolved from the alloy.[3] The absence of preferential dissolution in Pb-17 at. % Li may be due to a different dominant dissolution process or to the lack of a sufficient amount of time for substantial leaching to occur. Additionally, the porous surface region typical of type 316 stainless steel exposed to lithium[3] was not observed in the present case of Pb-17 at. % Li exposures. However, it is not known whether such features may develop after longer exposure times.

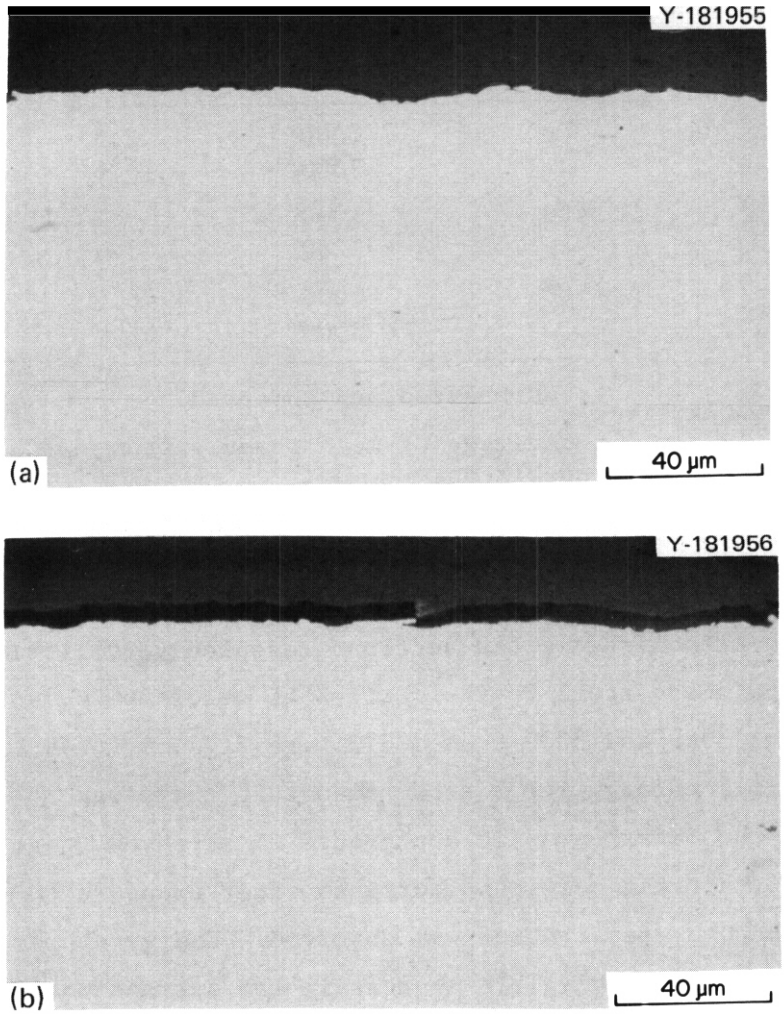

Fig. 9.1.2. Type 316 Stainless Steel Exposed to Static Pb–17 at. % Li at 300°C for 5000 h. (a) Near fracture surface. (b) Away from fracture area.

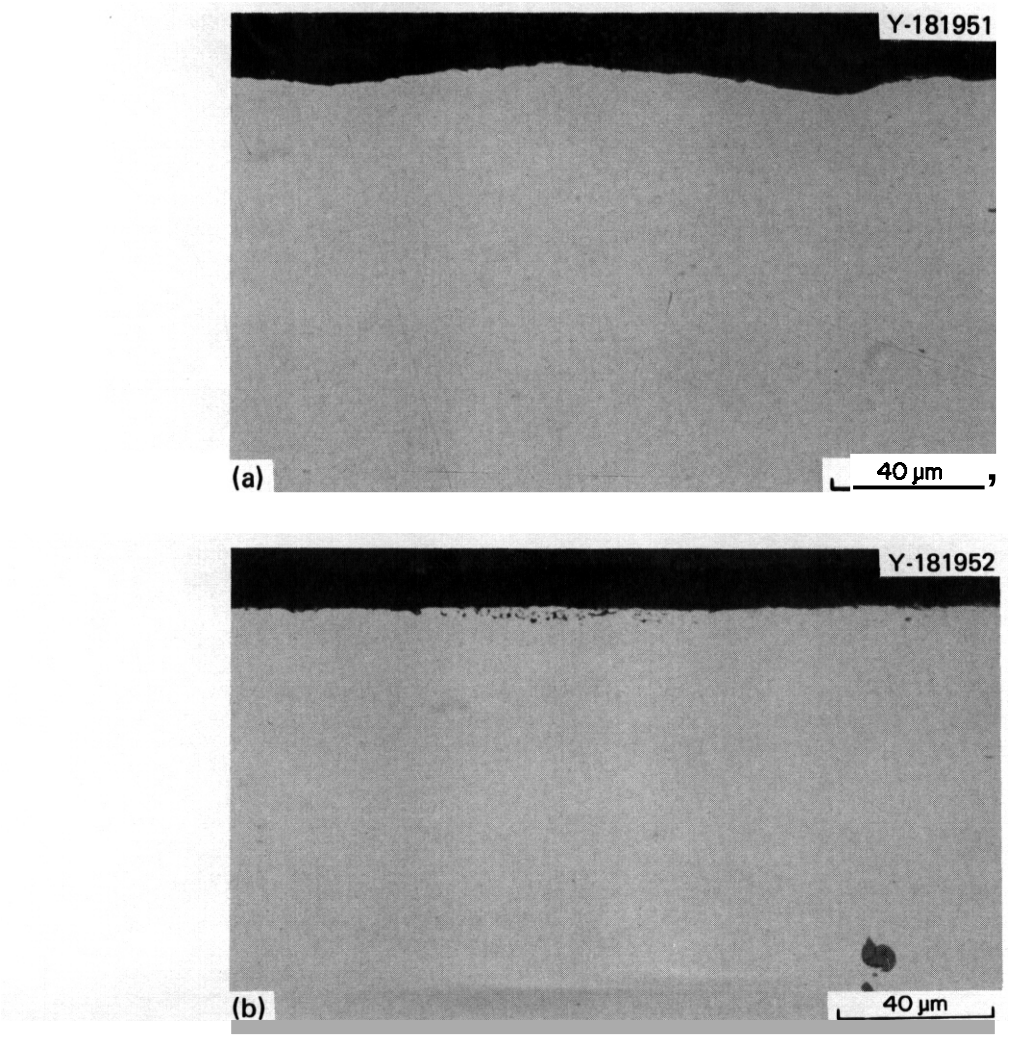

Fig. 9.1.3. Type 316 Stainless Steel Exposed to Static Pb–17 at. % Li at 400°C for 5000 h. (a) Near fracture surface. (b) Away from fracture area.

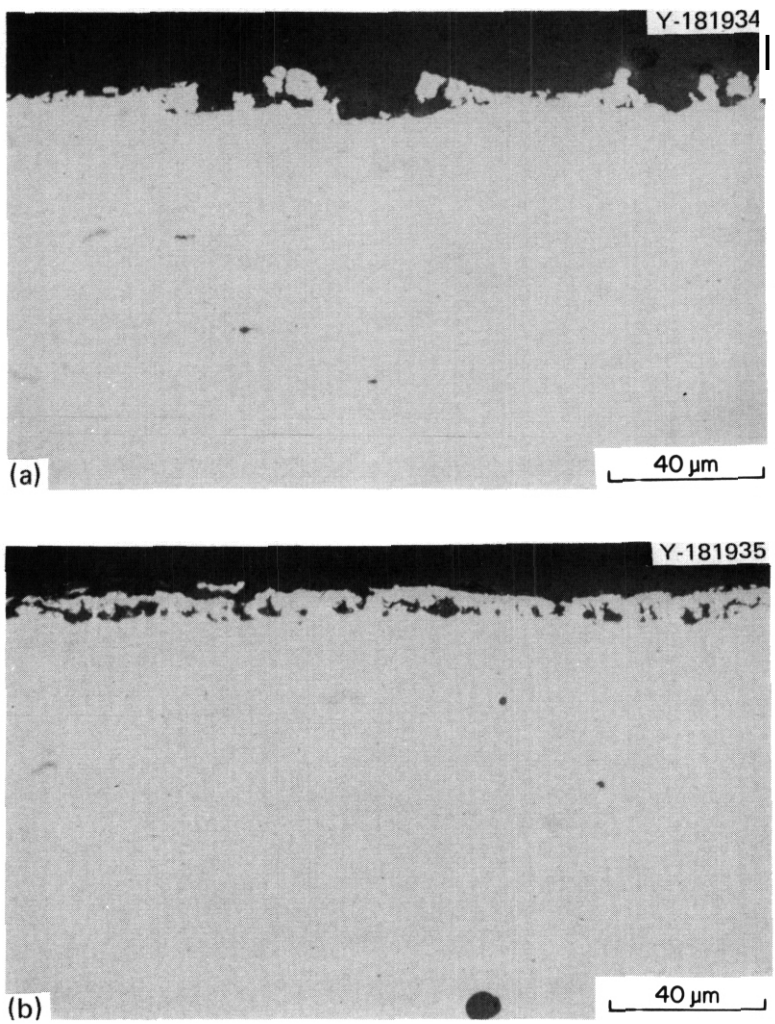

Fig. 9.1.4. **Type 316 Stainless Steel Exposed to Static Pb–17 at. % Li at 500°C for** *3000* **h. (a) Near fracture surface. (b) Away from fracture area.**

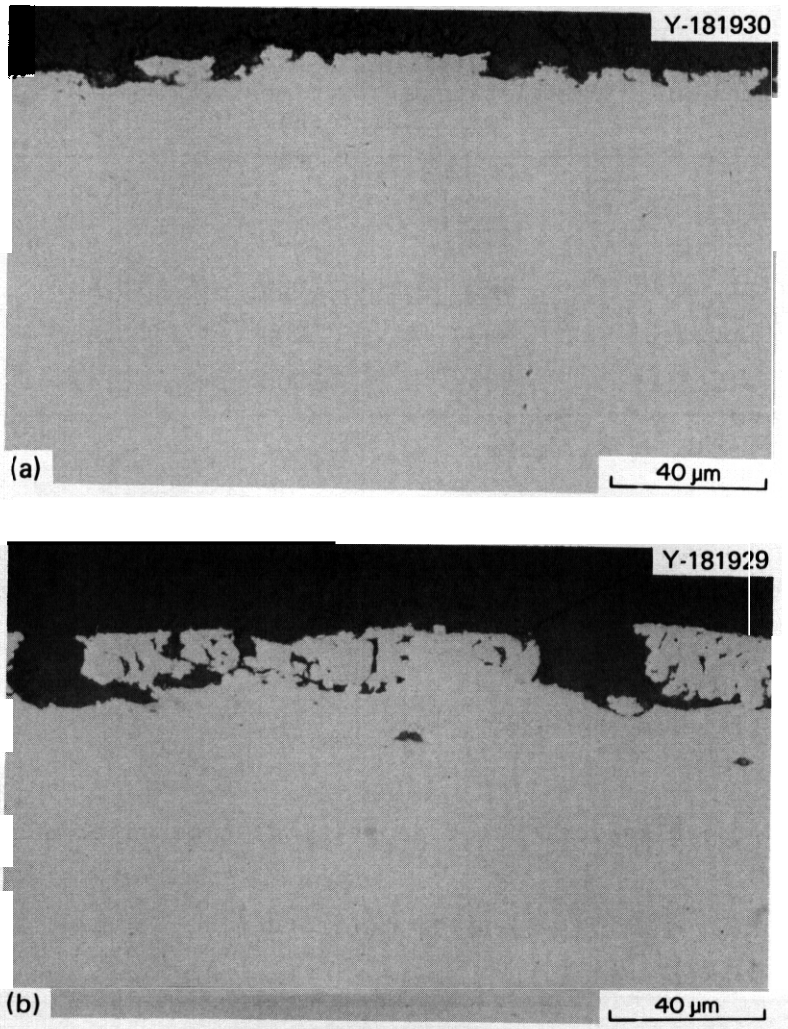

Fig. 9.1.5. Type 316 Stainless Steel Exposed to Static Pb–17 at. % Li at 500°C for 5000 h. (a) Near fracture surface. (b) Away from fracture area.

Table 9.1.3. Qualitative Elemental Ratios for Type 316 Stainless Steel as Determined by Energy Dispersive X-Ray Analysis

Environment	Exposure temperature (°C)	Exposure time (h)	Concentration ratio[a]	
			Cr/Fe	Ni/Fe
Control			0.36	0.15
Argon	500	5000	0.43	0.17
Pb-17 at. % Li	300	5000	0.45	0.14
Pb-17 at. % Li	400	5000	0.44	0.14
Pb-17 at. % Li	500	5000	0.47	0.14

[a]Ratio of K_α peaks.

The corrosion rate, R, of an alloy in a liquid metal can be expressed as

$$R = \Sigma R_i \ , \tag{1}$$

where R_i is the dissolution (or deposition) rate of element i:

$$R_i = k_i[C_s(i) - C(i)] \ , \tag{2}$$

where

k_i = rate constant for dissolution (deposition),
$C_s(i)$ = solubility of i in the liquid metal, and
$C(i)$ = actual concentration of i in the liquid metal.

In a static isothermal test it would be expected that the dissolution rate will decrease with time as $C(i)$ increases, and, eventually, weight losses should remain constant with time. In fact, the weight loss of type 316 stainless steel at 500°C did not increase after 3000 h of exposure to Pb-17 at. % Li (see Table 9.1.1 and Fig. 9.1.6).

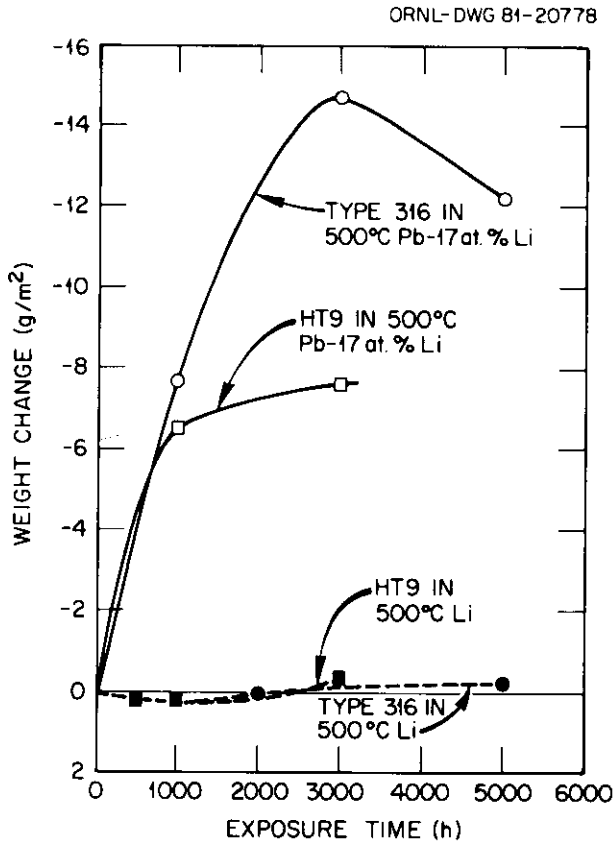

Fig. 9.1.6. Weight Change Versus Exposure Time for Type 316 Stainless Steel and HT9 in Static Lithium and Pb–17 at. % Li.

Studies of corrosion by pure lead[4-6] indicated that the corrosion rate of an alloy increased with increasing nickel content unless a resistant intermetallic compound was formed.[6] This trend was observed in the present study for the 500°C exposures: the weight loss of HT9 (0.5 wt % Ni) was significantly less than that for type 316 stainless steel. However, at 300 and 400°C, the weight losses of type 316 stainless steel were less than those of HT9. The reason for this deviation from expected behavior at the lower temperatures cannot be explained at the present time. Additional experiments are being conducted to investigate this behavior in more detail.

The weight losses reported in Tables 9.1.1 and 9.1.2 for HT9 and type 316 stainless steel exposed to Pb–17 at. % Li are relatively large. This is particularly true when these weight losses are compared to those measured when these alloys were exposed to pure lithium (see Fig. 9.1.6).

While negligible weight changes were measured for the lithium tests, significant material loss occurred in similar experiments with Pb-17 at. % Li. Such behavior should be expected; reported corrosion rates for alloys exposed to pure lead are much greater than comparable rates in pure lithium.[3] It thus appears that the corrosion rates of ferrous alloys in Pb-17 at. % Li tend to be similar to those in pure lead. Although the present results are preliminary and relevant only to isothermal conditions, it is apparent that, at comparable temperatures, Pb—17 at. % Li is much more corrosive toward ferrous alloys than pure lithium. The weight losses of HT9 and type 316 stainless steel reported above are significant and can be expected to be much larger in flowing Pb—17 at. % Li systems. Therefore, the use of this lead-lithium alloy as a semistagnant tritium breeding fluid will probably limit the allowed service temperatures to below 400°C. Implementation of corrosion inhibition techniques may be necessary. One possible method may be by elemental metal additions to the lead-lithium. For example, the presence of 500 wt % ppm Ti in lead effectively reduced the corrosion rate of ferrous alloys by the formation of protective TiN or TiC layers.[4,5] Alternately, the composition of the structural alloy can be optimized for corrosion protection. While further work with Pb—17 at. % Li is required to clearly define the effects of containment alloy composition on corrosion, lower-nickel and -chromium alloys will probably be preferred for use with this molten alloy.

9.1.5 Conclusions

1. Lead alloyed with 17 at. % Li is more aggressive toward ferrous alloys than lithium. Type 316 stainless steel and HT9 suffered significant weight losses when they were exposed to static Pb—17 at. % Li, particularly at 500°C, while under similar conditions the weight changes of these alloys in pure lithium were negligible.

2. For ferrous alloys, the applications of Pb-17 at. % Li as a semistagnant tritium breeding fluid in a fusion reactor may be limited to temperatures of 400°C or less when this molten alloy is used in conjunction with ferrous alloys. Containment alloys of low nickel and chromium activities would be preferable.

9.1.6 References

1. D. K. Sze, R. Clemmer, and E. T. Cheng, "LiPb, A Novel Material for Fusion Applications," UWFDM-378, University of Wisconsin, Madison, October 1980.

2. P. F. Tortorelli, J. H. DeVan, and C. T. Liu, "Compatibility of Static Lithium with a Long-Range-Ordered Fe-Ni-V Alloy and 2 1/4 Cr-1 Mo Steel," *ADIP Quart. Prog. Rep. June 30, 1980,* DOE/ER-0045/3, pp. 328-36.

3. P. F. Tortorelli and O. K. Chopra, "Corrosion and Compatibility Considerations of Liquid Metals for Fusion Reactor Applications," paper presented at Second Topical Meeting Fusion Reactor Materials, Seattle, Wash., August 1981, to be published in *Journal of Nuclear Materials.*

4. J. A. James and J. Trotman, "Corrosion of Steels in Liquid Bismuth and Lead," *J. Iron Steel Inst. (London)* 194: 319-23 (1960).

5. R. C. Asher, D. Davies, and S. A. Beetham, "Some Observations on the Compatibility of Structural Materials with Molten Lead," *Corros. Sci.* 17: 545-57 (1977).

6. J. V. Cathcart and W. D. Manly, "The Mass-Transfer Properties of Various Metals and Alloys in Liquid Lead," ORNL-2008, Oak Ridge National laboratory, Oak Ridge, Tennessee, October 1956.

9.2 CORROSION OF IRON-BASE ALLOYS IN FLOWING LITHIUM — P. F. Tortorelli, J. H. DeVan, and C. T. Liu (Oak Ridge National Laboratory)

9.2.1 ADIP Task

ADIP Task **I.A.3,** Perform Chemical and Metallurgical Compatibility Analyses.

9.2.2 Objective

The purpose of this task is to evaluate the corrosion resistance of candidate first-wall materials to flowing lithium in the presence of a temperature gradient. Corrosion rates (in both dissolution and deposition) are measured as functions of time, temperature, additions to the lithium, and flow conditions. These measurements are combined with chemical and metallographic examinations of specimen surfaces to establish the mechanisms and rate-controlling processes for dissolution and deposition reactions.

9.2.3 Summary

Weight loss data are reported for the long-range-ordered (LRO) alloy Fe—31.8 Ni—22.5 V4.4 Ti (wt %) exposed to lithium in type **316** stainless steel thermal-convection loops (TCLs) for up to 5000 h at 600°C. Very high corrosion rates were measured and extensive corrosive attack was observed. The exposed surfaces were depleted in nickel and correspondingly enriched in iron and vanadium. Another lithium-type **316** stainless steel TCL was used to study the dependence of the dissolution rate of type **316** stainless steel in flowing lithium on temperature. The observed temperature dependence was consistent with an apparent overall activation energy *of* **160** kj/mol **(38** kcal/mol). This is a higher activation energy than has been measured in earlier tests and this difference indicates problems with reproducibility of activation energies measured in different experiments.

9.2.4 Progress and Status

We previously found[1,2] that the **LKO-35** alloy composed **of** Fe—31.8 Ni—22.5 *W.4* Ti (wt %) was essentially unaffected by exposure to static

lithium at elevated temperatures while commercial Fe–Cr–Ni alloys with similar and higher nickel concentrations were readily attacked under the same exposure conditions. We therefore initiated experiments to assess the corrosion resistance of this LRO alloy to flowing lithium. Because of a lack of sufficient LRO material, the tests are being conducted in type 316 stainless steel TCLs that are designed[3] so that lithium samples can be taken and corrosion coupons can be withdrawn and inserted without altering loop operating conditions. The use of the stainless steel loop material imposes a severe chemical gradient between the LRO specimens and the loop wall, especially considering that surfaces of the loops' hot legs have been preferentially leached of nickel from prior exposures to lithium. Such an arrangement provides the worst case for the dissolution of the LRO alloy in flowing lithium. The LRO–35 coupons were placed in the two hottest positions (600 and 570°C) of two type 316 stainless steel TCLs.

In the preceding progress report,[4] it was reported that the corrosion rates of LRO–35 after 1500 h of exposure to flowing lithium were much greater than those of type 316 stainless steel previously exposed in the two loops. We have continued to expose the LRO coupons, and the updated results for the 600°C specimens are shown in Fig. 9.2.1. The weight losses for the LRO specimens in both TCLs (2B and 3B) are very much greater than comparable measurements for type 316 stainless steel. Also, as was noted previously,[5] despite similar operating conditions, the weight losses are different between the two loops. The difference is consistent with the trend established earlier when coupons of type 316 stainless steel were exposed in these two loops:[5] lower weight losses in loop experiment 2B (with respect to four other similar experiments) resulted after replacement of the loop's cold–leg section, which had operated for 5000 h. (Data for the 5000 h period fell within the uncertainty of the average of the four other tests.) This pattern was not repeated in loop 3B, whose cold–leg section was also replaced (see Fig. 9.2.1). Although there is a difference between the corrosion rates in the two loops, the weight losses of the LRO coupons in both loops are definitely

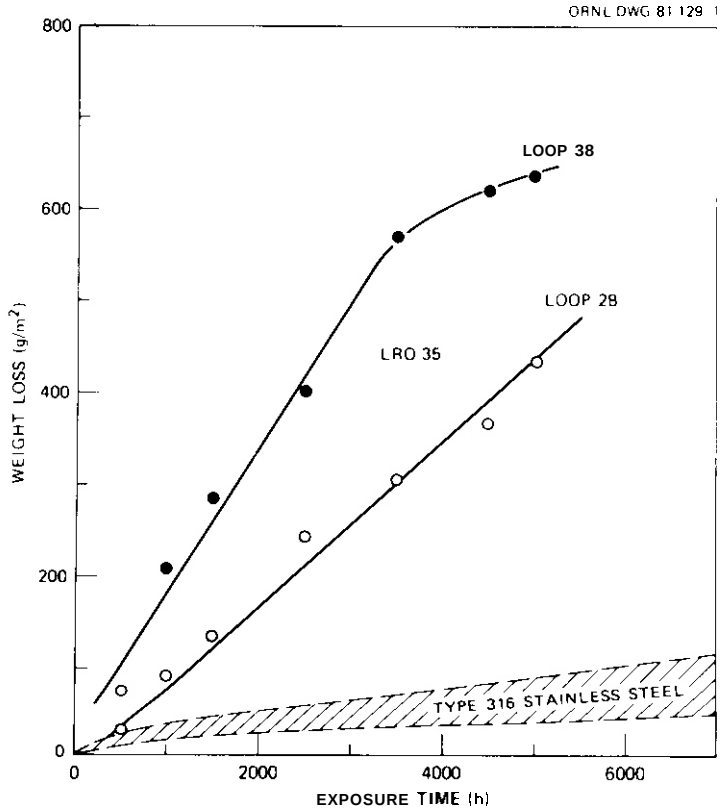

Fig. 9.2.1. Weight Loss Versus Exposure Time for LRO-35 Exposed to Flowing Lithium at 600°C in Two Different Type 316 Stainless Steel Loops.

much greater than those of type 316 stainless steel. However, there is some evidence that the corrosion rate is beginning tu decrease after 5000 h (see loop 38 data in Fig. 9.2.1).

As described in the preceding quarterly,[4] the coupon exposed at 570°C for 1000 h in loop 2B was found to have d loosely adhering layer that appeared to be composed principally of iron with some chromium and small concentrations of nickel and vanadium. Such layers were subsequently visible on both the 600 and 570°C LKO coupons in loop 2B after 2500 h and on the 570°C specimen in loop 3B after 3500 h. (Weight losses were measured after these layers were removed.) Portions of the detached layers from the 600 and 570°C specimens in loop 28 after 2500 h of exposure were analyzed by x-ray diffraction and found to be alpha iron.

Metallographic examination of clipped corners from the exposed LKO coupons in both loops revealed extensive surface attack. Consistent with their larger weight losses, the loop 3B specimens exhibited a much greater attack depth than those from loop 2B (see Fig. 9.2.2). In both cases, the

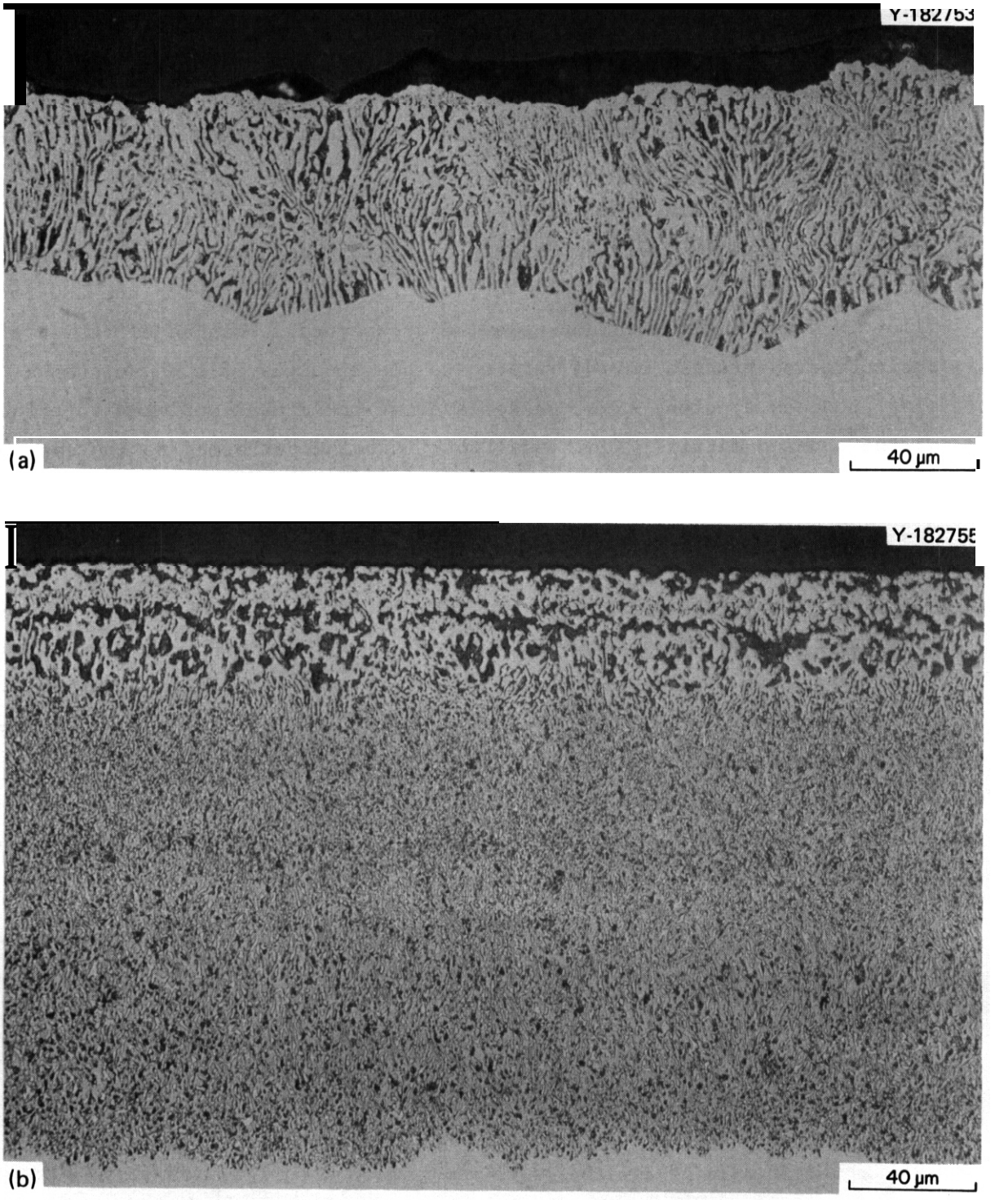

Fig. 9.2.2. Polished Cross-Sections of LRO-35 Exposed *to* Flowing Lithium for 2500 h at 600°C. (a) Loop 2B. (b) Loop 3B.

microstructure changes due to lithium exposure were much greater than those observed for austenitic stainless steel exposed under similar conditions. Electron microprobe analysis of the surfaces shown in Fig. 9.2.2 revealed a general depletion in nickel and the affected areas were enriched in iron and vanadium (see Fig. 9.2.3). The depletion of nickel from the surfaces of these specimens would be predicted based on tests of austenitic stainless steels and alloys with nickel concentrations similar to that of LRO–35. However, the rapidity with which the LRO–35 alloy is attacked in lithium was quite unexpected. This acceleration of the corrosion process may be related to the kinetics of a phase change that produces a porous sigma-phase layer at the nickel-depleted interface of the ordered matrix. Additional work is being performed to increase our understanding this phenomenon.

Another lithium type 316 stainless steel TCL of the type described above is being used to determine the dissolution rate of type 316 stainless steel in lithium as a function of maximum loop temperature. We first established the dissolution rate as a function of time at 600°C and are now varying the loop's maximum temperature while keeping a temperature differential of 150°C across the loop. The dissolution rate at each temperature is obtained by the slope of the least squares fit line on a weight loss versus exposure time plot. In this manner, we have measured the corrosion rate of type 316 stainless steel at 500, 550, and 600°C (see Fig. 9.2.4). As expected, the dissolution rate decreased with decreasing temperature. Steady-state dissolution rates measured for type 316 stainless steel in thermally convective lithium are shown below:

Temperature (°C)	R_s (mg/m^2·h)
500	0.8
550	3.6
600	13.6

Figure 9.2.5 shows that the dissolution rates measured at the maximum temperature positions in the respective tests are reasonably consistent with an Arrhenius-type behavior:

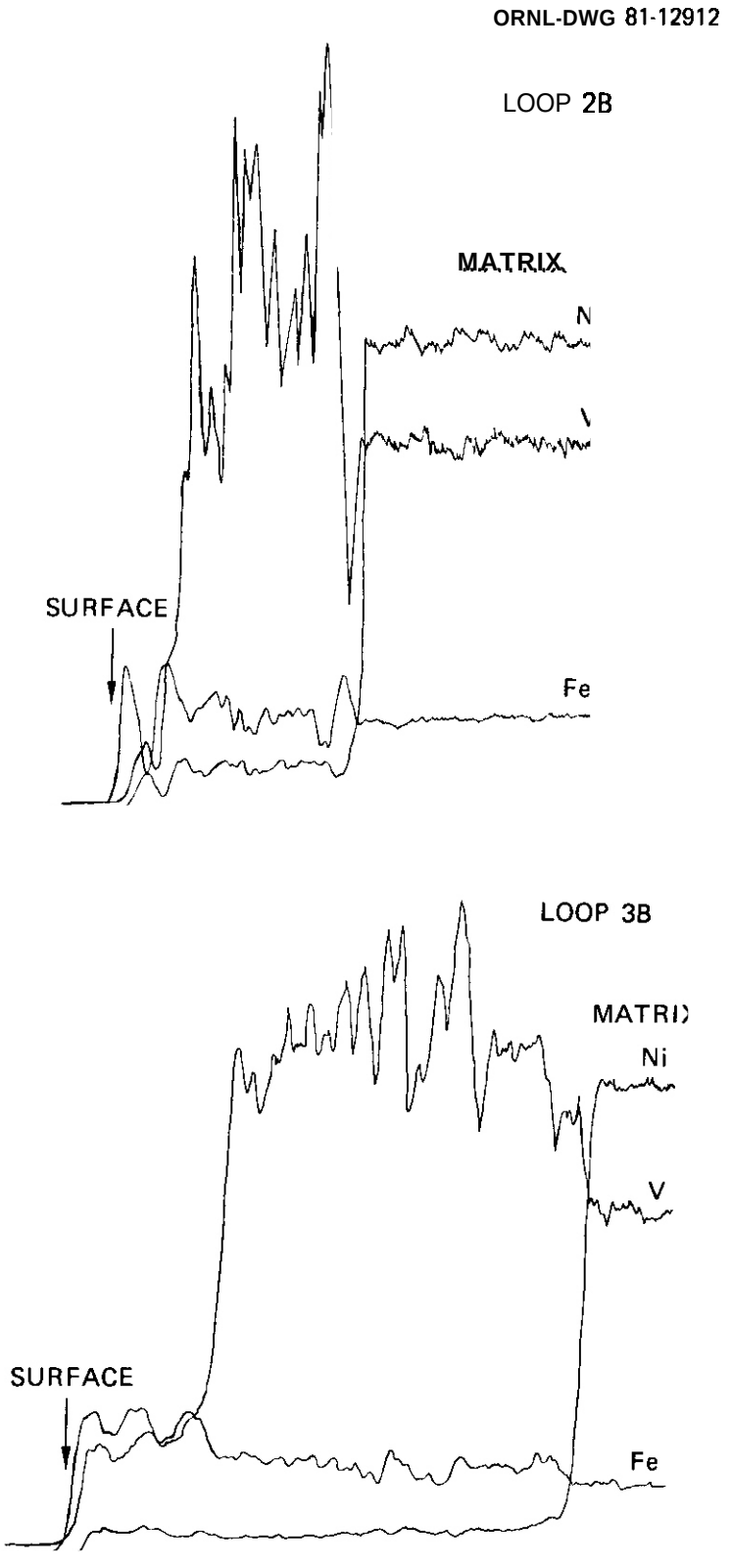

Fig. 9.2.3. Electron Microprobe Traces Across Cross Sections of LRO–35 Exposed to Flowing Lithium at 600°C for 2500 h. The nickel and vanadium concentrations are magnified relative to the iron trace.

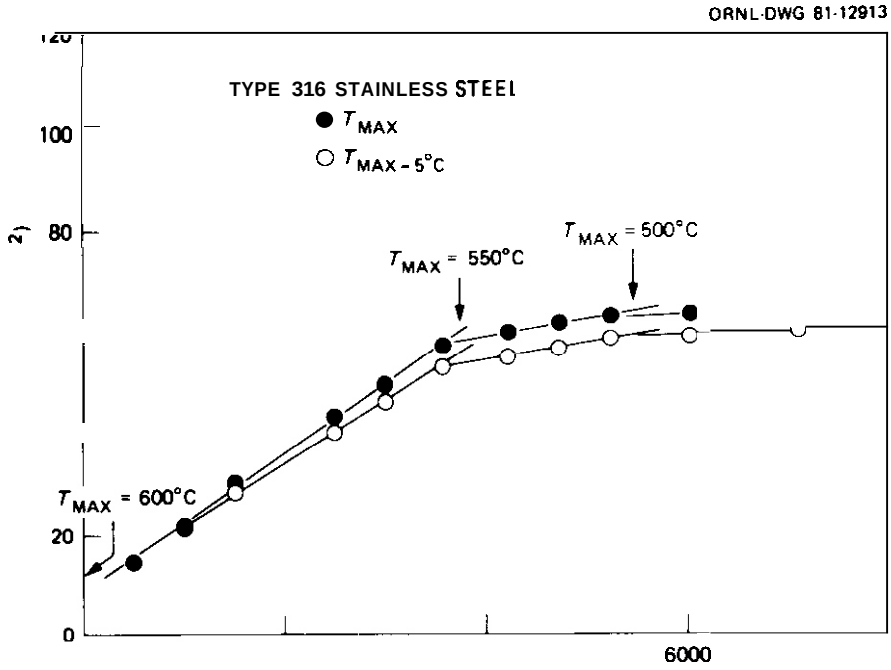

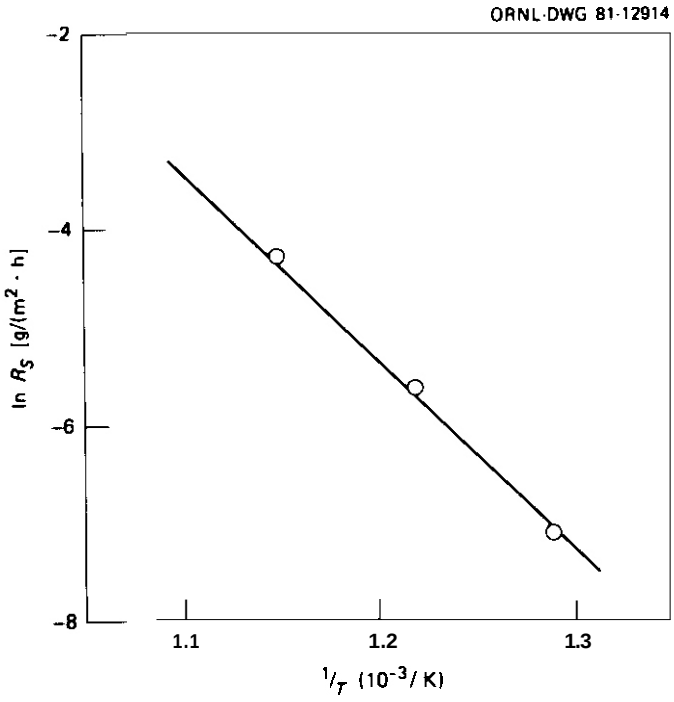

Fig. 9.2.5. Arrhenius Plot of the Dissolution Rate Versus Inverse Temperature for Type 316 Stainless Steel in Thermally Convective Lithium.

$$R_s = A \exp(-Q/RT) ,$$

where

R_s = steady-state dissolution rate at temperature T;
A = constant;
Q = overall (apparent) activation energy for dissolution.

The activation energy, based on a least-squares fit was determined to be 160 kJ/mol (38 kcal/mol). This magnitude is significantly larger than the activation energy measured in an earlier series of type 316 stainless steel thermal convection loop tests where the operating times were limited to 3000 h.[7] The difference in the apparent activation energy between the two test series indicates an important problem in applying a simple Arrhenius equation to the rates being measured in these tests. The dissolution rate can effectively be described in terms of a "forward" flux of atoms leaving the specimen surface controlled by the chemical activity of the atoms in the steel and an "escape" rate from the solid into the liquid. This is counterbalanced by a "reverse" flux of solute atoms returning from the liquid to the specimen that is controlled by the solute activity (concentration) and sticking probability. Although it can be reasonably assumed that the solute concentration at the maximum temperature position will remain constant with time in any given loop, there is no basis for assuming that this concentration will be the same from loop to loop. Furthermore, this solute concentration can be expected to depend on the particular temperature gradient chosen for the experiments as well as the loop geometry. Thus in analyzing the temperature dependence of dissolution rates in any set of loop experiments, it must be borne in mind that (1) the measured dissolution rate is the difference between a forward and backward reaction and (2) the experimental conditions governing the backward reaction are not necessarily consistent from experiment to experiment.

9.2.5 Conclusions

1. Specimens of LRO-35 [Fe-31.8 Ni-22.5 W .4 Ti (wt %)] corroded very rapidly when exposed to flowing lithium at 600°C in type 316

stainless steel TCLs. The resulting LRO surfaces were depleted in nickel and correspondingly enriched in iron and vanadium. Corrosion rates of the LRO are much greater than those of type 316 stainless steel previously exposed in these loops.

2. Dissolution rates of type 316 stainless steel exposed to flowing lithium decreased with decreasing loop temperatures. An "apparent" activation energy of 160 kJ/mol (38 kcal/mol) was measured.

9.2.6 References

1. P. F. Tortorelli, J. H. DeVan, and C. T. Liu, "Compatibility of Static Lithium with a Long-Range-Ordered Fe-N-V Alloy and 2 1/4 Cr-1 Mo Steel," *ADIP Quart. Prog. Rep. June 30, 1980,* DOE/ER-0045/3, pp. 328-36.
2. P. F. Tortorelli and J. H. DeVan, "Corrosion of Fe-Ni-Cr and Fe-Ni-V Alloys in Static Lithium," *ADIP Quart. Prog. Rep. Dec. 31, 1979,* DOE/ER-0045/1, pp. 152-57.
3. J. H. DeVan and J. R. DiStefano, "Thermal-Convection Loop Tests of Type 316 Stainless Steel in Lithium," *ADIP Quart. Prog. Rep. March 31, 1978,* DOE/ET-0058/1, pp. 200-08.
4. P. F. Tortorelli and J. H. DeVan, "Corrosion of an Iron-Base Long-Range-Ordered Alloy in Flowing Lithium," *ADIP Quart. Prog. Rep. March 31, 1981,* DOE/ER-0045/6, pp. 229-34.
5. P. F. Tortorelli and J. H. DeVan, "Corrosion of Type 316 Stainless Steel and a Long-Range-Ordered Fe-Ni-V Alloy in Naturally Convective Lithium," *ADIP Quart. Prog. Rep. Dec. 31, 1980,* DOE/ER-0045/5, pp. 256-62.
6. P. F. Tortorelli and J. H. DeVan, "Effect of Nickel Concentration on the Mass Transfer of Fe-Ni-Cr Alloys in Lithium," paper presented at Second Topical Meeting on Fusion Reactor Materials, Seattle, Wash., August 1981, to be published in *Journal of Nuclear Materials.*
7. P. F. Tortorelli, J. H. DeVan, and J. E. Selle, "Corrosion in Lithium Stainless Steel Thermal-Convection Systems," pp. 13-55-13-63 in *Proc. 2d Int. Conf. Liquid Metal Technology in Energy Production,* CONF-800401-P2, U.S. Department of Energy, 1980.

9.3 ENVIRONMENTAL EFFECTS ON PROPERTIES OF STRUCTURAL ALLOYS - O. K. Chopra and D. L. Smith (Argonne National Laboratory)

9.3.1 ADIP Task

ADIP tasks are not defined in the 1978 program plan.

9.3.2 Objective

The objective of this program is to investigate the influence of chemical environment on the compatibility, corrosion, and mechanical properties of structural alloys under conditions of interest in fusion reactors. Test environments to be investigated include lithium, water, and helium as well as candidate solid breeding materials and neutron multipliers. Emphasis will be placed on the combined effect of stress and chemical environment on corrosion and mechanical properties of materials. Tests have been formulated to determine the (1) effect of a liquid lithium environment on fatigue and creep-fatigue properties of ferritic and stainless steels and (2) compatibility of structural materials with lithium, lead-lithium, and candidate solid tritium-breeding materials.

9.3.3 Summary

Several constant-stress compatibility tests and continuous-cycle fatigue tests have been conducted on HT-9 alloy and Type 304 stainless steel at 755 K in a flowing lithium environment. The results indicate that for applied stresses below the yield stress of the material, the corrosion behavior of HT-9 alloy and Type 304 stainless steel is independent of stress. The fatigue properties of these materials are strongly influenced by the concentration of nitrogen in lithium. For HT-9 alloy, the fatigue life in lithium containing 100-200 wppm nitrogen is a factor of 2 to 5 greater than that in lithium with 1000-1500 wppm nitrogen. In low-nitrogen lithium, fatigue life is also independent of strain rate. The lower fatigue lives observed in high-nitrogen lithium may be attributed to corrosion. Fatigue tests on lithium-exposed

specimens are in progress to investigate the long-term environmental effects.

Construction of a forced-flow lead-lithium loop is in progress. Tests have been formulated to investigate the combined effects of stress and environment on the corrosion and mechanical properties of structural materials.

The compatibility of solid Li_2O, $LiAlO_2$, and Li_2SiO_3 breeding materials with several commercial alloys has been investigated at 873 and 973 K. The results show that Li_2O is the most reactive and $LiAlO_2$ is the least reactive of the three breeding materials. The reaction scales on alloys exposed with Li_2O ceramic contain Li_5FeO_4 and $LiCrO_2$ compounds. The formation of those compounds may explain the greater interaction between the alloys and Li_2O material. Compatibility tests at 773 K are in progress. A compatibility-test facility is being constructed to study the alloy/ceramic interactions in a flowing helium environment containing known amounts of moisture.

9.3.4 Progress and Status

9.3.4.1 Lithium Environment

A. Introduction. Liquid lithium has been proposed as the tritium breeder and possibly as a coolant in several designs for magnetic confinement fusion reactors. The cyclic plasma burn projected for some fusion reactor concepts will induce severe cyclic thermal stresses in the first wall/blanket structure. Consequently, the fatigue behavior of the material is an important consideration in the design of the first-wall/blanket region. On the basis of available materials property data, austenitic and ferritic steels have been proposed as candidate structural materials for this region. The austenitic stainless steels have been used extensively in liquid-metal fast-breeder reactor applications, and therefore, a substantial technology base has been generated. The primary incentive for consideration of ferritic

steels, such as Sandvik HT-9 and a developmental Fe-9Cr-1Mo alloy, is the low void swelling and high in-reactor creep resistance of these steels compared with austenitic stainless steels. Also, the higher thermal conductivity of the ferritic steels provides a reduced thermal stress factor. However, relatively little information is available on the influence of a liquid lithium environment on the compatibility and mechanical properties of austenitic and ferritic steels.

B. Experimental. The facility for conducting fatigue tests in a flowing lithium environment consists of an MTS closed-loop servohydraulic fatigue machine with an associated forced-flow liquid lithium loop. A schematic diagram of the test facility is shown in Fig. 9.3.1. The lithium loop, which is constructed of Type 304 stainless steel, consists of three test vessels and a cold-trap purification system. One test vessel was used for conducting fatigue tests and another for constant-stress compatibility tests. The quantity of lithium in the loop was ~20 liters, and the lithium within the test vessels was recirculated at ~1 liter/min. The cold-trap temperature was maintained at ~480 K. Filtered lithium samples were obtained for analysis of nitrogen and carbon in lithium. The hydrogen concentration in lithium was established by equilibrating yttrium samples in lithium and using the reported data' on the distribution of hydrogen between yttrium and lithium. During the fatigue tests, the concentration of carbon and hydrogen in lithium was ~8 and 120 wppm, respectively. The nitrogen concentration was maintained at ranges of 100-200, 500-700, or 1000-1500 wppm (designated low-, medium-, and high-nitrogen, respectively).

The combined effects of constant stress and liquid lithium environment on the corrosion behavior of structural materials was investigated by exposing monotonically stressed specimens of HT-9 alloy and Type 304 stainless steel to flowing lithium. A schematic of the constant stress fixture is shown in Fig. 9.3.2. The test specimen was fastened to the fixture and loaded through a pull rod by dead weights.

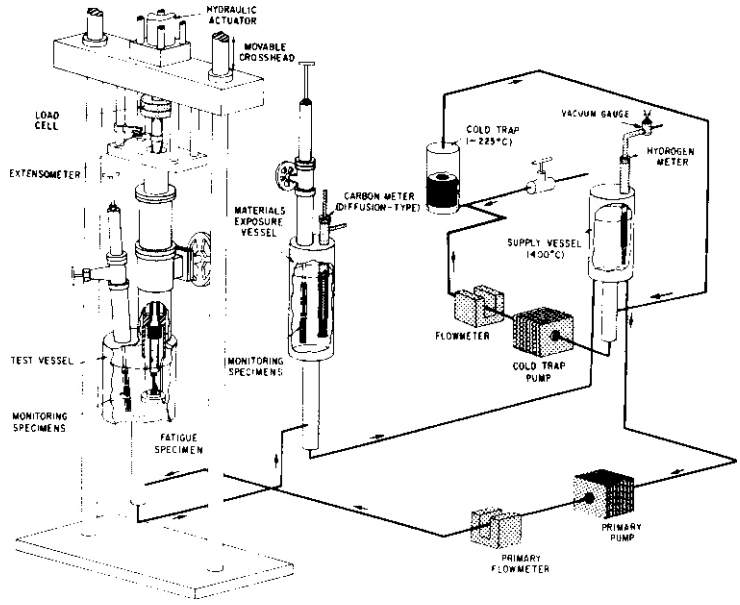

Fig. 9.3.1. Schematic of Facility for Fatigue Testing in Lithium.

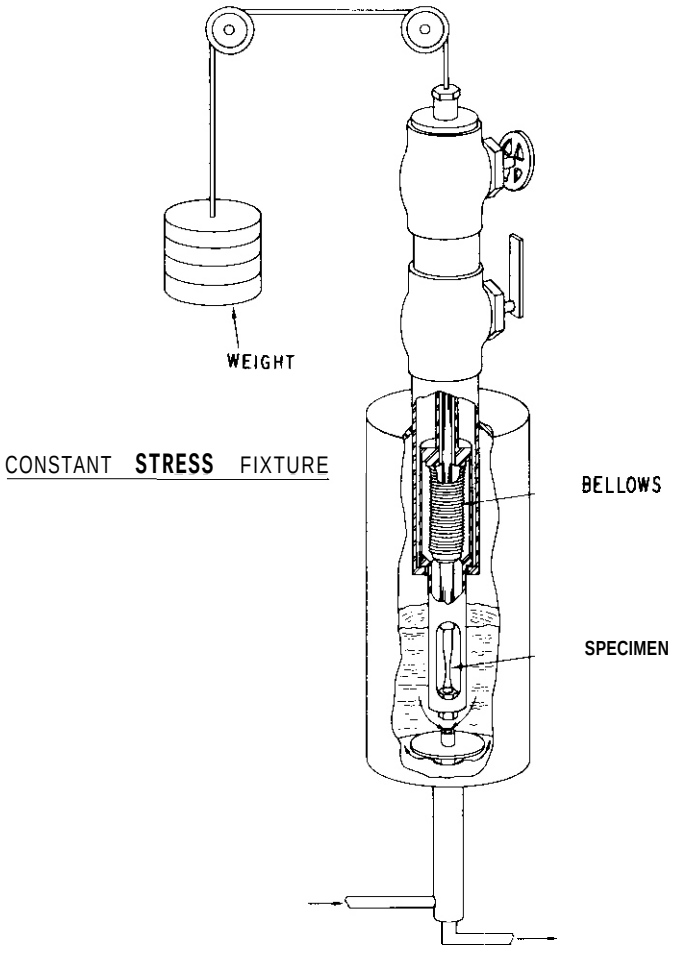

Fig. 9.3.2
Schematic of Constant Stress Test Fixture.

The fatigue test specimens were fabricated from 6.4-mm-diameter rod of HT-9 alloy (heat 91354) and 16-mm-diameter rod of Type 304 stainless steel (heat 9T2796). The gauge diameter and length of the specimens were, respectively, 2.5 and 6.4 mm for the HT-9 alloy and 5.1 and 12.7 mm for Type 304 stainless steel. Tapered gauge-length specimens were used for the constant stress compatibility tests. The gauge section had a total length of 44.5 mm and tapered uniformly from 6.3 mm to 2.2 mm diameter. After fabrication, the specimens of HT-9 alloy were heat treated in vacuum according to the following schedule: normalize at 1323 K for 30 min and air cool, then temper at 1053 K for 150 min and air cool, Type 304 stainless steel specimens were solution annealed in vacuum for 30 min at 1298 K.

The fatigue tests were conducted in the axial stroke-control mode with a fully reversed triangular waveform and strain rates in the range of 4×10^{-2} and 4×10^{-4} s^{-1}. The details of the procedure for strain control and strain measurement are given elsewhere.' Fatigue tests were also conducted in a flowing sodium environment for comparison, using a procedure similar to that for the lithium tests.

C. Results. The experimental conditions for the exposure of constant stress compatibility tests are given in Table 9.3.1. For both specimens, the maximum applied stress was below the yield stress of the material. After exposure, the specimens were examined metallographically to evaluate the corrosion behavior. Cross sections with different diameters along the length of the specimen were examined to determine the effect of stress on corrosion. The results indicate that for the experimental conditions of the present study, a variation in applied stress has no effect on corrosion. Both specimens of HT-9 alloy and Type 304 stainless steel had a uniform 7-μm-thick corrosion layer along the entire gauge length. Sections of the specimens subjected to different applied stress showed identical corrosion. However, the gauge surfaces of the specimens in contact with lithium had a spongy or etched

Table 9.3.1. Experimental Conditions for Exposure of Tapered Specimens of HT-9 Alloy and Type 304 Stainless Steel to Flowing Lithium

Material	Temp. (K)	Time (h)	Stress (MPa) Maximum	Stress (MPa) Minimum	Nitrogen Content in Lithium (wppm)
HT-9 Alloy	755	1000	136	22	~500
Type 304 SS	755	1000	69	11	~80

appearance. Micrographs of the gauge surface and cross section of HT-9 alloy and Type 304 stainless steel specimens are shown in Figs. 9.3.3 and 9.3.4, respectively. The HT-9 alloy specimen shows intergranular corrosion whereas a uniform and porous ferrite layer is observed on the Type 304 stainless steel specimen. It should be noted that during exposure of the HT-9 alloy, the concentration of nitrogen in lithium was higher than that for Type 304 stainless steel.

The dissolution of substitutional elements from the specimens was investigated by electron microprobe analyses. The distribution of the major elements across the corrosion layer on the HT-9 alloy and Type 304 stainless steel is shown in Fig. 9.3.5. A slight depletion of chromium is observed in the HT-9 alloy whereas Type 304 stainless steel shows depletion of both chromium and nickel. The composition of the ferrite layer on Type 304 stainless steel was 86% iron, 13% chromium, and 1% nickel.

The influence of lithium purity on the cyclic properties of HT-9 alloy and Type 304 stainless steel was investigated by conducting fatigue tests in lithium containing different concentrations of nitrogen. The total and plastic strain range vs fatigue life for HT-9 alloy tested at 755 K in flowing lithium is shown in Fig. 9.3.6. Fatigue data from two tests performed in a liquid sodium environment are also included for comparison. The results show that the fatigue life of HT-9 alloy is strongly influenced by the concentration of nitrogen in lithium. The fatigue life in lithium containing 1000-1500 wppm nitrogen

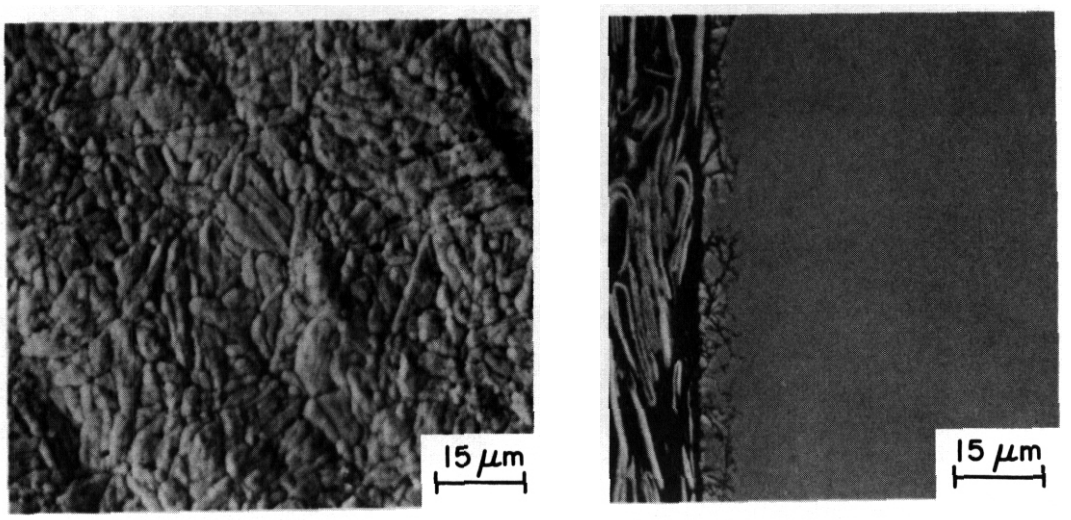

Fig. 9.3.3. Micrographs of the (a) Gauge Surface and (b) Cross Section of HT-9 Alloy Specimen Exposed with a Constant Tensile Stress in Lithium for 1000 h at 755 K. Concentration of nitrogen in lithium was ~500 wppm.

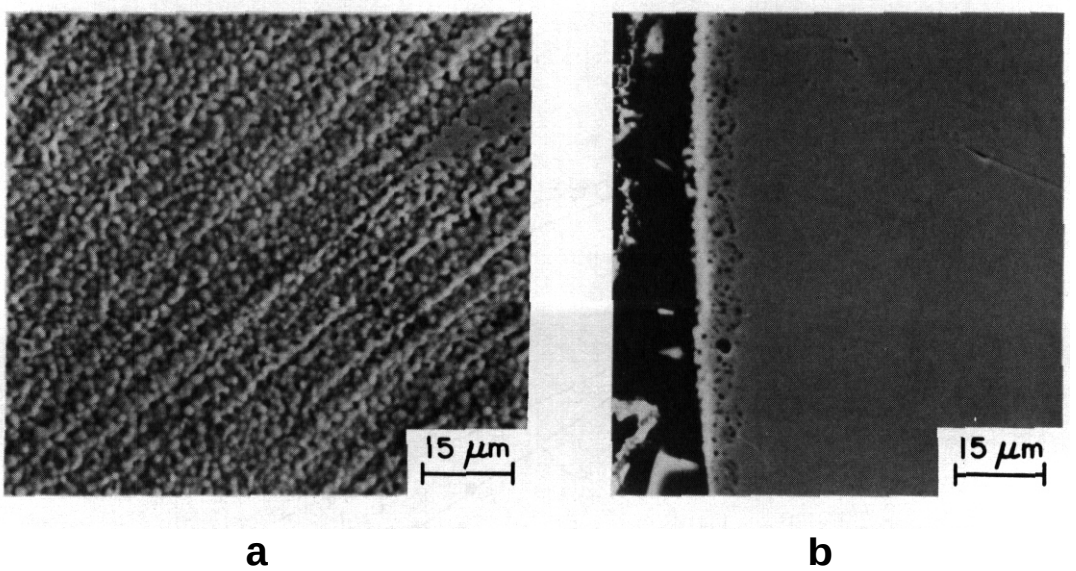

Fig. 9.3.4. Micrographs of the (a) Gauge Surface and (b) Cross Section of Type 304 Stainless Steel Exposed with a Constant Tensile Stress in Lithium for 1000 h at 755 K. Concentration of nitrogen in lithium was ~80 wppm.

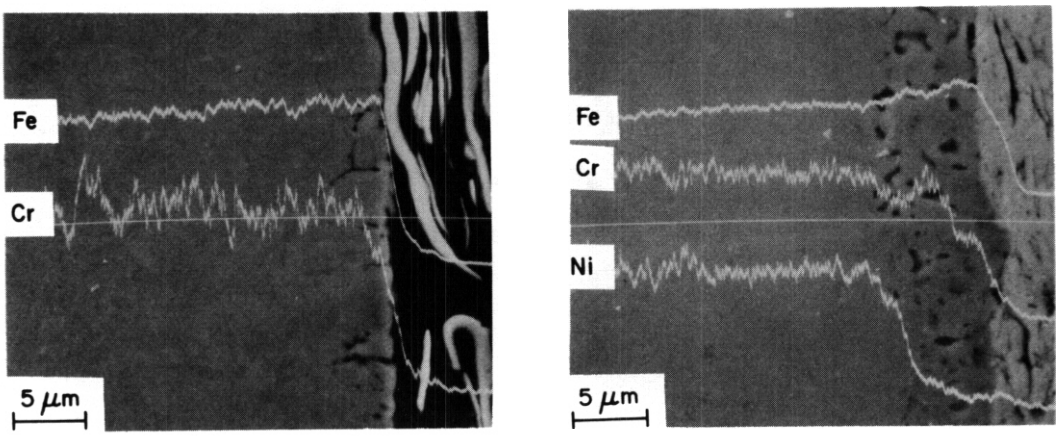

Fig. 9.3.5. Micrographs and Concentration Profiles for Iron, Chromium, and Nickel Across the Cross Section of (a) HT-9 Alloy and (b) Type 304 Stainless Steel Exposed in Lithium for 1000 h at 755 K.

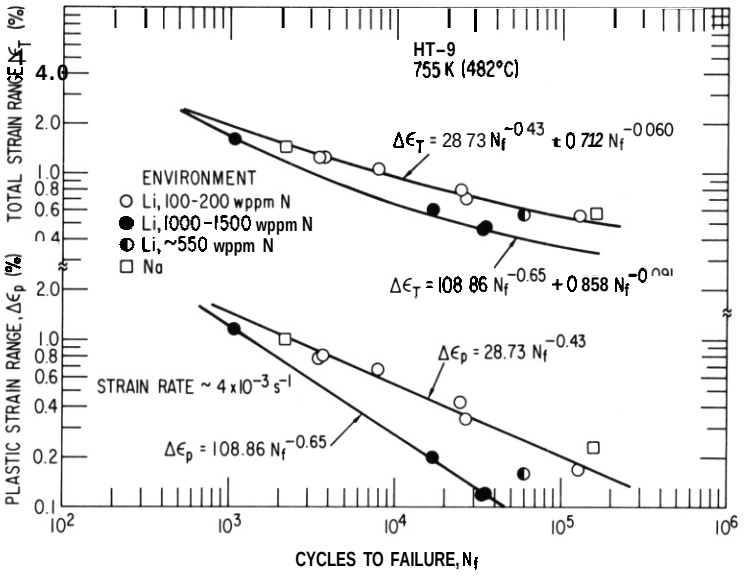

Fig. 9.3.6. Total and Plastic Strain Range vs Cycles to Failure for HT-9 Alloy Tested in Lithium and Sodium at 755 K.

is a factor of 2 to 5 lower than that in lithium with 100-200 wppm nitrogen. The difference in life is greater at total strain ranges <0.7%. Furthermore, the results suggest that the reduction in fatigue life is proportional to the concentration of nitrogen in lithium. For example, a test conducted in lithium with ~550 wppm nitrogen yielded a value of fatigue life of ~60,000 cycles compared to 20,000 and 130,000 cycles, respectively, for the tests in high- and low-nitrogen lithium. The fatigue life in a liquid sodium environment is similar to or slightly greater than that in low-nitrogen lithium. However, more data are needed to establish the difference in the strain-life behavior in liquid sodium and low-nitrogen lithium environments.

The plastic strain range, $\Delta\varepsilon_p$, and cycles to failure, N_f, can be expressed by a power-law relationship, given by

$$\Delta\varepsilon_p = AN_f^{-\alpha}. \qquad (1)$$

The values of the coefficient and exponent in Eq. (1) were determined from a linear least-squares analysis and are given in Fig. 9.3.6. The relationship between total strain range and fatigue life was obtained from the cyclic stress-strain behavior and Eq. (1). Figure 9.3.7 shows the cyclic stress-strain behavior for HT-9 alloy tested in lithium and sodium environments. The cyclic stress amplitude at half-life, $\Delta\sigma/2$, is expressed in terms of the plastic strain amplitude, $\Delta\varepsilon_p/2$, by the relationship

$$\Delta\sigma/2 = k(\Delta\varepsilon_p/2)^n. \qquad (2)$$

The constants in Eq. (2) were obtained using all the data, irrespective of the environment or the concentration of nitrogen in lithium. At lower strain amplitudes, the cyclic stress for the tests in high-nitrogen lithium is slightly higher than that for the tests in low-nitrogen lithium because of the cyclic hardening/softening behavior of the material. The variation in cyclic stress range as a function of fatigue cycles is shown in Fig. 9.3.8. After an initial period of ~1000

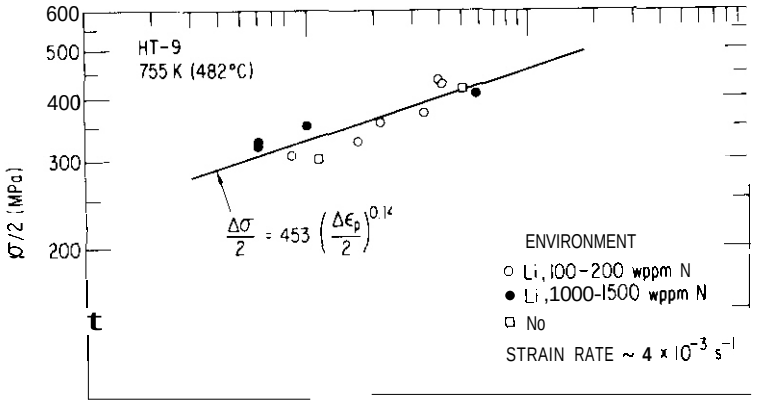

Fig. 9.3.7. Cyclic Stress–Strain Relationship for HT–9 Alloy Tested in Lithium and Sodium Environments.

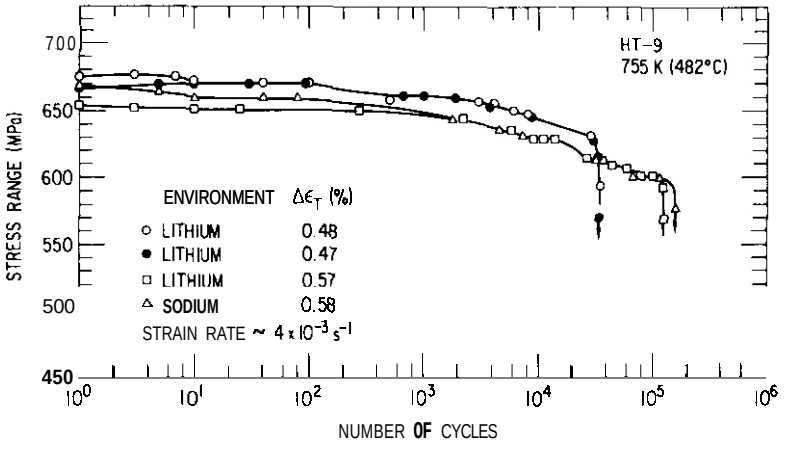

Fig. 9.3.8. Cyclic Stress Range as a Function of Fatigue Cycles for HT–9 Alloy Tested in Lithium and Sodium Environments.

cycles, during which the cyclic stress was relatively constant, all specimens showed gradual softening for the remaining lifetime. Consequently, for a given strain range, the tests with longer fatigue life, e.g., in sodium or low–nitrogen lithium, showed lower values of cyclic stress than the tests with a shorter fatigue life, e.g., in high–nitrogen lithium.

The relationships between elastic and total strain range and fatigue life can be determined from Eqs. (1) and (2). Thus,

$$\Delta\varepsilon_e = \frac{\Delta\sigma}{E} = \frac{2k}{E}\left(\frac{A}{2}\right)^n N_f^{-\alpha n} = BN_f^{-\beta} \qquad (3)$$

and

$$\Delta\varepsilon_t = \Delta\varepsilon_p + \Delta\varepsilon_e = AN_f^{-a} + BN_f^{-\beta}, \qquad (4)$$

where E is Young's modulus. The total-strain fatigue-life relationship is shown in Fig. 9.3.6.

The effect of strain rate on the fatigue life of HT-9 alloy in lithium at 755 K is shown in Fig. 9.3.9. These tests were conducted in lithium containing 100-200 wppm nitrogen. The results show that in a low-nitrogen lithium environment, strain rate has no effect on the fatigue life of HT-9 alloy. At all strain rates, the strain-life behavior follows the relationship established from tests performed at a strain rate of $4 \times 10^{-3}\ s^{-1}$. This behavior is different from that observed in an air environment. In air, the fatigue life decreases with a decrease in strain rate. The difference between the results in lithium and air environments can be attributed to oxidation of the material in air.

The continuous-cycle fatigue data for Type 304 stainless steel tested at 755 K in lithium and sodium environments are shown in Fig. 9.3.10. The tests in lithium were conducted at a nitrogen concentration range of 500-700 wppm. The total-strain/life relationship for the tests in air is also included in Fig. 9.3.10 for comparison. The results show that at a total strain range of <1.0%, the fatigue life in lithium is a factor of ~2 higher than that in air. This behavior is generally observed in a low-oxygen sodium environment.[3,4] The difference in fatigue life is attributed to the absence of oxidation effects in a liquid metal environment. The total strain-life behavior for the tests in lithium was expressed by the power-law relationship given in Eq. (4).

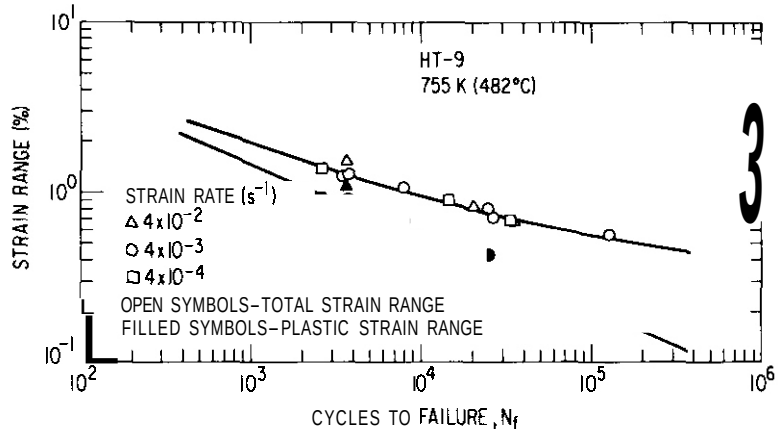

Fig. 9.3.9. Effect of Strain Rate on the Fatigue Life of HT-9 Alloy Tested in Lithium at 755 K. The concentration of nitrogen in lithium was in the range of 80-200 wppm.

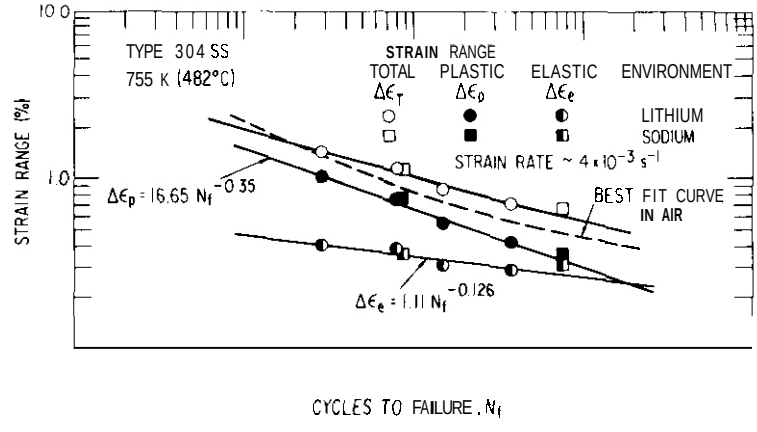

Fig. 9.3.10. Strain Range vs Cycles to Failure for Type 304 Stainless Steel Tested in Lithium and Sodium Environments at 755 K. The concentration of nitrogen in lithium was in the range of 500-700 wppm.

The test specimens were examined metallographically to evaluate the influence of the test environment on the mode of fracture, surface markings on the gauge section, and internal corrosive attack of the specimens. The fracture surfaces of ***HT-9*** alloy tested **in** sodium and low-nitrogen lithium at 755 K are shown in Figs. 9.3.11 and 9.3.12,

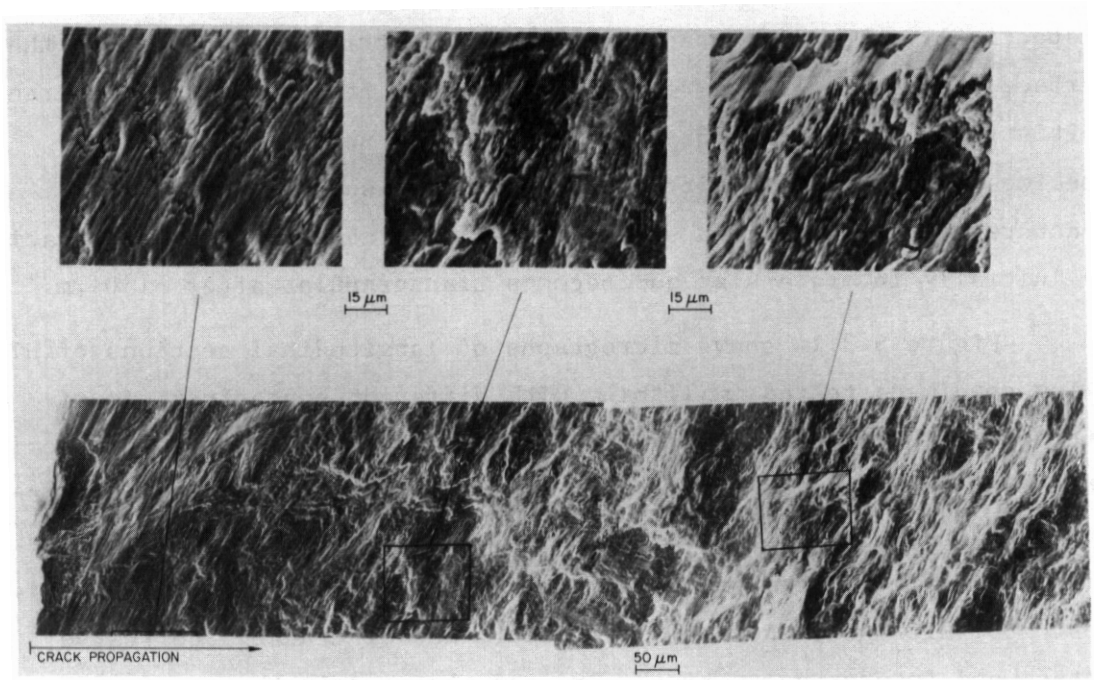

Fig. 9.3.11. Micrographs of the Fracture Surface of HT-9 Alloy Tested in Sodium at 755 K.

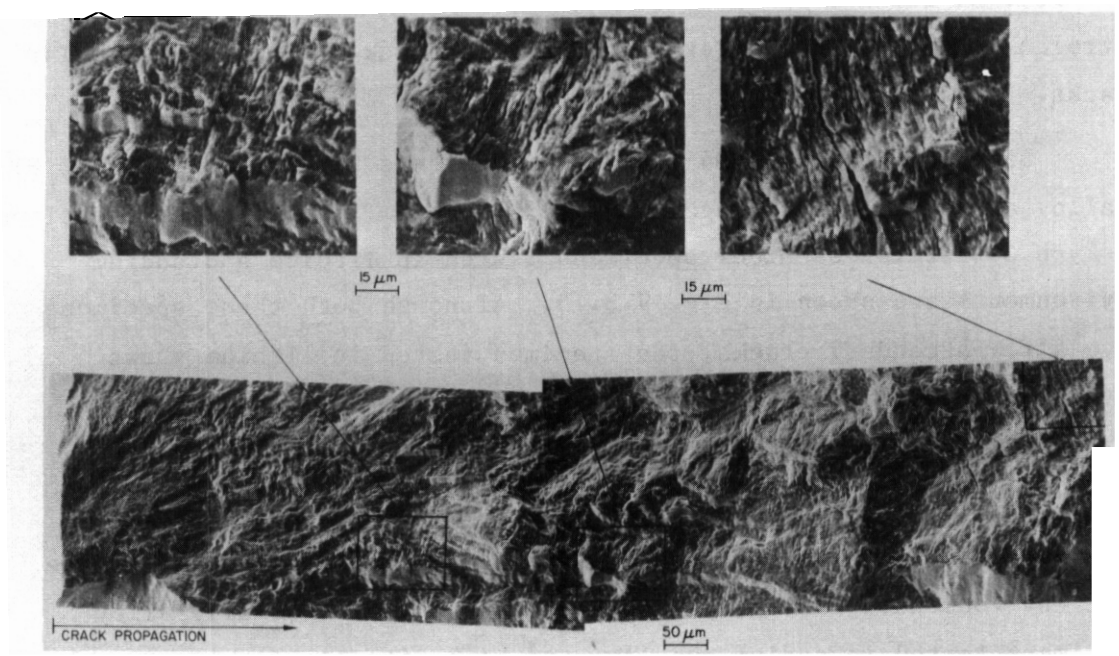

Fig. 9.3.12. Micrographs of the Fracture Surface of HT-9 Alloy Tested at 755 K in Lithium Containing 100–200 wppm Nitrogen.

respectively. The micrographs show diffuse striations throughout the surface and several ridges extending radially from the region of crack initiation. Figure 9.3.13 shows the fracture surface of the HT-9 specimen tested in high-nitrogen lithium. It shows intergranular fracture near the specimen surface, i.e., the mode of crack propagation is initially intergranular and becomes transgranular after ~150 μm.

Figure 9.3.14 shows micrographs of longitudinal sections of HT-9 alloy specimens tested in lithium with different concentrations of nitrogen. The specimen tested in high-nitrogen lithium shows corrosive attack to a depth of 5-10 μm along the entire gauge length and intergranular cracks extending as far as 150 μm along the prior austenite grain boundaries. The specimen tested in medium-nitrogen lithium (i.e., ~550 wppm nitrogen) shows shallow intergranular cracks. Corrosive attack and intergranular cracks are not observed in the specimen tested in low-nitrogen lithium. The influence of nitrogen on intergranular cracking was consistently observed in all the test specimens, i.e., intergranular cracks were not observed in the specimens tested either in low-nitrogen lithium or in sodium, while the specimens tested in high-nitrogen lithium showed internal corrosive attack and/or intergranular cracks.

Behavior for Type 304 stainless steel was similar to that for HT-9 alloy at comparable nitrogen levels in lithium. Longitudinal sections of Type 304 stainless steel specimens tested in lithium and sodium environments are shown in Fig. 9.3.15. Although both these specimens have a few secondary cracks, the specimen tested in lithium shows several transgranular cracks which are not observed in the specimen tested in sodium.

Examination of the surfaces of the gauge sections of the specimens also revealed differences in surface features caused by the test environment. Micrographs of the gauge surfaces of HT-9 alloy specimens tested in sodium and low- and high-nitrogen lithium are shown in Fig. 9.3.16. The specimen tested in sodium shows a smooth, shiny surface with a few slip markings. However, the specimens tested in

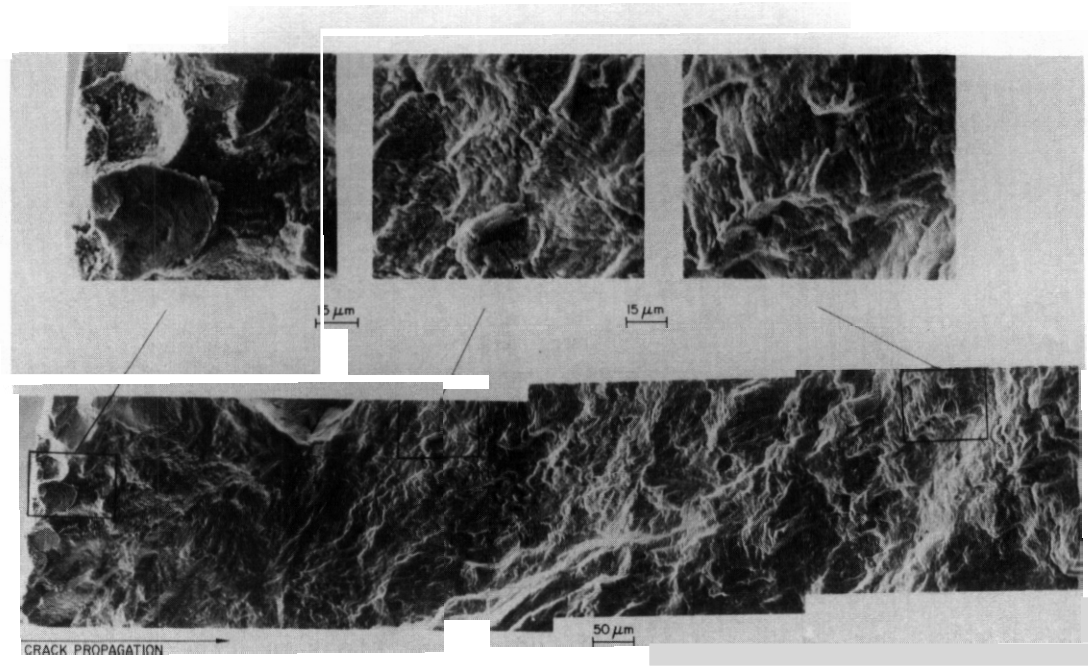

Fig. 9.3.13. Micrographs of the Fracture Surface of HT-9 Alloy Tested at 755 K in Lithium Containing 1000-1500 wppm Nitrogen.

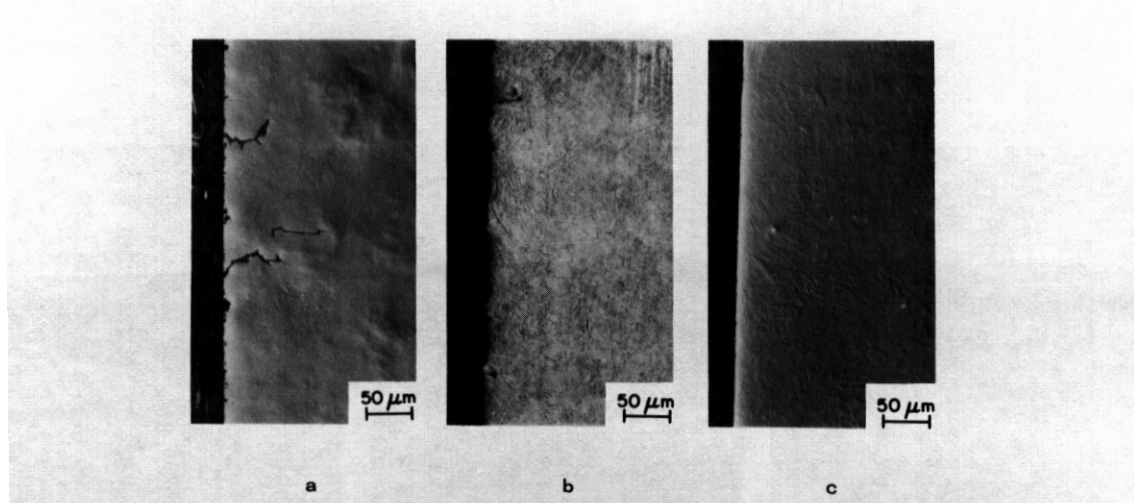

Fig. 9.3.14. Micrographs of Longitudinal Sections of HT-9 Alloy Specimens Tested in Lithium at 755 K. Concentrations of nitrogen in lithium: (a) 1000-1500 wppm, (b) ~500 wppm, and (c) 100-200 wppm.

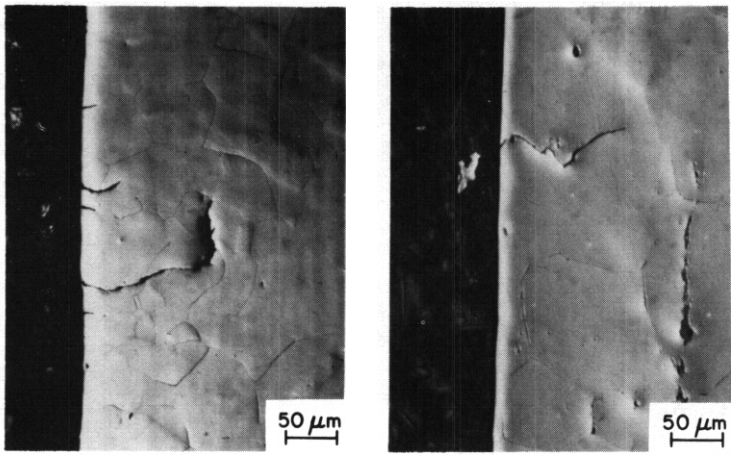

a b

Fig. 9.3.15. Micrographs of Longitudinal Sections of Type 304 Stainless Steel Specimens Tested at 755 K in (a) Lithium Containing 500-700 wppm Nitrogen and (b) Sodium.

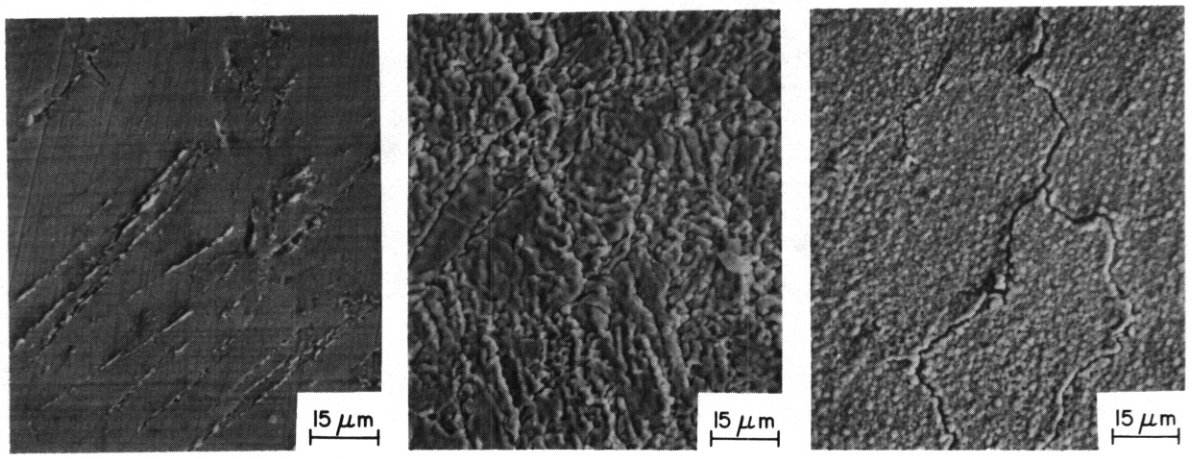

a b c

Fig. 9.3.16. Micrographs of the Gauge Surfaces of HT-9 Alloy Specimens Teated at 755 K in (a) Sodium, (b) Low-nitrogen Lithium, and (c) High-nitrogen Lithium.

lithium have a spongy surface and show appreciable corrosion. The extent of corrosion for the specimen tested in high-nitrogen lithium is higher than that for the specimen tested in low-nitrogen lithium. The former also contains several grain-boundary cracks, Similar behavior is observed for the Type 304 stainless steel. Figure 9.3.17 shows the gauge surfaces of Type 304 stainless steel specimens tested in sodium and lithium environments. The specimen tested in sodium shows a smooth surface with some slip markings, whereas the specimen tested in lithium is corroded and contains grain-boundary cracks.

D. Conclusions. In a flowing lithium environment, the corrosion behavior of constant stress specimens of HT-9 alloy and Type 304 stainless steel is independent of applied stress (stress levels below the yield stress of the material). The HT-9 alloy shows intergranular corrosion, whereas a uniform ferrite layer is observed on Type 304 stainless steel.

The fatigue properties of HT-9 alloy and Type 304 stainless steel in flowing lithium are strongly influenced by the concentration of nitrogen in lithium. For HT-9 alloy, the fatigue life in lithium containing 1000-1500 wppm nitrogen is a factor of 2 to 5 lower than that in lithium with 100-200 wppm nitrogen. Furthermore, in a low-nitrogen lithium environment, the fatigue life of HT-9 alloy is independent of strain rate in the range of 4×10^{-2} to 4×10^{-4} s^{-1}.

The reduction in fatigue life in high-nitrogen lithium can be attributed to internal corrosive attack of the material. Selective corrosion along grain boundaries or preferred crystallographic planes leads to early crack initiation and thereby reduces fatigue life. The reduction in life is greater at strain ranges <0.7% because at low strain ranges most of the fatigue life is spent in crack initiation. Furthermore, the decrease in fatigue life increases with an increase in nitrogen concentration in lithium.

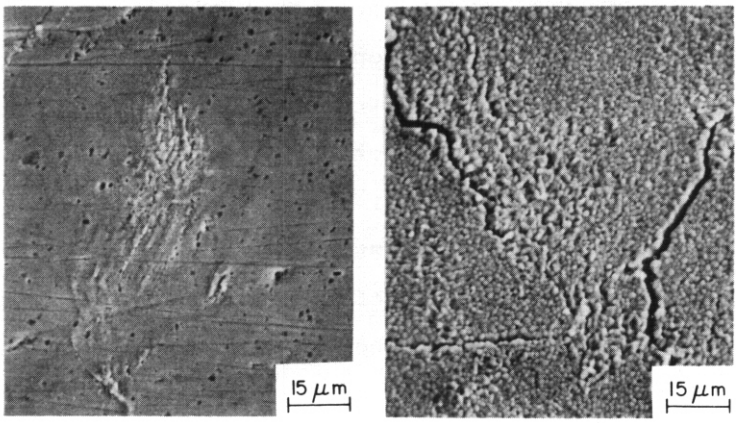

Fig. 9.3.17. Micrographs of the Gauge Surfaces of Type 304 Stainless Steel Specimens Tested at 755 K in (a) Sodium and (b) Lithium Containing 500-700 wppm Nitrogen.

For the tests conducted in high-nitrogen lithium, the mode of fracture is initially intergranular and becomes transgranular after ~150 μm of crack propagation. This indicates that the crack-propagation behavior may also be affected by the lithium environment. The fatigue fracture mode is intergranular when the rate of crack propagation is lower than the corrosion rate and becomes transgranular for crack propagation rates higher than the rate of corrosion.

9.3.4.2 Lead-Lithium Environment

Heavier metals, such as lead and bismuth, may be used for neutron multiplication in conjunction with tritium-breeding materials. Liquid lead-lithium can provide adequate tritium breeding with a reduced lithium inventory. However, the use of these liquid metals requires an assessment of the environmental effects on structural materials. Tests have been formulated to determine the combined effect of stress and environment on the corrosion behavior of candidate materials.

A forced-flow lead-lithium (17 at. % lithium) loop is being constructed. A schematic of the loop is shown in Fig. 9.3.18. The loop consists of a high-temperature test vessel and a cold leg. The test

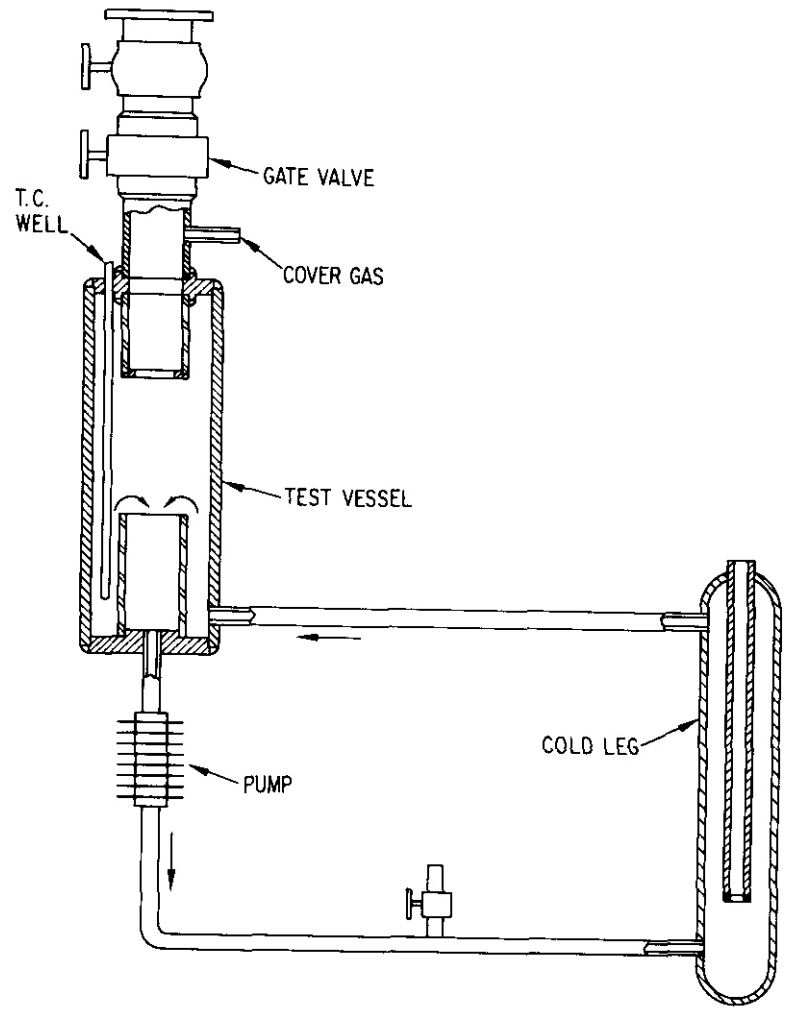

Fig. 9.3.18. Schematic of the Lead-Lithium Test Loop.

vessel is designed to accommodate the constant-stress fixture shown in Fig. 9.3.2. Compatibility tests will be conducted on tapered specimens to study the effect of flowing lead-lithium on the corrosion behavior.

9.3.4.3 Solid Ceramic Breeding Materials

A. Introduction. Several conceptual designs for fusion reactors incorporate a blanket system with solid ceramic tritium-breeding materials, such as Li_2O, $LiAlO_2$, and Li_2SiO_3. Compatibility of the solid breeding materials with candidate structural alloys is therefore a major consideration in assessing the viability of the design concepts.

The objective of the present program is to investigate the reactivity of solid breeding materials with commercial iron- and nickel-base alloys.

A comparative evaluation of the compatibility of HT-9 alloy, Type 316 stainless steel, and Inconel 625 exposed at 873 K for 1900 h in contact with pellets of Li_2O, γ-$LiAlO_2$, or Li_2SiO_3 tritium breeding materials was presented in earlier reports.[5,6] The results indicated that Li_2O is the most reactive of the three breeding materials. For this test, the various alloy/pellet reaction couples were retained in a common stainless steel test apparatus. The formation of volatile compounds, e.g., Li_5FeO_4 and $LiCrO_2$, resulted in cross contamination between the different reaction couples. A subsequent test was therefore designed to use isolated reaction couples.

B. Experimental. Tube specimens of HT-9 alloy and Type 316 stainless steel were packed with Li_2O, α-$LiAlO_2$, or Li_2SiO_3 ceramic powders. A flat specimen was also placed inside the tubes. Each alloy/ceramic couple was individually encapsulated to prevent cross-contamination by vapor transport between the couples. The configuration of the test capsules is shown in Fig. 9.3.19. The top and bottom plugs were machined from the same material as the test specimens. The capsules were baked at 973 K for 4 h under dynamic vacuum to remove adsorbed or reacted moisture and carbon dioxide from the ceramics. The tube specimens were then sealed, enclosed in a quartz tube, and annealed at 973 K for 1000 and 2000 h.

After the compatibility tests were completed, all alloy specimens were examined metallographically to determine the thickness of the reaction layers. The composition of the surface interaction scale was obtained by electron microprobe and energy dispersive x-ray analyses. The various reaction products were identified by x-ray diffraction analysis.

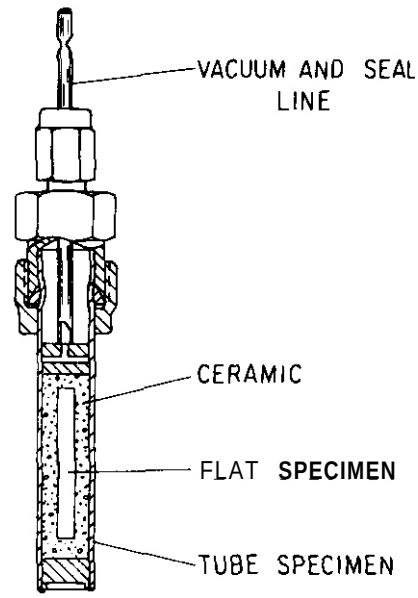

Fig. 9.3.19. Schematic of the Solid Breeder Compatibility Test Capsule.

Results. After annealing for 1000 and 2000 h at 973 K, the various capsule-test specimens were sectioned and examined metallographically to determine the thickness of the reaction scale and distribution of the constituents in the scale. Alloy specimens exposed with Li_2O ceramic had an adherent layer of the ceramic material; consequently, the thickness of the specimens after the compatibility test was greater than the initial thickness. Furthermore, the Li_2O had a brownish color. Such an interaction was not observed for the alloy/$LiAlO_2$ or alloy/Li_2SiO_3 capsules.

For all specimens, the total thickness of the reaction scale was obtained from the difference between the sound metal remaining (i.e., the unreacted material) and the specimen thickness after the test. The amount of metal loss (i.e., the thickness of the reacted metal) was determined from the difference between the initial thickness of the specimen and sound metal remaining. The average values of metal loss and total scale thickness for HT-9 alloy and Type 316 stainless steel exposed with Li_2O, $LiAlO_2$, and Li_2SiO_3 for 1000 and 2000 h at 973 K are given in Table 9.3.2. The results show that interaction for the

Table 9.3.2. Average Values of Metal Loss and Scale Thickness for Alloys Exposed with Li_2O, $LiAlO_2$, and Li_2SiO_3 at 973 K

Ceramic	Alloy	Ceramic/Alloy Interaction	Metal Loss (μm) 1000 h	Metal Loss (μm) 2000 h	Total Scale Thickness (μm) 1000 h	Total Scale Thickness (μm) 2000 h
Li_2O	HT-9	Strong	26	20	74	63
	316 SS	Strong	16	18	51	59
$LiAlO_2$	HT-9	Weak	8	5	8	5
	316 SS	Weak	6	5	6	5
Li_2SiO_3	HT-9	Weak	a	4	a	4
	316 SS	Weak	a	6	a	6

[a]Not tested.

alloy/Li_2O couples is significantly greater than that in the alloy/$LiAlO_2$ or alloy/Li_2SiO_3 couples. The values of metal loss and scale thickness are essentially the same after 1000 and 2000 h.

Micrographs and concentration profiles for iron, chromium, nickel, and oxygen across the reaction scale on HT-9 and Type 316 stainless steel specimens exposed with Li_2O for 1000 h are shown in Figs. 9.3.20 and 9.3.21, respectively. A very selective attack is observed in the HT-9 alloy, i.e., the specimen surface shows a network of oxides separated by regions of base metal. Electron microprobe analyses and concentration profiles for iron, chromium, and oxygen indicate that the gray regions are rich in chromium and oxygen whereas the light areas within the network consist of ~98% iron. Note that across the internal corrosion layer, the oxygen peaks coincide with the chromium peaks and with regions of decreased iron concentration. The outer adherent scale consists of the ceramic material embedded with various iron and chromium compounds. The interface between the outer scale and the internal corrosion scale contains a layer of relatively pure iron (i.e., region A in Fig. 9.3.20).

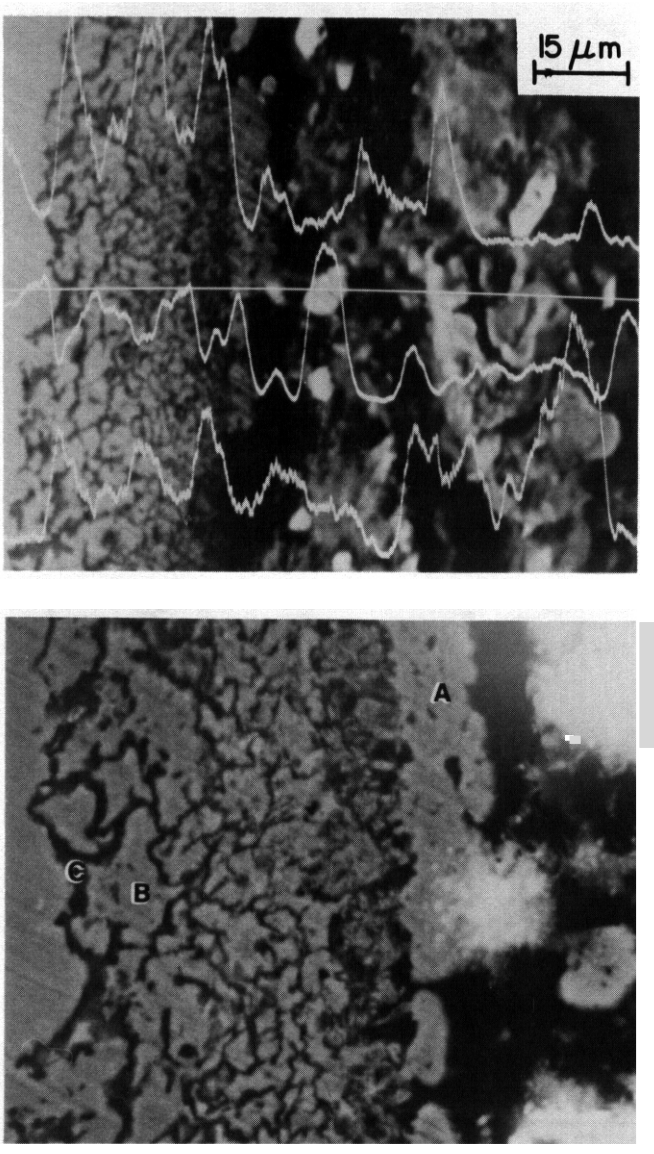

LOCATION	COMPOSITION (WT %) O	Fe	Cr
A	0.0	97.6	2.4
B	0.0	97.6	2.4
C	34.0	28.3	36.7

Fig. 9.3.20. Micrographs and Concentration Profiles for Iron, Chromium, and Oxygen Across, the Cross Section of HT-9 Alloy Exposed with Li_2O for 1000 h at 973 K.

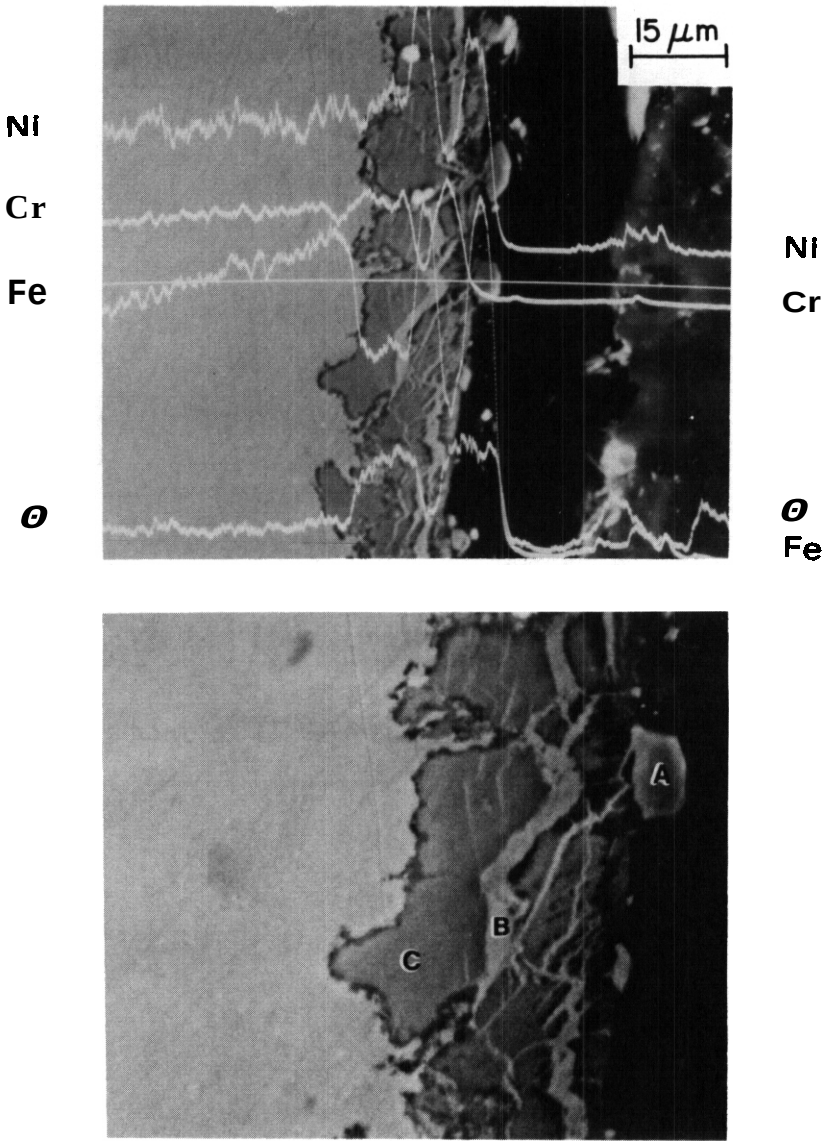

LOCATION	COMPOSITION (WT %) O	Fe	Cr	Ni	Mo
A	10.8	71.2	1.3	16.7	-
B	0.0	74.4	2.8	22.8	-
C	23.0	40.3	21.9	11.6	3.2

Fig. 9.3.21. Micrographs and Concentration Profiles for Iron, Chromium, Nickel, and Oxygen Across the Cross Section of Type 316 Stainless Steel Exposed with Li_2O for 1000 h at 973 K.

The Type 316 stainless steel specimen exposed with Li_2O shows a uniform attack (Fig. 9.3.21). Electron microprobe analyses and concentration profiles for iron, chromium, nickel, and oxygen indicate that the gray regions are oxides of iron and chromium and the light regions within the gray scale, i.e., region B in Fig. 9.3.21, are pure iron–nickel phase. The unreacted iron and nickel in the material grows as platelets within the reaction scale. The outer adherent scale is similar to that observed for HT-9 alloy and consists of the ceramic material embedded with pieces of the reaction product.

X-ray diffraction analysis of the surfaces of HT-9 alloy and Type 316 stainless steel exposed with Li_2O revealed Li_5FeO_4 and $LiCrO_2$ phases in the reaction scale. Diffraction patterns of the reaction products taken from different regions in the scale showed that $LiCr_2O$ was present near or on the specimen surface whereas the outer scale away from the specimen surface contained Li_5FeO_4. Pure iron was also detected in the outer scale.

D. Conclusions. Compatibility tests with isolated reaction couples indicate that Li_2O is the most reactive of the three breeding materials. Two products, Li_5FeO_4 and $LiCrO_2$, were detected in the reaction scales on HT-9 and Type 316 stainless steel specimens exposed with Li_2O material. Electron microprobe and x-ray diffraction analyses show that Li_5FeO_4 is predominant in the outer scale whereas $LiCrO_2$ is present near or on the alloy specimen. This behavior is consistent with the composition of these products, i.e., Li_5FeO_4 consists of $(Li_2O)_5 \cdot (Fe_2O_3)$ and $LiCrO_2$ contains $(Li_2O) \cdot (Cr_2O_3)$. The presence of volatile Li_5FeO_4 and $LiCrO_2$ compounds was also reported in similar studies on the compatibility of Fe–Cr–Ni alloys with Li_2O ceramic at temperatures between 773 and 1373 K.[7,8] The formation of Li_5FeO_4 may explain the greater interaction observed for the specimens exposed in contact with Li_2O material. The Li_5FeO_4 compound was not observed in the alloys exposed with either $LiAlO_2$ or Li_2SiO_3.

A significant result from the present study is that the thickness of the reaction scale is the same after 1000 or 2000 h. This behavior is observed for both Li_2O and $LiAlO_2$ ceramics. Similar studies with alloy/Li_2O diffusion couples showed that at 823 K, the reaction rate obeys a parabolic law with time.[8] However, the maximum test time for these studies was 1200 h. It is probable that after an initial period of rapid interaction, the reaction rate decreases to zero with time. Compatibility tests at 773 K are in progress.

9.3.5 Future Work

Fatigue tests are underway on lithium-exposed specimens to study long-term environmental effects. Preexposure of fatigue specimens of BT-9 alloy has been completed. The specimens were exposed at 755 K for 1000 h in lithium containing ~80 wppm nitrogen. The influence of lithium environment on the creep-fatigue behavior will he investigated by conducting fatigue tests using *a* sawtooth waveform. The results will be analyzed by damage-rate equations.

A compatibility-test facility is being constructed to study the alloy/ceramic interactions in a flowing helium environment containing known amounts of moisture.

9.3.6. References

1. D. L. Smith, R. H. Lee, and R. M. Yonco, "Investigation of Nonmetallic Element Interactions in Vanadium-Alloy/Lithium Systems," Proc. Second Intl. Conf. on Liquid Metal Technology in Energy Production, CONF-800401-P1, p. 2.72 (1980).

2. O. K. Chopra and D. L. Smith, "Effects of Lithium Environment on the Fatigue Properties of Ferritic and Austenitic Steels," Second ANS Topical Meeting on Fusion Reactor Materials, August 9-12, 1981, Seattle, WA, to be published in J. Nucl. Mater.

3. O. K. Chopra, K. Natesan, and T. F. Kassner, "Influence of Sodium Environment on the Low-Cycle Fatigue and Creep-Fatigue Behavior of Fe-2 1/4Cr-1Mo Steel," Proc. Second Intl. Conf. on Liquid Metal Technology in Energy Production, CONF-800401-P2, p. 19.9 (1980).

4. G. J. Zeman and D. L. Smith, "Low-Cycle Fatigue Behavior of Types 304 and 316 Stainless Steel Tested in Sodium at 550°C," Nucl. Technol. 42, pp. 82-89 (1979).
5. O. K. Chopra and D. L. Smith, "Environmental Effects on Properties of Ferritic Steels," ADIP Quarterly Progress Report, December 31, 1980, DOE/ER-0045/5.

6. O. K. Chopra and D. L. Smith, "Environmental Effects on Properties of Ferritic Steels," ADIP Quarterly Progress Report, September 30, 1980, DOE/ER-0045/4.

7. T. Kurasawa et al., "Reaction of Several Iron- and Nickel-based Alloys with Sintered Li_2O Pellets," J. Nucl. Mater. 80, pp. 48-56 (1979).

8. T. Kurasawa et al., "Compatibility between Several Heat Resistant Alloys and Sintered Li_2O in Static Helium Gas Environment," J. Nucl. Mater. 92, pp. 67-72 (1980).

DOE/ER-0045/7
Distribution
Category
uc-20, 20c

DISTRIBUTION

1. Ames Laboratory, Ames, IA 50011

F. V. Nolfi

2–6. Argonne National Laboratory, 9700 South Cass Avenue, Argonne, IL 60439

L. Greenwood
V. Maroni
R. E. Nygren
D. L. Smith
H. Wiedersich

7–8. Battelle-Pacific Northwest Laboratory, P.O. Box 999, Richland, WA 99352

J. L. Brimhall
D. Dingee

9. Brookhaven National Laboratory, Upton, NY 11973

C. L. Snead, Jr.

10. Carnegie-Mellon University, Schenley Park, Pittsburgh, PA 15213

J. C. Williams

11–231. Department of Energy, Technical Information Center, Office of Information Services, P.O. Box 62, Oak Ridge, TN 37830

For distribution as shown in TID-4500 Distribution Category, UC-20 (Magnetic Fusion Energy), and UC-20c (Reactor Materials)

232–238. Department of Energy, Office of Fusion Energy, Washington, DC 20545

M. M. Cohen
T. C. Reuther, Jr. (5 copies)
D. L. Vieth

239. Department of Energy, Oak Ridge Operations Office, P.O. Box E, Oak Ridge, TN 37830

Office of Assistant Manager for Energy Research and Development

240. General Atomic Company, P.O. Box 81608, San Diego, CA 92138

D. I. Roberts

241–248. Hanford Engineering Development Laboratory, P.O. Box 1970, Richland, WA 99352

H. R. Brager
D. G. Doran
F. A. Garner
D. S. Gelles
G. L. Wire
E. C. Opperman
R. W. Powell
J. L. Straalsund

249–251. Lawrence Livermore Laboratory, P.0. Box 808, Livermore, CA 94550

E.N.C. Dalder
M. Guinan
C. M. Logan

252. Massachusetts Institute of Technology, 138 Albany Street, Cambridge, MA 02139

O. K. Harling

253–254. Massachusetts Institute of Technology, 77 Massachusetts Ave., Cambridge, MA 02139

N. J. Grant
V. B. Vander Sande

255–256. McDonnell Douglas Astronautics Company, East, P.O. Box 516, St. Louis, MO 63166

J. W. Davis
D. L. Kummer

257. National Materials Advisory Board, 2101 Constitution Ave., Washington, DC 20418

K. M. Zwilsky

258–260. Naval Research Laboratory, Washington, DC 20375

Superintendent, Materials Science and Technology Division
J. A. Sprague
H. Watson

261–297. Oak Ridge National Laboratory, P.O. Box X, Oak Ridge, TN 37830

Central Research Library (2 copies)
Document Reference Section
Laboratory Records Department (2 copies)

Laboratory Records Department, RC
ORNL Patent Section
E. E. Bloom (10 copies)
D. N. Braski
J. H. DeVan
I. T. Dudley
M. L. Grossbeck
M. R. Hill (3 copies)
R. L. Klueh
R. A Lillie
C. T. Liu
K. C. Liu
L. K. Mansur
P. J. Maziasz
C. J. McHargue
T. K. Roche
A. F. Rowcliffe
J. L. Scott
P. F. Tortorelli
J. M. Vitek
F. W. Wiffen

298. Rensselaer Polytechnic Institute, Materials Engineering Department, Troy, NY 12181

N. Stoloff

299–300. Sandia National Laboratories, Livermore Division 8316, Livermore, CA 94550

W. Bauer
J. Swearengen

301. University of California, Department of Chemical, Nuclear, and Thermal Engineering, Los Angeles, CA 90024

R. W. Conn

302. University of California, Santa Barbara, CA 93106

G. R. Odette

303. University of Missouri, Department of Mechanical and Aerospace Engineering, Columbia, MO 65211

M. Jolles

304. University of Virginia, Department of Materials Science, Charlottesville, VA 22901

W. A. Jesser

305. University of Wisconsin, 1500 Johnson Drive, Madison, WI 53706

W. G. Wolfer

306. Westinghouse Electric Company, Fusion Power Systems Department, P.O. Box 10864, Pittsburgh, PA 15236

R. E. Gold

307. Westinghouse Electric Corporation, Advanced Reactors Division, P.O. Box 158, Madison, PA 15663

W. A. Boltax